MOLECULAR BEAM EPITAXY AND OPTICAL PERFORMANCE IN GROUP IV AND GROUP III-V SEMICONDUCTORS FOR PHOTONIC APPLICATIONS

BY

Rigo Alberto Carrasco, B.A.

A dissertation submitted to the Graduate School

in partial fulfillment of the requirements

for the degree

Doctor of Philosophy

Major Subject: Physics

New Mexico State University

Las Cruces New Mexico

December 2021

Rigo A. Carrasco

Candidate

Physics

Major

This dissertation is approved on behalf of the faculty of New Mexico State University, and it is acceptable in quality and form for publication:

Approved by the Dissertation Committee

Dr. Preston Webster

---

co-Chairperson

Dr. Stefan Zollner

---

co-Chairperson

Dr. Igor Vasiliev

Committee Member

Dr. Vassili Papavassiliou

Committee Member

Dr. David Voelz

Committee Member

DEDICATION

I dedicate this work to my father Rigoberto, my mother Rosa, and my siblings Fernando, Anna, Adrianna, and Manuel for their love and support.

ACKNOWLEDGMENTS

I would like to begin by thanking Dr. Preston Webster, and Dr. Perry Grant for being patient in teaching me how to design and grow novel Group III-V superlattices and quinary alloys through molecular beam epitaxy and taking me on as a full-time researcher under their guidance. I would also like to thank Dr. Christian Morath for giving me exposure on the more applied side of materials research, which allowed me to understand how the fundamental materials science ties in to the higher level applications of device physics. I'd also like to thank my colleagues in the Advanced electro-optical space sensors group (AEOSS) for providing great feedback during our group meetings.

Next, I would like to thank our collaborators at the University of Delaware: Ryan Hickey, John Hart, Ramsey Hazbun, Dominic Imbrenda, and Dr. James Kolodzey for providing the high Sn content GeSn samples grown by molecular beam epitaxy and working with us to characterize them using spectroscopic ellipsometry. I would like to thank Dr. Arnold Kiefer who supplied the α-Sn samples and was willing to introduce and mentor me on growing group IV alloys by molecular beam epitaxy. This hands-on experience gave me exposure on the experimental efforts required to achieve large-scale research endeavors.

Last, but certainly not least, I would like to thank my New Mexico State University advisor, Dr. Stefan Zollner, for his patience, encouragement and guidance

in the field of materials science. I would like to thank him for introducing me to the wide array of research opportunities that the Air Force Research Laboratory has to offer. Without them, I wouldn't have had the chance to meet and work with great scientists at Wright-Patterson Air Force Base, Kirtland Air Force Base, and the University of Delaware. I'd like to also thank Farzin Abadizaman, Carola Emminger, Nuwanjula Samarasingha, and Cesy Zamarripa for being amazing colleagues in this ellipsometry research group.

The research presented in this dissertation wouldn't have been possible without support from the Air Force Office of Scientific Research (FA9550-16RYCOR296); the Air Force Research Laboratory, Section 219 Commanders Research and Development Funds; 2018 summer faculty fellowship program, and the National Science Foundation (DMR-1505172).

VITA

2015	Transfer, San Joaquin Delta College, Stockton, California
2017	B.A. in Physics, University of California, Berkeley, California
2017-2019	Teaching Assistant, Department of Physics New Mexico State University
2019	Comprehensive exam passed for PhD candidacy New Mexico State University
2020-2021	Physicist, Applied Technologies Associates, a BlueHalo Company Albuquerque, New Mexico

PROFESSIONAL AND HONORARY SOCIETIES

Society of Physics Students

Physics graduate student organization, President 2018 - 2019

AWARDS

- Best poster award, 2021 Center for Integrated Nanotechnologies User Meeting, Sep. 2021
- Outstanding Graduate Assistant Award from the New Mexico State University Graduate School, Apr. 2019

PUBLICATIONS

- D. Imbrenda, **R. A. Carrasco**, R. Hickey, N. S. Fernando, S. Zollner, J. Kolodzey, "Band structure critical point energy in germanium-tin alloys with high tin contents," *Appl. Phys. Lett.* **119**, 162102 (2021)

- **R. A. Carrasco**, J. George, D. Maestas, Z. M. Alsaad, D. Garnham, C. P. Morath, J. M. Duran, G. Ariyawansa, and P. T. Webster, "Proton irradiation effects on InGaAs/InAsSb mid-wave barrier infrared detectors," *J. Appl. Phys.* **130**, 114501 (2021).

- **R. A. Carrasco**, C. P. Morath, P. C. Grant, G. Ariyawansa, C. A. Stephenson, C. N. Kadlec, S. D. Hawkins, J. F. Klem, E. A. Shaner, E. H. Steenbergen, S. T. Schaefer, S. R. Johnson, and P. T. Webster, "Recombination rate analysis in long minority carrier lifetime mid-wave infrared InGaAs/InAsSb superlattices," *J. Appl. Phys.* **129**, 184501 (2021).

- **R. A. Carrasco**, S. Zollner, S. A. Chastang, J. Duan, G. J. Grzybowski, B. B. Claflin, and A. M. Kiefer, "Dielectric function and band structure of $Sn_{1-x}Ge_x$ (x<0.06) alloys on InSb," *Appl. Phys. Lett.* **114**, 062102 (2019).

- **R. A. Carrasco**, C. M. Zamarripa, S. Zollner, J. Menéndez, S. A. Chastang, J. Duan, G. J. Grzybowski, B. B. Claflin, and A. M. Kiefer, "The direct bandgap of gray α-tin investigated by infrared ellipsometry," *Appl. Phys.*

Lett. **113**, 232104 (2018).

- D. Imbrenda, R. Hickey, **R. A. Carrasco**, N. S. Fernando, J. VanDerslice, S. Zollner, and J. Kolodzey, "Infrared dielectric response, index of refraction, and absorption of germanium-tin alloys with tin contents up to 27% deposited by molecular beam epitaxy," *Appl. Phys. Lett.* **113**, 122104 (2018).

- N. S. Fernando, **R. A. Carrasco**, R. Hickey, J. Hart, R. Hazbun, S. Schoeche, J. N. Hilfiker, J. Kolodzey, and S. Zollner,"Band gap and strain engineering of pseudomorphic $Ge_{1-x-y}Si_xSn_y$ alloys on Ge and GaAs for photonic applications," *J. Vac Sci. Technol. B.* **36**, 021202 (2018).

CONFERENCE CONTRIBUTIONS

- (invited) **R. A. Carrasco**, P. C. Grant, H. Orozco, M. S. Milosavljevic, C. P. Morath, S. R. Johnson, P. T. Webster, *Photoluminescence and Minority Carrier Lifetime of Quinary GaInAsSbBi Alloys Grown by Molecular Beam Epitaxy*, Air Force Research Laboratory RVS Tech Talk, Kirtland AFB NM, Sep. 2021

- **R. A. Carrasco**, P. C. Grant, H. Orozco, M. S. Milosavljevic, C. P. Morath, S. R. Johnson, P. T. Webster, *Photoluminescence and Minority Carrier Lifetime of Quinary GaInAsSbBi Alloys Grown by Molecular Beam Epitaxy*,

21st International Conference on Molecular Beam Epitaxy, Puerto Vallarta, Mexico, Sep. 6 - 9, 2021 (virtual)

- **R. A. Carrasco**, D. Maestas, Z. M. Alsaad, D. Garnham, C. P. Morath, P. C. Grant, P. T. Webster, *Proton Irradiation Effects on InGaAs/InAsSb Mid-Wave Infrared pBpn Detectors*, 21st International Conference on Molecular Beam Epitaxy, Puerto Vallarta, Mexico, Sep. 6 - 9, 2021 (virtual)

- M. S. Milosavljevic, S. T. Schaefer, R. R. Kosireddy, **R. A. Carrasco**, P. C. Grant, P. T. Webster, S. R. Johnson, *Optical Properties of GaInAsSb, InAsSbBi, and GaInAsSbBi Grown on GaSb Substrates*, 15th International Conference on Mid-Infrared Optoelectronic Materials and Devices, Surrey, United Kingdom, Sep. 2021 (virtual)

- (Invited) P. T. Webster, **R. A. Carrasco**, D. Maestas, Z. M. Alsaad, D. Garnham, C. P. Morath, P. C. Grant, *Proton Irradiation Effects on InGaAs/InAsSb Mid-Wave Infrared pBpn Detectors*, 2021 IEEE Research and Applications of Photonics in Defense, Aug. 2021 (virtual)

- (Invited) **R. A. Carrasco**, D. Maestas, Z. M. Alsaad, D. Garnham, C. P. Morath, P. C. Grant, P. T. Webster, *Proton irradiation effects on InGaAs/InAsSb mid-wave infrared pBpn detectors*, Air Force Research Laboratory RVS Tech Talk, Kirtland AFB NM, Jul. 2021

- (Invited) P. T. Webster, **R. A. Carrasco**, D. Garnham, J. George, P. C. Grant, C. P. Morath, D. Maestas, *Minority Carrier Lifetime of Strain-Balanced InGaAs/InAsSb Superlattices and Associated Detector Performance Gains in Mid-Wave Infrared Space Applications*, American Physical Society March Meeting, Mar. 2021 (virtual)

- (Invited) P. T. Webster, **R. A. Carrasco**, D. Garnham, J. George, P. C. Grant, C. P. Morath, D. Maestas, *Minority Carrier Lifetime of Strain-Balanced InGaAs/InAsSb Superlattices and Associated Detector Performance Gains in Mid-Wave Infrared Space Applications*, Air Force Research Laboratory RVS Tech Talk, Kirtland AFB NM, Mar. 2021

- **R. A. Carrasco**, C. M. Zamarripa, S. Zollner, J. Menéndez, *The Direct Band Gap of α-Sn Investigated by Infrared Ellipsometry*, 8th International Conference on Spectroscopic Ellipsometry, Barcelona, Spain, May 26 - 31, 2019

- **R. A. Carrasco**, C. M. Zamarripa, S. Zollner, J. Menéndez, *Direct Band Gap of Alpha-Tin Investigated by Infrared Ellipsometry*, DPG Frühjahrstagung, Regensburg, Germany, Mar. 31 - Apr. 5, 2019

- **R. A. Carrasco**, C. M. Zamarripa, S. Zollner, J. Menéndez, *The Direct Band Gap of α-Sn Investigated by Infrared Ellipsometry*, Physics and Chemistry of Surfaces, and Interfaces 46^{th} Conference, Santa Fe, NM, Jan 13 - 17,

2019

- P. Paradis, **R. A. Carrasco**, S. Zollner, V. Dahiya, A. Kasemi, J. Carlin, and S. Krishna, *Mid-infrared optical constants of InAsSb alloys and bulk GaSb*, AVS 65th International Symposium and Exhibition, Long Beach, CA, October 21 - 26, 2018

- **R. A. Carrasco**, C. Emminger, N. Samarasingha, F. Abadizaman, and S. Zollner, *Temperature-dependent dielectric function and critical point comparison of bulk Ge and α-Sn on InSb* AVS 65th International Symposium and Exhibition, Long Beach, CA, October 21 - 26, 2018

- C. M. Zamarripa, N. Samarasingha, F. Abadizaman, **R. A. Carrasco**, and S. Zollner, *Temperature-dependent ellipsometry and thermal stability of $Ge_2Sb_2Te_5C$ phase change memory alloys*, AVS 65th International Symposium and Exhibition, Long Beach, CA, October 21-26, 2018

- C. Emminger, **R. Carrasco**, N. Samarasingha, F. Abadizaman, and S. Zollner, *Temperature dependent dielectric function and critical points of bulk Ge compared to α-Sn on InSb*, IEEE Photonics Society 2018 Summer Topicals Meeting Series, Waikoloa, HI, July 9-11, 2018

- P. Paradis, **R. A. Carrasco**, S. Zollner, V. Dahiya, A. Kazemi, J. Carlin, and S. Krishna, *Mid-infrared optical constants of InAsSb alloys and bulk*

GaSb, 2018 NMAVS Symposium and Exhibition, Albuquerque, NM, May 22 2018

- C. M. Zamarripa, N. Samarasingha, F. Abadizaman, **R. A. Carrasco**, and S. Zollner, *Temperature dependent ellipsometry and thermal stability of* $Ge_2Sb_2Te_5C$ *phase change memory alloys*, 2018 NMAVS Symposium and Exhibition, Albuquerque, NM, 22 May 2018

- P. Paradis, **R. A. Carrasco**, S. Zollner, V. Dahiya, A. Kazemi, J. Carlin, S. Krishna, *Mid-infrared optical constants of InAsSb alloys and bulk GaSb*, Butler University 30th Annual Undergraduate Research Conference, Indianapolis, IN,13 April 2018

- **R. A. Carrasco**, N. Samarasingha, B.-Y. Nguyen, S. Zollner, *Ellipsometry analysis of germanium-on-insulator wafers*, APS March Meeting, Los Angeles, California, March 5 - 9, 2018

- N.S. Fernando, **R.A. Carrasco**, R. Hickey, J. Hart, R. Hazbun, J. Kolodzey, and S. Zollner, *Optical and structural characterization of pseudomorphic and relaxed* $Ge_{1-y}Sn_y$ *alloys (y<18.5%) grown on Ge by MBE*, Lawrence Symposium on Semiconductor Epitaxy, Scottsdale, AZ, February 2018

- **R. Carrasco**, N. S. Arachchige, C. Zamarripa, S. Zollner, S. Chastang, G.Grzybowski, J. Duan, B. Claflin, and A. Kiefer, *Spectroscopic Ellipsome-*

try and Band Structure of α-tin on InSb, Dayton, OH, January 10 2018

- **R. Carrasco**, N. Samarasingha, B.-Y. Nguyen, and S. Zollner, *Ellipsometry Analysis of Germanium-on-Insulator Wafers*, AVS 64th International Symposium and Exhibition, Tampa, Florida, October 30 – Sep 3, 2017

ABSTRACT

MOLECULAR BEAM EPITAXY AND OPTICAL PERFORMANCE IN GROUP IV AND GROUP III-V SEMICONDUCTORS FOR PHOTONIC APPLICATIONS

BY

RIGO ALBERTO CARRASCO, B.A.

Doctor of Philosophy

New Mexico State University

Las Cruces, New Mexico, 2021

Dr. Preston Webster, co-chair

Dr. Stefan Zollner, co-chair

This work presents the optoelectronic properties of mid-wave infrared III-V Ga-free InAs/InAsSb and InGaAs/InAsSb type-II superlattices, quinary GaInAsSbBi, and GeSn alloys grown by molecular beam epitaxy. The optoelectronic properties of the superlattices were probed with temperature dependent steady-state photoluminescence ranging from 4 K to 300 K to extract the bandgap as a function of temperature. The In(Ga)As/InAsSb superlattices' optoelectronic

performance were compared with temperature-dependent time-resolved photoluminescence measurements, and results indicate that there is little effect on the minority carrier lifetime with the inclusion of Ga. A recombination rate analysis is performed to determine the Shockley-Read-Hall, radiative, and Auger recombination lifetimes and is described in chapter 3. Then, photodetector process evaluation chips are made with *pBpn* InGaAs/InAsSb device structures and the devices' dark current and quantum efficiency are measured as a function of temperature and proton irradiation to simulate device degradation in a space radiation environment. Results show that with proton irradiation, a full recovery in quantum efficiency and negligible recovery in detector dark current post-irradiation-anneal is attributed to the permanent modification in the doping profile of the devices. The result is in stark contrast with the *nBn* photodetector which exhibits only partial recovery in both performance metrics and is discussed in chapter 4. Then, a quinary GaInAsSbBi is grown by molecular beam epitaxy and shows a minority carrier lifetime improvement due to the incorporation of Bi in comparison to a calibration quaternary GaInAsSb. This result is attributed to the surfactant behavior of Bi when it's introduced during growth. The quinary bandgap exhibits a 4.4 μm cutoff, a 0.5 μm extension beyond lattice matched InAsSb and is similar to a quaternary InAsSbBi previously grown at 360 °C, the results are reported and discussed in chapter 5. Furthermore, high-Sn content GeSn alloys ($\leq$27%) are grown by molecular beam epitaxy and their optical constants are extracted

by spectroscopic ellipsometry. The results show evidence of absorption beyond 6 μm, showing potential for mid-wave sensing in group IV alloys, and the results are discussed in chapter 6. Finally, the optical constants of Sn-rich GeSn alloys grown by molecular beam epitaxy with dilute Ge contents ranging from 0% to 5.9% are explored. A strong $\bar{E}_0$ absorption peak near 0.41 eV is found to be independent of temperature, strain, and Ge content. The peak is assigned to allowed intravalence band transitions from the Γ_7^- (electron-like) VB to the Γ_8^{+v} heavy hole VB and/or interband transitions from Γ_7^- to the Γ_8^{+c} light "hole" conduction band. These results are discussed in chapters 7 and 8.

CONTENTS

LIST OF TABLES

LIST OF FIGURES

1 Introduction

Group III-V semiconductors have potential in satisfying the need for a ≥ 5 μm (mid- to long-wave) photodetector. This is due to the fact that the telecommunications industry is already taking advantage of III-V semiconductor materials in the near- to short-wave infrared to support the telecommunication networks. Applications in the mid-wave infrared range include thermal imaging,[3] gas sensing,[4] and possible uses in medical diagnostics.[5] With the availability of low-cost, commercially available substrates, it becomes academically and technologically interesting to explore new design spaces for potential applications in mid-wave sensing campaigns. One way to achieve a mid-wave capable III-V device is by growing strain-balanced type-II superlattices where alternating constituent layers are grown to engineer the bandgap. In this work a comparative study was performed on the optical quality of InAs/InAsSb and InGaAs/InAsSb superlattices to understand the benefits of adding Ga in this superlattice system. Then, the radiation tolerance of these InGaAs/InAsSb photodetector performance metrics are measured. Radiation tolerance in the photodetectors becomes relevant when considering space-based sensing for missile warning. Another group III-V solution to achieving mid-wave infrared sensing is through alloying Bi in a III-AsSb material. Here, I report the minority carrier lifetime of quinary GaInAsSbBi and discuss the benefits of growing the quinary over a quaternary InAsSbBi.

Alternatively, alloying group IV semiconductors to achieve 5 μm would allow for monolithic integration with mature Si-based microelectronics, leading to high performance group IV-based photonics. Therefore, it's important to understand the optical constants of the group IV alloy system from high Sn contents to the endpoint constituent α-Sn, in order to design appropriate photodectors and device structures.

2 Semiconductor growth and characterization

2.1 Molecular beam epitaxy

Molecular beam epitaxy is a material growth process that involves heating ultra pure solid sources to their vapor phase, creating molecular beams that are then aimed at a substrate. These constituent molecular beams impinge and stick to the substrate and bond, resulting in material of high crystalline quality. This growth method is made possible by maintaining background chamber pressures at $\leq 5\times10^{-10}$ torr with the use of ion and cryogenic vacuum pumps. The low pressure maintained in the growth chamber allows for the molecular beams to have mean free paths larger than the diameter of the growth chamber.[6] If any gas remains in the chamber and collides with the chamber walls, it can be considered lost from the system since the chamber is lined with a cryoshroud within which a constant supply of liquid nitrogen is flowing. Molecular beam epitaxy provides high tunability to growth rates and allows for manifesting quantum structures such as quantum wells and superlattices through the use of mechanical shutters and valves to precisely control the beam fluxes.

Group III-V materials are grown using a VG-V80H molecular beam epitaxy system with In, Ga, and Al group-III effusion cells, As and Sb group-V valved cracker cells, and a valved Bi effusion cell. All substrates are first transported to a load lock where initial pumping begins on the sample and then are transported to

a prep chamber where an outgas stage is available to heat the substrate and outgas contaminants that could degrade the quality of subsequent growths if they were outgassed in the growth chamber. Figure 2.1 shows the molecular beam epitaxy system used to grow the III-V materials. The utility and process flow of source calibration, sample prep and sample growth will be discussed in the proceeding section.

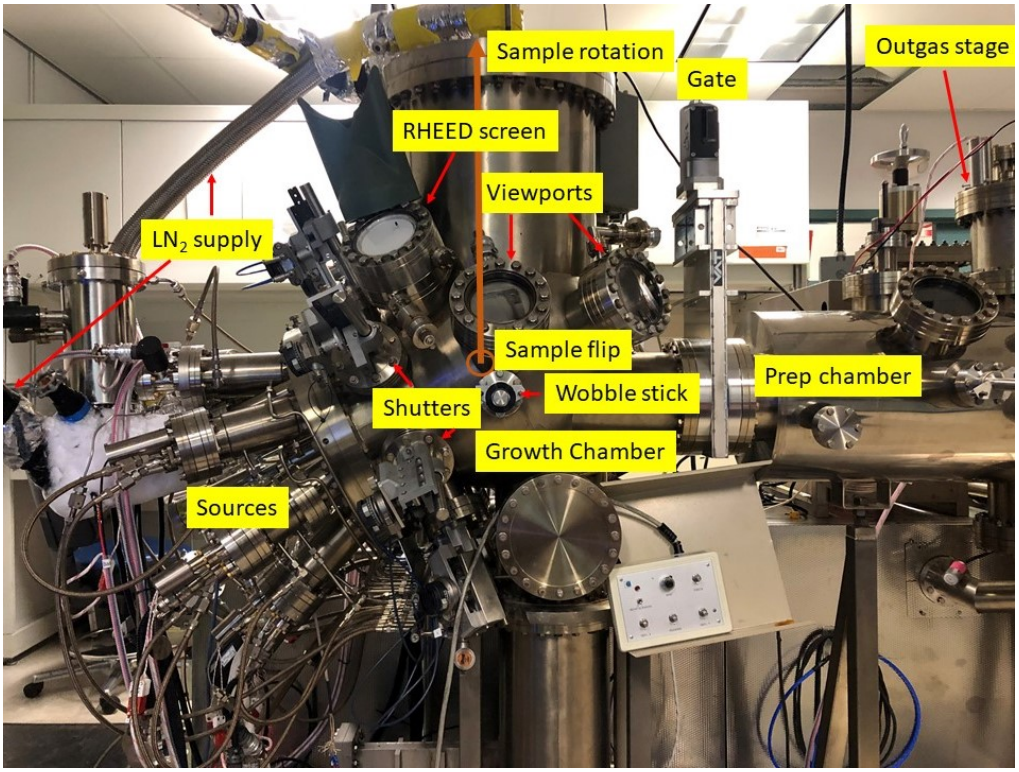

Figure 2.1: VG-V80H solid source molecular beam epitaxy system. Various parts of the system are labeled that are used to grow III-V materials. Red arrows point to the components that are used for growing III-V material while the orange circle and arrow indicate the different axes of rotation of the manipulator for substrate flip and rotation. The vertical orange axis allows for substrate rotation and the axis pointing into the picture allows for the substrate to flip to the growth, load, or flux positions.

2.1.1 Chamber and source calibration

Group III growth rates and V/III flux ratios must be calibrated before any superlattice or alloy growth can commence.[7] We begin by measuring with an ion gauge the beam flux of the group-III cells as a function of cell thermocouple temperature. Then, a subsequent growth of a binary III-V material (InAs for In growth rate calibration and GaAs for Ga growth rate calibration) is homoepitaxially grown at roughly 1 um/hr with an As overpressure.

During the growth, an electron gun with a current of 1.5 A and 12.4 kV is aimed at grazing incidence where the electrons undergo diffraction by the surface of the material. The surface can be thought of as a 2 dimensional grating where the reciprocal lattice is a set of rods normal to the surface, and the rods that intersect with the Ewald sphere of elastic reflections are viewed on a phosphor screen, showing the streaks seen in Fig. 2.2. This *in-situ* method of observing surface conditions is known as reflection high energy electron diffraction (RHEED). Through RHEED, the growth rate can be extracted by measuring the period of intensity oscillations of the RHEED streaks with a camera and software that can track the intensity of the major and minor streaks.[8] With a given growth rate corresponding to an In cell temperature, a lookup function is created, providing a relationship between growth rates to thermocouple cell temperatures. After an approximate growth rate is provided, the unity flux ratio is determined by closing

the As valve while observing the RHEED pattern change from an As-rich surface to an In-rich surface. The As flux reading at the As valve position provides the unity As/In flux ratio required at the provided growth rate. Fig. 2.2 shows the RHEED pattern for an As-rich and an In-rich surface during growth with arrows drawn to guide the eye.

Before a new GaSb wafer is introduced in the growth chamber to grow a calibration InAs/InAsSb superlattice, the wafer is heated at 400 °C for about 1 hour in a prep chamber to outgas any atmospheric contaminants adhered to the wafer and block surfaces. After this heat treatment, the sample is then introduced into the growth chamber and heated to a pyrometer temperature reading of 540 °C, while also bringing the In cell to the desired growth temperature. During the heating process, the shutter and valve of the Sb cell are fully opened once the pyrometer reaches 400 °C to prevent excessive Sb desorbing from the GaSb substrate surface and creating a Ga-rich surface. This Sb flux prevents growths from commencing on a Ga-terminated surface, which would create a sample with poor optoelectronic quality. Once the substrate temperature reaches 540 °C, the pyrometer is monitored for another 15 minutes, increasing the substrate heater power to maintain the 540 °C target. After 15 minutes of outgassing the GaSb substrate, the substrate is cooled to 500 °C to grow a GaSb buffer. The substrate temperature is then cooled to 440 °C to grow a lattice matched InAsSb layer. The InAsSb layer acts as a confinement layer for the 5 μm wavelength InAs/InAsSb

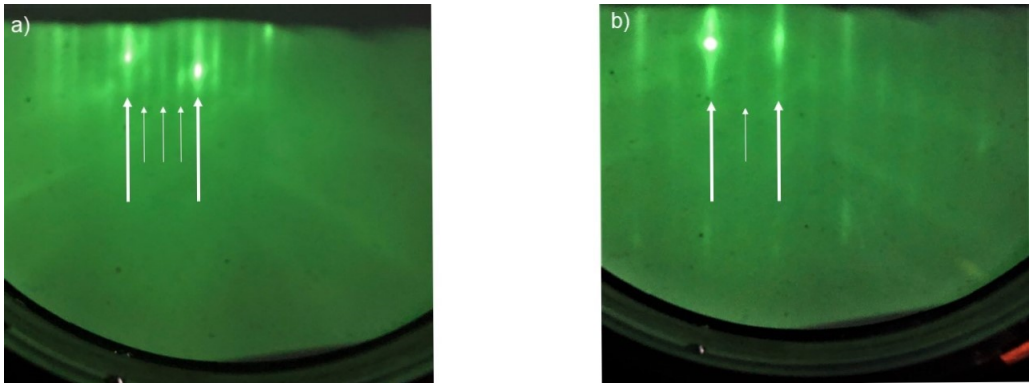

Figure 2.2: RHEED patterns of InAs with an As-rich and an In-rich surface being grown at the same sample azimuth. Subplot a) shows a RHEED pattern of InAs being grown with an As-rich surface and subplot b) shows a RHEED pattern with InAs being grown with an In-rich surface. The bold arrows point to the major streaks while the thinner arrows point to the minor streaks to guide the eye.

material that follows, which is grown at a lower temperature. After the buffer is grown, the strain-balanced mid-wave infrared InAs/InAsSb superlattice is grown at 1 um/hr to more precisely refine the In growth rate calibration, to calibrate the Sb flux ratio, and to gauge whether the chamber vacuum conditions are ideal for growing samples with long minority carrier lifetimes, (>1 μs) a technologically relevant material performance metric. Growth parameters chosen for an InAs/InAsSb superlattice can be found in Ref. [9] where a Krönig Penney model was used to design superlattices at different wavelength cutoffs.

After growth and through X-ray diffraction, the superlattice satellite peaks provide a period thickness, where the ratio of the measured to target period thickness is equal to the ratio of the actual growth rate to the target growth rate for the sample, providing feedback to determine the In cell temperature needed

for a desired growth rate. With the newly determined period thickness, the InAs and InAsSb constituent layer thicknesses can be extracted since the superlattice period thickness mismatch will scale with the constituent layer thicknesses. Once the superlattice constituent layer thicknesses are determined, the amount of Sb incorporated in the superlattice can be evaluated by aligning the zeroth order simulated superlattice peak to the measured zeroth order peak.

2.1.2 Quinary growth

With growth rates and flux ratios calibrated for growing strain-balanced superlattices and lattice-matched InAsSb, a few more calibration growths will be required for growing a quinary material. For more efficient Bi incorporation, growths are conducted at a substrate temperature of 400 °C; this will degrade the optical quality in terms of the minority carrier lifetime in comparison to a substrate growth temperature of 440 °C, but will improve the amount of Bi incorporation in the alloy.[10, 11] To begin, a compressive InAsSb alloy is grown at 400 °C with a targeted unity As/In flux ratio, and a 1 μm/hr In growth rate. The relatively lean As/In flux condition is required to achieve near stoichiometric flux ratios, this acts to encourage Bi incorporation at higher growth temperatures. Otherwise, growing with an As/In flux ratio of $\sim$1.5 (typical for growing high quality InAsSb) would inhibit Bi incorporation, evidenced by previous experiments.[12, 13] The amount of strain in this ternary measured by X-ray diffraction will provide a guide as to

how much Ga would need to be incorporated in order to grow a lattice matched quaternary.

Following the compressive ternary, a similar growth is performed but Ga is then introduced to lattice match the system to the GaSb substrate. The total group III growth rate is maintained at 1 μm/hr and the V/III flux ratios were kept constant. This is to ensure a lattice-matched quaternary can be grown before incorporating Bi to reduce the bandgap. The group III constituents have high sticking coefficients during growth and hence it's valid to assume that consistent group III flux conditions over subsequent growths will result in similar growth rates and mole fractions. Finally, the growth is repeated with the same growth conditions, but now Bi is introduced in the quaternary growth and any changes that are observed by X-ray diffraction, steady-state photoluminescence and time-resolved photoluminescence will be attributed to the incorporation of Bi. Table 2.1 shows the calibration growths performed to arrive at the quinary, and Fig. 2.3 shows the resulting X-ray diffraction patterns for the compressively strained ternary InAsSb, quaternary GaInAsSb, and quinary GaInAsSbBi.

The X-ray results display observable Pendellösung fringes on either side of the GaSb substrate, where the shorter period fringes are indicative of high crystalline quality of the samples grown, and the shift of the quinary peak angle to a more compressive angle suggests that Bi was incorporated in the sample. Further investigation on the bandgap and optical quality of the quinary bismide is reported

Table 2.1: Sample and growth conditions used to calibrate a lattice-matched quaternary to grow a quinary III-V bismide.

Sample	Growth Temp. (°C)	Strain (arcsec)	Growth rates (μm/hr)		Flux Ratios		
			In	Ga	As/III	Sb/III	Bi/III
InAsSb	400	-462	1.008	0	0.953	0.110	0
GaInAsSb	400	-22	0.969	0.029	0.963	0.112	0
GaInAsSbBi	400	-54	0.985	0.029	0.966	0.108	≈0.02

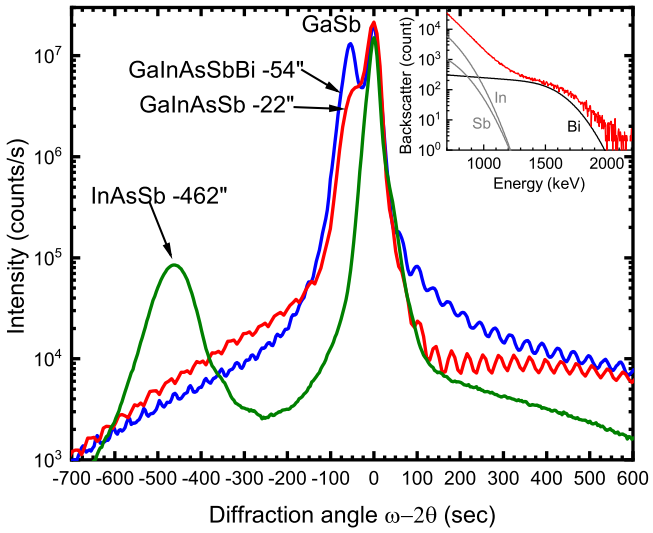

Figure 2.3: X-ray diffraction of quaternary $InAs_{0.911}Sb_{0.081}Bi_{0.008}$ (green), quaternary $Ga_{0.029}In_{0.971}As_{0.882}Sb_{0.118}$ (blue), and quinary $Ga_{0.029}In_{0.971}As_{0.883}Sb_{0.116}Bi_{0.001}$ (red). Inset shows Rutherford backscattering spectroscopy of the $Ga_{0.029}In_{0.971}As_{0.883}Sb_{0.116}Bi_{0.001}$ sample (red) and simulated fit of Bi mole fraction (black).

in chapter 5.

2.2 Spectroscopic ellipsometry

Spectroscopic ellipsometry is a non-contact, optical probing method that allows determination of a material's complex refractive index. This is made possible due to the capability of measuring relative magnitude ψ and phase change Δ of reflected light, allowing for extraction of two material parameters $(n + ik)$. In typical reflectivity measurements, only the real part of the complex refractive index can be extracted and the imaginary part is calculated by a Kramers-Kronig transform.

Spectroscopic ellipsometry is capable of providing film thickness, and the result can confirm the thickness extracted through other experimental techniques such as X-ray diffraction. Furthermore, with second derivative analysis of the real and imaginary parts of the dielectric function, band structure critical point parameters can be provided from the results. This would give insight in material strain state and provide a window to energy band splittings in the electronic structure for engineered materials such as alloys.[14] The relation between the complex refractive index and the dielectric function is,[15]

$$n = \frac{1}{\sqrt{2}}\left(\epsilon_1 + \left(\epsilon_1^2 + \epsilon_2^2\right)^{1/2}\right)^{1/2}; k = \frac{1}{\sqrt{2}}\left(-\epsilon_1 + \left(\epsilon_1^2 + \epsilon_2^2\right)^{1/2}\right)^{1/2}, \qquad (1)$$

where $\epsilon_1 + i\epsilon_2$ is the complex dielectric function and $n+ik$ is the complex refractive

index. When it comes to designing optoelectronic devices such as sensors and lasers, the absorption coefficient is a technologically relevant material property, as it is fundamental when determining the quantum efficiency of the device. The absorption coefficient is calculated by the material's fundamental optical constants by,

$$\alpha = \frac{4\pi k}{\lambda}, \tag{2}$$

where λ is the free space wavelength of light, and k is the extinction coefficient in Eq. (1).

2.2.1 Experimental background

In principle, ellipsometry measures the change in polarization state of reflected light, and understanding the underlying physics of the technique requires a brief review of the Fresnel equations. Consider an electromagnetic wave incident on an interface between two media as shown in Fig. 2.4. When solving the boundary condition problem for an electromagnetic wave polarized parallel to the plane of incidence (p-wave), the ratio of magnitudes of the reflected wave to the incident wave (reflectance ratio) will be, [16, 17]

$$r_p = \frac{E_{rp}}{E_{ip}} = \frac{-N_2^2\cos(\theta_i) + N_1\sqrt{N_2^2 - N_1^2\sin^2(\theta_i)}}{N_2^2\cos(\theta_i) + N_1\sqrt{N_2^2 - N_1^2\sin^2(\theta_i)}} = \tan(\psi_p)\exp(i\Delta_p), \tag{3}$$

where $N_j = n_j + ik_j$ is the complex refractive index of the jth layer, and θ_i is the angle of incidence. On the right side of Eq.(3), $\tan(\psi_p)$ is the ratio of magnitudes

of the reflected wave to the incident p-polarized wave, and Δ_p is the relative phase difference.

For the case of waves polarized perpendicular to the plane of incidence (s-waves, meaning *senkrecht* which is German for perpendicular), the reflectance ratio is,

$$r_s = \frac{E_{rs}}{E_{is}} = \frac{N_1 \cos(\theta_i) - \sqrt{N_2^2 - N_1^2 \sin^2(\theta_i)}}{N_1 \cos(\theta_i) + \sqrt{N_2^2 - N_1^2 \sin^2(\theta_i)}} = \tan(\psi_s) \exp(i\Delta_s), \tag{4}$$

where the sign convention follows that of Tompkins.[17] A conceptual illustration

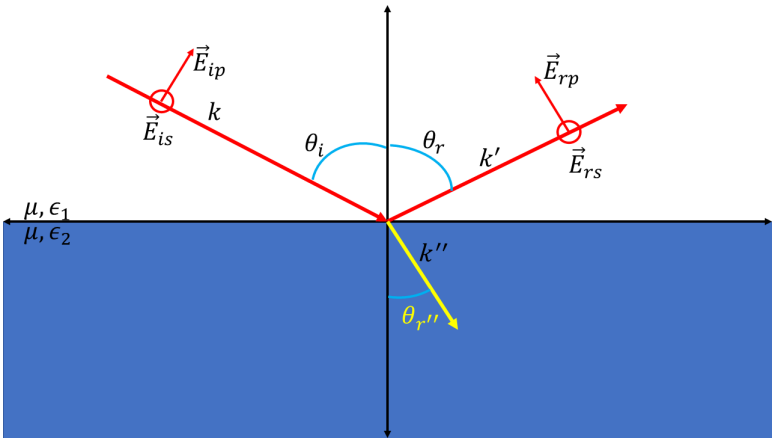

Figure 2.4: A ray optics illustration of light incident on an interface. An electromagnetic wave incident on a boundary between two media will result in a reflected wave k′ and a refracted wave k″ following the boundary conditions of Maxwell's wave equation. Image modeled after Ref. [16]

of ellipsometry can be seen in Fig. 2.5. Light with a known polarization state (it can be a linear combination of s- and p-polarization) is incident on a material of interest. Then, the light is reflected and the polarization components follow their respective Fresnel criterion in Eqs. (3, 4). The light is then collected by a detector

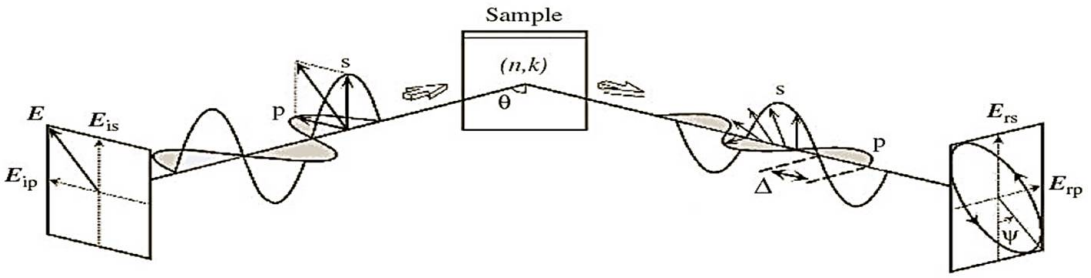

Figure 2.5: Experimental visualization of an ellipsometry measurment. Light with a known polarization state (in this case linear polarized light) is incident on a sample with optical constants N = n + ik. The reflected light is now in an elliptically polarized state where the change in polarization is described by the ellipsometric angles ψ and Δ. Image taken from https://ellipsometry.nmsu.edu/ellipsometry/; accessed on 04-01-2021.

that proceeds a second rotating polarizer (also referred to as the analyzer), and the reflectance ratio is extracted, resulting in the ellipsometric angles,

$$\tan\psi \exp i\Delta = -\frac{r_p}{r_s} = -\frac{\tan(\psi_p)}{\tan(\psi_s)} \exp i(\Delta_p - \Delta_s) \tag{5}$$

where $\tan(\psi)$ is the ratio $|r_p/r_s|$, and Δ is the phase difference. The name ellipsometry comes from the general polarization state of reflected light, *elliptically polarized light*.

The ellipsometry measurements were performed on two commercially available ellipsometers to probe an optical range of 0.031 eV - 6.5 eV (40 μm - 191 nm). The first ellipsometer in Fig. 2.6 is a J.A. Woollam vertical-variable angle spectroscopic ellipsometer (V-VASE) configured to perform a temperature-dependent spectroscopic ellipsometry experiment. The cryostat is capable of reaching liquid helium temperatures, as well as temperatures as high as ∼740 K.[18] The V-VASE has

a rotating analyzer, and it is equipped with a computer controlled Berek wave-plate compensator allowing for high accuracy measurements in the range from 0.5-6.5 eV. The instrument is configured in a direct spectroscopy setup where the monochromator scans through the spectrum of a Xe lamp to provide incident light at single energies. The light then passes through the polarizer, followed by the compensator to provide a wide range of polarization states before the light is incident on the sample. The reflected light then enters the detector side of the instrument where it passes through the analyzer and is finally collected by the detector. The reflected light is measured as a function of different compensator angles to extract the ellipsometric angles ψ and Δ. The spectroscopic ellipsometry measurement is analyzed by modeling the spectra with trial optical constants; once there is good agreement between the simulated model and measured data, the material's optical constants are extracted.

The V-VASE is only capable of performing spectroscopic ellipsometry from the ultraviolet down to the near infrared regime. In order to measure the complex reflectivity of a sample in the infrared regime, an instrument capable of producing and detecting photon energies in the infrared is required. This is achieved through the use of a Fourier transform infrared variable angle spectroscopic ellipsometer. Fig. 2.7 shows a Fourier transform infrared variable angle spectroscopic ellipsometer[19] (IR-VASE) configured to perform in-air measurements, but is also capable of performing temperature dependent measurements with the cryostat at-

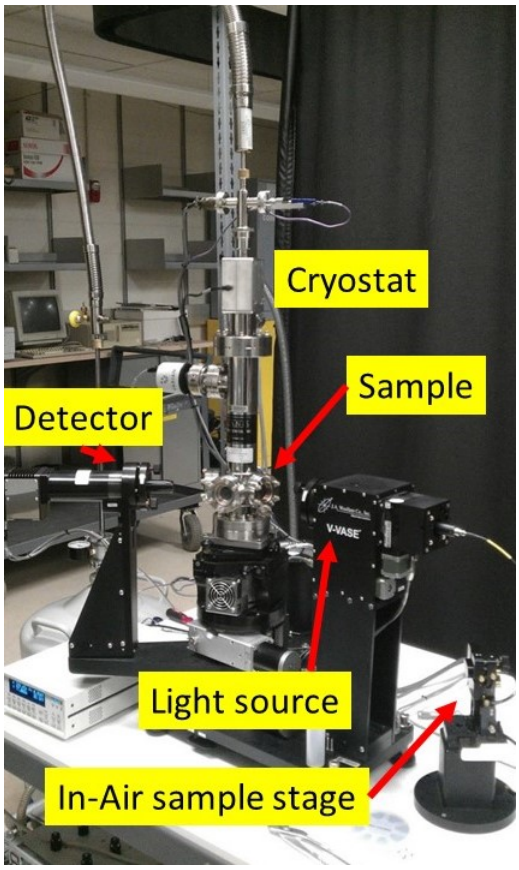

Figure 2.6: A J.A. Woollam V-VASE. The setup shown has a cryostat mounted on the stage where temperature-dependent measurements can be conducted. The instrument is controlled through the WVASE software.

tachment, (shown behind the ellipsometer). The IR-VASE is configured with a compensator placed after sample reflection. The Si-C black-body spectrum is passed through an interferometer and then a wire grid polarizer before the light is incident on the sample. Upon reflection, the light is sent to the detector side where a compensator rotates the polarization of the reflected light, then it passes through the analyzer, and is finally incident on the detector where an interferogram is measured. A Fourier transform is performed on the interferogram and the resulting output is the spectrum. After measuring the spectrum at different compensator angles, the ellipsometric angles can be extracted.

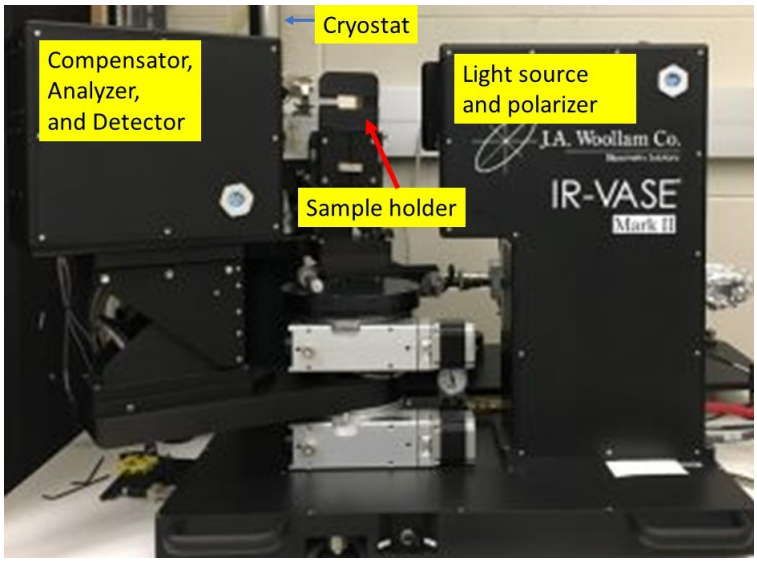

Figure 2.7: A J.A. Woollam IR-VASE.

After an ellipsometry measurement is performed, data modeling is needed in order to further understand the results. One technique to model the ellispometric

angles is to reference a database of material optical constants, which is readily available in the WVASE32 sofware.[20] This can serve as a starting point for bulk material. When a material's optical constants are unknown, the optical response can be modelled with a Kramers-Kronig consistent oscillator model provided by the WVASE software, provided the optical constants and thicknesses of every other layer in the structure are known.

2.2.2 Band structure critical points

Once the dielectric function of a material of interest has been extracted, features of shoulders and peaks will be observed at different energies. These features in the material's dielectric function correspond to band structure critical points attributed to areas in the Brillouin zone where electrons in a filled valence band transition to an empty conduction band (the critical points are also known as Van Hove singularities).[21] Critical point analysis involves taking the numerical second derivative of the extracted dielectric function and fitting the features to an analytical lineshape. The second derivative of the dielectric function is analyzed to remove any constant background and low-order influence from other critical points. For the electronic transitions located at the Γ-point of the Brillouin zone (E_0 and $E_0 + \Delta_0$ critical points), 3 dimensional critical points are assigned,[22]

$$\epsilon(\hbar\omega) = C - Ae^{i\phi}(\hbar\omega - E_g + i\Gamma)^{1/2}, \tag{6}$$

where C is a constant, A is the amplitude related to the electron-dipole oscillator strength, $\hbar\omega$ is the photon energy, E_g the critical point energy, Γ is the critical point broadening, and ϕ is the excitonic phase angle, that describes the amount of mixing.

Then, for direct electronic transitions located in the direction of the L-valley, (E_1 and $E_1 + \Delta_1$ critical points) a mixture of a two-dimensional minimum and a saddle point is assigned,[23]

$$\epsilon(\hbar\omega) = C - Ae^{i\phi} \ln(\hbar\omega - E_g - i\Gamma). \tag{7}$$

For critical point pairs that are located in the same region of the Brillouin zone (Γ-point, L-valley, etc.) but the energies are separated by spin-orbit coupling Δ, a single excitonic angle ϕ is assigned to the pair. Fig. 2.8 illustrates the dielectric function of α-Sn and the corresponding critical point analysis that follows in order to extract the critical point parameters in Eq (7).

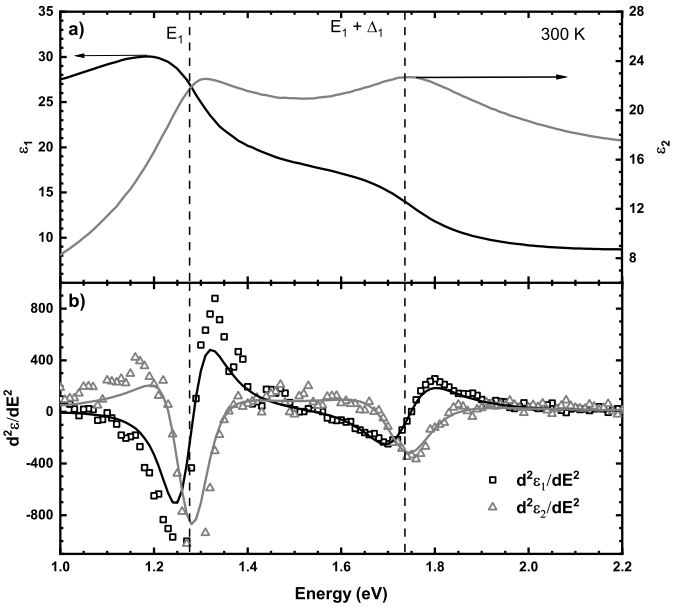

Figure 2.8: Dielectric function and critical point analysis of α-Sn from 1.0-2.2 eV. Subplot a) is the extracted dielectric function of α-Sn in the 1.0-2.2 eV range where the E_1 and $E_1 + \Delta_1$ critical points are shown. The black and gray lines are the real and imaginary parts to the dielectric function, respectively. Subplot b) is the second derivative analysis of the data (symbols) and the best fit parameters of Equation (7) to the data (solid lines). The vertical dashed lines are the extracted E_1 and $E_1+\Delta_1$ energies. Data and critical point parameters taken from Ref. [24].

Fig. 2.8(a) shows the real and imaginary parts of the dielectric function denoted by the black and gray solid lines, respectively. The vertical dashed lines denote the critical point energies of the E_1 and $E_1+\Delta_1$ transitions extracted from second derivative analysis in Fig. 2.8(b). It can be seen that the critical point energies don't necessarily correspond to the peak energies observed in the imaginary part of the dielectric function.

2.3 Time-resolved photoluminescence, and recombination rate analysis

Time-resolved photoluminescence is an optical performance benchmarking tool that allows for extraction of the minority carrier lifetime τ_{mc} of materials with high optical quality. This experimental technique is a non-contact, non-destructive characterization method that can provide rapid feedback on the conditions of the growth environment in a material synthesis reactor, such as a molecular beam epitaxy system. The minority carrier lifetime is also a fundamental material parameter that has an influence on the higher level device performance metrics such as the device quantum efficiency and dark-current. The minority carrier lifetime is related to the quantum efficiency through the diffusion length L_D of a material where,

$$L_D = (D\tau_{mc})^{1/2} = (k_B T \mu \tau_{mc}/e)^{1/2}. \tag{8}$$

In Eq. (8), D is the diffusion coefficient of the material that quantifies the effectiveness with which the minority carriers can transport under diffusion through the material. Then, on the right-hand side of Eq. (8), the diffusion coefficient is equivalent to the product of the Boltzmann constant k_B and temperature T over the electron charge e, and minority carrier mobility μ. This is then found in Van de Wiele's expression for the quantum efficiency in the quasi-neutral absorbing

region η_{qn} of a detector,[25]

$$\eta_{qn} = \left(\frac{\alpha^2 L_D^2}{1-\alpha^2 L_D^2}\right)\left\{e^{-\alpha L_A} - \frac{1}{\cosh\left(L_A/L_D\right)} + \frac{e^{-\alpha L_A}\tanh\left(L_A/L_D\right)}{\alpha L_D}\right\}. \quad (9)$$

In Eq. (9), the quantum efficiency is dependent on the material's absorption coefficient α, the length of the absorbing material L_A and the diffusion length L_D determined in Eq. (8). In regards to engineering the material's performance, maximizing the minority carrier lifetime τ_{mc} by producing low defect concentration material is paramount for achieving a high-quality, high performance photodetector, whereas other parameters such as the absorption coefficient, and minority carrier mobility are intrinsic to the material's band structure and material design.

Furthermore, the diffusion dark-current in an n-type absorber in the thin-based limit ($L_D \gg L_A$) is,

$$J_{diff} = e\frac{n_i^2 L_A}{n_0 \tau_{mc}}, \quad (10)$$

where the diffusion current J_{diff} is inversely proportional to the product of the majority carrier concentration n_0 and the minority carrier lifetime τ_{mc}. Here, we see again the dependence of a device's performance metric on the minority carrier lifetime. Therefore, understanding the minority carrier lifetime and its temperature dependence is relevant when exploring new material designs for possible device applications. Proceeding this section is a discussion on the time-resolved photoluminescence experimental setup, followed by a description on the recombination rate analysis of the temperature dependent minority carrier lifetime.

2.3.1 Experimental setup

Time-resolved photoluminescence is performed by pumping the mid-wave infrared samples with a 1535 nm (0.81 eV) pulsed laser with samples mounted in a liquid nitrogen cooled cryostat. The laser pulses are 3.5 ns long and the excitation is varied to inject 10^{11} - 10^{12} photons/cm^2 per pulse in the active region using a motorized half-waveplate compensator and polarizing beam splitter combination. Beam spot size is then adjusted using an iris. The photoluminescence signal is collected and collimated with a 2 in. diameter f/2 90° off-axis parabolic mirror and then focused with a second off-axis parabolic mirror (2 in.; f/1; 90°) to transmit through a 2.4 μm cutoff long-pass filter to remove the pump laser pulses and is measured by a 6 μm cutoff VIGO Systems PVI-4TE detector. A Teledyne Lecroy HD 4096 oscilloscope averages 100,000 time-resolved photoluminescence decays to acquire one photoluminescence decay signal per excitation condition per temperature from 77 to 300 K. An optical block diagram illustrating the experimental setup can be seen in Figure 2.9. The minority carrier lifetime is determined by fitting the low-excitation regime of the signal with a characteristic single exponential decay where the decay constant corresponds to the minority carrier lifetime at the specified temperature. Determining the minority carrier lifetime as a function of temperature provides information on the different recombination mechanisms, which will be discussed in the proceeding section.

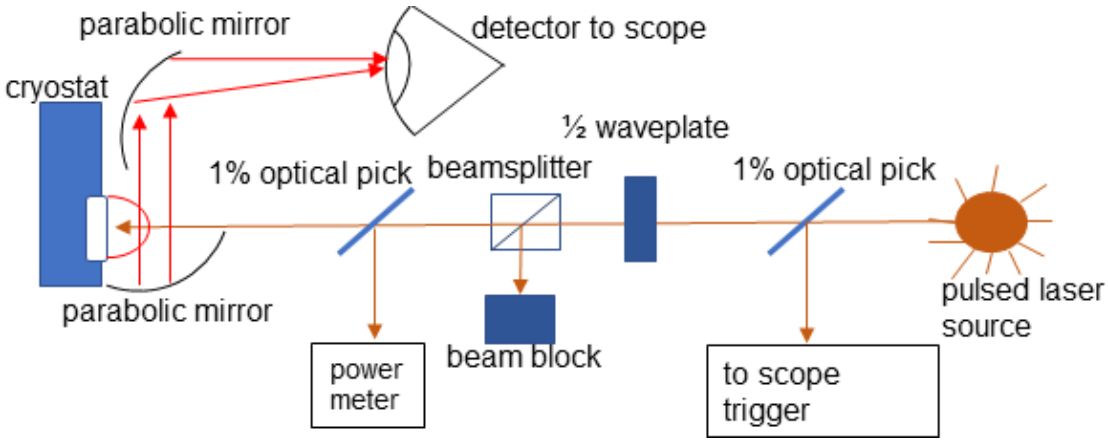

Figure 2.9: An optical block diagram illustrating the time-resolved photoluminescence setup. The sample is first pumped by a pulsed laser, creating an instantaneous injection of electron-hole pairs where the photoexcited carriers then recombine, causing sample photoluminescence that is collimated and focused to a 6 μm photodetector with a set of parabolic mirrors.

2.3.2 Recombination rate analysis

The temperature dependent minority carrier lifetime provides further information on the fundamental material parameters where a recombination rate analysis can be performed to extract the defect level, defect-concentration-cross-section product, doping concentration and Auger Bloch overlap parameter. Application of the recombination rate analysis is performed and reported in chapters 3 and 4. The analysis involves fitting the sum of the recombination mechanisms,

$$\frac{1}{\tau_{mc}} = \frac{1}{\tau_{SRH}} + \frac{1}{\phi\tau_{rad}} + \frac{1}{\tau_{Auger}}, \tag{11}$$

where τ_{SRH} is the Shockley-Read-Hall (SRH) lifetime, $\phi\tau_{rad}$ is the product of the photon recycling factor and the radiative recombination lifetime, and τ_{Auger} is the Auger recombination lifetime and is illustrated in Figure 2.10 . The photon

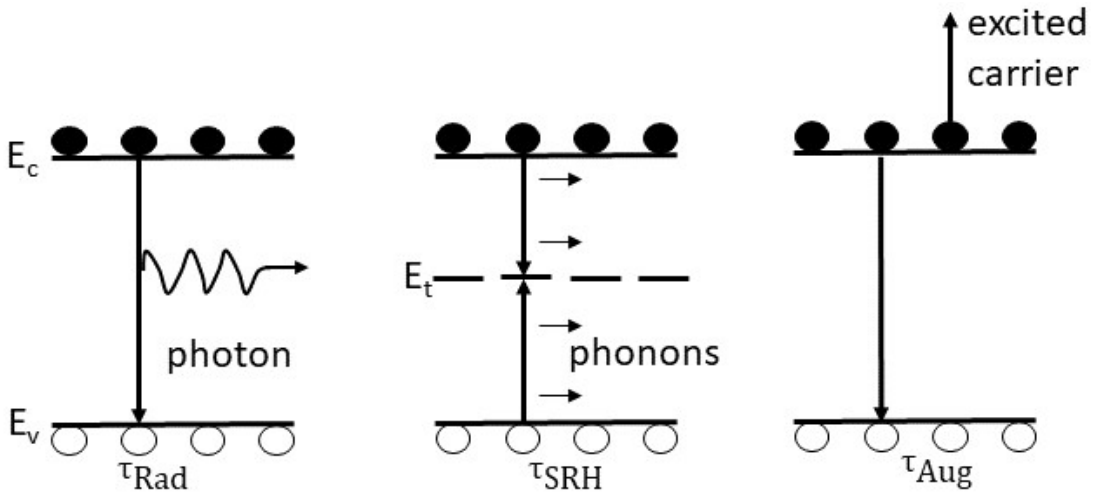

Figure 2.10: An illustration of three recombination mechanisms photogenerated electron-hold pairs undergo. The first is radiative recombination τ_{rad}, then Shockley-Read-Hall recombination τ_{SRH} and Auger recombination τ_{Auger}. Image modelled after Ref. [28].

recycling factor quantifies the geometry-dependent probability that an emitted photon is reabsorbed in the material which acts to increase the observed radiative lifetime. The photon recycling factor is calculated following the methods in Refs. [26, 27] conservatively using the InAs bandgap absorption coefficicent of 2550 cm^{-1},[9] but ultimately has little impact on the recombination rate analysis for the samples investigated thus far due to their minority carrier lifetime being firmly SRH- or Auger-limited.

The SRH recombination process describes the recombination of photogenerated carriers through trap states located in the bandgap, caused by lattice defects and impurities.[29] The observed SRH lifetime τ_{SRH} is a function of the electron and hole recombination lifetimes τ_{n0} and τ_{p0}, the equilibrium electron and hole

concentrations n_0 and p_0, and characteristic carrier concentrations n_1, and p_1 as expressed in Eqs. (12-14),

$$\tau_{SRH} = \frac{\tau_{p0}(n_0 + n_1) + \tau_{n0}(p_0 + p_1)}{n_0 + p_0}. \tag{12}$$

The expressions for the recombination lifetimes of holes in n-type material τ_{p0} and electrons in p-type material τ_{n0} are given in Eq. (13), which shows that minority hole recombination is minimized by reducing the concentration of SRH recombination centers N_t, the thermal velocity of the carriers v_p, or capture cross section σ_p,

$$\frac{1}{\tau_{p0}} = \sigma_p v_p N_t, \; \frac{1}{\tau_{n0}} = \sigma_n v_n N_t. \tag{13}$$

The thermal velocities in the recombination lifetime expressions in Eq. (13) impart a $T^{1/2}$ dependence to τ_{SRH} which is prominent when $n_0 >> p_0, n_1, p_1; p_0 >> n_0, n_1, p_1$ or $n_0 = p_0 >> n_1, p_1$. The term n_1 (p_1) is the density of electrons (holes) in the conduction (valence) band with effective density of states N_c (N_v) for the case that the Fermi level is located at the defect energy level E_t as expressed in Eq. (14),

$$n_1 = N_c \exp\left(\frac{-(E_c - E_t)}{k_B T}\right), \; p_1 = N_v \exp\left(\frac{-(E_t - E_v)}{k_B T}\right). \tag{14}$$

These parameters define electron and hole populations characteristic of the trap's energy level within the bandgap. While the temperature dependence of τ_{p0} and τ_{n0} dominates τ_{SRH} at low temperatures, the simple power law is perturbed as

k_BT approaches E_c - E_t in n-type material or $E_t - E_v$ in p-type material.

When analyzing the temperature-dependent lifetime, the majority carrier concentration n_0 or p_0, defect level E_t, and the product $\sigma_p N_t$ (or $\sigma_n N_t$) are fit parameters to the data. The defect concentration in $\sigma_p N_t$ primarily modifies the magnitude of τ_{SRH}, with higher defect concentration resulting in lower lifetime. The majority carrier concentration and trap level primarily define the amplitude and position of the feature imparted by the competition between the majority carrier concentration with n_1 and p_1. The trap level E_t is fit relative to the conduction band consistent with the work of Olson *et al.*[30] Figure 2.11 illustrates the influence of the fit parameters on the temperature dependent SRH lifetime and it can be seen in Figure 2.11 (a) and (c), the SRH lifetime is independent of the defect level and the donor density at sufficiently low temperatures, indicative that Eq. (13) dominates the SRH lifetime in this regime. Based on Figure 2.11 (b), the defect-concentration-cross-section product is determined by the overall low temperature minority carrier lifetime. It is therefore important to include the full formalism of the SRH recombination mechanism to analyze the temperature dependent minority carrier lifetime. Approximating the recombination lifetime to a single regime loses utility when performing a temperature-dependent recombination rate analysis.

Aside from SRH recombination, the material can always release excess energy through radiative emission, where the photogenerated conduction band electrons

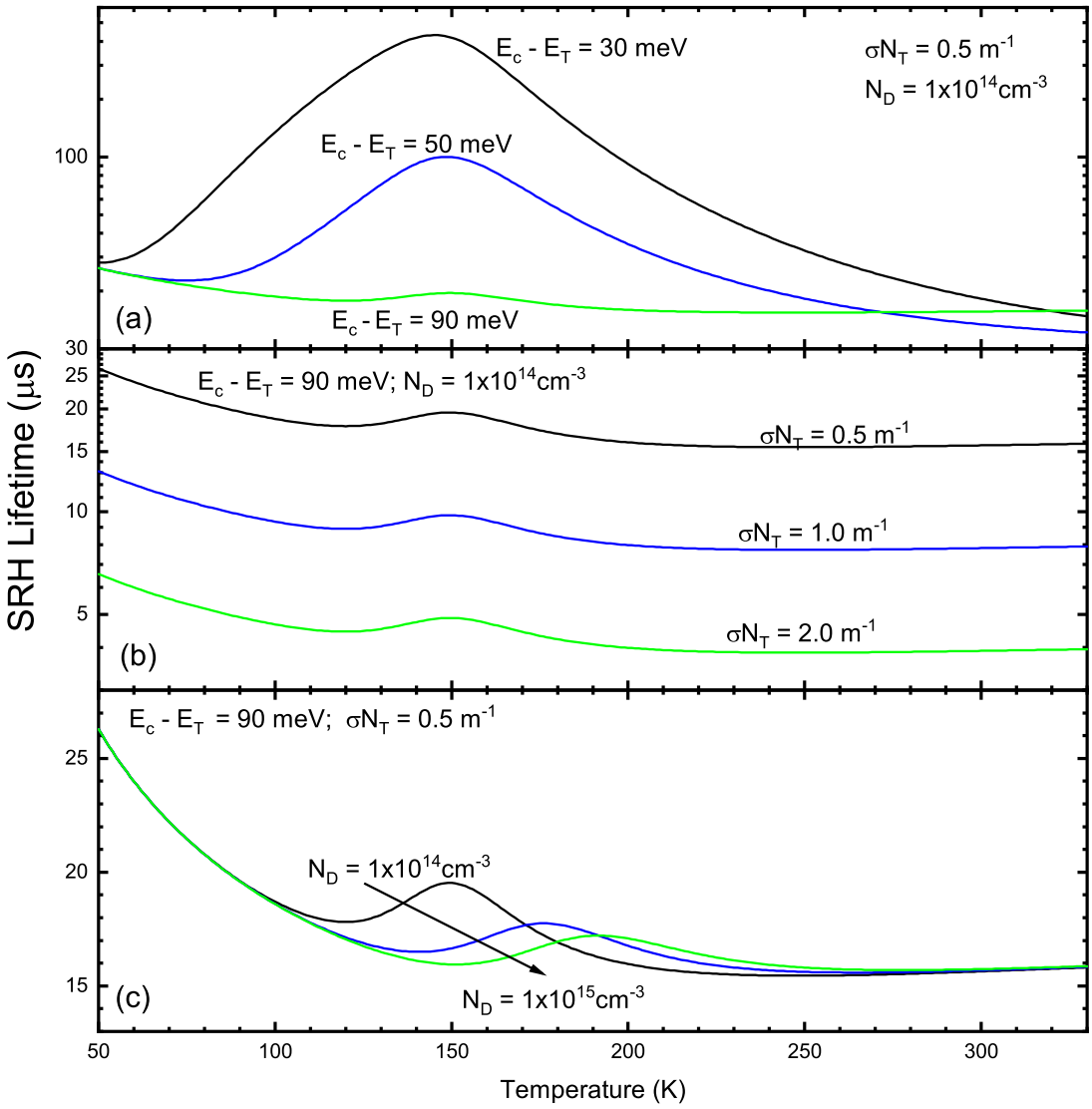

Figure 2.11: The influence of tunable parameters on the SRH lifetime where different (a) defect levels, (b) defect-concentration-cross-section products, and (c) doping densities are chosen while keeping the remaining parameters fixed.

recombine with valence band holes and produce photons as a result. The radiative lifetime is determined by the material's bandgap E_g, carrier concentrations $n_i; n_0; p_0$, and thermal generation rate G_r as expressed in Eq. (15),

$$\tau_{rad} = \frac{n_i^2}{G_r(n_0 + p_0)}. \tag{15}$$

Where the thermal generation rate G_r, as introduced by van Roosbroeck and Shockley, is the integrated thermal emission spectrum given in Eq. (16),[31]

$$G_r = B_0 n_i^2 = \frac{8\pi}{h^3 c^2} \int_{E_g}^{\infty} \frac{\epsilon_1(h\nu)\alpha(h\nu)(h\nu)^2 d(h\nu)}{\exp\left(h\nu/k_B T\right) - 1}, \tag{16}$$

where B_0 is the radiative coefficient, $h\nu$ is the photon energy, $\epsilon_1(h\nu)$ is the real part of the dielectric function, and $\alpha(h\nu)$ is the absorption coefficient. The dispersion of the dielectric function is ignored and the high-frequency dielectric constant[32] ($\epsilon_\infty = 12.2$) of InAs is used, and classical Boltzmann statistics is used. Eq. (16) then becomes,

$$G_r = B_0 n_i^2 = \frac{8\pi\epsilon_\infty}{h^3 c^2} \int_{E_g}^{\infty} \frac{\alpha(h\nu)(h\nu)^2 d(h\nu)}{\exp\left(h\nu/k_B T\right)}. \tag{17}$$

The band gap E_g is measured as a function of temperature before performing a recombination rate analysis. The absorption coefficient is approximated by an analytic form similar to the method used by Refs. [31, 33, 34, 35] in Eq. (18),

$$\begin{aligned} \alpha_{direct}(h\nu) = \quad & \frac{2^{3/2}}{3\epsilon_\infty^{1/2}} \frac{m_0 e^2}{\hbar^2} \left(\frac{m_e^* m_h^*}{m_0(m_e^* + m_h^*)} \right)^{3/2} \\ & \times \left(1 + \frac{m_0}{m_e^*} + \frac{m_0}{m_h^*}\right) \left(\frac{E - E_g}{m_0 c^2} \right)^{1/2}, \end{aligned} \tag{18}$$

where m_e^* is the electron effective mass, m_h^* is the heavy-hole effective mass, m_0 is the electron rest mass, and e is the electron charge. The absorption coefficient in Eq. (18) was calculated by the parabolic band approximation at $\mathbf{k} = 0$, ignoring excitonic effects. The effective masses ($m_e^* = 0.026; m_h^* = 0.333$),[36] like the dielectric constant, were approximated as those of bulk InAs. Incorporating the expression for the absorption coefficient into Eq. (17) provides an analytic form of the thermal emission rate and allows for calculation of the radiative lifetime in Eq. (15), which is scaled by the photon recycling factor. Similar expressions can be made for p-type samples by switching the role of n- and p-type carriers.

For n-type material, the Auger-1 process describes electron-electron collisions in the conduction band which result in a non-radiative loss of energy. In the low-excitation limit, the Auger recombination mechanism can be expressed as shown in Eq. (19),[37, 38]

$$\tau_{Auger} = \frac{2n_i^2}{n_0^2 + n_0 p_0} \times \frac{3.8 \times 10^{-18} \epsilon_\infty^2 (1+\gamma)^{1/2}(1+2\gamma)}{(m_e^*/m_0)|F_1 F_2|^2} \times \left(\frac{E_g}{k_B T}\right)^{3/2} \exp\left(\frac{1+2\gamma}{1+\gamma}\frac{E_g}{k_B T}\right), \tag{19}$$

where γ is a ratio determined by the dominant Auger mechanism, and in the case of the Auger-1 process where $m_h^* > m_e^*$, $\gamma = m_e^*/m_h^*$. The Auger-1 process is also valid for samples that are moderately p-doped.[37] $|F_1 F_2|$ is the Bloch overlap integral that can take on values between 0.1 and 0.3; this parameter will be a fit

parameter for the Auger recombination component of the samples investigated in chapters 3 and 4.

3 Recombination rate analysis in long minority carrier lifetime mid-wave infrared InGaAs/InAsSb superlattices

This article was published in the Journal of Applied Physics volume **129**, 184501 (2021).

Rigo A. Carrasco,

Department of Physics, New Mexico State University, P. O. Box 30001,

Las Cruces, New Mexico 88003, USA

Christian P. Morath, Perry C. Grant, Elizabeth H. Steenbergen,

Preston T. Webster,

Air Force Research Laboratory, Space Vehicles Directorate, Kirtland AFB, New Mexico 87117, USA

Gamini Ariyawansa,

Air Force Research Laboratory, Sensors Directorate, Wright-Patterson AFB, Ohio 45433, USA

Chad A, Stephenson, Clark N. Kadlec, Samuel D. Hawkins, John F. Klem, Eric A. Shaner,

Sandia National Laboratories, Albuquerque, New Mexico 87185, USA

Stephen T. Schaefer and Shane R. Johnson

Center for Photonics Innovation and School of Electrical, Computer, and Energy Engineering, Arizona State University, Tempe, Arizona 85287, USA

3.1 Abstract

Gallium is incorporated into the strain-balanced In(Ga)As/InAsSb superlattice system to achieve the same mid-wave infrared cutoff tunability as conventional Ga-free InAs/InAsSb type-II superlattices, but with an additional degree of design freedom to enable optimization of absorption and transport properties. Time-resolved photoluminescence measurements of InGaAs/InAsSb superlattice characterization and doped device structures are reported from 77 to 300 K and compared to InAs/InAsSb. The low-injection photoluminescence decay yields the minority carrier lifetime, which is analyzed with a recombination rate model, enabling the determination of the temperature-dependent Shockley-Read-Hall, radiative, and Auger recombination lifetimes and extraction of defect energy levels and capture-cross-section defect-concentration products. The Shockley-Read-Hall-limited lifetime of undoped InGaAs/InAsSb is marginally reduced from 2.3 to 1.4 μs due to the inclusion of Ga; however, given that Ga improves the vertical hole mobility by a factor of $>10\times$, a diffusion-limited InGaAs/InAsSb superlattice nBn could expect a lower bound of $2.5\times$ improvement in diffusion length with significant impact on photodetector quantum efficiency and radiation hardness. At temperatures below 120 K, the doped device structures are Shockley-Read-Hall limited at 0.5 μs, which shows promise for detector applications.

3.2 Introduction

Considering the excellent opoelectronic properties and high yield of mature, commercial III-V infrared sensing technologies such as InGaAs in the short-wave and InSb in the mid-wave infrared spectral regions, there is a logical inclination to examine other III-V material systems to optimally cover the short- to long-wave infrared at increasingly higher operating temperatures. One such system, the strain-balanced InAs/InAsSb type-II superlattice initially proposed in 1995,[39] has been the subject of considerable research due to the high degree of freedom to which the band structure and optoelectronic properties can be designed across the technologically relevant mid-wave infrared spectrum (3-5 μm wavelength).[40] Research into this superlattice system took off with the discovery of long (>100 ns) minority carrier lifetimes in the long-wave infrared,[41] and since then lifetimes of several microseconds in mid-wave material have been achieved.[30, 42, 43, 44] Even now, there is ongoing research into understanding and mitigating known non-radiative recombination centers in these materials.[43, 44]

Despite advances made in the strain-balanced InAs/InAsSb system, there remain certain problems that will require a new degree of design freedom to overcome. One fundamental limitation in this system is inherent to the InAs/InAsSb strain-balance condition, which is necessary to enable the growth of thick superlattice active regions free of strain-induced misfit dislocations. As seen in Figure 3.1,

InAs is under a small degree of tensile strain on GaSb (as indicated by its smaller lattice constant relative to GaSb), whereas $InAs_{1-x}Sb_x$ compositions utilized in mid- to long-wave infrared InAs/InAsSb superlattices (x > 0.3) are highly compressive by comparison. As a result, the InAs layers of the superlattice are much thicker than the InAsSb layers, typically by a factor of $\sim 3\times$. Electrons in the superlattice see a wide potential well in the InAs layers, and the electron wavefunction strongly couples to adjacent InAs layers due to the lower electron effective mass and thinness of the InAsSb. On the other hand, the ground state heavy holes are subject to a deep potential well in the InAsSb layers and do not couple strongly to adjacent wells, yielding a hole wavefunction that is highly localized to the InAsSb. Consequently, electron-hole wavefunction overlap is fundamentally limited and hole transport is inhibited in strain-balanced InAs/InAsSb.[45, 9]

Vertical hole transport properties in mid- and long-wave infrared InAs/InAsSb superlattices were investigated to understand the effects of these limitations,[46, 47] and analysis of the vertical mobility as a function of temperature identified two unique activation energies. For the case of the mid-wave superlattice ($\sim$5.7 μm cutoff at 100 K), results indicated that transport is limited by trap-controlled mobility due to localized states between 350 and 150 K, and limited by phonon-assisted hopping between localized states between 150 and 77 K.[46] These same mechanisms are observed in the long-wave superlattice, albeit at lower temperatures due to the reduced wavefunction coupling at longer wavelengths ($\sim$12 μm

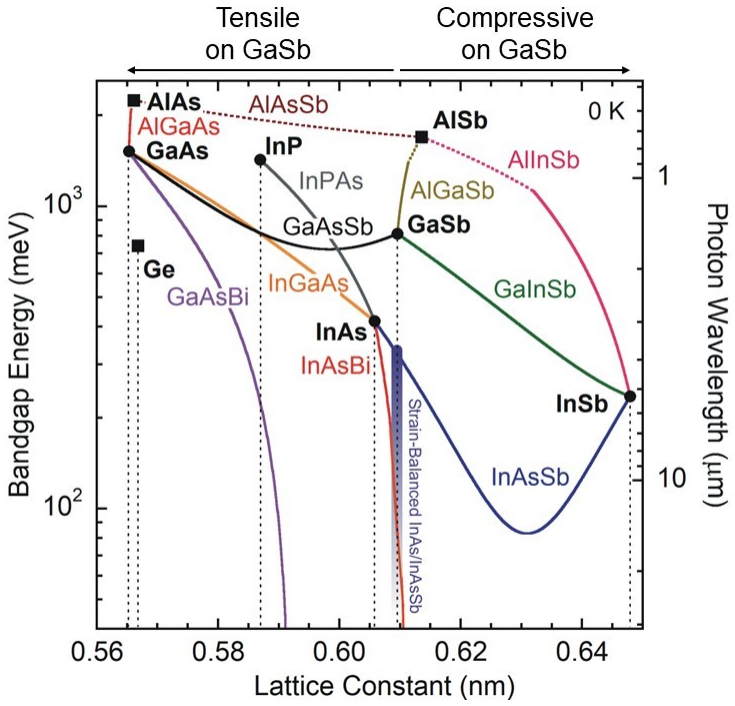

Figure 3.1: Low temperature (0 K) bandgap energy as a function of the lattice constant for selectred III-V semiconductors with the lattice constants of common binary substrates indicated with vertical dashed lines. Circles and solid curves designate direct bandgap binary and ternary alloys, while squares and dotted curves designate indirect bandgap materials. The spectral range of the strain-balanced InAs/InAsSb superlattice is shown as the vertical line at the GaSb lattice constant, with dark to light color-gradient depicting the reduction in electron-hole wavefunction overlap with decreasing bandgap in the superlattice.

at 12 K) with trap-controlled mobility being observed between 110 and 67 K, and phonon-assisted hopping between 67 and 33 K.[47] Below these temperatures, extended Bloch states could no longer be supported at which point carrier localization dominates and mobility limits the diffusion length which impacts detector quantum efficiency and diffusion dark current.

These limitations could be circumvented if the InAs layers of the superlattice were under greater tensile strain. By incorporating Ga into InAs (see Figure 3.1), the resulting InGaAs/InAsSb superlattice can be designed to achieve a more symmetric strain-balance profile providing stronger hole wavefunction coupling, enhanced electron-hole wavefunction overlap, and correspondingly stronger hole transport and absorption properties. This increase has been demonstrated in quantum efficiency and absorption coefficient experiments with Ga mole fractions ranging up to 19% in the InGaAs layer.[48, 49] The results show promise in delivering higher performance mid-wave infrared detectors in comparison to the familiar InAs/InAsSb design.

In order to gauge whether this superlattice system is viable for mid-wavelength infrared detector technologies, the minority carrier lifetime and mobility need to be measured to evaluate the minority carrier diffusion length L_D of the material expressed in Eq. (20).

$$L_D = (D\tau_{mc})^{1/2} = (k_B T \mu \tau_{mc}/e)^{1/2} \tag{20}$$

In Eq. (20), D is the diffusion coefficient that quantifies the effectiveness with which the minority carriers can transport under diffusion through the material. As seen in the right-hand side of Eq. (20), the diffusion coefficient is equivalent to the product of the Boltzmann constant k_B and temperature T over the electron charge e, and minority carrier mobility μ that can be determined from magnetotransport measurements.[46] The minority carrier lifetime τ_{mc} is a statistical measure of the time an excited minority carrier exists before it recombines with a majority carrier. For a minority carrier device such as the nBn photodetector, more efficient collection of photogenerated carriers occurs when the diffusion length is much greater than the thickness of the absorbing region where the electron-hole pairs are generated. As the absorption coefficient primarily dictates the thickness of the absorber, the absorption coefficient, mobility, and minority carrier lifetime are fundamental parameters governing quantum efficiency and dark current.

In this work, the minority carrier lifetime of mid-wave infrared InGaAs/InAsSb superlattices with 20% Ga in the InGaAs layers are measured as a function of temperature by time-resolved photoluminescence. The trend of the temperature-dependent lifetime provides insight into the nature of the various recombination processes occurring in the material, which are evaluated using a recombination rate model. The results presented provide a metric to quantify the defect content in these materials and the positive impact of gallium incorporation in InGaAs/InAsSb superlattices.

3.3 Molecular beam epitaxy

Optical characterization structures as well as *nBn* and *npBp* device structures are grown in a Veeco Gen 930 molecular beam epitaxy system on *n*-type GaSb substrates. The optical characterization sample structures consist of a 1.0 μm thick layer of undoped *n*-type superlattice confined by 0.1 μm thick lattice-matched $InAs_{0.91}Sb_{0.09}$ to provide confinement to photogenerated carriers. The *nBn* structure consists of a 4.0 μm thick Si-doped *n*-type superlattice absorber region followed by an undoped AlGaAsSb barrier and an n^+ top contact. The *npBp* structure consists of a 0.5 μm Si-doped *n*-type superlattice preceding the 3.5 μm thick superlattice Be-doped *p*-type absorber, followed by a *p*-type AlGaAsSb barrier and a p^+ contact. All samples are examined by X-ray diffraction to confirm accurate production of the layer structures, and Normarski interference contrast imaging to verify that smooth surface morphologies are obtained. A total of four samples are examined and detailed in Table 3.1.

3.4 Steady-state photoluminescence

The photoluminescence spectrum of each sample is measured as a function of temperature from 12 to 300 K using a closed-cycle helium cryostat and a Nicolet Instrument Corporation Magna-IR 760 Fourier transform infrared spectrometer. The samples are excited using a 785 nm wavelength laser, and the resulting photoluminescence is coupled into the spectrometer. The photoluminescence is passed

Table 3.1: Sample structures and Einstein single oscillator model bandgap parameters (E_0, S_0, T_E) determined from steady-state photoluminescence experiments.

Sample ID	Superlattice Layer structure	Superlattice Thickness (μm)	120 K Bandgap Energy E_g (meV)	Einstein single oscillator parameters		
				E_0 (meV)	S_0	T_E (K)
A	n-InAs/InAsSb	1.0	227	233	2.49	283
B	n-InGaAs/InAsSb	1.0	217	219	2.77	509
C	n-InGaAs/InAsSb	4.0	221	225	2.76	396
D	p-InGaAs/InAsSb	3.5	225	228	2.46	381

through a 0.87 μm wavelength long-pass filter to remove the reflected pump laser emission prior to reaching the liquid nitrogen cooled 15.5 μm cutoff HgCdTe detector.

The 120 K photoluminescence spectra of InAs/InAsSb Sample A (dotted curve) and InGaAs/InAsSb Sample B (solid curve) are shown in Figure 3.2 which both emit around 5 μm wavelength with comparably narrow full-width at half max of 31 meV in InAs/InAsSb and 35 meV in InGaAs/InAsSb. While the 100 nm thick $InAs_{0.91}Sb_{0.09}$ cap provides effective confinement to photogenerated electron-hole pairs in the superlattice, it also parasitically absorbs 50% of the 785 nm pump radiation before it reaches the superlattice active region. Fortunately, most of the electron-hole pairs in the cap either recombine at the sample's surface or diffuse into the lower bandgap superlattice as evidenced by the much lower intensity of the 3.9 μm wavelength photoluminescence peak characteristic of $InAs_{0.91}Sb_{0.09}$.

The bandgap energy is determined by fitting an exponentially-modified Gaussian to the photoluminescence spectrum.[50] The bandgap energy of each sample is then determined at the first derivative maximum of the exponentially modified Gaussian which identifies the rapid onset of the coninuum states at the band edge.[40, 45, 51] The temperature dependent bandgap energies of InAs/InAsSb Sample A (unfilled circles) and InGaAs/InAsSb Sample B (filled circles) are plotted in the inset of Figure 3.2, and fit to an Einstein single oscillator model temperature dependence (dotted and solid curves).[40, 12] Both samples exhibit carrier

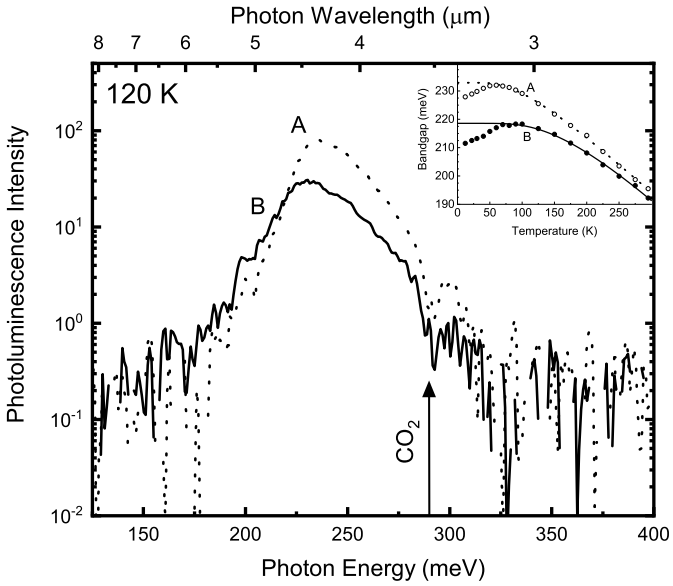

Figure 3.2: Photoluminescence spectra from InAs/InAsSb (sample A, dotted line) and InGaAs/InAsSb (sample B, solid line) superlattices at 120 K. The vertical arrow denotes the CO_2 absorption line which is not completely removed by the throughput correction. The inset in the graph shows the temperature dependent bandgap energies, where an Einstein single oscillator model is fit to data down to 70 K (unfilled and filled circles). Bandgap values below 70 K exhibit carrier localization and are excluded from the model fit.

localization at low temperatures as evidenced by the narrowing of the bandgap by a few meV from 70 to 10 K, which are excluded from the single oscillator model fit. The single oscillator model parameters, as well as the 120 K bandgap energy of each sample are provided in Table 3.1.

3.5 Time-resolved photoluminescence

Time-resolved photoluminescence measurements are performed using a 1535 nm (0.81 eV) pulsed laser with samples mounted in a liquid nitrogen cooled cryostat. The laser pulses are 3.5 ns long, and the excitation is varied to inject 10^{11} to

10^{12} photons/cm^2 into the superlattice active region per pulse using a motorized half-waveplate compensator and polarizing beam splitter combination. Beam spot size is then adjusted using an iris. The photoluminescence signal is collected and collimated with a 2 in. diameter f/2 90° off-axis parabolic mirror and then focused with a second off-axis parabolic mirror (2 in.; f/1; 90°) to transmit through a 2.4μm cutoff long-pass filter to remove the pump laser pulses and is measured by a 6 μm cutoff VIGO Systems PVI-4TE detector. A teledyne Lecroy HD 4096 oscilloscope averages 100,000 time-resolved photoluminescence decays to acquire one photoluminescence decay signal per excitation condition per temperature from 77 to 300 K. An optical schematic of the system can be found in Ref. [52].

The excitation conditions are selected to establish low-injection conditions in the samples. Supposing all the photoexcited electron-hole pairs distribute across the 1 μm thickness of the superlattice active region in the optical characterization structure, then the lowest excitation of 10^{11}m photons/cm^2 per pulse reaching the superlattice results in an initial photogenerated carrier density of 10^{15} electron-hole pairs/cm^3. This is comparable to the $\sim 10^{15}$ cm^{-3} background carrier concentration determined by the recombination rate analysis in the undoped material indicating that low-injection conditions are quickly established. Low-injection conditions are furthermore confirmed by the observed single exponential nature of the photoluminescence decay. As the excitation is increased to 10^{12} photons/cm^2 per pulse and higher, non-single exponential decay is observed at

short time-scales, indicating high injection conditions and a corresponding transient reduction of the lifetime to return the system to low-injection. However, even in the high injection case, after the short transient of non-single exponential decay the system returns to low-injection and the single exponential decay that results are consistent with low-injection pumping.

The minority carrier lifetime is determined as a function of temperature by fitting the characteristic slopes of the photoluminescence decays in the low excitation regime to a single exponential decay. Figure 3.3 shows the time-resolved photoluminescence decays of InGaAs/InAsSb superlattice Sample B at two excitation levels at 120 K. The photoluminescence decay data is given by the black curves, while the subset of data used to determine the characteristic slope of the single exponential region is shown by the gray highlighted range. The dashed black line shows the single exponential slope fit in that range, with the lifetime value indicated alongside the line. It can be seen that the photoluminescence decay from the lowest injection case is purely single exponential whereas the higher injection case is initially non-single exponential, but becomes single exponential and converges to the same characteristic slope after a sufficient number of carriers have recombined to return the system to low-injection conditions.

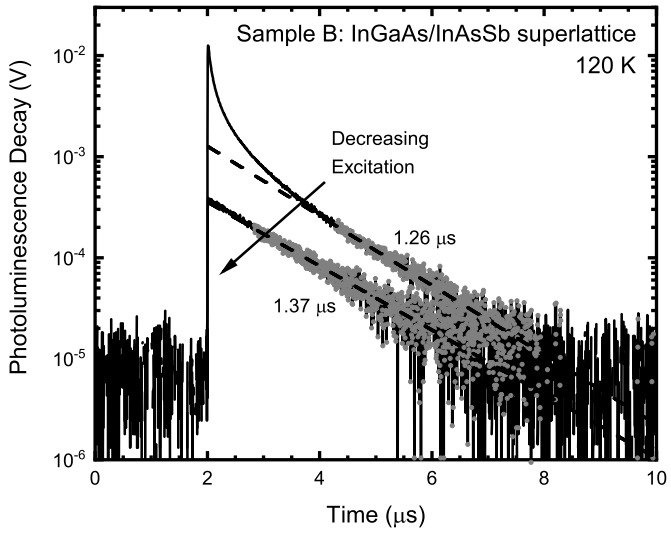

Figure 3.3: Time-resolved photoluminescence decay of InGaAs/InAsSb superlattice sample B at two different excitation levels measured at 120 K (black curves).The higher excitation level corresponds to an estimated injected carrier density of $1\times\ 10^{16}$ electron-hole pairs/cm^3, while the low-excitation measurment has an estimated $2\ \times\ 10^{15}$ electron-hole pairs/cm^3. The gray highlighted range is the subset of data in the low-excitation regime used to fit the single exponential characteristic slope shown by the dashed black lines, resulting in the extracted minority carrier lifetime.

3.6 Recombination rate analysis

The temperature-dependent minority carrier lifetime τ_{mc} evaluated from the low-injection photoluminescence decay is analyzed as a sum of the rates of the individual recombination mechanisms as detailed in Eq. (21),

$$\frac{1}{\tau_{mc}} = \frac{1}{\tau_{SRH}} + \frac{1}{\phi\tau_{rad}} + \frac{1}{\tau_{Auger}}. \tag{21}$$

The measured lifetime is the minority carrier lifetime τ_{mc}, which is a function of the Shockley-Read-Hall (SRH) lifetime τ_{SRH}, the product of the photon recycling factor ϕ and radiative lifetime τ_{rad}, and the Auger lifetime τ_{Auger}. The photon recycling factor quantifies the geometry-dependent probability that an emitted photon is reabsorbed in the material which acts to increase the observed radiative lifetime. The photon recycling factor is calculated following the methods is Refs. [26, 27] conservatively using the InAs bandgap absorption coefficicent of 2550 cm^{-1},[9] but ultimately has little impact on the recombination rate analysis in these samples.

The SRH recombination process describes the recombination of photogenerated carriers through trap states located in the bandgap, caused by lattice defects and impurities.[29] The observed SRH lifetime τ_{SRH} is a function of the electron and hole recombination lifetimes τ_{n0} and τ_{p0}, the equilibrium electron and hole concentrations n_0 and p_0, and characteristic carrier concentrations n_1, and p_1 as expressed in Eqs. (22-24),

$$\tau_{SRH} = \frac{\tau_{p0}(n_0 + n_1) + \tau_{n0}(p_0 + p_1)}{n_0 + p_0}. \tag{22}$$

The expressions for the recombination lifetimes of holes in n-type material τ_{p0} and electrons in p-type material τ_{n0} are given in Eq. (23), which shows that minority hole recombination is minimized by reducing the concentration of SRH recombination centers N_t, the thermal velocity of the carriers v_p, or capture cross section σ_p,

$$\frac{1}{\tau_{p0}} = \sigma_p v_p N_t, \; \frac{1}{\tau_{n0}} = \sigma_n v_n N_t. \tag{23}$$

The thermal velocities in the recombination lifetime expressions in Eq. (23) impart a $T^{1/2}$ dependence to τ_{SRH} which is prominent when $n_0 >> p_0$, n_1, p_1; $p_0 >> n_0$, n_1, p_1 or $n_0 = p_0 >> n_1$, p_1. The term n_1 (p_1) is the density of electrons (holes) in the conduction (valence) band with effective density of states N_c (N_v) for the case that the Fermi level is located at the defect energy level E_t as expressed in Eq. (24),

$$n_1 = N_c \exp\left(\frac{-(E_c - E_t)}{k_B T}\right), \; p_1 = N_v \exp\left(\frac{-(E_t - E_v)}{k_B T}\right). \tag{24}$$

These parameters define electron and hole populations characteristic of the trap's energy level within the bandgap. While the temperature dependence of τ_{p0} and τ_{n0} dominates τ_{SRH} at low temperatures, the simple power law is perturbed as $k_B T$ approaches E_c - E_t in n-type material or $E_t - E_v$ in p-type material.

When analyzing the temperature-dependent lifetime, the majority carrier concentration n_0 or p_0, defect level E_t, and the product $\sigma_p N_t$ (or $\sigma_n N_t$) are fit parameters to the data. The defect concentration in $\sigma_p N_t$ primarily modifies the magnitude of τ_{SRH}, with higher defect concentration resulting in lower lifetime. The majority carrier concentration and trap level primarily define the amplitude and position of the feature imparted by the competition between the majority carrier concentration with n_1 and p_1. The trap level E_t is fit relative to the conduction band consistent with the work of Olson *et al.*[30]

In the absence of SRH recombination, a material can always release its excess energy radiatively through the emission of a photon produced by the recombination of a conduction band electron with a valence band hole. The radiative lifetime is a function of the bandgap energy, carrier concentrations, and the thermal generation rate as expressed in Eq. (25),

$$\tau_{rad} = \frac{n_i^2}{G_r(n_0 + p_0)}. \tag{25}$$

The factor G_r, as introduced by Van Roosbroeck and Shockley, is the integrated thermal emission spectrum given in Eq. (26),[31]

$$G_r = B_0 n_i^2 = \frac{8\pi}{h^3 c^2} \int_{E_g}^{\infty} \frac{\epsilon(h\nu)\alpha(h\nu)(h\nu)^2 dh\nu}{\exp(h\nu/k_B T) - 1} \tag{26}$$

where B_0 is the radiative coefficient, n_i is the intrinsic carrier concentration, $h\nu$ is the photon energy, $\epsilon(h\nu)$ is the dielectric constant and $\alpha(h\nu)$ is the absorption coefficient. The bandgap E_g is measured as a function of temperature in this

work. The absorption coefficient is approximated by an analytic form similar to the method used by Refs. [31, 33, 34, 35] in Eq. (27),

$$\alpha_{direct}(h\nu) = \frac{2^{3/2}}{3\epsilon_\infty^{1/2}} \frac{m_0 e^2}{\hbar^2} \left(\frac{m_e^* m_h^*}{m_0(m_e^* + m_h^*)} \right)^{3/2} \times \left(1 + \frac{m_0}{m_e^*} + \frac{m_0}{m_h^*} \right) \left(\frac{E - E_g}{m_0 c^2} \right)^{1/2}, \quad (27)$$

where m_e^* is the electron effective mass, m_h^* is the heavy-hole effective mass, m_0 is the electron rest mass, and e is the electron charge. The effective masses[36] and the dielectric constant[32] were approximated as those of bulk InAs. Incorporating the expression for the absorption coefficient into Eq. (26) provides the thermal emission rate and allows for calculation of the radiative lifetime in Eq. (25), which is scaled by the photon recycling factor. Similar expressions can be made for p-type samples by switching the role of n- and p-type carriers.

For n-type material, the Auger-1 process describes electron-electron collisions in the conduction band which result in a non-radiative loss of energy. In the low-excitation limit, the Auger recombination mechanism can be expressed as shown in Eq. (28),[37, 38]

$$\tau_{Auger} = \frac{2n_i^2}{n_0^2 + n_0 p_0} \times \frac{3.8 \times 10^{-18} \epsilon_\infty^2 (1+\gamma)^{1/2}(1+2\gamma)}{(m_e^*/m_0)|F_1 F_2|^2} \times \left(\frac{E_g}{k_B T} \right)^{3/2} \exp\left(\frac{1+2\gamma}{1+\gamma} \frac{E_g}{k_B T} \right), \quad (28)$$

where γ is a ratio determined by the dominant Auger mechanism, and in the case

of the Auger-1 process where $m_h^* > m_e^*$, $\gamma = m_e^*/m_h^*$. The Auger-1 process is also valid for samples that are moderately p-doped.[37] $|F_1F_2|$ is the Bloch overlap integral that can take on values between 0.1 and 0.3; this parameter will be a fit parameter for the Auger recombination component of the samples.

Figure 3.4 shows the minority carrier lifetime of InAs/InAsSb superlattice sample A as a function of temperature, plotted on a log scale to show the individual SRH, radiative, and Auger components. The uncertainties in the measured data points are comparable to the size of the data markers on this scale, on the order of 0.2 μs. The solid curve shows the model fit of Eq. (21) to the data with fit parameters n_0, E_t, σN_t, and $|F_1F_2|$ given in Table 3.2, where the fit parameter uncertainties are calculated through the covariance matrix.[53] The minority carrier lifetime of the InAs/InAsSb superlattice is Auger-limited above 200 K, and is SRH-limited at $\sim$2.3μs below 200 K which benchmarks the optoelectronic quality of InAsSb-based alloys that this molecular beam epitaxy system is producing.

The fit results in Table 3.2 indicate that the background carrier concentration of undoped InAs/InAsSb superlattice sample A is 1.22×10^{14} cm^{-3} n-type, and the defect level is 99 meV below the conduction band edge. These two parameters are primarily defined by the competition between n_0 and n_1 in the SRH-limited regime, which is unfortunately rather subtle when the carrier concentration is low, within the uncertainty of the measured data points of this sample. This leads to a reduced degree of accuracy in the determination of the carrier concentration and

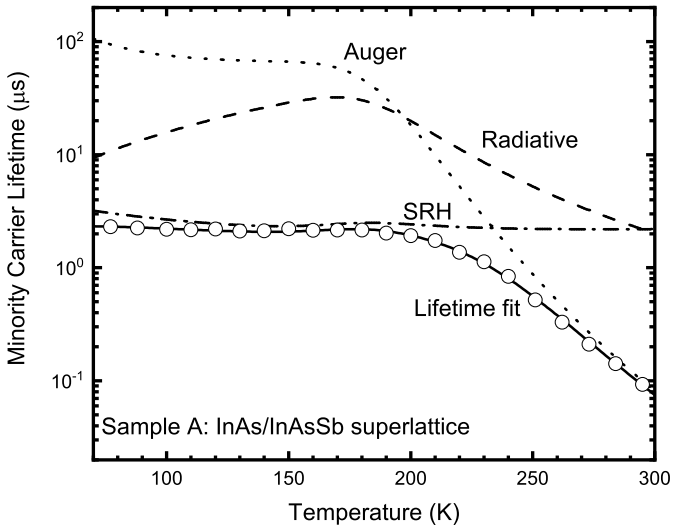

Figure 3.4: Minority carrier lifetime of undoped InAs/InAsSb superlattice Sample A (unfilled circles) plotted as a function of temperature. The solid curve shows the lifetime fit Eq. (21), with the fundamental radiative, Auger, and SRH lifetime components shown with dashed, dotted, and dotted-dashed lines respectively.

defect energy level in the undoped samples which is not adequately characterized by the fit parameter uncertainties given in Table 3.2. Realistically, the fit quality is indistinguishable within the noise of the measurement for any carrier concentration in the 10^{13}-10^{14} cm^{-3} range, and thus this result only indicates that the carrier concentration of undoped InAs/InAsSb sample A is less than 10^{15}cm^{-3}.

The InGaAs/InAsSb optical characterization structure is evaluated using the same procedure outlined above in Figure 3.5 (filled circles) and is shown to possess a similar lifetime to the InAs/InAsSb lifetime below 200 K, being SRH-limited around 1.4 μs. The solid black curve shows the resultant fit, which exhibits a small hump around 150 K affected by the SRH recombination lifetime. The position and height of this feature are functions of the carrier concentration and trap level.

Table 3.2: Best fit parameters governing minority carrier lifetime; majority carrier concentration n_0 or p_0, defect energy E_c-E_t, product of capture cross section and trap density σN_t, and Bloch overlap integral $|F_1F_2|$. The parentheses in the table entries denote the uncertainty of the least significant digit.

Sample ID	Type	Majority Carrier Concentration (cm^{-3})	E_c-E_t (meV)	σN_t (10^{-2} cm^{-1})	$\lvert F_1F_2 \rvert$
A	n-type	$1.22(6)\times10^{14}$	99.42(2)	3.82(1)	0.14728(2)
B	n-type	$0.29(4)\times10^{14}$	105.0(2)	7.39(5)	0.1600(1)
C	n-type	$3.65(3)\times10^{15}$	118.3(1)	18.42(4)	0.14762(3)
D	p-type	$7.79(3)\times10^{15}$	55.22(5)	4.214(3)	0.16252(7)

Like sample A, these features are smaller than the error bars on the measured data, and as a result the model fit for samples A and B may be insensitive to the defect level and the carrier concentration. Additional measurements do not significantly reduce the uncertainty of the characteristic slope fits in the >1 μs range of samples A and B; however in the high temperature range >200 K the uncertainty decreases to levels comparable to Samples C and D in the same range.

Taken together, the data for samples A and B indicate that within the limits of this measurement, the introduction of ∼20% Ga into the InGaAs layers of the InGaAs/InAsSb superlattice does not introduce any new defect levels that are electrically distinguishable from those in high quality InAs/InAsSb. There may be upwards of a 2× increase in defect concentration resulting in a <2× decrease

in minority carrier lifetime. However, historically the inclusion of Ga has resulted in orders of magnitude degradation in lifetime[54] and thus this work presents a significant technological achievement in optoelectronic quality of InGaAs/InAsSb. Reports on the transport properties in the InGaAs/InAsSb superlattice indicate that the vertical hole mobility is 10× that of InAs/InAsSb.[49] Given that photodetector quantum efficiency is governed by the diffusion length which depends on the product of the mobility μ and lifetime τ_{mc} (Eq. 20), a marginal decrease in lifetime is acceptable to gain a large increase in mobility. For the lifetime results presented here, a 2.5× enhancement in diffusion length would be expected compared to its InAs/InAsSb counterpart optimized for maximum wavefunction overlap at the same cutoff, and longer lifetimes are likely achievable with further growth refinement. This, along with an increase in absorption,[48] would serve to enhance quantum efficiency or enable utilization of a thinner absorber, and it would improve radiation tolerance in space-base applications as the diffusion length remains larger than the absorber thickness.

The intentionally-doped *nBn* and *npBp* device samples C and D exhibit a much more prominent peak in the lifetime data, which enables more accurate determination of the defect level and carrier concentration. To model such peaks in the device samples, the defect levels become shallower and deviate away from the midgap level, in contrast to the approximately midgap defect levels extracted from the unintentionally doped samples. The trap level for the *npBp* device

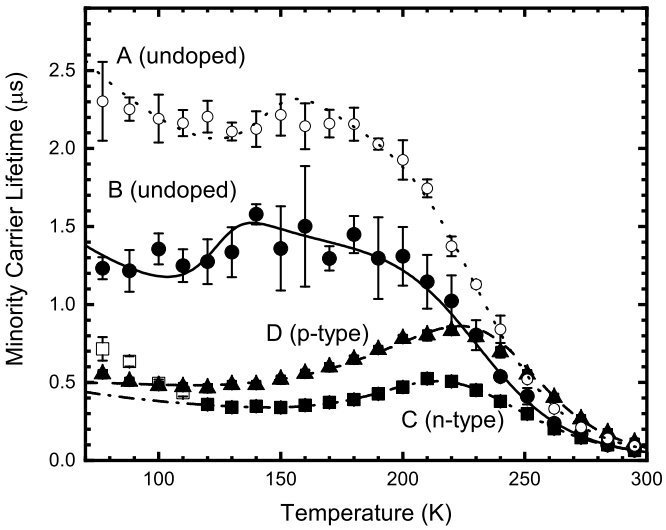

Figure 3.5: Temperature dependent minority carrier lifetime and model fit of InGaAs/InAsSb superlattice samples A, B, C, D using the formalism developed in Equations (22)-(28). Unfilled circle markers and the dotted curve represent the undoped InAs/InAsSb optical characterization structure; filled circle markers and the solid black curve represent the undoped InGaAs/InAsSb optical characterization structure; squares and the dotted-dashed curve represent n-type material in the nBn device structure; triangles and the dashed curve represent p-type material in the $npBp$ structure. Unfilled squares denote data excluded from the fit in the nBn sample.

(sample D) is 55 meV and is shalower than that of the *nBn* device (sample C) at 118 meV. The longer lifetimes observed in the *npBp* device compared to the *nBn* device can be attributed to the shallower defect level and the lower defect concentration product identified in the *p*-type material.

The overall decrease in lifetime as a function of doping density is commonly observed in InAs/InAsSb.[44] The extracted carrier concentrations of 3.65×10^{15} cm^{-3} and 7.79×10^{15} cm^{-3} in Table 3.2 are close to the target doping of 4×10^{15} cm^{-3} Si in *nBn* sample C and 8×10^{15} cm^{-3} Be in *npBp* sample D, which provide additional confidence that the fit procedure is accurate.

While *pn*-junction devices are not ideal for optical characterization, the fact that the junction is buried deep within the layer structure, far from the bulk of the pump photoexcitation, greatly reduces its impact on the lifetime results and analysis. As time evolves after initial photexcitation, the *p*-type region's minority electrons diffuse to spatially equilibriate the population, recombination readiatively and nonradiatively in the process emitting the obeserved photoluminescence decay. The junction acts as a sink, removing minority electrons from the *p*-type region at some rate like any other lossy interface or layer. As a result, the junction only looks like an additional non-radiative recombination rate, as it extracts minority electrons from the *p*-type region of sample D. However, given the signal intensity of sample D was among the strongest and the recombination rate analysis indicates that the material parameter fitting is consisten with

the calibrated p-type doping in this sample, it appears that the junction is not significantly impacting the analysis.

A different type of behavior is observed for the doped InGaAs/InAsSb nBn structure (sample C) at temperatures below 110 K when comparing to the $npBp$ structure (sample D). The inverse square root behavior where τ_{p0} dominates (Eq. (23)) with a fixed InAs effective mass does not accurately characterize the observed increase in lifetime below 100 K. Including data below 110 K compromised the fit as the model returned a doping density with an uncertainty larger than the value itself. This could mean that the minority carrier lifetime at low temperatures is sensitive to the effective mass but fitting the effective masses to the data introduces significant correlation among fit parameters. Capacitance-voltage or Hall effect measurements of the carrier concentrations in benchmark characterization structures would augment the minority carrier lifetime modeling.

3.7 Conclusions

In conclusion, the minority carrier lifetime of undoped, n-type, and p-type InGaAs/InAsSb type-II superlattices is reported. The recombination mechanisms are analyzed and compared to a 5 μm wavelength InAs/InAsSb superlattice reference. The lifetime of the intrinsic InGaAs/InAsSb design is comparable to its Ga-free InAs/InAsSb counterpart. This suggests that incorporating Ga will be advantageous to mid-wave infrared photodetector designs as it will allow for sym-

metric strain balancing, as well as improved minority hole transport and absorption due to an increase in hole wavefunction coupling. It becomes more apparent of the potential promise the InGaAs/InAsSb system will bring with the result of long minority carrier lifetimes in n-type and p-type device structures reported.

3.8 Acknowledgments

The authors acknowledge financial support through research sponsored by the Air Force Research Laboratory, Section 219 Commanders Research and Development Funds. This work was performed, in part, at the Center for Integrated Nanotechnologies, an Office of Science User Facility operated for the U.S. Department of Energy (DOE) Office of Science. Sandia National Laboratories is a multimission laboratory managed and operated by National Technology & Engineering Solutions of Sandia, LLC, a wholly owned subsidiary of Honeywell International Inc., for the U.S. Department of Energy's National Nuclear Security Administration under contract DE-NA0003525. In addition, we acknowledge the use of facilities within the Eyring Materials Center at Arizona State University supported in part by NNCI-ECCS-1542160. The views expressed in the article do not necessarily represent the views of the U.S. DOE or the United States Government.

3.9 Data Availability

The data that support the findings of this study are available from the corresponding author upon reasonable request.

4 Proton irradiation effects on InGaAs/InAsSb mid-wave barrier infrared detectors

This article was published in the Journal of Applied Physics volume **130**, 114501 (2021).

Rigo A. Carrasco,

Department of Physics, New Mexico State University, P.O. Box 30001, Las Cruces, New Mexico 88003, USA

James George, Zinah M. Alsaad, David Garnham,

A-Tech, LLC, a BlueHalo Company (ATA BlueHalo), 1300 Britt St. SE, Albuqeuerque, New Mexico 87123, USA

Joshua M. Duran, Gamini Ariyawansa,

Air Force Research Laboratory, Sensors Directorate, Wright-Patterson AFB, Ohio 45433, USA

Diana Maestas, Christian P. Morath, and Preston T. Webster

Air Force Research Laboratory, Sensors Directorate, Wright-Patterson AFB, Ohio 45433, USA

4.1 Abstract

Semiconductor-based mid-wave infrared photon detectors that functionalize space-based imaging systems are susceptible to both cumulative ionization and displace-

ment damage, especially due to proton irradiation. Here, the dark current density and quantum efficiency of a midwave infrared detector utilizing a strain-balanced InGaAs/InAsSb superlattice active region are examined as a function of a 63 MeV proton radiation dose. Proton-irradiation is performed in an incremental stepwise dose up to a total ionizing dose of 100 krad(Si) or an equivalent proton fluence of 6.1×10^{11} protons/cm^2. All characterization work is conducted with the detectors held at an operating temperature of 130 K throughout the experiment to limit thermal annealing effects. Prior to irradiation, the quantum efficiency of the top-side illuminated device without anti-reflection coating is 59.5%. The quantum efficiency is largely independent of temperature below 150 K, indicative of an electron minority carrier. As irradiation progressed the typical linear increase in inverse quantum efficiency with increasing proton fluence was observed, which led to a quantum efficiency damage factor of 1.12×10^{13} e cm^2/ph. This value is shown to be an order of magnitude lower than typically observed in III-V nBn devices and is likely due to the higher mobility of minority electrons in the active region of this device. A full analysis of the characterization results suggests that displacement damage creates a significant population of donor states that modify the doping profile, in addition to Shockley–Read–Hall recombination centers that generally form as a result of proton irradiation.

4.2 Introduction

Infrared detector devices operating in space demand a unique set of performance requirements due to environmental conditions. Not only do the detectors require higher sensitivity in low photon irradiance scenarios in comparison to land-based detection campaigns, but they also require radiation-tolerance due to their exposure to various sources of ionizing radiation. On orbit, detector performance degrades over time mostly due to the damaging effects of high-energy protons coming from the Van Allen belts, solar events, and cosmic rays.[55] Given the recent interest in their improved performance,[56] there have been numerous campaigns investigating the effects of ionizing radiation on different performance metrics of III-V-based infrared imaging detectors ranging from the minority carrier lifetime of the absorber material,[57, 58] to the quantum efficiency, dark current, and noise of photodetectors such as *nBn*s.[59, 60, 61, 62]

The two primary damage mechanisms that result from high-energy protons impinging on the photodetectors are effects due to ionization, also referred to as the total ionization dose (TID) damage, and displacement damage effects, where the protons displace atoms from their lattice sites, disrupting the local crystal structure. In photodiode detectors, the former often leads to additional surface leakage current due to surface charging, while the latter results in degradation of the minority carrier lifetime and the subsequent consequences from that. Due to the

nature of the barrier's surface,[63] the *nBn* device structure largely blocks the *n*-type surface shunt current and, therefore, is very tolerant to the TID damage.[64] As a result, the *nBn* predominantly suffers from displacement damage, which is exacerbated by its comparatively weaker tolerance to proton irradiation.[65] A third irradiation damage mechanism, increased *n*-type doping due to proton irradiation, was also observed in certain *nBn* detectors where it limited the rate at which diffusion-limited dark-current increased with proton irradiation.[60] However, this damage mechanism does not always clearly manifest making further study necessary.[57]

Although the InAs/InAsSb superlattice has demonstrated long minority carrier lifetimes and competitive detector properties, the material performance is ultimately limited by the high degree of hole confinement inherent to the system.[9, 48] This is mainly a consequence of strain-balancing a low tensile-strained InAs layer with a high Sb-content, high compressively-strained InAsSb layer. Strain-balancing this system leads to an InAs layer that is $\sim$3$\times$ thicker than the InAsSb layer, which in turn leads to a low vertical minority hole mobility in superlattice *nBns* due to the mobility's exponential dependence on the layer thickness, barrier height, and effective mass.[46, 66] The low vertical mobility manifests in a smaller diffusion length of carriers in the absorber. Coupled with a decrease in superlattice absorption due likewise to the poor overlap between electron and hole wavefunctions, this leads to a decrease in both *nBn* detector quantum ef-

ficiency and in radiation tolerance of the quantum efficiency when subjected to high energy protons that degrade the minority carrier lifetime.[61]

In order to achieve a more symmetric strain-balanced superlattice, Ga is incorporated in the InAs layers to produce more tensilely strained InGaAs layers that can be grown thinner than less tensile InAs. This results in an overall thinner period thickness with improved hole wavefunction coupling and enhanced hole vertical mobility and superlattice absorption coefficient.[48, 49] Improvements on superlattice growth methods have also shown that long minority carrier lifetimes (>1 μs) are achievable in this mid-wave InGaAs/InAsSb system,[67] thus potentially improving the diffusion length of the material.[48, 49]

The Shockley-Read-Hall (SRH) recombination mechanism limits the minority carrier lifetime of an intentionally doped mid-wave III-V material at temperatures $\leq$200 K, where the total carrier concentration is dominated by the extrinsic doping. At these temperatures, and assuming a single defect species dominates recombination, the SRH recombination rate R_{SRH} can be described by[29]

$$R_{SRH} = \frac{1}{\tau_{SRH}} = \sigma v_{th} N_T, \tag{29}$$

where τ_{SRH} is the SRH limited minority carrier lifetime, σ is the recombination cross section, v_{th} is the thermal velocity, and N_T is the defect concentration. In the presence of proton irradiation, the minority carrier recombination rate increases proportionally to the increasing proton fluence Φ_p due to a corresponding

increase in N_T with displacement damage. This is most simply theoretically accounted for by including a linear damage factor $K_{1/\tau}$ in the definition of the SRH recombination rate as in the following:[55, 68]

$$\begin{aligned} R_{SRH}(\Phi_p) &= \frac{1}{\tau_{SRH}(\Phi_p = 0)} + K_{1/\tau}\Phi_p \\ &= \sigma v_{th} N_{T0} + \sigma v_{th} \left(\frac{dN_T}{d\Phi_p} \right) \Phi_p \end{aligned} \tag{30}$$

where N_{T0} is the defect concentration at $\Phi_p = 0$ and $dN_T/d\Phi_p$ is the defect introduction rate. Since the minority carrier lifetime is a factor in the diffusion length, the defect introduction rate also plays a role in the radiation damage factors for higher level device performance metrics such as the dark current density and the quantum efficiency. However, as described in Refs. 60 and 61, respectively, these damage factors are less well theoretically defined, given their changes with proton fluence are only linear under certain limits. Typical past results show a minority carrier recombination rate linear damage factors of $K_{1/\tau} \sim 5 - 10 \times 10^{-6} cm^2/s$[58] got InAs/InAsSb *nBn*s with a device cutoff of ~5μm at 120 K.

This paper presents experimental findings of quantum efficiency and dark current performance of *pBpn* infrared detectors that utilize an InGaAs/InAsSb superlattice absorbing layer in a proton radiation environment. Optical and dark current characterizations of similar *nBn* and *pBp* detectors were previously reported;[59, 69] however, in contrast to a traditional *pBp* where the barrier is implied to be in the valence band to block majority hole conduction, *pBpn* examined in this work utilizes a conduction band barrier like that in a traditional

nBn. As a result, *pBpn* behaves like a traditional *pn*-junction photodiode, and the barrier serves primarily to block surface shunt current that would otherwise introduce impractically high dark current.[70] In exploring the utility of *nBn* detectors for potential space applications, the scope of this paper is to present this *pBpn* detector material's tolerance to proton irradiation and compare it with the collective results of radiation tolerance for detectors previously characterized and reported by the authors.

The photodetector examined in this work was grown in a Veeco Gen930 molecular beam epitaxy system on a 3 in. diameter (100)-oriented *n*-type GaSb substrate. The absorber region of the photodetector (*pn* region) is a 4 μm thick strain-balanced InGaAs/InAsSb superlattice optimized for maximum electron-hole wavefunction overlap at a 5 μm cutoff wavelength.[9] The 3.5 μm thick *p*-type absorber region is doped 8×10^{15} cm^{-3} to take advantage of the high mobility of electrons as the minority charge carrier in the superlattice. In contrast, the $4 \times 10^{1}5$ cm^{-3} *n*-type absorber region is limited to a thickness of 0.5 μm to maximize the collection of minority holes. The material exhibits a 0.5 μs lifetime over the operating temperature range of interest (77–150 K),[67] comparable to its Ga-free counterpart. This results in a long diffusion length and high quantum efficiency in the device.

Variable size square mesa devices are fabricated by defining mesas using standard photolithography followed by wet chemical etching. The dimension of the

square mesas varies from 200 to 1000 μm, while the mesa depth is the combined layer thickness measured from the top surface down to the bottom contact layer. As the next step, top and bottom contact metal layers are fabricated using a standard metallization process, where a stack of Ti/Pt/Au layers are deposited on the top and bottom contact layers using metal evaporation. A window on the top of the mesas is left open for the photocurrent measurement under front side illumination geometry. The mesa sidewalls are not encapsulated or passivated in this fabrication process. As the final step, the detector dies are packaged in leadless chip carriers and individual detectors are wirebonded by connecting the metal contacts to the chip carrier pads. The detectors use a fully reticulated mesa geometry, as opposed to a shallow etched mesa geometry, eliminating the lateral collection of photogenerated carriers. The detectors are front-side illuminated and possess no anti-reflection coating. Accounting for a $\sim$33% reflection and $\sim$8% parasitic loss of illumination through the top contact, the expected maximum external quantum efficiency in these devices is $\sim$61.5%.

Prior to the proton irradiation experiment, the spectral response of the detector is measured with a Bruker Vertex 80v Fourier transform infrared spectrometer using a Keithley 428 trans-impedance amplifier to bias the detector under test to -50 mV. The spectral quantum efficiency at the intended operating temperature of 130 K can be seen as the solid curve in Fig. 4.1, which shows its 5.3 μm cutoff identified at the maximum of the first derivative of the spectral response. The

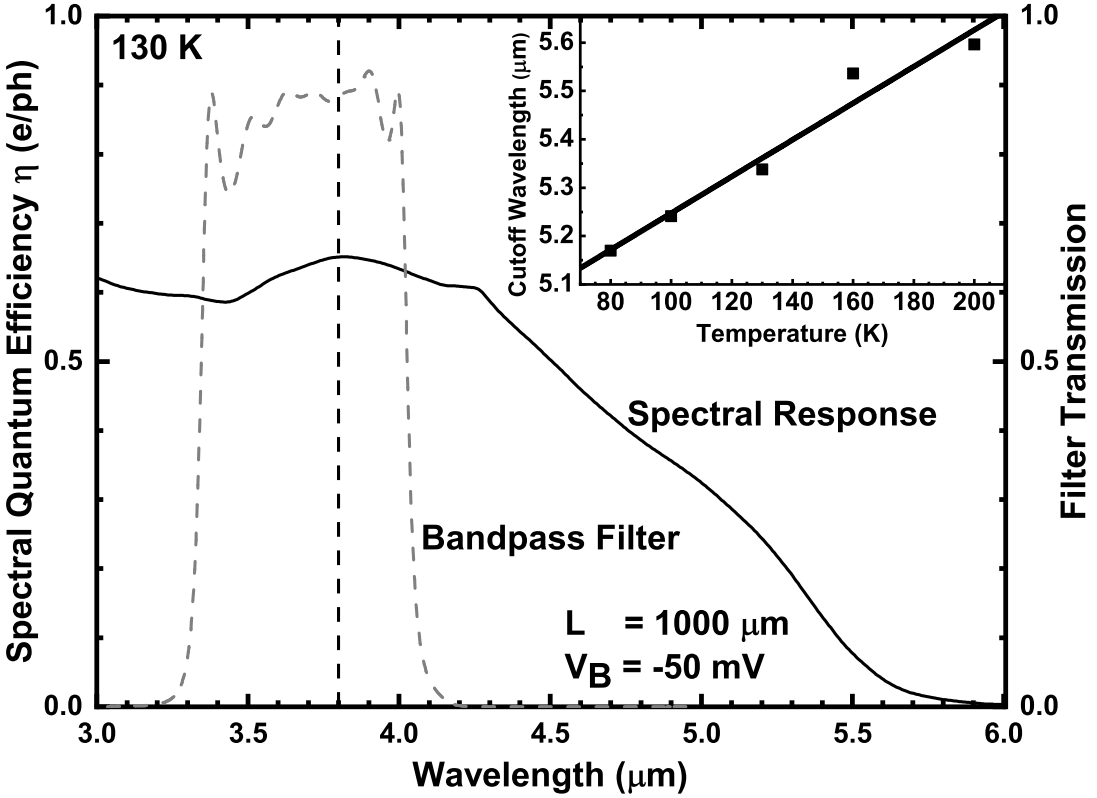

Figure 4.1: Spectral quantum efficiency of the InGaAs/InAsSb superlattice *pBpn* photodetector at 130 K (solid curve, left-hand vertical axis) alongside the transmission spectrum of the bandpass filter used for quantum efficiency calculation (dashed curve, right-hand vertical axis). The inset shows the cutoff wavelength as a function of operating temperature.

dashed curve shows the transmission spectrum of the bandpass filter utilized for the determination of the detector's quantum efficiency also at 130 K. The filter is determined to have cut-on and cut-off wavelengths of 3.3 and 4.0 μm, respectively, with a center wavelength around 3.8 μm. The measurement is repeated as a function of operating temperature, resulting in the determination of a $\sim$0.38 μm cutoff shift per 100 K over the 80 to 200 K range seen in the inset.

During the irradiation experiments, 11 variable area detectors are held at the

operating temperature, while the optical and electrical properties are measured before and after the stepwise proton irradiation, attaining total ionizing doses of 0, 10, 20, 50, and 100 krad(Si); or equivalently proton fluences of 0, 0.61, 1.22, 3.05, and 6.10 $\times$ 10^{11} protons/cm^2. The protons pass through a separate radiation port on the test station with a thin kapton window which negligibly modifies the proton beam before reaching the detectors under test. In addition to characterizing quantum efficiency and dark current as a function of proton fluence, quantum efficiency and dark current are also characterized as a function of temperature before and after the proton irradiation. Subsequent analyses provide insight into the quantum efficiency and dark current density damage factors, dark current activation energies, and recovery phenomena via post-radiation thermal annealing. Details about the characterization system and the test protocols are found in Ref. 69.

4.3 Experiment Setup

The proton irradiation is performed at the Crocker Nuclear Laboratory at the University of California Davis.[71] The cyclotron is tuned to irradiate the detectors at 63 MeV in order to introduce a spatially uniform damage profile through the depth of the device. The detectors are held at a temperature of 130 K for the duration of the proton irradiation experiment, and the detector bias is applied across all of the detectors during radiation doses to simulate the conditions that

would be present if the detector was used on a platform operated in space. Photocurrent and dark current are measured on seven square variable area detectors sized 200, 300, 500, 750, and 1000 μm as a function of proton fluence up to 6.1 $\times$ 10^{11} protons/cm^2. Measurements are performed using an incremental stepwise irradiation-measurement approach where the detectors are measured, dosed with protons, re-measured, and so on. This stepwise approach allows for degradation rates to be determined across the fluence range. After completion of irradiation experiments, the devices are returned to room temperature, which enables some fraction of the radiation damage to anneal out, after which the devices are remeasured after cooling down to the operating temperature to determine the impact of annealing.

The *pBpn* detectors are thermally mounted to the cold-finger of liquid nitrogen cooled vacuum Dewar and held at an operating temperature of 130 K. The Dewar is configured to flood illuminate the detectors by using a 4.0 mm pinhole placed at a distance of 160.5 mm from the device corresponding to an f/# of $\sim$42. The pinhole, along with the 3.3–4.0 μm narrow band spectral filter, are configured within a mechanical shutter assembly mounted to the 77 K shield within the Dewar, allowing dark current measurements to be performed. The shutter door in its open position allows a 900 K blackbody source to illuminate the device for photocurrent measurements. The blackbody source fills the field of view of the detectors as its output passes through an attached optical chopper, the room-

temperature ZnSe Dewar window, followed by the 77 K pinhole, and bandpass filter. The resulting incident photon flux determined at the filter peak wavelength of 3.8 μm is $E_Q = 3.5 \times 10^{14}$ photons/s cm^2. The Dewar and blackbody are placed on a custom kinematic mounting setup to remove uncertainty in the photo-response relative to the incident photo-irradiance on the detectors due to the placement of the blackbody between doses.

For dark current measurements, the devices are biased using two Keithley 6430 source units. One unit is used to source voltage to the top terminal of the device and measure the corresponding current flowing into the top terminal, while the second unit is used to measure the current flowing out of the ground plane of the detector. Voltage ranging from 0.1 to -0.5 V is applied as a stepped-sweep across the detector while simultaneously measuring the current through the device.

4.4 Characterization data

Photocurrent measurements are taken with the detectors held at the operating bias, V_B = -50 mV. To determine the optimal bias, the signal-to-noise ratio (SNR) is estimated using SNR $\propto I_{ph}/\sqrt{I_{dark}}$, where I_{ph} is the photocurrent and I_{dark} is the dark current. An operating bias near the maximum SNR is chosen where I_{dark} is diffusion-limited and I_{ph} is plateaued. The photocurrent I_{ph} is estimated as

$$I_{ph} = q\eta E_Q A_{Det} = q\eta E_Q (L + 2L_{oc})^2, \tag{31}$$

where q is the charge of an electron, η is the quantum efficiency, E_Q is the photon irradiance, and A_{Det} is the active detector area.[72] For the square mesa detectors being evaluated in this work, the detector area can be expressed as the square of the sum of the fill factor corrected mesa length L and the lateral optical collection length L_{oc} as shown in the right-hand side of Eq. (31). The quantum efficiency is determined by least squares linear fitting of the square root of I_{ph} as a function of the fill factor corrected variable detectors mesa lengths. The resultant slope fit parameter m then yields the quantum efficiency according to Eq. (32). The lateral optical collection length is confirmed to be near zero, consistent with the expectation for these fully-reticulated mesa devices,

$$\eta = \frac{m^2}{qE_Q}. \tag{32}$$

Prior to irradiation, the quantum efficiency of the InGaAs/InAsSb *pBpn* detector is measured at 130 K to be 59.5% at the bandpass filter's 3.8 μm center wavelength (see Fig. 4.1). Comparing the pre-radiation quantum efficiency of 59.5% to the expected maximum external quantum efficiency of 61.5% determined by accounting for the losses due to reflection and parasitic absorption in the top contact, the pre-radiation internal quantum efficiency is nearly 97%. The inset to Fig. 4.2 plots the external quantum efficiency as a function of operating temperature, which shows that the quantum efficiency is largely insensitive to a temperature below 150 K at -50 mV reverse bias. This constant quantum efficiency at low tem-

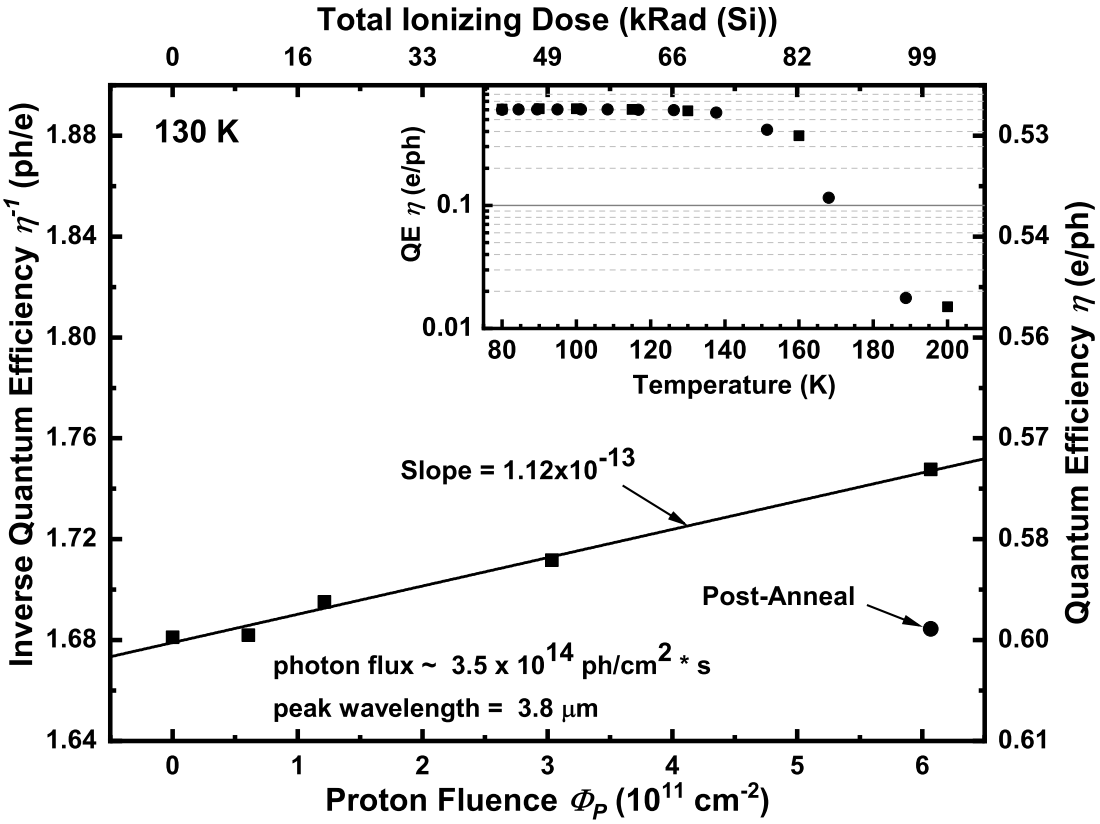

Figure 4.2: Inverse quantum efficiency at 3.8 μm wavelength plotted as a function of proton fluence (lower horizontal axis) and total ionizing dose (upper horizontal axis). Black squares represent quantum efficiency measured after each irradiation dose, while the black circle indicates the value measured after annealing at room temperature. The linear fit leads to an inverse quantum efficiency damage factor $K_{1/\eta} = 1.12 \times 10^{-13}$ e cm^2/ph. The inset is the pre-radiation (black squares) and post-anneal (black circles) quantum efficiency plotted as a function of temperature.

perature is in stark contrast to that of superlattice *nBn* devices where quantum efficiency decreases due to the analogous behavior of the hole mobility at lower temperatures, which suffers from localization-induced hopping transport.[46] At temperatures above 150 K, a sharp decrease in quantum efficiency is apparent, however, increasing the reverse bias shifts the knee in the quantum efficiency temperature dependence to higher temperatures. Measurements of the detector's 130 K quantum efficiency as a function of proton fluence are shown in Fig. 4.2. The quantum efficiency plotted on the right-hand vertical axis is observed to degrade with increasing fluence down to 57.2% at 6.1×10^{11} p/cm^2, resulting in an overall 3.8% decrease in quantum efficiency for the total proton dose (black squares). Following irradiation, the detector is returned to room temperature allowing for some thermal annealing of radiation damage and then re-measured. Quantum efficiency is observed to recover to 59.4% (black circle) following this anneal, which is close to its pre-radiation quantum efficiency. This near full recovery is completely atypical of III-V *nBn* detectors, where lifetime,[65] quantum efficiency,[61] and dark-current[59] all recover to only $\sim$1/3 of their pre-rad values following similar anneal conditions.

Taking a least squares linear fit of the inverse quantum efficiency data plotted on the left-hand vertical axis, the slope of the fit yields the inverse quantum efficiency damage factor,[61] $K_{1/\eta} = 1.12 \times 10^{-13}$ e cm^2/ph. For comparison,[61] a mid-wave (5.2 μm at 130 K) anit-reflection coated InAs/InAsSb *nBn* detector

has shown degradation in external quantum efficiency from ∼0.70 to ∼0.37 e cm^2/ph at a proton fluence of 5.3×10^{11} p/cm^2. This provides an inverse quantum efficiency damage factor of $\sim 2.41 \times 10^{-12}$ e cm^2/ph, suggesting that the quantum efficiency of this InGaAs/InAsSb *pBpn* device is $> 10\times$ more radiation tolerant than a comparable InAs/InAsSb *nBn*.

Measurements of the dark current density for a 200 μm mesa-length detector show a linear increase as a function of proton fluence in Fig. 4.3 suggests that either diffusion or depletion (generation–recombination or G–R) dark current is dominating this change, as both are functions of the minority carrier lifetime τ_{SRH}.[60] The lack here of any annealing of J_D is again atypical and strikingly contrasts with near full recovery of the quantum efficiency seen in Fig. 4.2. Further examination of the minority carrier lifetime, quantum efficiency, and dark current as a function of temperature below provides some insight into both these anomalous phenomena.

The dark current variation with the temperature is also evaluated from 82 to 250 K under pre-rad, post-rad, and post-anneal conditions. To gain insight into the dark current limiting mechaniss, an Arrhenius analysis is performed to determine the activation energies E_a as a function of temperature. This analysis for the 200 μm detector is shown in Fig. 4.4. The pre-rad results plotted in filled square markers show two distinctly different regimes of temperature dependence, with a transition near 125 K, where the dashed lines intersect.

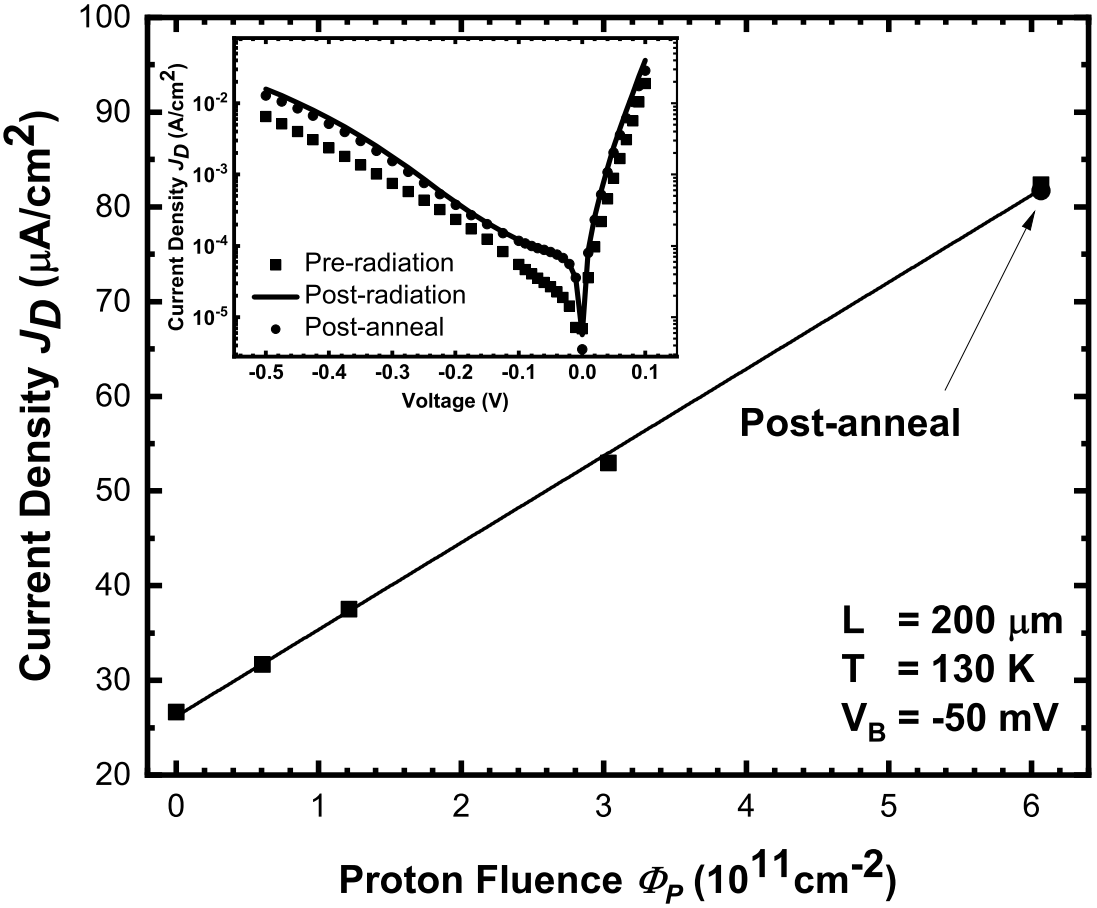

Figure 4.3: Black squares show the dark current density of a 200 μm device as a function of proton fluence at an operating temperature of 130 K. The black circle indicates the post-anneal dark current density. The inset shows the dark current density J-V curves for the device under pre-radiation, post-radiation, and pos-anneal conditions.

In the low temperature region below 125 K, the data in Fig. 4.4 suggest dark current behavior typical of tunneling with a very small activation energy of 26 meV (dotted line). In contrast, the activation energy is 203 meV in the high temperature region above 125 K before irradiation (dashed line), ∼87% of the 234 meV bandgap energy (5.3 μm wavelength cutoff) at 130 K. The 130 K point lies just above the 203 meV activation energy slope fit (dashed line), which indicates that the dark current is mostly diffusion-limited with some tunneling contribution at 130 K.[59] This is consistent with what is observed in the dark current density vs bias voltage, which shows that tunnelling goes on to dominate the dark current with increasing reverse bias (pre-rad, square markers in the inset of Fig. 4.3).

After irradiation, the dark current density increases and no longer exhibits tunneling-limited behavior at low reverse bias between 0 and -100 mV (solid line, the inset of Fig. 4.3), as the reduced minority carrier lifetime has increased the diffusion dark current contributions, and only marginally modified the tunneling current as seen in the low temperature (<125 K) region of Fig. 4.4. The post-rad and post-anneal dark current data exhibit activation energies of 200 and 190 meV, respectively, above 125 K, only somewhat lower than the 203 meV determined pre-rad and consistent with the observation that diffusion dark current increased due to a decrease in minority carrier lifetime after irradiation. The diffusion dark current's negligible recovery and slightly smaller activation energy post-anneal, however, suggests a secondary competing effect is also present.

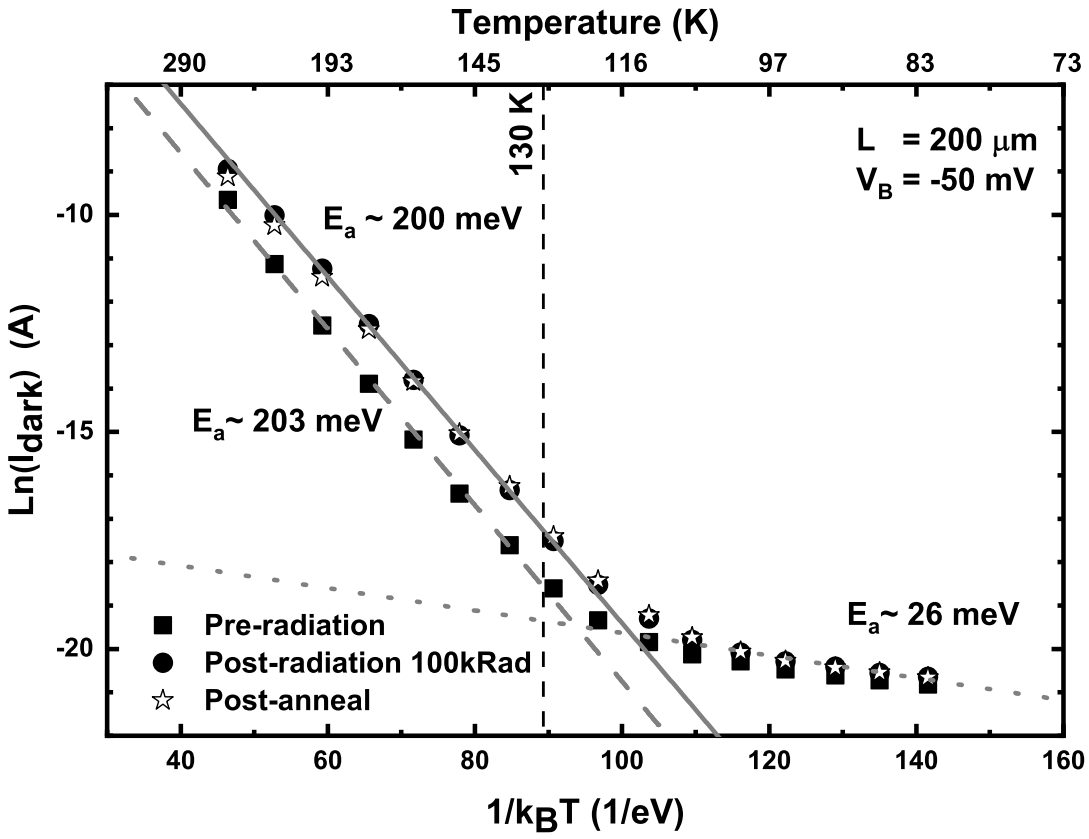

Figure 4.4: Dark current from the 200 μm detector as a function of temperature (upper horizontal axis) and inverse of the thermal energy (lower horizontal axis). Pre-rad, post-rad, and post-anneal data are shown in filled squares, filled circles, and unfilled stars, respectively. Pre-rad Arrhenius analysis indicates that the detector dark current is diffusion dominated above 125 K, whereas the dark current is dominated by tunneling below 125 K (dotted gray line). After irradiation, the activation energy decreases slightly from 203 (dashed gray line) to 200 meV (solid gray line).

Together, the post-anneal observations of complete recovery of quantum efficiency, negligible recovery of dark current, and a small decrease in activation energy provide evidence of radiation-induced displacement damage producing a population of donor states in addition to the increased defect concentration, which has been previously observed in III-V's.[60] A recombination rate analysis on the temperature-dependent minority carrier lifetime before and after irradiation shows irradiation resulted in the creation of a density of donor states that act to increase the n-type and decrease the p-type regions' majority carrier concentrations.[73] Moreover, performing the recombination rate analysis on the minority carrier lifetime post-anneal shows that the n-type region's net donor concentration largely recovers to its pre-irradiation level, whereas the p-type region net acceptor concentration recovered negligibly leaving the p-type region acceptor (hole) concentration 50% lower than it was before irradiation.

This asymmetric modification to the net acceptor and donor concentrations of the p- and n-type regions of the pn-junction after anneal would result in multiple competing effects impacting both the quantum efficiency and dark current. Specifically, the lower acceptor concentration in the p-type region will result in the depletion region extending further into the p-region after irradiation, which serves to enhance photogenerated carrier collection. This damage did not anneal, which could explain why the quantum efficiency in this device recovered completely after anneal in contrast to a typical nBn, which does not benefit from this mechanism

and whose quantum efficiency does not recover completely. Similarly, the dark current in an *nBn* typically partially recovers after anneal due to partial ($\sim$2$\times$) recovery of the minority carrier lifetime, but here this appears to be largely offset by the $\sim$50% lower net acceptor concentration in the *p*-region. The diffusion dark current is inversely proportional to the product of the acceptor concentration and minority carrier lifetime, and as a result these competing effects largely cancel each other out in this device resulting in a permanently higher diffusion dark current after irradiation.

4.5 Technology comparison

To assess the performance of these detectors in aggregate, the inverse quantum efficiency damage factor $K_{1/\eta}$ is plotted alongside previously tested detectors in Fig. 4.5. This metric is plotted on a scatterplot as a function of the inverse product of operating temperature and cutoff wavelength[60] to allow for a technology comparison against detectors that have been characterized at different cutoffs and temperatures. This detector's inverse quantum efficiency damage factor $K_{1/\eta}$ is circled in Fig. 4.5 and is among the lowest measured, comparable to the best devices with anti-reflection coatings, which further improve quantum efficiency and inverse quantum efficiency damage factor. Correcting for the lack of an anti-reflection coating on this device, the damage factor would be expected to improve by a factor of one minus the top surface reflection coefficient ($\sim$2/3).

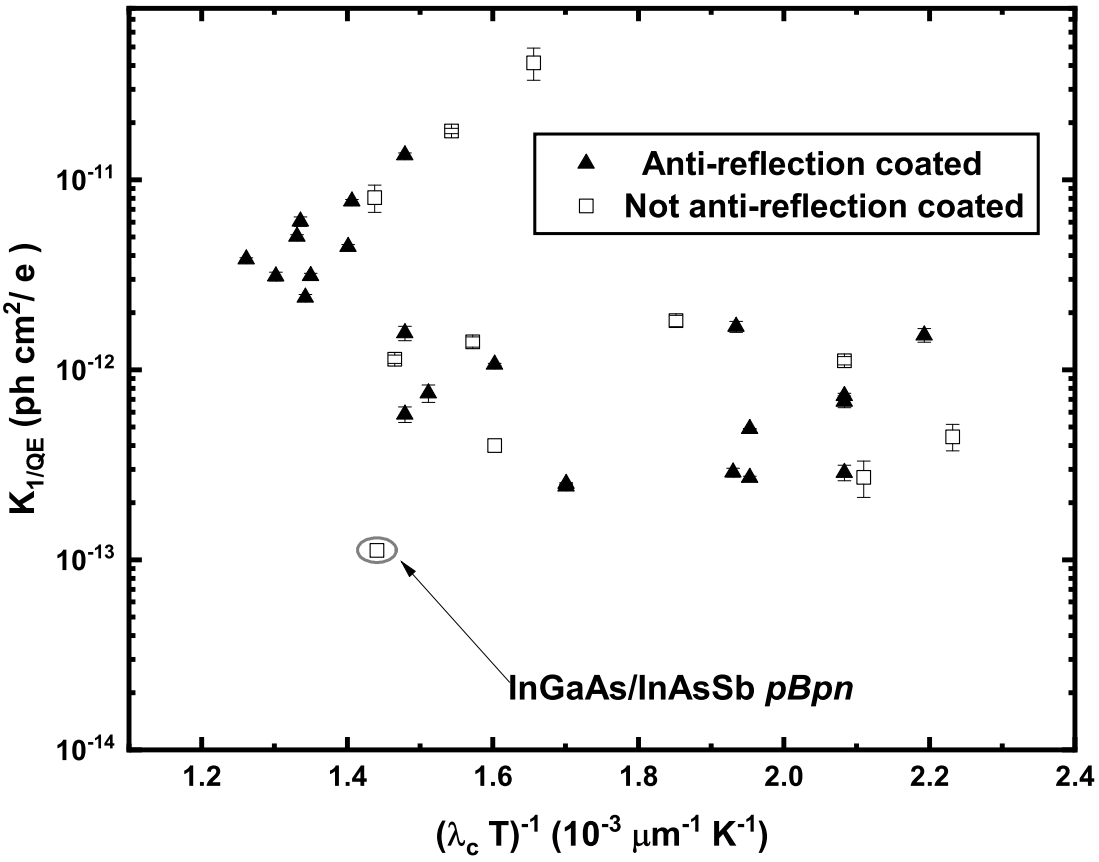

Figure 4.5: Comparison of detector's inverse quantum efficiency damage factor $K_{1/\eta}$ against other III-V *nBn* detectors tested. Filled triangles are anti-reflection-coated devices tested and unfilled squares are uncoated.

The high quantum efficiency and low damage factor observed are likely due to the longer electron diffusion length in the *p*-type active region, and its performance is further enhanced by the stronger absorption coefficient of the InGaAs/InAsSb superlattice that can now be produced with long minority carrier lifetimes comparable to its Ga-free counterpart. In addition, since the dark current below 125 K increases only slightly with radiation, the tunneling dark current observed is likely dominated by the band-to-band process, which can be minimized by re-

ducing doping in the vicinity of the junction to increase the depletion width. By lowering the tunneling dark current floor, the diffusion-limited detector dark current can be further reduced by cooling the detector to lower temperatures and without loss of quantum efficiency as seen in the inset of Fig. 4.2. This is of key technological importance, as III-V *nBn* quantum efficiency and overall sensitivity decrease with decreasing temperature due to poor transport of minority holes, limiting the effectiveness of further cooling to improve *nBn* detector performance. With these fundamental material property and design enhancements, a more radiation tolerant III–V mid-wave infrared detector is realized.

4.6 Conclusion

In conclusion, a radiation tolerance characterization of mid-wave infrared strain-balanced InGaAs/InAsSb pBpn detectors is conducted using 63 MeV proton irradiation. Measurements of quantum efficiency and dark current reflect a degradation of the detector performance with increasing proton fluence that results in a 3.8% drop in the quantum efficiency and a 3× increase in dark current at proton fluence of 6.1×10^{11} p/cm^2 [100 krad(Si)]. Following room-temperature anneal, the quantum efficiency unexpectedly recovers to the pre-radiation value, while in a striking contrast the dark current shows negligible recovery. Examination of the quantum efficiency and dark current degradation due to irradiation and the asymmetry in the recovery of each after anneal suggests that the damage observed

is due to a combination of displacement damage that degrades the minority carrier lifetime and incorporation of irradiation-induced donors, which presumably increases the depletion region width as well as impacts the lifetime and diffusion current. Finally, the detector's performance metrics are compared against the aggregate III-V devices that have been characterized by the authors. The comparison reflects how this *pBpn* detector excels with high quantum efficiency and a low inverse quantum efficiency radiation damage factor; however, future detector designs would need to address the higher than expected tunneling dark current. If the tunneling dark current that dominates below 125 K can be further suppressed, the detector can potentially be operated at lower temperatures with lower dark current and no loss in quantum efficiency, thereby improving overall sensitivity which typically degrades in *nBn* photodetectors at lower temperatures. Additionally, if on-orbit annealing becomes an option the asymmetry between recovery of quantum efficiency and dark-current tends favorably for the sensitivity, which depends more strongly on the former.

4.7 Acknowledgments

The authors acknowledge financial support through research sponsored by the Air Force Research Laboratory, Section 219 Commanders Research and Development Funds. This work was performed, in part, at the Center for Integrated Nanotechnologies, an Office of Science User Facility operated for the U.S. De-

partment of Energy (DOE) Office of Science. Sandia National Laboratories is a multimission laboratory managed and operated by National Technology and Engineering Solutions of Sandia, LLC, a wholly-owned subsidiary of Honeywell International Inc., for the U.S. Department of Energy's National Nuclear Security Administration under Contract No. DE-NA0003525. The views expressed in the article do not necessarily represent the views of the U.S. DOE or the United States Government. Approved for public release: distribution is unlimited. AFMC PA No. 2021-2155.

4.8 Data availability

The data that support the findings of this study are available from the corresponding author upon reasonable request.

5 Photoluminescence and minority carrier lifetime of quinary GaInAsSbBi grown on GaSb by molecular beam epitaxy

This article is a manuscript draft in progress and intended for submission to the Applied Physics Letters once it is publication-ready.

Rigo A. Carrasco,

Department of Physics, New Mexico State University, P.O. Box 30001, Las Cruces, New Mexico 88003, USA

Marko S. Milosavljevic,

A-Tech, LLC, a BlueHalo Company (ATA BlueHalo), 1300 Britt St. SE, Albuqeuerque, New Mexico 87123, USA

Shane R. Johnson.

Center for Photonics Innovation and School of Electrical, Computer, and Energy Engineering, Arizona State University, Tempe, Arizona 85287, USA

Haylie Orozco,

COSMIAC at University of New Mexico, Albuquerque, New Mexico 87106, USA

Ganesh Balakrishnan

Center for High Technology Materials, University of New Mexico, Albuquerque, New Mexico 87106, USA

Christian P. Morath, Perry C. Grant, Julie V. Logan, and Preston T. Webster

Air Force Research Laboratory, Space Vehicles Directorate, Kirtland AFB, New

Mexico 87117, USA

5.1 Abstract

Quinary GaInAsSbBi is grown for the first time by molecular beam epitaxy, and the alloy is demonstrated with a bandgap energy of 294 meV (4.2 μm wavelength) and a minority carrier lifetime of 0.34 μs at 120 K. The GaInAsSbBi epilayer is grown to a thickness of 1 μm at 400 °C, and lattice-matched to the GaSb substrate with a Bi mole fraction of 0.13% measured by Rutherford backscattering spectroscopy. Steady-state and time-resolved photoluminescence measurements are performed to gauge the comparative band gaps and optical quality of GaInAsSbBi as well as InAsSbBi and GaInAsSb reference samples. A recombination rate analysis is performed on the low-injection temperature-dependent minority carrier lifetime to extract the intrinsic Shockley-Read-Hall defect level and intrinsic doping concentration of the GaInAsSbBi.

The need for efficient, high performance mid- to long-wave infrared technologies is growing due to their applications in thermal imaging,[3] gas sensing,[4] and growing potential in noninvasive medical detection/diagnostics.[5] The telecommunications industry has taken advantage of the low cost and high manufacturability of near- to short-wave infrared III-V semiconductor materials to support the ever increasing performance requirements of our world's telecommunications networks. Given the pervasiveness of this industry and its expanding markets,

there would be great value in leveraging that industrial base for mid-wave infrared optoelectronic applications. In fact, this is a major advantage for III V mid-wave infrared superlattices such as strain-balanced InAs/InAsSb and InGaAs/InAsSb, which are highly manufacturable due to their high yield and large-area commercially-available substrates, and can be produced with long minority carrier lifetimes.[67]

While the bandgap engineering flexibility of superlattice material systems have furthered our capabilities in the mid-wave infrared,[74] superlattices gain this tunability at the expense of electron and hole wavefunction coupling,[9] which leads to lower mobilities[46] and lower absorption coefficients in type-II superlattices. Given these challenges, a more ideal mid-wave infrared solution would be a bulk III-V alloy with sufficient tunability in its bandgap and band edge alignments to form effective heterostructures with other alloy systems at the lattice constant of a large-area commercially-available substrate. One potential design space that could enable this technology is an alloy of Bi in a III-AsSb material. Bi is the largest, non-radioactive and low-toxicity group V element that dramatically reduces the bandgap of InAs at a rate of $\sim$55 meV/% Bi.[75] Incorporated into InAsSb(Bi), the quaternary takes advantage of that large bandgap tunability while maintaining a lattice-match to the nearby GaSb substrate which provides a multitude of neighboring alloys to form heterostructures with.[10, 12, 13, 76] All that remains is to achieve band edge tunability and long minority carrier lifetimes, which can

be realized with the inclusion of Ga in the quinary alloy GaInAsSbBi.

In order to evaluate GaInAsSbBi as a candidate for mid-wavelength infrared detection, a sufficient quantity of Bi should be incorporated to achieve a 5 µm wavelength cutoff, (∼2% mole fraction Bi for a 120 K operating point[13, 76]) and fundamental optoelectronic quality metrics such as the alloy's minority carrier lifetime τ_{mc} need to be investigated. The minority carrier lifetime is a strong function of the growth conditions utilized during the material's growth, with particularly strong dependence on the growth temperature.[77] Low growth temperatures below 350 °C have traditionally been utilized to facilitate more efficient Bi incorporation in InAsBi and InAsSbBi;[13, 76] however, photoluminescence has yet to be observed in thick bulk layers grown under these conditions. In contrast, InAsSbBi grown at higher temperatures (between 360 and 380 °C) exhibits strong photoluminescence and minority carrier lifetimes comparable to equivalent InAsSb samples grown at the same temperatures (hundreds of ns). However Bi incorporation is severely reduced at these temperatures (∼0.2-0.5% mole fraction incorporated to date),[10] and Bi incorporation efficiency will be further reduced at temperatures $>$ 400 °C where the longest lifetimes can be achieved.[10] This leaves InAsSbBi in a compromised position where it is difficult to simultaneously achieve sufficient Bi incorporation to reach a 5 μm mid-wave infrared cutoff while maintaining a technologically relevant (or acceptable) minority carrier lifetime.

The addition of Ga in GaInAsSbBi may present a solution to this impasse in

InAsSbBi. GaAsBi with ∼1% mole fraction of Bi has been grown at 400 °C, and higher Bi incorporation rates have been demonstrated at similar temperatures.[11, 78] This suggest that Bi forms a stronger bond to Ga than to In at ∼400 °C growth temperatures, and thus co-alloying Bi with Ga should result in a lower alloy formation energy and better Bi incorporation efficiency as a result.[79] Here, we demonstrate a quinary GaInAsSbBi alloy grown at 400 °C by molecular beam epitaxy which achieves the same cutoff wavelength due to Sb and Bi incorporation as a quaternary InAsSbBi alloy grown under similar flux conditions at 360 °C, but with a substantially longer minority carrier lifetime consistent with the higher growth temperature. The structural and optical properties are examined by Nomarski interference contrast microscopy, X ray diffraction, Rutherford backscattering spectroscopy, steady-state photoluminescence, and time-resolved photoluminescence. A recombination rate analysis is performed on the temperature dependent minority carrier lifetime to determine the intrinsic doping density of the quinary GaInAsSbBi as well as the InAsSbBi and GaInAsSb references.

The samples are grown on (100)-oriented n-type GaSb substrates using a VG-V80H molecular beam epitaxy (MBE) system with valved group-V sources. The quaternary and quinary GaInAsSb(Bi) samples are sandwiched between a 500 nm thick buffer and a 30 nm thick cap of lattice matched InAsSb which provides confinement to photogenerated carriers. The quaternary InAsSbBi sample from Ref. [10] was sandwiched between a 400 nm thick buffer and a 100 nm cap of

lattice matched InAsSb. Before a quinary is grown with desired constituent mole fractions, group-III growth rates and V/III flux ratios are calibrated,[7] followed by three alloy composition calibration growths. The first calibration is a lattice-matched InAsSb layer grown at 440 °C with an In-limited growth rate of 1 μm/hr, an As/In flux ratio of $\sim$1.4, and an Sb/In flux ratio of $\sim$0.11 to achieve lattice-match on the GaSb substrate and produce a high quality InAsSb reference. These growth conditions are repeated for the second composition calibration, except that the growth temperature is reduced to 400 °C and the As/In flux ratio is reduced to near unity, resulting in increased Sb incorporation and intentionally compressive InAsSb. Next, Ga is introduced in the third composition calibration with a target 0.027 µm/hr Ga growth rate and 0.973 µm/hr In growth rate to compensate the compressive strain, producing lattice-matched GaInAsSb. The total group III growth rate target is 1 μm/hr so that the Sb/III and As/III flux conditions are maintained. Finally, the lattice-matched quaternary GaInAsSb will be grown again, but with the addition of Bi to grow quinary GaInAsSbBi. Table 5.1 summarizes the growth conditions and the (004) layer-substrate peak separation (in arcseconds) of each layer measured by X-ray diffraction.

Smooth, droplet free surfaces are observed for all samples with Normarski imaging. The inset to Figure 5.1 shows the region of the Rutherford backscattering spectroscopy yield signal that is uniquely characteristic of Bi (red curve), and the backscattering model fit of 0.13% Bi mole fraction in the GaInAsSbBi

Table 5.1: Summary and growth conditions of the calibration compressive InAsSb, quaternary GaInAsSb, and quinary GaInAsSbBi.

Sample	Growth Temp. (°C)	Strain (arcsec)	Growth rates (μm/hr)		Flux Ratios		
			In	Ga	As/III	Sb/III	Bi/III
InAsSb	400	-462	1.008	0	0.953	0.110	0
GaInAsSb	400	-22	0.969	0.029	0.963	0.112	0
GaInAsSbBi	400	-54	0.985	0.029	0.966	0.108	≈0.02

sample (black curve). Figure 2.3 shows the (004) X-ray diffraction pattern of the GaInAsSb sample which exhibits -22" compressive strain (blue curve), while the GaInAsSbBi (red curve) is slightly more compressive at -54" due to the incorporation of 0.13% Bi. The tetragonal distortion inferred from the measured strain is used to determine the As and Sb mole fractions of the smaples, given the calibrated group-III fluxes and Bi mole fraction from Rutherford backscattering, resulting in alloy compositions of $Ga_{0.029}In_{0.971}As_{0.882}Sb_{0.118}$ in the quaternary and $Ga_{0.029}In_{0.971}As_{0.883}Sb_{0.116}Bi_{0.001}$ in the quinary. Despite the small degree of strain observed, the 1 μm thick samples are still well within the critical thickness, and exhibit high structural and interface quality as evidenced by the Pendellösung fringes in both the quaternary $Ga_{0.029}In_{0.971}As_{0.882}Sb_{0.118}$ and quinary $Ga_{0.029}In_{0.971}As_{0.883}Sb_{0.116}Bi_{0.001}$. In contrast, the $InAs_{0.911}Sb_{0.081}Bi_{0.008}$ sample grown at 360 °C in Ref. [10] is still closely lattice-matched with slightly greater compressive strain at -81" (green curve), however the Pendellösung fringes

are characteristic of only the cap layer of the sample.

A comparison of the Bi mole fractions in the Ga-free quaternary $InAs_{0.911}Sb_{0.081}Bi_{0.008}$ grown at 360 °C and quinary $Ga_{0.029}In_{0.971}As_{0.883}Sb_{0.116}Bi_{0.001}$ grown at 400 °C provide only marginal evidence for the enhanced Bi incorporation efficiency in the presence of Ga. Detailed analysis of the Bi incorporation in InAsSbBi as a function of growth temperature indicates that the Bi sticking coefficient decreases with increasing growth temperature with a characteristic slope of 20.56 °C.[13] Thus the 40 °C increase in growth temperature should result in a factor of 0.14 reduction in Bi incorporation coefficient, resulting in an expected 0.11% Bi mole in an equivalent InAsSbBi alloy grown at 400 °C. Rutherford backscattering analysis shows that the Bi mole fraction is 0.13% in the quinary $Ga_{0.029}In_{0.971}As_{0.883}Sb_{0.116}Bi_{0.001}$, indicating that if Ga enhances the Bi incorporation efficiency, then the 2.7% Ga flux used in this sample was too low to conclusively observe the effect.

Steady-state photoluminescence is measured from the GaInAsSb(Bi) samples using a Bruker 80V Fourier transform infrared spectrometer and a 785-nm wavelength pump laser. The double modulation technique is utilized to increase the signal to noise ratio, with the laser modulated at 50 kHz.[80] The steady-state 120 K photoluminescence spectra of the GaInAsSb(Bi) samples are shown in Figure 5.2 along with the quaternary $InAs_{0.911}Sb_{0.081}Bi_{0.008}$ sample for comparison. The red curve in Figure 5.2 corresponds to the GaInAsSbBi sample grown with

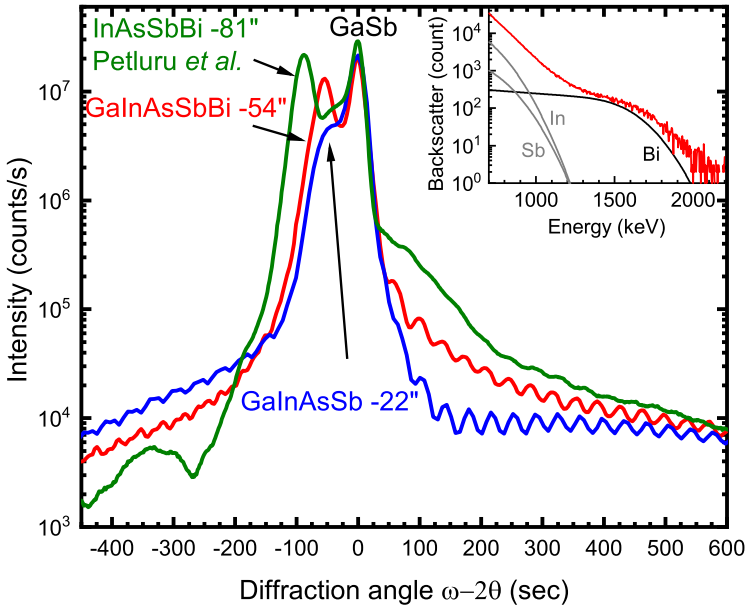

Figure 5.1: X-ray diffraction of quaternary InAsSbBi (green), quaternary GaInAsSb (blue), and quinary GaInAsSbBi (red). The blue and red curves are data from this work and the green curve is data from Ref. [10].

the same growth conditions as the quaternary GaInAsSb alloy (blue curve), but with Bi introduced during growth. The 6 meV red shift in the rising edge of the photoluminescence is consistent with the measured 0.13% Bi mole fraction measured by Rutherford backscattering, and results in a cutoff wavelength identical to $InAs_{0.911}Sb_{0.081}Bi_{0.008}$ due to the latter's lower Sb content. However, the photoluminescence signal of the quinary $Ga_{0.029}In_{0.971}As_{0.883}Sb_{0.116}Bi_{0.001}$ is brighter than that of the quaternary $InAs_{0.911}Sb_{0.081}Bi_{0.008}$ grown at 360 °C, affirming the benefit of utilizing a higher growth temperature.

The temperature dependent minority carrier lifetime of the quaternary and quinary alloys are measured using time-resolved photoluminescence. The

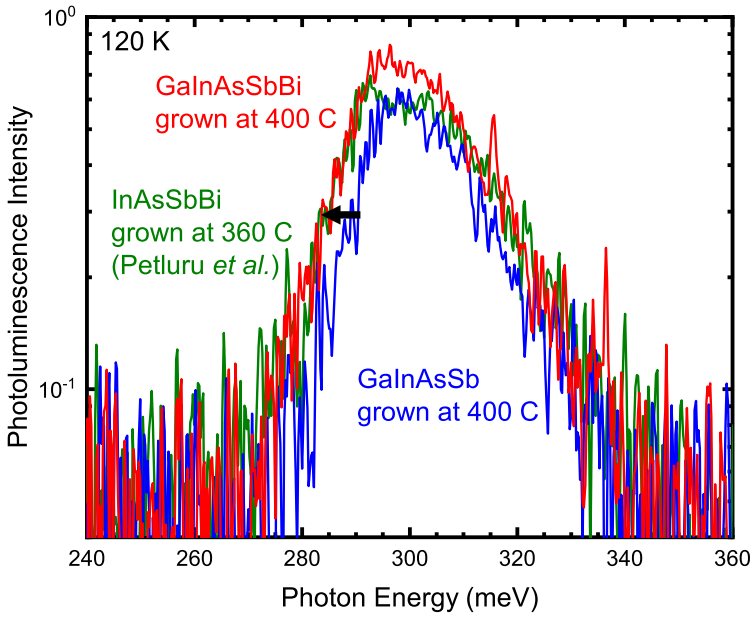

Figure 5.2: Photoluminescence spectra of quaternary InAsSbBi (green), quaternary GaInAsSb (blue), and quinary GaInAsSbBi (red). The black arrow indicates the red shift of the photoluminescence signal due to the incorporation of Bi in the quinary, which emits at the same cutoff as an InAsSbBi sample grown under similar flux conditions at a lower temperature. The green and blue curves are from this work and the green curve is data from Ref. [10].

GaInAsSb(Bi) samples are pumped with a 1535 nm (0.81 eV) pulsed laser with samples mounted in a liquid nitrogen cooled cryostat. The laser pulses are 3.5 ns long and the excitation is varied to inject 10^{11} - 10^{12} photons/cm^2 per pulse into the GaInAsSb(Bi) active region using a motorized half-waveplate compensator and polarizing beam splitter combination. The photoluminescence signal is collected and collimated with a 2 inch diameter f/2 90° off-axis parabolic mirror and then focused with a second off-axis parabolic mirror, transmitted through a 2.4 μm cutoff long-pass filter, and measured by a 6 μm cutoff VIGO Systems PVI-4TE detector. A Teledyne Lecroy HD 4096 oscilloscope averages 100,000 time-resolved photoluminescence decays to acquire one photoluminescence decay signal per excitation condition per temperature from 77 to 300 K. An optical schematic of the system can be found in Ref. [65].

The excitation conditions are selected to establish low-injection conditions in the samples. Supposing all the photoexcited electron-hole pairs distribute across the 1 μm active region absorber, then the lowest excitation of 10^{11} photons/cm^2 per pulse reaching the absorber results in an initial carrier density of 10^{15} electron-hole pairs/cm^3. This is just higher than the mid-high 10^{14} cm^3 background carrier density determined by the recombination rate analysis in the materials indicating low-injection conditions are quickly established. As the excitation level is increased, non-single exponential decay is observed at short time scales, indicating high injection conditions and a corresponding transient reduction of the lifetime.

However, even in the high injection case, after the short transient of non-single exponential decay, the system returns to low-injection behavior with a characteristic slope consistent with low-injection pumping.

The minority carrier lifetime is determined as a function of temperature by fitting the characteristic slope of low-injection regime photoluminescence signals with a single exponential decay. Figure 5.3 shows the time-resolved photoluminescence decays for the quaternary $Ga_{0.029}In_{0.971}As_{0.882}Sb_{0.118}$ and quinary $Ga_{0.029}In_{0.971}As_{0.883}Sb_{0.116}Bi_{0.001}$ samples under low excitation conditions at 117 K. The black curves are the photoluminescence decay data, while the subset of gray points show the data used to fit the single exponential slope in the low excitation range. The red and blue dashed lines are the best fit exponential slopes for the quinary and quaternary, respectively. It can be seen by the photoluminescence signals and slope fits that the quinary $Ga_{0.029}In_{0.971}As_{0.883}Sb_{0.116}Bi_{0.001}$ has a longer minority carrier lifetime (0.34 μs) than the quaternary (0.09 μs).

The recombination rate analysis is performed on the GaInAsSb(Bi) samples by fitting the three recombination rate mechanisms to the temperature dependent minority carrier lifetime determined by,

$$\frac{1}{\tau_{mc}} = \frac{1}{\phi\tau_{rad}} + \frac{1}{\tau_{SRH}} + \frac{1}{\tau_{Auger}}. \tag{33}$$

In Eq. (33), the minority carrier lifetime τ_{mc} is modeled as a function of the radiative lifetime τ_{rad} scaled by the photon recycling factor ϕ, the Shockley-Read-

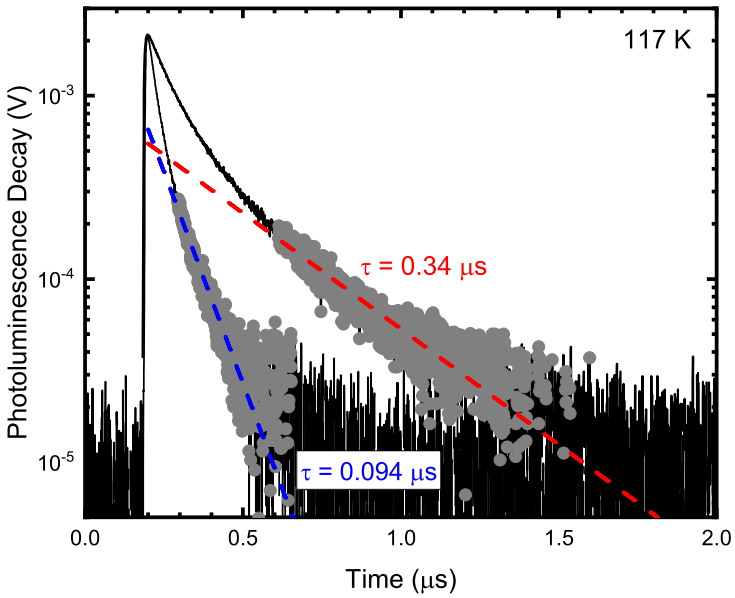

Figure 5.3: Time-resolved photoluminescence at low excitation conditions for $Ga_{0.029}In_{0.971}As_{0.882}Sb_{0.118}$ and $Ga_{0.029}In_{0.971}As_{0.883}Sb_{0.116}Bi_{0.001}$ at 117 K. The black curves are the photoluminescence decay data while the subset of gray points show the data used to fit the region of single exponential decay. The red and blue dashed lines show the resulting slope fit for the quinary and quaternary, respectively. The decay rates of the exponential slope correspond to the minority carrier lifetimes.

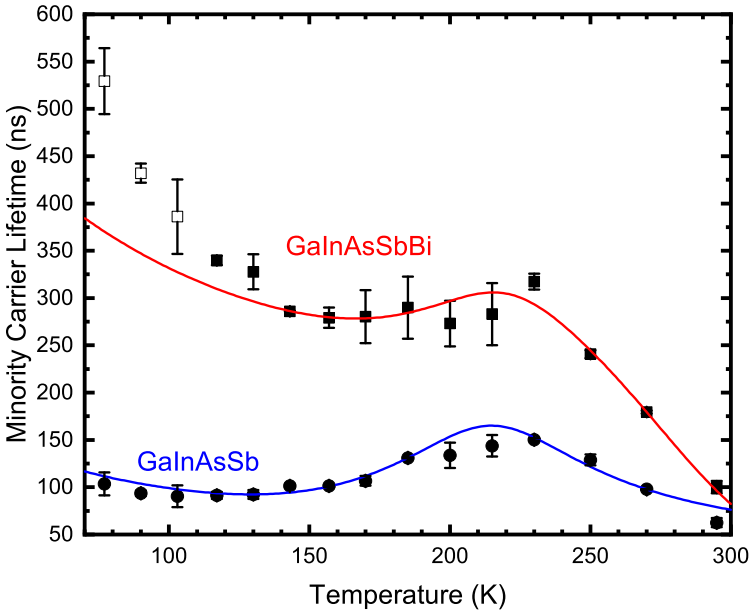

Figure 5.4: Temperature dependent minority carrier lifetime of the GaInAsSb(Bi) samples. The circles and blue curve correspond to the data and model fit for the quaternary GaInAsSb and the squares and red curve are the data and model fit for quinary GaInAsSbBi.

Hall (SRH) lifetime τ_{SRH} and the Auger lifetime τ_{Auger}. Further description of the recombination rate analysis can be found in Ref. [67] and references therein.

Figure 5.4 shows the temperature dependent minority carrier lifetime of the samples grown in this study alongside the solid curves showing the resultant recombination rate fit in Eq. (33). The temperature-dependent minority carrier lifetime of the quaternary $Ga_{0.029}In_{0.971}As_{0.882}Sb_{0.118}$ (circles and blue curve) is lower than the quinary $Ga_{0.029}In_{0.971}As_{0.883}Sb_{0.116}Bi_{0.001}$ (squares and red curve). This could be due to the intrinsic defects introduced in the InAsSb ternary by adding Ga into the system.[81] Once Bi is introduced in the quinary growth, however, the minority carrier lifetime increases by $>3\times$ in the SRH-limited regime,

possibly a result of the surfactant behavior of Bi, an additional benefit of Bi being introduced during growth.

The 0.34 μs lifetime observed in the quinary grown at 400 °C is consistent with the trends in Ref. [10], where the lifetime in the InAsSbBi alloys grown in the same molecular beam epitaxy system is consistently just under the expectation for lattice-matched $InAs_{0.91}Sb_{0.09}$ (0.39 μs at 400 °C).While the conclusions that can be drawn from comparisons of material quality metrics like minority carrier lifetime in samples grown at different times are typically limited, careful periodic benchmarking of the lifetime of material produced by this molecular beam epitaxy system enables the comparisons here. The minority carrier lifetime of a mid-wave infrared InAs/InAsSb superlattice benchmark structure has been carefully tracked over time, and is comparable at a Shockley-Read-Hall-limited lifetime of 2 μs during the growth campaigns which produced the GaInAsSb(Bi) samples examined here as well as the Ga-free $InAs_{0.911}Sb_{0.081}Bi_{0.008}$ sample from Ref. [10]. This indicates that the state of the molecular beam epitaxy system and quality of the mid-wave infrared InAsSb-based material produced in these time frames is comparable.

Table II provides the best-fit parameters to the temperature dependent minority carrier lifetime. The majority carrier concentration determined by a recombination rate analysis of the time-resolved photoluminescence becomes increasingly less sensitive as the majority carrier concentration decreases (particularly

in undoped samples), however, this approach is sufficient for the purposes of this report.[67, 74] The defect levels of both samples seem to be shallow toward the conduction band. The defect cross-section-concentration product is consistent with the observed minority carrier lifetime increase in the quinary GaInAsSbBi sample, further highlighting that Bi may have aided in growing a higher quality material with fewer defects. The Bloch overlap parameter —*F1F2*— typically has large influence on the minority carrier lifetime at higher temperatures where the Auger recombination intrinsically dominates. However, the fact that the minority carrier lifetime of the quaternary GaInAsSb is heavily dominated by the SRH recombination could suggest that the model is less sensitive to the Bloch overlap parameter in these samples. More growth and minority carrier lifetime studies are required to further understand the benefits of adding Ga and understand its relationship with Bi incorporation efficiency. The findings presented here provide evidence that the inclusion of Ga in quinary GaInAsSbBi may be the enabling factor to achieve long minority carrier lifetime mid-wave infrared material, however whether or not Ga significantly modifies the Bi sticking coefficient remains to be determined.

In conclusion, quinary GaInAsSbBi is grown for the first time at 400 °C achieving a similar cutoff wavelength as a quaternary InAsSbBi grown under similar flux conditions at 360 °C. The increase in growth temperature improves the minority carrier lifetime but significantly decreases the Bi incorporation efficiency for

Table 5.2: Best fit parameters extracted from a recombination rate analysis on the temperature dependent minority carrier lifetime of the GaInAsSb(Bi) samples grown.

Sample	Type	Majority Carrier Concentration (cm^{-3})	$E_c - E_t$ (meV)	σN_t (10^{-2} cm^{-1})	$\lvert F_1 F_2 \rvert$
GaInAsSb	*n*-type	6.08×10^{14}	73.9	86.3	0.0699
GaInAsSbBi	*n*-type	8.60×10^{14}	96.6	24.3	0.4674

InAsSbBi. Incorporating Ga may improve Bi incorporation efficiency, enabling growth of GaInAsSbBi at higher temperatures than InAsSbBi where longer minority carrier lifetimes are be obtained, opening a new design space to explore for mid-wave infrared sensing applications.

6 Infrared dielectric response, index of refraction, and absorption of germanium-tin alloys with tin contents up to 27% deposited by molecular beam epitaxy

This article was published in Applied Physics Letters, volume **113**, 122104 (2018).

Dominic Imbrenda, Ryan Hickey, James Kolodzey,

Department of Electrical and Computer Engineering, University of Delaware,

Newark, Delaware 19716, USA

Rigo A. Carrasco, Nalin S. Fernando, Stefan Zollner,

Department of Physics, New Mexico State University, Las Cruces, New Mexico

88003, USA

Jeremy VanDerslice

J.A. Woollam Co., Inc., 645 M Street, Suite #102, Lincoln, Nebraska 68508,

USA

6.1 Abstract

The dielectric spectral response of $Ge_{1-x}Sn$ thin film alloys with relatively high Sn contents ($0.15 \leq x \leq 0.27$) and thickness from 42 to 132 nm was characterized by variable angle spectroscopic ellipsometry over the wavelength range from 0.190 to 6 μm. The $Ge_{1-x}Sn_x$ thin files were deposited on Ge substrates by molecular beam epitaxy using an electron-beam source for Ge to achieve a substrate temper-

ature below 150 °C to prevent the surface segregation of Sn. From the measured dielectric function, the complex refractive index was calculated indicating an increase in the real index with the Sn content at mid-infrared wavelengths. The ellipsometry revealed that the band structure critical point energies red-shifted with the increasing Sn content. The optical absorption coefficiecnt was calculated from the imaginary index and showed a strong absorption into, and beyond, the mid-infrared with the increasing Sn content.

Germanium-Tin ($Ge_{1-x}Sn_x$) alloys have received considerable attention as a possible direct bandgap group IV semiconductor optoelectronic material compatible with Si and Ge fabrication processes.[82, 83] The introudction of Sn into the Ge lattice alters the electronic band structure and causes the Γ-valley to decrease faster than the L-valley in relaxed films, allowing the bandgap to become direct for Sn contents greater than around 6%-12%.[83] Photodetectors,[84, 85] photoemitters,[86, 87, 88, 89] photoconductors,[90] and optically pumped lasers fabricated[91] from $Ge_{1-x}Sn_x$ have been recently demonstrated. Group IV photonic devices that operate in the 2-5 μm wavelength mid-infrared (IR) regime are particularly attractive for sensing applications and can integrate directly with Si to overcome the challenges associated with the integration of group III-V materials.[92] To get the maximum utility from devices made from such materials, it is important to understand the relationship between the alloy composition and the effect on the optical properties such as the index of refraction and absorption

coefficient. For example, the ability to tune the index of refraction in the mid-IR is desirable for IR anti-reflective coatings and as layers for photonic devices.[93] Yet in $Ge_{1-x}Sn_x$ alloys, the relationship between the alloy composition and the effect on the index of refraction in the mid-IR is still not well understood for Sn contents above 15%, which is addressed in this report. As a consequence of lowering the bandgap by increasing the Sn concentration in $Ge_{1-x}Sn_x$ alloys, the sensitivity to photon absorption persists further into the IR. For example, a relaxed $Ge_{1-x}Sn_x$ alloy with x = 0.15 is predicted to have a direct bandgap of 0.3 eV, which corresponds to a wavelength value of 4.1 μm, whereas for a relaxed alloy with x = 0.18, the direct bandgap is predicted to be 0.22 eV which corresponds to a wavelength value of 5.6μm.[83, 14] There have been few publications, however, of the optical properties for such high Sn contents, which is addressed in this report.

The low thermal stability, low solid solubility (<1%),[94] and large lattice mismatch between Ge and Sn (14.7%)[95] require non-equilibrium deposition techniques. Because of these challenges, the availability of $Ge_{1-x}Sn_x$ films of appreciable thickness (>20 nm)[96] has restricted to atomic Sn contents of less than 22%,[97] until now. To enable larger Sn percentages (>18%), molecular beam epitaxy (MBE) was used with an electron beam (e-beam) evaporation source for elemental Ge to reduce the substrate temperatures below about 150 °C so that Sn does not segregate on the layer surface. There have been many investigations into the dielectric function and associated optical critical points of $Ge_{1-x}Sn_x$ alloys

into the mid-IR, but with lower Sn fractions x<0.20,[98, 22, 99, 100, 101, 102] as well as studies of the index of refraction and absorption with x $\leq$0.10.[93] In this report, we used visible and IR variable angle spectroscopic ellipsometry (VASE), to characterize the optical properties of $Ge_{1-x}Sn_x$ thin films with x = 0.15 to x = 0.27, including the index of refraction and absorption coefficient, for wavelengths from 0.190 μm to 6 μm.

$Ge_{1-x}Sn_x$ thin film alloys with up to 27 at % of Sn were deposited on 76.2 mm diameter undoped (001) oriented Ge substrates (u-Ge) with a resistivity of 40 Ω-cm by MBE as described previously.[103] Using thermal (Knudsen) effusion cell sources, the relatively low vapor pressure of Ge necessitated high cell temperatures upwards of 1240 °C, which approached the thermal limit of the pBN crucible, and radiated a substantial amount of heat to the substrate. In the current configuration of our MBE system, the growth of $Ge_{1-x}Sn_x$ alloys with Sn concentrations above 19% required an e-beam evaporation source (MBE Komponenten) for Ge, which had a smaller heated volume than the Knudsen source, allowing for less heat radiated to the substrate so that substrate temperatures below 150 °C could be achieved, as well as much higher growth rates and higher Sn contents. The native oxide of germanium was difficult to remove from the wafer surface, and care was taken when cleaning the substrates, including heating in the growth chamber to remove the surface germanium oxide, as described elsewhere.[103]

The file quality, crystallinity, strain state, surface quality, thickness, and Sn

concentrations were confirmed by high-resolution X-ray diffraction (HRXRD), reciprocal space mapping (RSM), atomic force microscopy (AFM), X-ray reflectivity (XRR), and channeling Rutherford backscattering spectrometry (RBS) as described elsewhere.[103] RSM plots of diffracted X-ray intensity versus reciprocal lattice vectors were used to determine the crystalline state, strain state, and the Sn composition of the films. As shown in Fig. 6.1, the broadened shape of the $Ge_{1-x}Sn_x$ film peaks was attributed to relaxation[104] and to possible disorder at the substrate interface but where the film regains high-quality crystallinity as it grows thicker. The cause for interface disorder, which was previously reported in channeling RBS measurements, was likely the lattice mismatch between the $Ge_{1-x}Sn_x$ and the Ge substrate.[103] Channeling RBS was performed on other samples in this series which verified alloy composition uniformity and the accuracy of these composition calculations.[95] RBS backscattered yield ratios showed that over 95% of the Sn was substitutional in the lattice.[103] The films in Fig.6.1 are typical of the films in this study. The Sn concentration and film relaxation along with other film characterization parameters are given in Table [bleck].

To determine the optical constants of the $Ge_{1-x}Sn_x$ thin films, VASE ellipsometry measurements were performed at room temperature in the ambient atmosphere. All samples were cleaved into 2 cm $\times$ 2 cm pieces and then sonicated for 15 min. in deionized water, 15 min in isopropyl alcohol, then for again 15 min in deionized water, and finally dried with nitrogen gas to remove any surface

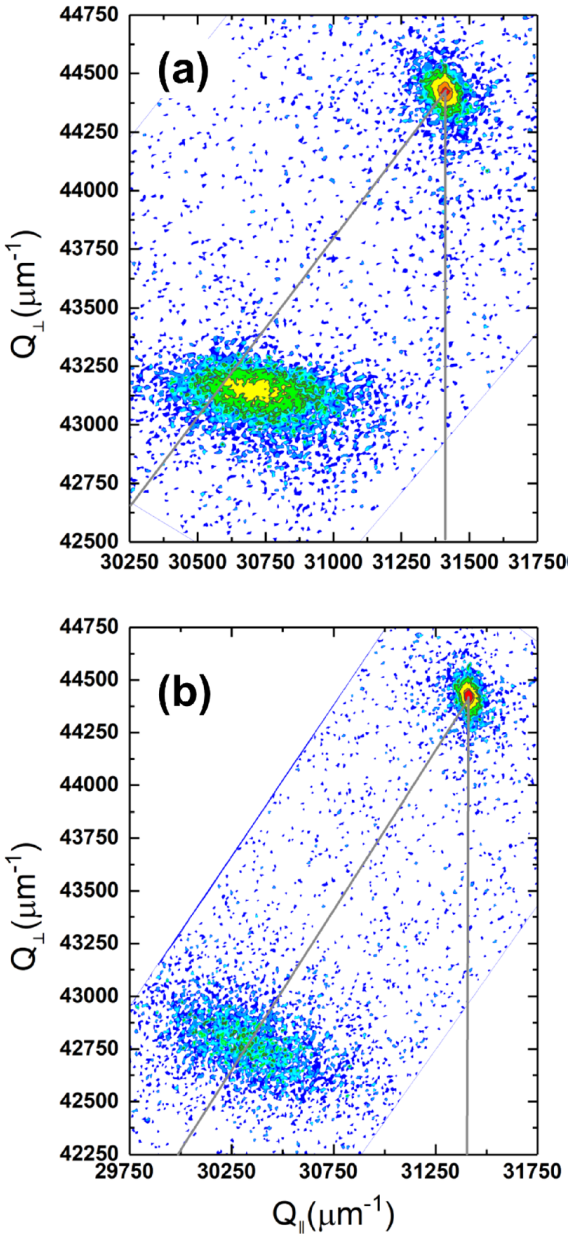

Figure 6.1: Reciprocal space map of X-ray intensity contours versus the out-of plane and the in-plane reciprocal lattice vectors of the (a) 18% and (b) 25% Sn concentration samples. The Ge substrate peak is at the top and the film peak is at the bottom. The vertical line through the Ge peak represents 100% compressive strain, so a layer peak centered on this line would have an in-plane parallel lattice constant equal to that of the Ge substrate. The diagonal line represents complete relaxation, as a peak centered anywhere on this line would have equal parallel and perpendicular lattice constants.

contaminants. Measurements of the ratio of the Fresnel reflection coefficients for parallel and perpendicular components of linearly polarized light at each selected wavelength were used to obtain the ellipsometric angles ψ and Δ, given by

$$\frac{r_p}{r_s} = \tan\psi e^{i\Delta}. \tag{34}$$

The films were characterized with a combination of two ellipsometers to cover different spectral ranges. In the wavelength range from 0.190 to 1.690 μm, measurements were performed at multiple angles of incidence (60°, 65°, and 70°) with a spectral resolution of 4 nm, using a Berek waveplate compensator (J.A. Woollam, V-Vase). In the infrared wavelength range from 1.532 to 6.173 μm (833-1620 cm^{-1} wavenumbers), measurements were performed on a J. A. Woollam FTIR-VASE ellipsometer, which is based on a fixed analyzer (0° and 180°) and polarizer (±45°) with a rotating compensator, at multiple angles of incidence (60°, 65°, and 70°). Above about 4 μm, the signal-to-noise ratio, the spectral resolution was set to 16 cm^{-1} with long signal averaging (three measurement cycles, each with 15 spectra per compensator revolution and 20 revolution scans per spectrum).

To extract the optical constants from the ellipsometric angles, we assumed a model comprising four layers including a vacuum ambient, a surface layer incorporating both surface roughness and any native oxide layer that may be present,[106] the $Ge_{1-x}Sn_x$ film layer, and finally a semi-infinite bulk Ge substrate. The dielectric function of the surface layer was obtained using an effective medium ap-

Table 6.1: Material characterization and energy band parameters of $Ge_{1-x}Sn_x$ thin film alloys used in this study. Sn% is the atomic percentage of each sample as determined from RSM measurements. Film relaxation is the ratio between the mismatch at the interface at the interface and the mismatch for a completely relaxed layer[105] and is determined from RSM measurements. T_{sub} was the substrate temperature during film deposition. The film thickness was determined from XRR and VASE measurements. Surface roughness was determined from XRR, AFM, and VASE measurements. $E_{\Gamma,Theory}$ is the direct bandgap at the Γ-point predicted from compositional dependence and deformation potential theory.[14] MSE is mean squared error from the ellipsometry experimental data fitting. The model developed to fit the ellipsometric data and descrive the optical properties of the film provided the lowest MSE and obeys the sum rule. In addition, a single surface layer was modeled to account for both oxide growth and surface roughness. The surface layer likely does not create a sharp interface with the film, reducing film model sensitivity to the surface layer thickness and resulting in correlation between the film and surface layer thicknesses. To mitigate the effects of correlation, the sum of the VASE thickness and roughness is used to compare to the XRR thickness

			Thickness		Surface roughness				
Sn (%)	Film relaxation (%)	T_{sub} (C°)	XRR (nm)	VASE (nm)	XRR (nm)	AFM (nm)	VASE (nm)	$E_{\Gamma,Theory}$ (eV)	MSE
15	54	120	42.5	34.4	1.00	0.62	4.7	0.351	0.92
18	87	100	100.2	97.2	3.60	0.99	5.5	0.230	1.29
25	96	100	132.3	118.6	1.46	1.83	8.8	0.040	1.46
27	94	100	125.9	114.2	1.80	2.86	9.1	0.001	1.31

proximation layer that consisted of 50% film and 50% ambient. The dielectric functions of the $Ge_{1-x}Sn_x$ films and Ge substrate were described using a Johs-Herzinger parametric oscillator model, which imposes Kramers-Kronig (K-K) consistency between the real and imaginary parts to ensure causality. The parametric oscillator model consists of 8 oscillators with multiple fit parameters (about 40 total) each representing, in principle, critical point energy transitions for Ge and $Ge_{1-x}Sn_x$. Although this model has been successfully used to determine the optical properties of many semiconductors, one must be careful not to assign too much physical meaning to the fit parameters. Because of strong correlations between parameters, two solutions with different fit parameters could yield the same dispersion results, whereas the usefulness of the model is strictly in the optical constants it provides not in the values of the fitting parameters. The $Ge_{1-x}Sn_x$ film thicknesses from XRR measurements were used as an initial starting point for the parametric model thicknesses which, along with the parametric oscillator parameters, were treated as adjustable parameters during the model fitting iterations. A dielectric function dispersion model fit was considered satisfactory when a good agreement between the calculated and measured ellipsometric angles was achieved, as determined by regression analysis using the Levenberg-Marquardt algorithm until the weighted mean squared error (MSE) between the calculated and experimental data was minimized. All MSE values were less than 1.5. The largest differences between the calculated and measured ellipsometric angles oc-

cured below 0.3 eV (about 0.4° for ψ and 3.5° for Δ, corresponding to 1 in units of the pseudo-dielectric function).

The spectral dependence of the complex index of refraction, $\tilde{n} = n + ik$, was determined from the parametric dielectric function dispersion model, $\tilde{\epsilon} = \tilde{n}^2$, and the absorption coefficient from the relation

$$\alpha = \frac{4\pi k}{\lambda}, \tag{35}$$

where k is the imaginary part of the complex index of refractions, also known as the extinction coefficient. and λ the wavelength of light. The complex dielectric function from the parametric model is given in Fig. 6.2. As the Sn concentration increased, there was a red shifting and broadening of the complex dielectric function. The 25% and 27% Sn concentration samples have a broadened peak in ϵ_2,0.9 eV, which was not observed in the other samples.

To verify whether these peaks were an artifact of the fittings or due to a property of these samples, two additional fittings to the measured ellipsometry data were performed on the 25% and 27% Sn concentration films.In the first additional fitting, we modeled the 25% and 27% Sn concentration films with a K-K consistent model that consisted of a combination of 11 Gaussian and Lorentz oscillators, rather than parametric oscillators. In the second additional fitting, we performed an uncorrelated all-wavelength inversion of the ellipsometric angles with the thickness fixed to the values obtained in the parametric oscillator fit,

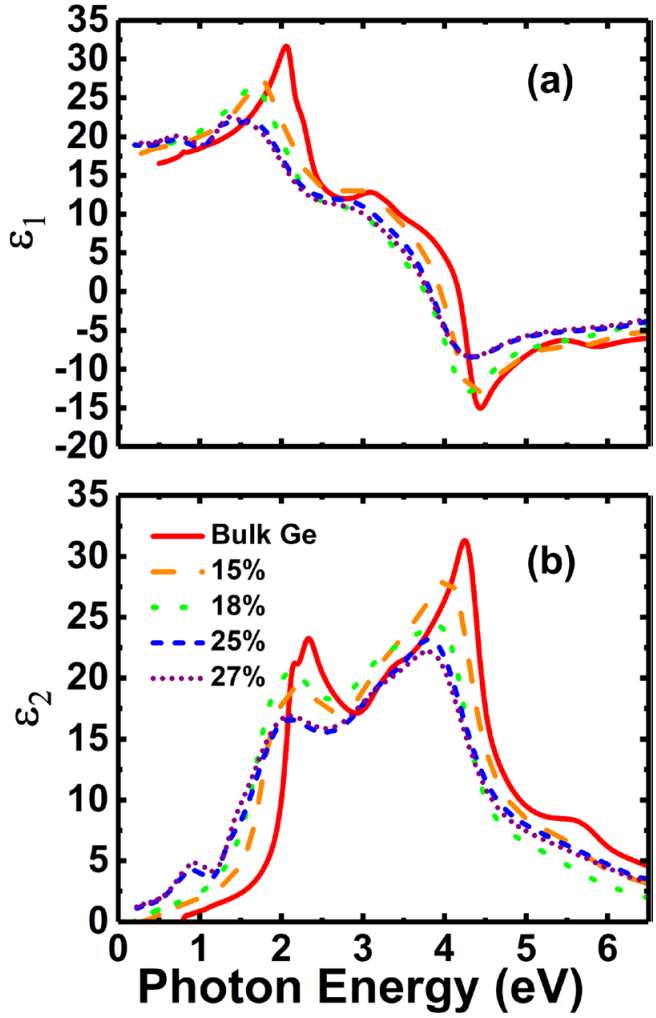

Figure 6.2: (a) Real, ϵ_1, and (b) imaginary part, ϵ_2, of the complex dielectric function vs. photon energy for $Ge_{1-x}Sn_x$thin film alloys deposited on Ge. The atomic Sn percentage is indicated by the value in the legend. Data have been combined from both the UV-VIS and the IR ellipsometers used in this study.

where K-K consistency is not enforced (this fitting is known as a point-by-point fit). The MSE of the two additional fittings changed only slightly from the initial fitting and the broadened peak in ϵ_2 near 0.9 eV was still present in the optical constants obtained from these new fits, indicating that this peak is a result of a property of these samples rather than an artifact of the parametric oscillator fitting. The broadened peak is possibly caused by an intrinsic feature such as from the band structure, an extrinsic one such as from a defect, or an interference fringe from the substrate.

Since Ge and Sn are group-IV elements, they both have four electrons per atom. Therefore, $\int \omega\epsilon_2(\omega)d\omega$ should be approximately independent of the Sn content, if the integral is taken over the measured spectral range from 0.2 to 6.5 eV. This is known as the sum rule for the oscillator strength[107] and can be used to test the accuracy of optical constants for new materials. In our case, the integral deviates no more than 7% from its bulk Ge value for all Sn contents, if we assume a surface layer thickness of about between 4 and 8 nm. The sum rule analysis therefore provides a strong argument for the accuracy of the optical constants presented in this work.

At wavelength above about 1.5 μm, the index of refraction, n, increased with the Sn concentration (Fig. 6.3). The peak at the lower wavelengths in each curve is due to the E_1 energy critical point.[14] It is known that alloying with Sn causes a red-shifting and broadening of the electronic critical points[103] due

to lowering of the bandgap, and this is observed more easily in the inset to Fig. 6.3, where the energy level for the E_1 critical point is red-shifted and broadened with the increasing Sn concentration. The inflection in the E_1 critical point peak for the 25% Sn concentration sample near 0.8 μm that is not present in the same peak for the 27% smaple was also confirmed with the three fitting methods described above and attributed to spin-orbit splitting of the valence band. The dispersion characteristics of $Ge_{1-x}Sn_x$ are not well known, and thus far, there has been little quantitative treatment of a relation to determine their value at mid-IR wavelengths.[93] At a wavelength of 5 μm, an empirical linear fitting of the index of refraction was found to be $n = mx + b$, for Sn% x, where slope $m = 0.01373 \pm 6.12489 \times 10^{-4}$ and the intercept $b = 4.01707 \pm 0.01195$. A wavelength of 5 μm was chosen because for small deviations, the index was slowly changing. The empirical linear fitting was found useful for the Sn compositions from bulk Ge to 27% measured here but was not evaluated for other Sn contents.

The absorption coefficients determined from the experimentally measured data for different $Ge_{1-x}Sn_x$ compositions are given in Fig. 6.4 With the increasing Sn content, the absorption persisted to longer wavelengths out to the far IR and also increased in strength at a given wavelength, which is expected as the bandgap at the Γ-point is predicted to decrease with the increasing Sn concentration.[83, 98] The 25% and 27% Sn concentration samples continued absorbing past our mea-

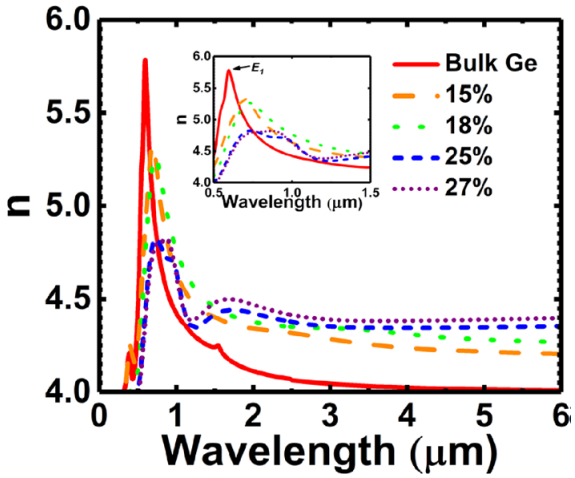

Figure 6.3: The real part of the index of refraction(n) vs. wavelength of light for $Ge_{1-x}Sn_x$ thin film alloys deposited on Ge. The atomic Sn percentage is indicated by the value in the legend. At wavelengths greater than about 3 μm,the index of refraction increased with greater Sn percentage. The inset is a close up of the peak in each curve between about 0.5 and 1.5 μm due to the E_1 critical point. The E_1 peak for bulk Ge is indicated in the inset. Tabulated values for the bulk Ge substrate were taken from Ref. [108] up to 2.4 μm and from Ref. [109] up to 6 μm.

surement spectral range of 6 μm, while there is a decrease in the absorption coefficient for the 15% and 18% Sn concentration samples because the bandgaps for these concentrations are predicted to lie within the measured spectral range. The bandgap at the Γ-point of $Ge_{1-x}Sn_x$ alloys depends on both the composition and the film strain state. For purposes of comparison, the theoretically predicted bandgap at the Γ-point, determined from compositional dependence and deformation potential theory as described elsewhere,[14] is given in Table 6.1. As seen in Table 6.1, at high Sn concentrations, the bandgap at the Γ-point is predicted to correspond to wavelengths in the far-IR regime beyond about 8 μm, raising the possibility that $Ge_{1-x}Sn_x$ may be used for devices in far-IR applications beyond the mid-IR. It should be noted that defects in a $Ge_{1-x}Sn_x$ film could alter its optical properties, as with any material. Although we believe that the films in this study are of high quality as evidenced by XRD, we cannot rule out the presence of defects nor their effects on film properties.

Using ellipsometry, we have measured the dielectric function of $Ge_{1-x}Sn_x$ thin film alloys with Sn concentrations of 15, 18, 25, and 27%, in the spectral range of 0.190–6 μm. From the dielectric function, we have determined that the index of refraction and absorption coefficient of these $Ge_{1-x}Sn_x$ thin film alloys can be tuned by varying the Sn concentration which alters these optical properties. As the Sn concentration increased, both the index of refraction and the absorption coefficient increased to larger values at longer wavelengths. For instance, for the

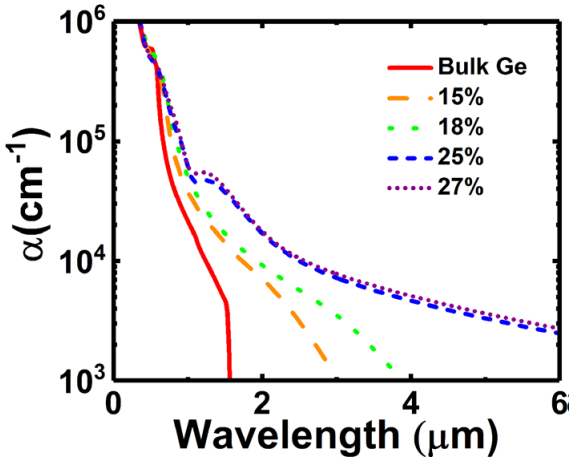

Figure 6.4: The absorption coefficient vs. wavelength for $Ge_{1-x}Sn_x$ thin film alloys deposited on Ge. The atomic Sn percentage is indicated by the value in the legend. The minimum value of absorption plotted is 1000 cm^{-1} because ellipsometry measurements are not sensitive to lower absorption values.[106] Tabulated data for bulk Ge were taken from Ref. [108].

27% Sn alloy, the absorption at a wavelength of 4.4 μm was comparable to that of unalloyed Ge at about 1.5 μm. An empirical linear fit to the index of refraction at 5 μm was obtained, which can be used to estimate the Sn concentration needed for an application-specific refractive index, such as for use in mid-IR optical devices or coatings. We have shown that for high Sn concentrations, the absorption persists past 6 μm, which corresponds to a higher photodetector sensitivity, responsivity, and specific detectivity at the mid-IR wavelengths. The characterization of these parameters will be critical in the design of future $Ge_{1-x}Sn_x$ optoelectronic devices that utilize high Sn concentrations. This work was funded in part by grants from the Air Force (AFOSR Award Nos. FA9550-14-1-0207, FA9550-13-1-0022, and FA9550-17-1-0134), the Army Research Office (ARO Award No. W911NF-12-

1-0380), and by gifts from Thorlabs, Inc. The work at NMSU was supported by the National Science Foundation (No. DMR-1505172). Special thanks to D. Beatson, C. Pinzone, J. Wei, J. Kouvetakis, J. Menendez, and S.-Q. (Fisher) Yu for valuable discussions. The work reported here was partially carried out in the Nanofabrication Facility at the University of Delaware.

7 The direct bandgap of gray α-tin investigated by infrared ellipsometry

This article was published in Applied Physics Letters, volume **113**, 232104 (2018).

Rigo A. Carrasco, Cesy M. Zamarripa, Stefan Zollner

Department of Physics, New Mexico State University, P. O. Box 30001,

Las Cruces, New Mexico 88003, USA

Josè Menèndez

Department of Physics, Arizona State University, Tempe, Arizona, 85287, USA

Stephanie A. Chastang, Jinsong Duan, Gordon J. Grzybowski

KBRwyle, 2601 Mission Point Blvd., Suite 300, Dayton, Ohio 45431, USA

Bruce B. Claflin, and Arnold M. Kiefer

Air Force Research Laboratory, Sensors Directorate, Wright-Patterson

Air Force Base, Ohio 45433, USA

7.1 Abstract

Using Fourier-transform infrared ellipsometry, the authors provide spectroscopic evidence about the valence band (VB) structure of diamond-like α-tin. The mid-infrared dielectric function of α-tin grown pseudomorphically on InSb or CdTe by molecular beam epitaxy shows a strong $\bar{E}_0$ peak near 0.41 eV. This peak is assigned to allowed intravalence band transitions from the Γ_7^- (electron-like)

VB to the Γ_8^{+v} heavy hole VB and/or interband transitions from Γ_7^- to the Γ_8^{+c} light "hole" conduction band. The strength of this peak requires a hole density in the mid-10^{18} cm^{-3} range at room temperature, which might be caused by unintentional doping, thermal electron-hole pair generation, or by the possibility that the L_6^+ conduction band might have an energy slightly lower than the Γ_8^+ VB maximum. Alternatively, this $\bar{E}_0$ peak might be enhanced by the M-shape of the Γ_7^- VB caused by interactions with the Γ_7^+ split-off hole VB. A sum-rule analysis of the dielectric function between 0.16 and 6.5 eV is consistent with a high-frequency dielectric constant of 24, which has at most a weak temperature dependence between 100 and 300 K.

It was established[1] over fifty years ago and is now universally acknowledged that diamond-like gray tin (α-tin) is a zero band-gap semiconductor. But is this really true? Our manuscript addresses the question if α-tin might better be described as a semimetal, where the conduction and valence bands overlap by a few meV. (For this article, we consider a semimetal to have a small, but non-zero overlap between the valence and conduction band.[110] The literature is not consistent in the use of this term as so-called Dirac semimetals as well as zero-gap α-Sn itself are often referred to as semimetals.[111])

Gray tin can be produced in single-crystal form by solution growth in mercury[112, 113] or with molecular beam epitaxy[114, 115] on InSb or CdTe substrates. The availability of these bulk crystals or thin epitaxial layers enabled much research

in the 1960s and 1980s, respectively. Interest in α-Sn has been revived recently because it forms the endpoint of $Ge_{1-x}Sn_x$ alloys, which have potential applications as mid-infrared detectors and lasers,[116, 117] and because under stress it becomes a topological insulator or Dirac semimetal.[111, 118]

The band structure[118, 119, 120, 121, 122, 123, 111] of α-Sn (see Fig. 7.4 in supplementary materials) is similar to Ge, with the following considerations: As in Ge, the Γ_8^+ and Γ_7^+ p-bonding orbitals are split by $\Delta_0 \approx 0.8$ eV due to spin-orbit interaction. The Γ_7^- s-antibonding level, which forms the conduction band (CB) in Ge, moves downward in α-Sn[1] and appears between Γ_8^+ and Γ_7^+ with a negative energy E_0 if we conventionally choose Γ_8^+ as the zero energy level. Due to $\vec{k}\cdot\vec{p}$ interaction, the upper Γ_8^+ band (light holes in Ge) reverses curvature and becomes a CB. Conversely, the Γ_7^- s-antibonding orbital becomes a valence band (VB). The curvature of this band near the Γ-point of the Brillouin zone is negative, if $|E_0| < \frac{2}{3}\Delta_0 \approx 0.53$ eV, and positive otherwise. (In the latter case, the band may acquire an M-shape, i.e., the maximum of the Γ_7^- VB will not appear at the Γ-point. This M-shape has been found in some calculations.[118]) Since the two Γ_8^+ bands are degenerate at the Γ-point (protected by cubic symmetry), the band gap is exactly zero, independent of temperature and hydrostatic pressure, which makes α-Sn a zero band-gap semiconductor.

Evidence for this band ordering was originally derived from electrical measurements under a magnetic field.[1] It was later confirmed with magnetoreflectance[113]

and angle-resolved photoemission.[118, 124] Just like in Ge, optical transitions between the Γ_7^- and Γ_8^+ bands are allowed. They form the direct band gap E_0 in Ge, which, as indicated above, is negative in α-Sn. Therefore, we will use the notation $E_0{=}{-}\bar{E}_0$ for the optical transition energy between the two bands. This gap $\bar{E}_0$ near 0.41 eV is the topic of our manuscript. It has so far been ignored in the literature: Lindquist and Ewald[125] determined the complex refractive index for α-Sn using polarized variable-angle reflectance (an early form of ellipsometry), but they only measured at discrete energies of 0.3, 0.4, and 1.0 eV and therefore missed the $\bar{E}_0$ peak in the extinction coefficient. Reflectance,[126] electroreflectance,[127] and spectroscopic ellipsometry[23] measurements only studied interband transitions above 1 eV. Optical constants due to interband transitions calculated using the $\vec{k}{\cdot}\vec{p}$ method[119, 128] found the $\bar{E}_0$ peak insignificant, just like in Ge.

In this work, we determined the dielectric function of α-Sn from 0.16 to 6.5 eV between 100 and 300 K using layers between 69 and 127 nm thickness grown on InSb and CdTe by molecular beam epitaxy. At such large thicknesses, we do not expect confinement effects.[129, 123] The InSb (001) substrates have an electron concentration of 10^{14} cm^{-3} at 77 K. Prior to film growth, they were cleaned *in vacuo* using atomic hydrogen with a substrate temperature of 200°C and monitored with reflection high-energy electron diffraction (RHEED) until a sharp diffraction pattern of a $c\,(2\times 8)$ surface reconstruction is observed. The sample radiatively cools to near room temperature and is then exposed to a

tin flux from an effusion cell. The RHEED pattern immediately changes to a (2×1) pattern typical of the (001) surface reconstruction of a diamond crystal structure[130] and remains so throughout deposition. Post-growth examination by high-resolution x-ray diffraction (XRD) establishes the diamond crystal structure, crystalline quality, epitaxial coherency to the substrate lattice, and the sample thickness. The in-plane and out-of-plane strains (measured by XRD) are -0.15% and 0.13%, respectively, in agreement with the ratio of the elastic constants.[131]

Our substrate cleaning with atomic hydrogen avoids potential issues with preferential sputtering leading to an In-rich surface.[124] Nevertheless, we are unable to exclude the presence of In or other p-type dopants in our α-Sn layers, as was reported by others.[124, 118]

We acquired the pseudo-dielectric functions from 0.16 to 6.5 eV at four angles of incidence from 60° to 75° using spectroscopic ellipsometry as described in the supplementary material. Figure 7.1 shows results for 127 nm α-Sn on InSb at 300 K. Similar results for other α-Sn layers on InSb and CdTe are shown in Figs. 7.5-7.7. Above 1.2 eV, our results are very similar to earlier measurements,[23] showing several critical points related to optical interband transitions from the VB to the CB.[128] The maximum of $\langle \epsilon_2 \rangle$ near E_2 is between 15 and 20 for our three layers, slightly lower than the maximum of 21 observed previously.[23] This indicates that the surface layer region on our samples is slightly thicker than in Ref. [23]. We observe one interference fringe in each $\langle \epsilon_2 \rangle$ spectrum, which moves

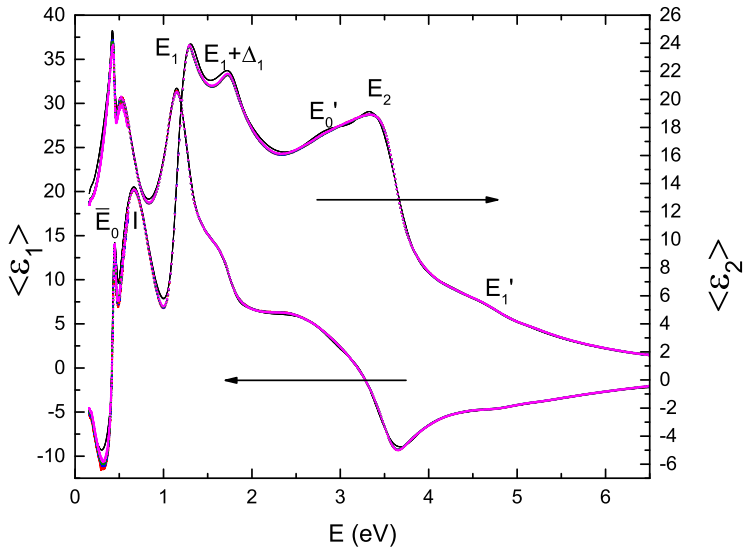

Figure 7.1: (Color online) Pseudo-dielectric function for 127 nm α-Sn on InSb (001) measured by spectroscopic ellipsometry (circles) and Fourier-transform infrared ellipsometry (squares) from 0.16 to 6.5 eV at four incidence angles at 300 K. Model data are shown by lines. Several critical points[23] and an interference fringe (I) are labeled.

from 1.10 eV in the 69 nm thick layer to 0.69 eV for the thickest layer (127 nm). All three $\langle\epsilon_2\rangle$ spectra show a sharp peak at 0.41 eV, which we attribute to the $\bar{E}_0$ transition. This transition has not previously been reported as a peak in an optical spectrum.

To analyze these data in more detail, we extract the dielectric function of α-Sn on InSb (shown in Fig. 7.2) using a three layer model[132, 14, 108] (oxide, α-Sn, InSb), as described in the supplementary material. Our optical constants at 0.4 eV are quite different from those obtained on bulk crystals.[125]

There has been considerable uncertainty[133] about the high-frequency dielectric constant ϵ_∞ (which is equal to the low-frequency dielectric constant in α-tin,

since there are no infrared-active phonons).[21] ϵ_∞ is the contribution to the static dielectric constant from optical interband transitions. A value of ϵ_∞=24 was found from infrared polarized reflectance measurements at oblique incidence in the free-carrier regime at very low energies.[125] Our two-side polished InSb substrate does not allow ellipsometry measurements below 0.1 eV. However, we can determine ϵ_∞=23.4 at 300 K from the sum rule[21, 134]

$$\epsilon_\infty = 1 + \frac{2}{\pi}\int_0^\infty \epsilon_2(\omega)\,\omega^{-1} d\omega, \tag{36}$$

confirming the results of Lindquist and Ewald.[125] (Taking 0.16 and 6.5 eV as the limits of the integral only provides a lower bound for ϵ_∞, since absorption at lower and higher energies has been neglected.) We found a small ($\approx$5%) decrease of ϵ_∞ at 100 K, but that is within the measurement uncertainty.

The optical constants for α-Sn are quite similar to those of Ge[108] (with the obvious shifts of the critical points) except that the $\bar{E}_0$ gap of α-Sn at 0.41 eV is much stronger than the E_0 gap of Ge.[108] The point-by-point results show a slope change in the rise of ϵ_2 at 0.92 eV, shown by the downward arrow in Fig. 7.2. The absorption of p-type semiconductors usually shows a minimum at the spin-orbit splitting energy Δ_0 due to forbidden intravalence band (IVB) transitions.[135, 136, 137, 138] Since $\Delta_0\approx$0.8 eV in α-Sn, we also attribute this feature in our spectra to IVB transitions from the Γ_7^+ to the Γ_8^+ VB, which might be much stronger in α-Sn than in Ge because of the very high hole concentration

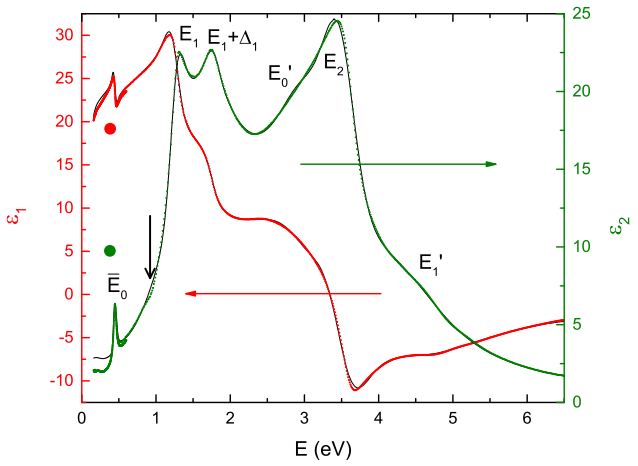

Figure 7.2: (Color online) Dielectric function of α-tin from 0.16 to 6.6 eV at 300 K determined from spectroscopic ellipsometry of three Sn layers on InSb. The solid lines show a parametric oscillator fit, the small symbols the results of an uncorrelated wavelength-by-wavelength fit using the thicknesses derived from the parametric oscillator fit. The large symbols show results from Lindquist and Ewald.[125] The downward arrow points to a change in the slope of ϵ_2 at 0.92 eV.

(see below).

To compare the strengths of the E_0 peak in Ge and the $\bar{E}_0$ peak in α-tin, we consider that the $\vec{k}\cdot\vec{p}$ dipole matrix element P for this transition is about the same for both materials,[21] with E_P=$2P^2/m_0$≈20 eV, where m_0 is the free electron mass.[113] The E_0 or $\bar{E}_0$ transitions have a square root-like energy dependence with an amplitude prefactor proportional to $\mu^{\frac{3}{2}}$, where μ is the optical (reduced) mass.[21] For Ge (InSb), μ=0.037 (0.014) is calculated from the heavy hole Γ_8^+ and the electron Γ_7^- masses.[21] For α-tin, μ=0.017 is obtained from the light "hole" Γ_8^+ CB and the "electron" Γ_7^- VB masses given in Table 7.1. The $\bar{E}_0$ transition in α-Sn therefore should have about the same square root-like shape as the E_0 gaps

in Ge[108] or InSb (Fig. 7.11) within our simple effective mass theory, if excitonic effects (which scale like $\mu\epsilon_\infty^{-2}$) are neglected. See the dashed line Fig. 7.3. There is no reason within this parabolic band theory at 0 K for a strong peak riding on the usual interband absorption continuum.

To further discuss the strong $\bar{E}_0$ peak in ϵ_2, we consider the band structure of α-tin in more detail (see Fig. 7.4) and also take into account thermal excitation of intrinsic electron-hole pairs. As indicated above, at the Γ-point there are three VBs: Γ_7^+, Γ_7^-, and the lower Γ_8^+ band (heavy hole Γ_8^{+v}). The CB at Γ is formed by the upper Γ_8^+ (light "hole" Γ_8^{+c}) band, but there is also a CB minimum at the L-point with L_6^+ symmetry,[139] just like in Ge, GaAs, or GaSb, which is close to the CB minimum in energy. Most calculations[119, 120, 121] as well as low-temperature magnetotransport measurements[115, 140, 141] place the L_6^+ CB about 0.1 eV above Γ_8^+, but at room temperature Hoffmann *et al.*[115] find that this indirect gap has been reduced to only about $5-7$ meV. The effective masses of all five bands are known, see Table 7.1.

The VB maximum and the lowest two CB minima are all at about the same energy at room temperature, but the density of states of the four L_6^+ CB valleys is nearly one hundred times higher than that of the Γ_8^{+c} (light "hole") CB, because of the large L_6^+ effective mass.[115] For this zero band-gap semiconductor, at moderate doping concentrations and at room temperature, the free carriers are essentially instrinsic. At 300 K, the intrinsic electron and hole densities are

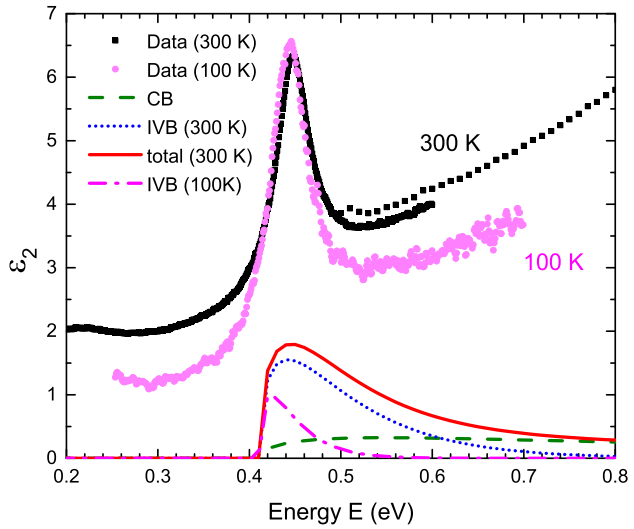

Figure 7.3: (Color online) ϵ_2 for α-tin on InSb near $\bar{E}_0$ from point-by-point fits at 100 and 300 K (symbols); contributions from Γ_7^- to Γ_8^{+c} (dashed) and for IVB transitions to the heavy hole Γ_8^{+v} at 300 K (dotted) and 100 K (dot-dashed). Total ϵ_2 at 300 K (solid, assuming a constant matrix element and parabolic spherical bands).

about 4×10^{18} cm^{-3}. Using the approach of Ref. [115], this implies a Fermi level $E_F\approx-16$ meV relative to the top of the VB, which is only consistent with a vanishing value of the indirect gap, as indicated above.[115] The holes are all located in the Γ_8^{+v} heavy hole VB, while most electrons are in the L_6^+ CB. The Γ_8^{+c} CB (light "hole") is nearly empty.

The $\bar{E}_0$ transition therefore has two components, the Γ_7^- to Γ_8^{+c} (light "hole") inverted interband transitions (which are similar to Ge or InSb, as discussed above) and the allowed Γ_7^- to Γ_8^{+v} (heavy hole) IVB transitions. These allowed IVB transitions in α-Sn are much stronger than the forbidden ones in Ge (from the split-off to the heavy hole band), because the momentum matrix element between

Γ_7^- to Γ_8^+ is non-zero (see above), while the matrix element between Γ_7^+ (split-off hole) and Γ_8^+ is zero at Γ and linear in k. This makes forbidden IVB transitions in Ge very weak.[137, 138] The allowed IVB contribution to $\bar{E}_0$ in α-Sn is described by an optical mass μ_{IVB}=0.075 (considering that the initial and final states both curve downward and therefore the inverse of the "electron" and heavy hole masses must be subtracted). The IVB transitions into the Γ_8^{+v} VB therefore should be $(\mu_{\mathrm{IVB}}/\mu)^{1.5}$=9 times larger than interband transitions into the Γ_8^{+c} CB.

A simple theory (based on parabolic spherical bands) for the forbidden IVB transitions in Ge was given by Kahn.[136] This can be modified for the allowed Γ_7^- to Γ_8^{+v} IVB transitions in α-Sn: We multiply the square root-like onset of interband transitions[21] (see supplementary material) with a Maxwell-Boltzmann factor describing the probability of finding a hole in the final Γ_8^{+v} state. (A more accurate expression, yielding similar results, can be found using Fermi-Dirac statistics.) If the photon energy $\hbar\omega$ exceeds $\bar{E}_0$,

$$\epsilon_2^{\mathrm{IVB}}(\hbar\omega) = A\frac{\sqrt{x-1}}{x^2}\exp\left[-\frac{\hbar\omega-\bar{E}_0}{k_BT}\frac{m_e}{m_{\mathrm{hh}}-m_e}\right], \tag{37}$$

where $x = \hbar\omega/\bar{E}_0$ and the amplitude prefactor A is given in the supplementary material. Figure 7.3 shows the room-temperature contributions of both interband and IVB transitions and their sum in comparison with experimental data at 300 K. We are satisfied with the qualitative agreement of our simple theory (which ignores warping and non-parabolicity) with the experimental data at 300 K near

$\bar{E}_0$=0.41 eV, since we have neglected the Drude absorption of free carriers and the forbidden Γ_8^{+v} to Γ_8^{+c} transitions at low energies as well as the onset of E_1 transitions at higher energies. Our calculations confirm that IVB transitions to the heavy hole band are the dominant contribution to the $\bar{E}_0$ peak, but underestimate the strength of the transition and predict a broader peak. We believe that better agreement with theory can be found by fully incorporating the unusual complexity of the α-tin VB structure, especially the non-parabolicity and warping.

Additional information about IVB contributions to $\bar{E}_0$ can be found from the temperature dependence of the $\bar{E}_0$ peak for α-Sn on InSb and CdTe (Figs. 7.3, 7.9). At 100 K, the intrinsic electron/hole concentration is much smaller than the doping density[115] and therefore the total hole concentration should be about an order of magnitude lower than at 300 K. The $\bar{E}_0$ peak therefore should also be an order of magnitude less intense at 100 K than at 300 K. A comparison of experimental spectra at both temperatures for α-tin on InSb (Fig. 7.3) shows that the magnitude of $\bar{E}_0$ is nearly independent of temperature. The background is reduced at 100 K, but the magnitude and broadening of the $\bar{E}_0$ peak are about the same. We conclude from our experimental data that the density of heavy holes in the Γ_8^{+v} VB of α-Sn on InSb is nearly independent of temperature between 100 and 300 K, in contrast to Maxwell-Boltzmann statistics. To explain this, either the unintentional dopant density in our nominally undoped samples must be unexpectedly high, or perhaps α-Sn on InSb is a semimetal with a small density

of states at the Fermi level on the order of 10^{18} cm^{-3} because the L_6^+ CB minimum has a lower energy than Γ_8^+.

Preliminary data for α-Sn on CdTe (see Fig. 7.9) indicate that $\bar{E}_0$ behaves as expected from Maxwell-Boltzmann statistics, see Eq. (37). The $\bar{E}_0$ peak is strong at 300 and 250 K, weak at 200 K, and not visible at lower temperatures. New α-Sn layers will be grown on single-side polished CdTe substrates to investigate this further. The comparison between InSb and CdTe substrates suggests, however, that α-Sn is indeed a zero-gap semiconductor, with a positive indirect gap $\Gamma_8^+ - L_6^+$. α-tin layers on CdTe have lower doping[115] and therefore the carrier density follows Maxwell-Boltzmann statistics, while the layers on InSb seem to have a high hole density independent of temperature.

We need to mention another possible contribution (in addition to IVB transitions to Γ_8^{+v}) to the $\bar{E}_0$ peak: Some, but not all, band structure calculations[122, 118, 123, 111] predict a strong non-parabolicity of the Γ_7^- VB leading to a weak M-shape (similar to an inverted fourth-order polynomial with a local minimum at Γ). The shape of this feature depends critically on the magnitude of the spin-orbit splitting Δ_0 at Γ_{25}' (which is not known precisely, since the $E_0 + \Delta_0$ or Δ_0 IVB transitions are not observable in α-tin) and spin-orbit contributions to the momentum matrix element E_P. Under some scenarios, if the curvatures of the Γ_7^- and Γ_8^{+c} bands are similar, the M-shape might lead to a van Hove singularity in the joint density of states at an energy $\bar{E}_0$, which might contribute to the peak in

our ellipsometry experiments. This Γ_7^- to Γ_8^{+c} transition should be independent of temperature, in contrast to results for α-Sn on CdTe.

It is also remarkable that the energy of the $\bar{E}_0$ peak is independent of temperature, while the E_0 gap of InSb and most other semiconductors blueshifts at lower temperatures. This had already been recognized in magnetoreflection experiments,[113] but our results in Fig. 7.3 show this more directly.

We also considered the effects of biaxial stress in a pseudomorphic α-tin layer on the $\bar{E}_0$ transitions. After a detailed analysis (see Fig. 7.14), we conclude that the strain splittings[2] and shifts are less than half of k_BT at room temperature and therefore strain in pseudomorphic α-Sn alloys grown on InSb or CdTe is not a significant factor in the discussion of our dielectric function. The strain splittings and shifts of the Γ_8^+ and L_6^+ states may be important for the analysis of Hall measurements.[115]

In summary, we find a very strong $\bar{E}_0$ peak at 0.41 eV in the dielectric function of α-tin layers on InSb and CdTe, which is independent of temperature for α-Sn on InSb (see Fig. 7.3), but strongly varies with temperature for α-Sn on CdTe (see Fig. 7.9). We assign this peak to allowed intravalence band transitions from the Γ_7^- electron-like VB to the Γ_8^{+v} heavy hole VB. The strength of these transitions depends on the hole concentration, which could be intrinsic (as in α-Sn on CdTe) or extrinsic (on InSb, because of In doping). An unusual M-shape of the Γ_7^- VB might also contribute to $\bar{E}_0$. The strength of this peak suggests a

heavy hole density in the mid-10^{18} cm^{-3} range, which decreases with decreasing temperature for α-Sn on CdTe. We conclude that the L_6^+ CB has a higher energy than the Γ_8^+ VB maximum, at least at low temperatures. If this can be confirmed, then pseudomorphic α-tin on InSb or CdTe is a zero-gap semiconductor, not a semimetal.

Supplementary Material

See supplementary material for additional information about growth of epitaxial layers, data acquisition and data analysis (including optical constants for InSb), additional experimental data, theoretical models for optical interband transitions, critical-point parameters, and a detailed discussion of the influence of strain on the warped valence and conduction bands of α-tin, including the topological phase transition under strain.

This work was supported by the Air Force Office of Scientific Research (FA9550-16RYCOR296). Measurements at NMSU were supported by the National Science Foundation (DMR-1505172). JM was supported by AFOSR (FA9550-17-1-0314). RAC and SZ acknowledge support from the AFOSR Summer Faculty Fellowship Program. CMZ was supported by the New Mexico Alliance for Minority Participation (NSF HRD-1305011). We are grateful to Dr. Wolfgang Windl for stimulating discussions.

7.2 Supplementary Material

7.2.1 Epitaxial growth

The epitaxial growth of α-tin on InSb was described in the main text. The CdTe (001) substrates (JX Nippon) were undoped and essentially intrinsic, with a resistivity of about 7×10^8 Ωcm. They were prepared for growth by immersion in a series of solvents and then etching in a 1% BrM (bromine in methanol) solution (by volume) for 30 s. They were subsequently rinsed in methanol, then in deionized water, and finally dried with nitrogen. The substrate is immediately introduced into ultra-high vacuum, where it is slowly heated to approximately 115°C. During heating, RHEED monitors the desorption of the amorphous Te overlayer that develops during etching until a (2×1) reconstruction emerges. Atomic hydrogen was not used for CdTe.

7.2.2 Data acquisition

We acquired the pseudo-dielectric functions from 0.16 to 0.6 eV at four angles of incidence from 60° to 75° on a J.A. Woollam Fourier-transform infrared ellipsometer at room temperature with 16 cm^{-1} resolution, as described elsewhere.[14] Below 0.16 eV, the incoherent backside reflections from the two-side polished InSb substrate made data analysis impossible. Above 0.6 eV, the data were too noisy to be useful due to the intensity drop of the infrared light source towards the

Table 7.1: Density of states masses for the valence and conduction bands of α-Sn at Γ and L.

Band	Symmetry	Mass	Reference
L-valley CB[a]	L_6^+	0.19	Refs. 115 and 141
Light "hole" CB	Γ_8^+	0.024	Refs. 115 and 140
Heavy hole VB	Γ_8^+	0.26	Refs. 115 and 140
"Electron" VB	Γ_7^-	0.058	Ref. 113
Split-off hole VB	Γ_7^+	0.04	Ref. 113

[a]The specified mass is for a single L_6^+-valley. The resulting density of states must be multiplied by four to account for the number of equivalent L-valleys.[115]

visible. We also measured the pseudo-dielectric functions from 0.5 to 6.5 eV in 0.01 eV steps at the same incidence angles on a J.A. Woollam variable-angle ellipsometer equipped with a computer-controlled Berek waveplate compensator. We followed the same procedure as for bulk Ge.[108] The pseudo-dielectric functions did not depend on the angle of incidence and agreed reasonably well in the range of overlap of the two instruments from 0.5 to 0.6 eV. (A small mismatch of the data sets can be seen in Figs. 7.1-7.3.)

Room temperature measurements at variable angles were peformed in air. Using a Janis ST-400 cryostat with ZnSe windows, infrared spectra could also be acquired at 70° angle of incidence from 100 to 300 K using liquid nitrogen cooling, at a residual pressure of about 10^{-8} Torr. Rough temperature measurements could

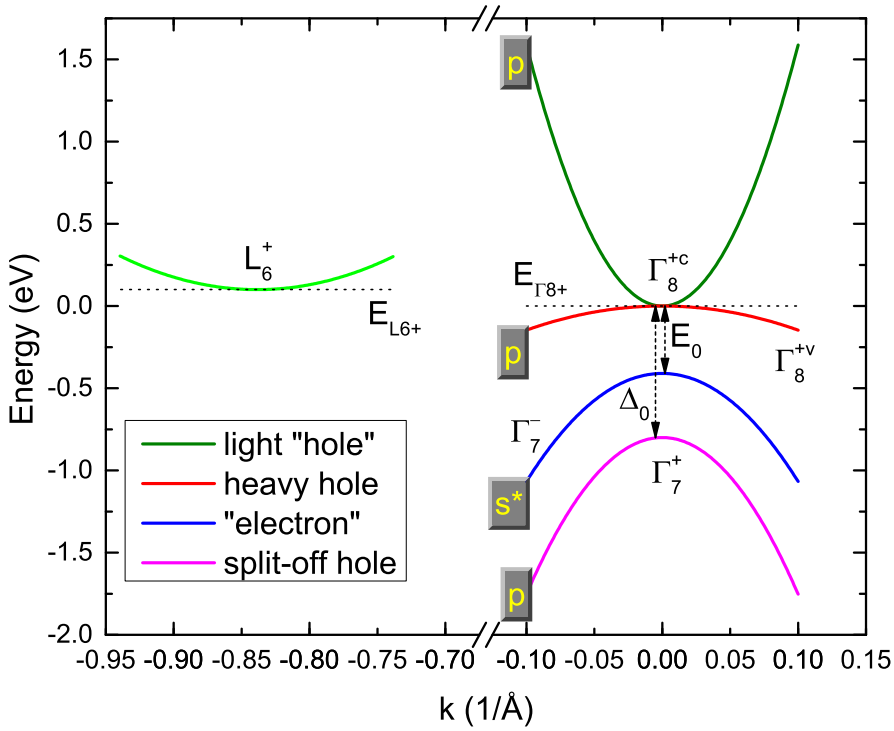

Figure 7.4: Schematic band structure of α-tin adapted from Groves and Paul,[1] drawn to scale using the density-of-states masses given in Table 7.1. Warping, strain, and non-parabolicity are ignored. The Γ_8^+ valence and conduction bands (total angular momentum j=3/2) and the Γ_7^+ valence band (j=1/2) are derived from the Γ'_{25} p-bonding orbitals, split by spin-orbit interactions with spin-orbit splitting Δ_0=0.8 eV. Note the positive curvature of the Γ_8^{+c} conduction band. The Γ_7^-/Γ'_2 valence band is derived from the s-antibonding orbital (s*), which has moved below Γ_8^+ and changed the sign of its curvature compared to other semiconductors like Ge or InSb. The legend shows the names of these bands commonly used in Ge. Quotation marks indicate that the "electron" band of Ge has become a valence band in tin and the light "hole" band a conduction band. If $E_{L_6^+} \geq E_{\Gamma_8^+}$ (as shown in the figure), then α-tin is a zero-gap semiconductor with its Fermi level at $E_{\Gamma_8^+}$. If $E_{L_6^+} < E_{\Gamma_8^+}$ (negative indirect gap), then α-Sn becomes a semimetal with a small overlap of the conduction and valence bands.

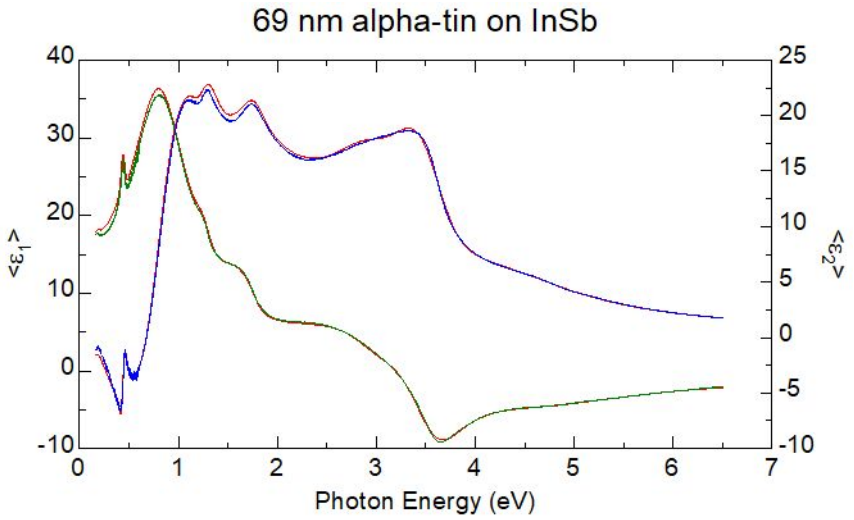

Figure 7.5: As Fig. 7.1, but for 69 nm α-Sn on InSb. The real part of the pseudo-dielectric function is shown in green, the imaginary part in blue, and the fit in red.

be made with a type E thermocouple located near the nitrogen reservoir. The sample was mounted on the Cu sample holder using silver paint. We applied UHV-compatible carbon paint to exposed areas of the sample holder (not covered by the sample) to avoid stray reflections of the infrared light beam. Such reflections from the sample holder can be recognized by depolarization and by differences of measurements taken in air and in the cryostat. The ZnSe cryostat windows affect the polarization state of the incident and reflected light beam. These window effects were calibrated using an SiO_2/Si sample and our data were corrected using a proprietary algorithm included in the data acquisition software.

A polished rear surface on a transparent substrate causes significant systematic errors in ellipsometry measurements (Fujiwara 2007), since the reflections from the front and rear surface are not coherent. This can be recognized by depolarization

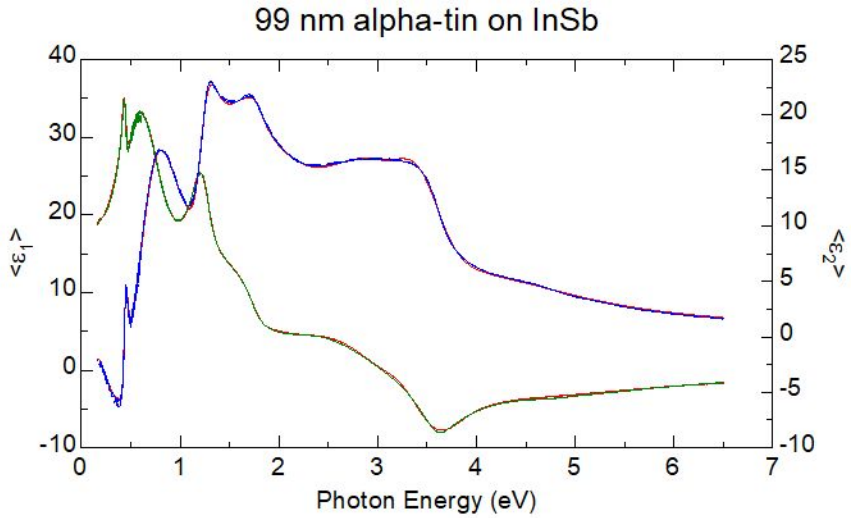

Figure 7.6: As Fig. 7.1, but for 99 nm α-Sn on InSb. The real part of the pseudo-dielectric function is shown in green, the imaginary part in blue, and the fit in red.

Table 7.2: Parameters of the parametric oscillator model used to fit the optical contants of α-Sn on InSb. See US patent 5796983A by Herzinger and Johs for an explanation of the values.

Parameterized Semiconductor Layer

Layer Name: tin_p

Comment: Tin parametric (thin film from AFRL) 01/22/2018

Thickness: 0.00 Å Fit

Optical Constants >> | Ok | Delete Layer | Replace Layer

Opt Const Fit: n, k

Position (eV): Magnitude:

Pole #1: 11 56.837

Pole #2: 0.01 0

Joint DOS Parameters: Change

Sel:	Energy:	Amp:	Connect:	Br:	Discont:	Left of CP: Mid Pos	Left of CP: Mid Amp	Left of CP: 2nd order	Right of CP: Mid Pos	Right of CP: Mid Amp	Right of CP: 2nd order
#0:	0.4317 F	6.7492 F	0 , 1	18.641 F	0.2941 F	0.5000	0.5000	0.0000	0.9030 F	0.1782 F	0.0000
#1:	1.2613 F	13.5381 F	0 , 4	62.704 F	0.2260 F	0.3736 F	0.0010 F	1.0000	0.8000	0.4000	0.0000
#2:	1.8296 F	15.1557 F	0 , 4	81.451 F	-0.1000	0.3000	0.2944 F	0.0000	0.1000	0.0797 F	0.0000
#3:	3.2146 F	31.7910 F	2 , 6	395.430 F	-0.3408 F	0.3462 F	0.0961 F	0.0000	0.7679 F	0.2247 F	0.0000
#4:	3.3998 F	41.7021 F	3 , 5	216.479 F	0.2222 F	0.9508 F	0.0076 F	0.0000	0.4667 F	0.0143 F	0.0000
#5:	4.2166 F	6.5447 F	4 , 6	477.083 F	0.0801 F	0.2947 F	0.5000	0.0000	0.1066 F	0.0010	0.0000
#6:	6.5000	1.5788 F	5 , 7	200.000	0.0000	0.5000	0.5000	0.0000	0.5000	0.5000	0.0000

of the reflected light beam. For α-tin on InSb, this was not a problem, since the InSb substrate is opaque above 0.16 eV, in the area of interest. The band gap of CdTe is much larger, however, and therefore infrared ellipsometry spectra for α-Sn on CdTe are only qualitative at this point. We are unable to convert ellipsometric angles of samples into infrared dielectric functions of α-tin on two-side polished CdTe substrates. We will address this issue in the future with measurements of α-Sn on single-side polished CdTe substrates. We also need to build a database for the optical constants of CdTe as a function of temperature for precise analysis of temperature-dependent infrared ellipsometry spectra of α-Sn on CdTe.

Some pseudo-dielectric function data were also acquired in a cleanroom environment immediately after growth, from 0.6 to 4.7 eV with 0.01 eV steps on a Horiba UVISEL phase-modulation ellipsometer at a 70° angle of incidence. We performed a high-accuracy merge of two data sets taken with different orientations of the modulator (0°/90° and ±45°), with the analyzer kept at ±45°.

7.2.3 Data analysis

We analyze our raw ellipsometry data (which can be expressed as ellipsometric angles or as a pseudo-dielectric function shown in Fig. 7.1) and extract the dielectric function of α-Sn on InSb (shown in Fig. 7.2) as follows: First, we merge all data sets for the three α-Sn layers on InSb with different thicknesses (69, 99, and 127 nm) and fit them with a three layer (oxide, α-Sn, InSb) model. Since

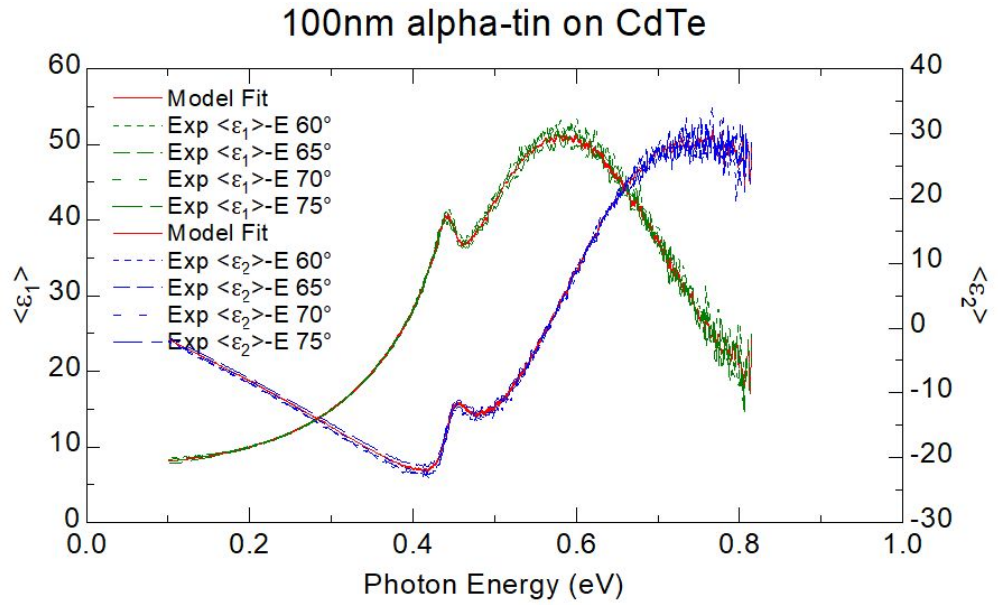

Figure 7.7: As Fig. 7.1, but for 100 nm α-Sn on two-side polished CdTe. The real part of the pseudo-dielectric function is shown in green, the imaginary part in blue, and the fit in red.

the dielectric function for the native oxide on α-Sn is not known we approximate it with that on InSb[132] ($\epsilon \approx 3.8+0.22i$ below 1 eV). The optical constants of α-Sn are described with a Kramers-Kronig-consistent parametric oscillator model, similar to $Ge_{1-y}Sn_y$ or Ge,[14, 108] and a Drude term for free carrier absorption. Since the dielectric function for InSb is not well known, we measured a bare InSb substrate to derive approximate optical constants. The pseudo-dielectric functions for all three samples are fitted simultaneously with the parametric oscillator variables for α-Sn, the epilayer thicknesses (69, 99, and 127 nm), and the native oxide layer thicknesses (2−4 nm) as parameters. The results from this fit are shown by solid lines in Figs. 7.1 and 7.2. The resulting parameters are listed in

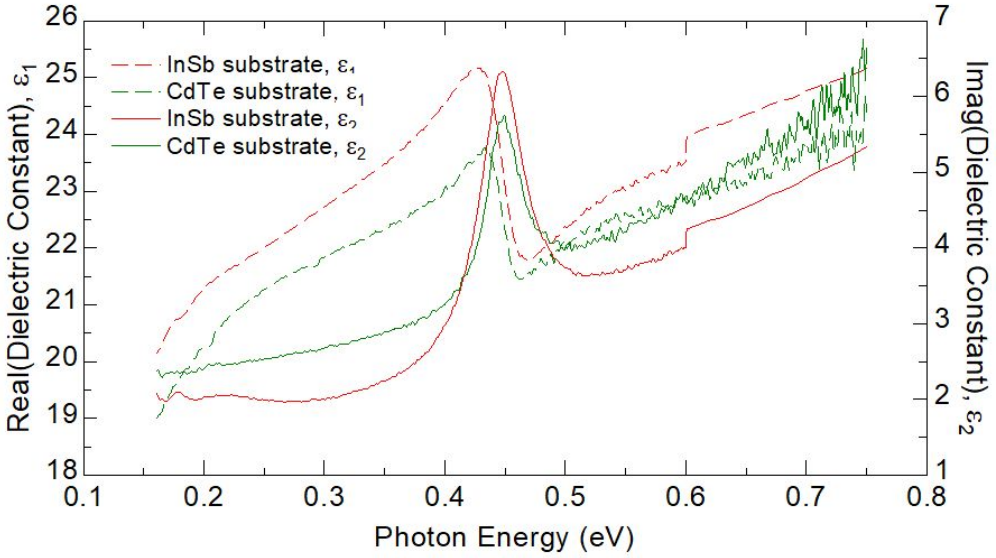

Figure 7.8: Comparison of the real (dashed) and imaginary (solid) parts of the dielectric functions of α-tin on InSb (red) and CdTe (green) substrates (preliminary). The $\bar{E}_0$ peak at 0.41 eV is similar in both epitaxial layers, independent of the substrate. Differences in the non-resonant background are likely due to depolarization from the two-side polished CdTe substrate and uncertainties in the dielectric functions of the substrates. The step at 0.6 eV (on InSb) is due to the slight mismatch of data from two instruments.

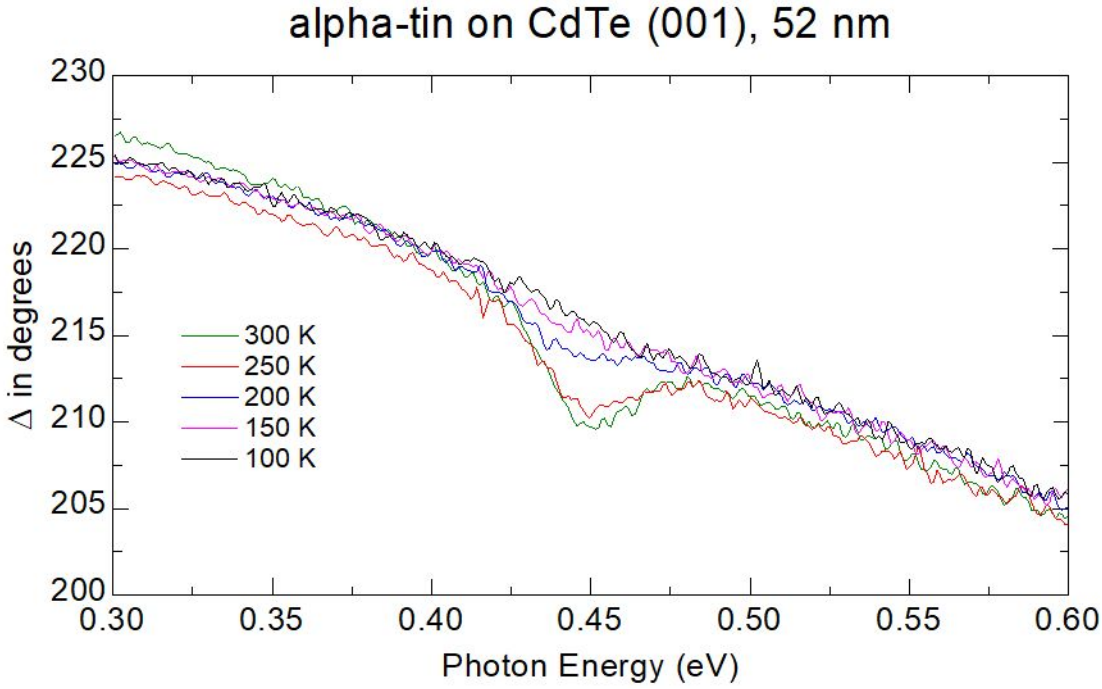

Figure 7.9: Ellipsometric angle Δ versus photon energy for 52 nm α-tin grown on CdTe (001) taken at 70° incidence angle for different temperatures (preliminary results on a two-side polished substrate, with large systematic errors due to a linear background with 20-30% depolarization). The temperature dependence of the amplitude of the $\bar{E}_0$ peak at 0.41 eV is cleary visible.

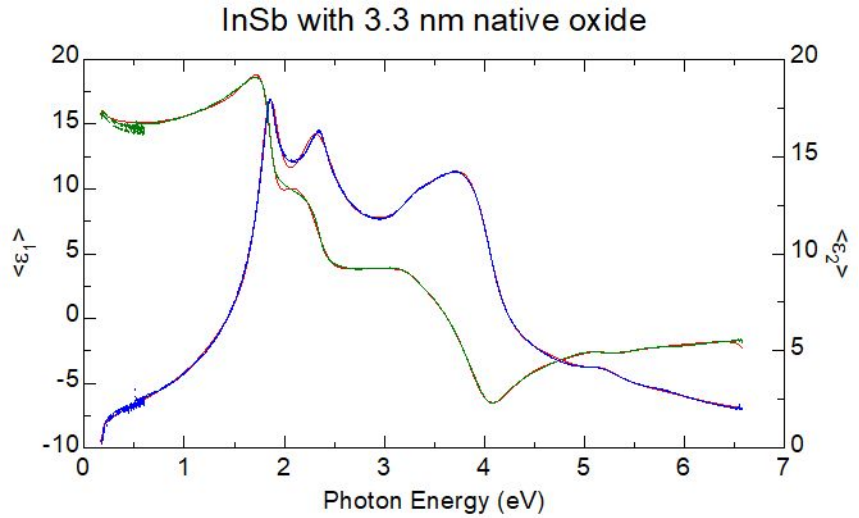

Figure 7.10: Pseudo-dielectric function for a bare InSb substrate. Experimental data for the real (imaginary) parts are shown in green (blue) and the red lines show the best fit using a parametric oscillator model for InSb with 3.3 nm of native oxide.

Table 7.2. In a second step, we fix the thicknesses at the values determined in the first step, discard the parametric oscillator model for α-Sn to remove bias, and instead fit the experimental data for the three samples by using the real and imaginary parts of the dielectric function of α-Sn as adjustable parameters. The fit is carried out in a point-by-point fashion, using the fit values at a given energy as the seed values for the next energy step. Results are given in Fig. 7.2. Our fit successfully removed the interference fringes seen in the pseudo-dielectric functions of the three samples. Both models agree very well with each other, except below 0.4 eV. Since the lineshape of the $\bar{E}_0$ peak is hard to describe within the parametric oscillator model, the point-by-point optical constants are expected to be more accurate than those from the parametric oscillator model at low energies.

7.2.4 Comparison for α-tin on InSb and CdTe

We also acquired infrared ellipsometry data for an α-tin epilayer on a two-side polished CdTe substrate, where the higher band gap of CdTe (1.5 eV) made the data analysis difficult due to depolarization from the smooth back surface of the substrate. Nevertheless, it is clear from the pseudo-dielectric function shown in Fig. 7.7 that the $\bar{E}_0$ peak is also seen for α-tin on CdTe.

Apart from the problems with depolarization mentioned above, a detailed analysis of the pseudo-dielectric function of α-tin on CdTe to extract the optical constants of α-tin is also difficult due to the uncertainty of the mid-infrared optical constants of CdTe. Therefore, we can only present a tentative comparison of the dielectric functions of α-tin on InSb and CdTe, see Fig. 7.8. This comparison shows that the $\bar{E}_0$ peak is present, with similar amplitude, position, and broadening in α-tin layers on both substrates.

Because of depolarization caused by backside reflection (see above), it is even more difficult to quantify the temperature dependence of the $\bar{E}_0$ peak for α-Sn on CdTe. Instead, we show raw uncorrected data for the ellipsometric angle Δ in the region of interest in Fig. 7.9. It is apparent that the $\bar{E}_0$ peak is strong at 300 and 250 K, weak at 200 K, and not visible at lower temperatures. From the optical sum rule in Eq. (38), it should be possible to determine the temperature dependence of the hole density from the data in Fig. 7.9, but that is beyond the

scope of this initial publication on the $\bar{E}_0$ peak.

7.2.5 Sum rule analysis of dielectric function

We checked the validity of the α-Sn optical constants in Fig. 7.2 using the sum rule[21, 134]

$$\int_0^\infty \omega\epsilon_2(\omega)\, d\omega = \frac{\pi}{2}\omega_P^2, \tag{38}$$

where ω_P is the plasma frequency (usually calculated with four electrons per atom). Taking the upper limit of the integral as 6.5 eV, the upper range of our ellipsometer, we obtain an effective plasma frequency of 13.3 eV for Ge, but only 11.4 eV for α-Sn, a reduction by 15%. Since the plasma frequency is proportional to $a_0^{-\frac{3}{2}}$, where a_0 is the lattice constant (see Table 7.4), we expect a reduction by 19%, quite similar to our measurements.

7.2.6 Dispersion of bands

We assume parabolic spherical bands near the Γ-point. The CBs curve upwards, while the VBs curve downward. The effective masses for both CBs and VBs are taken to be positive. We also assume that there is no shear strain and therefore the Γ_8^+ state is doubly degenerate. The VB maximum is at the same energy as the CB minimum, which makes α-tin a zero-gap semiconductor.

The lowest CB is the upper Γ_8^+ band, also called light "hole" (based on the equivalent band in Ge) or Γ_8^{+c}. Its energy as a function of wave vector k is given

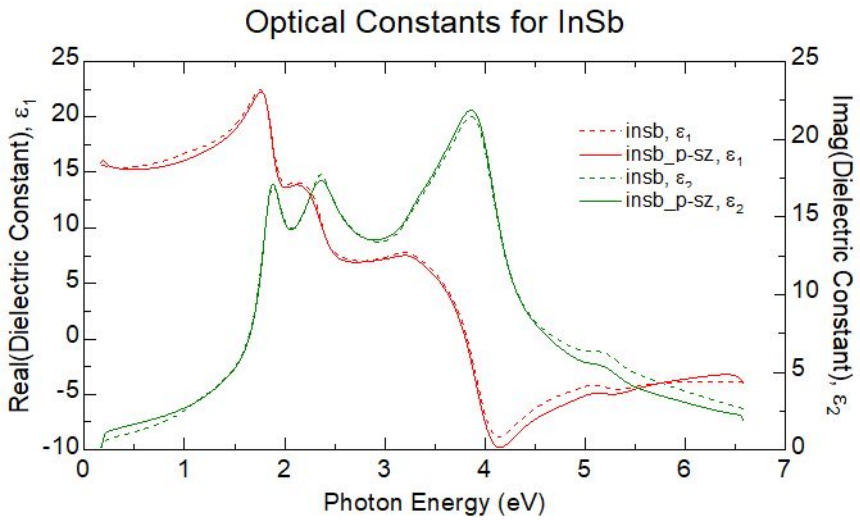

Figure 7.11: Comparison of optical constants for bulk InSb determined from our measurements shown in Fig. 7.10 (solid) and those in the J.A. Woollam database supplied with the ellipsometers (dotted). Some differences can be seen at the highest and lowest energies.

by[110, 21]

$$E_{\Gamma_8^{+c}}(k) = \frac{\hbar^2 k^2}{2m_{\mathrm{CB}}}. \tag{39}$$

The highest VB is the lower Γ_8^+ band, also called heavy hole or Γ_8^{+v}. Its energy is given by

$$E_{\Gamma_8^{+v}}(k) = -\frac{\hbar^2 k^2}{2m_{\mathrm{hh}}}. \tag{40}$$

The second-highest VB is the Γ_7^- band, also called "electron" (based on the equivalent band in Ge). Its energy is given by

$$E_{\Gamma_7^-}(k) = -\bar{E}_0 - \frac{\hbar^2 k^2}{2m_{\mathrm{e}}}. \tag{41}$$

The third-highest valence band is the Γ_7^+ band, also called split-off hole. Its

energy as a function of wave vector k is given by

$$E_{\Gamma_7^+}(k) = -\Delta_0 - \frac{\hbar^2 k^2}{2m_{\rm so}}. \tag{42}$$

The effective masses for all four bands are known, at least approximately, see Table 7.1. In some cases the masses can determined from Hall measurements. In other cases, they were calculated from $\vec{k} \cdot \vec{p}$ band structures, which relate the curvature of the bands to the band separation energies (Lawaetz 1971).

To perform numerical calculations, we write

$$E(k) = \frac{\hbar^2 k^2}{2m^*} = \frac{\hbar^2 k^2}{2m_0 m_{\rm eff}} = \frac{\hbar^2}{2m_0}\frac{k^2}{m_{\rm eff}}, \tag{43}$$

where $\frac{\hbar^2}{2m_0}$=3.812 eVÅ^2. $m_{\rm eff}$ is a dimensionless effective mass and k is specified in units of Å^{-1}.

7.2.7 Dielectric function of optical interband transitions

We are interested in optical transitions from the Γ_7^- VB into the lower and higher Γ_8^+ bands. The momentum matrix element for this transition is known. This matrix element is large and usually assumed to be independent of k. Both transitions have the same matrix element, since they are both related to the doubly degenerate Γ_8^+ state. The transition from Γ_7^- to Γ_8^c is an interband (valence to conduction band) transition. On the other hand, we consider the transition from Γ_7^- to Γ_8^v an intravalence band (IVB) transition with a finite (non-zero) matrix element.

The energy for interband transitions from the Γ_7^- VB into the Γ_8^+ CB is

$$\Delta E_{\text{inter}}(k) = \frac{\hbar^2 k^2}{2m_{\text{CB}}} + \bar{E}_0 + \frac{\hbar^2 k^2}{2m_{\text{e}}} = \bar{E}_0 + \frac{\hbar^2 k^2}{2m_0 \mu_{\text{inter}}}, \tag{44}$$

where the optical mass μ_{inter}=0.017 is defined by

$$\frac{1}{m_0 \mu_{\text{inter}}} = \frac{1}{m_{\text{CB}}} + \frac{1}{m_e}. \tag{45}$$

The energy for intravalence band (IVB) transitions from the Γ_7^- VB into the Γ_8^+ VB is

$$\Delta E_{\text{IVB}}(k) = -\frac{\hbar^2 k^2}{2m_{\text{hh}}} + \bar{E}_0 + \frac{\hbar^2 k^2}{2m_{\text{e}}} = \bar{E}_0 + \frac{\hbar^2 k^2}{2m_0 \mu_{\text{IVB}}}, \tag{46}$$

where the optical mass μ_{IVB}=0.075 is defined by

$$\frac{1}{m_0 \mu_{\text{IVB}}} = \frac{1}{m_e} - \frac{1}{m_{\text{hh}}}. \tag{47}$$

Therefore, the IVB transitions from the Γ_7^- VB into the Γ_8^{+v} heavy hole VB (if it is empty) should be about $(\mu_{\text{IVB}}/\mu_{\text{inter}})^{1.5}$=9 times stronger than into the Γ_8^{+c} CB.

The imaginary part of the dielectric function arising from optical interband transitions at an allowed direct gap $\bar{E}_0$ is given by[21]

$$\epsilon_2(\hbar\omega) = A\frac{\sqrt{x-1}}{x^2} \tag{48}$$

for photon energies $\hbar\omega$ larger than the band gap, where $x = \hbar\omega/\bar{E}_0$ and

$$A = \frac{e^2\sqrt{m_0}}{\sqrt{2}\pi\epsilon_0\hbar}\mu^{\frac{3}{2}}\frac{E_P}{3}\bar{E}_0^{-\frac{3}{2}}. \tag{49}$$

We already defined $E_P = 2P^2/m_0$ and the optical mass μ (which is given in units of the free electron mass m_0). The constants e (electronic charge), $\hbar$ (reduced Planck's constant), and ϵ_0 (permittivity of free space) have their usual meaning. The first fraction in Eq. (49) has the value 14.76 $\sqrt{\text{eV}}$. For α-tin, we use E_P=24 eV (Lawaetz 1971) and $\bar{E}_0$=0.41 eV. The masses are in Table 7.1.

In the notation of Yu and Cardona,[21] the matrix element for allowed direct optical dipole transitions is given by

$$|P_{cv}|^2 = |\langle c\,|\hat{e}\cdot\vec{p}|\,v\rangle|^2\,, \tag{50}$$

where $|c\rangle$ and $|v\rangle$ are the initial and final state wave functions, respectively. $\hat{e}$ is the unit vector along the direction of the vector potential $\vec{A}$, and $\vec{p}$ is the momentum operator. It is tempting to fix the z-axis along the direction of the vector potential and then average over all directions of the initial and final wave functions. (Averaging over an s-state is trivial, since it is spherically symmetric.) It is more convenient, however, to fix the z-axis by the j_z component of the total angular momentum of the wave function and then average over all possible orientations of the vector potential.

This average can be shown to be

$$\begin{aligned} |P_{cv}|^2_{\text{ave}} &= \tfrac{1}{3}\left[|\langle s\,|p_x|\,Z\rangle|^2 + |\langle s\,|p_y|\,Z\rangle|^2 + |\langle s\,|p_z|\,Z\rangle|^2\right] \\ &= \tfrac{1}{3}\,|\langle s\,|p_z|\,Z\rangle|^2 = \tfrac{1}{3}P^2, \end{aligned} \tag{51}$$

where $|s\rangle$ is the wave function for the s-antibonding Γ_7^- state and $|X\rangle$, $|Y\rangle$, and

$|Z\rangle$ are the p-bonding Γ'_{25} wave functions, from which the heavy and light hole states belonging to Γ_8^+ are derived.

The matrix elements are given by $\vec{k}\cdot\vec{p}$ theory as[21]

$$\langle X\,|p_x|\,s\rangle = \langle Y\,|p_y|\,s\rangle = \langle Z\,|p_z|\,s\rangle = iP, \tag{52}$$

$$\langle Z\,|p_x|\,s\rangle = \langle Z\,|p_y|\,s\rangle = 0. \tag{53}$$

This explains the factor $\frac{1}{3}$ in Eq. (49), which connects the matrix element P_{cv} for optical interband transitions with the $\vec{k}\cdot\vec{p}$ momentum matrix element P in the book by Yu and Cardona.[21]

7.2.8 Critical point parameters

The resonant portion of the E_1 and $E_1 + \Delta_1$ critical points[21] can be described with a two-dimensional analytical lineshape[23, 14]

$$\epsilon\left(\hbar\omega\right) = C - A\ln\left(\hbar\omega - E_g - i\Gamma\right)e^{i\phi}, \tag{54}$$

where C is a constant describing the non-resonant background. The amplitude A, band gap E_g, broadening Γ, and phase angle ϕ are the critical-point (CP) parameters. They were obtained by fitting the second derivatives calculated from our data with Eq. (54). (To calculate the second derivatives of our dielectric functions with respect to photon energy, we used the Savitzky-Golay algorithm and fitted third-order polynomials to sets of ten equidistant data points, separated by 10 meV.) Results are listed in Table 7.3 for several α-Sn layers on InSb (001)

with different thicknesses. One epilayer on CdTe (001) was also included. It is customary[23] to require the same value of the phase angle for E_1 and $E_1 + \Delta_1$ (and those results are listed in Table 7.3). If the $E_1 + \Delta_1$ phase angle is treated as an additional free parameter, the $E_1 + \Delta_1$ energies increase by about 5−15 meV, while the other parameters remain the same.

When requiring the same phase angle for E_1 and $E_1 + \Delta_1$, we determined a spin-orbit splitting of Δ_1=0.46 eV, somewhat lower than Viña's value[23] of Δ_1=0.48 eV. When fitting the phase angle of $E_1 + \Delta_1$ separately, the agreement with Ref. 23 becomes slightly better. Viña *et al.*[23] did not tabulate their room temperature critical point energies, but our values are reasonable in comparison with their data listed at 200 K and the linear temperature coefficients. Most importantly, our E_1 broadenings are comparable or better to Ref. 23, indicating that our epilayer quality is excellent. Our phase angle of 73±4° is also in good agreement with Ref. 23. It appears that our E_1 energies (and perhaps also the E_1 amplitudes) are correlated with the α-Sn epilayer thickness. This indicates that we were not entirely successful in removing interference effects with our point-by-point fits. The E_1 and $E_1 + \Delta_1$ CP point energies listed in Table 7.3 are experimental values measured for strained α-tin on InSb (001). The critical point energies for relaxed α-Sn are about 5 meV lower, calculated using the deformation potential formalism described elsewhere.[14]

The absolute values of the E_1 and $E_1 + \Delta_1$ amplitudes for relaxed α-Sn are

Table 7.3: Critical point parameters energy E, broadening Γ, amplitude A, and phase angle ϕ for E_1 and $E_1 + \Delta_1$, obtained from ellipsometry measurements of α-Sn layers on InSb (001) with various thicknesses t. The phase angle was forced to be equal for both CPs. To obtain the $\bar{E}_0$ energy, 30 meV was subtracted from the energy of the ϵ_2 peak. Units in parentheses.

E_1	Γ_{E_1}	A_{E_1}	ϕ	$E_1 + \Delta_1$	$\Gamma_{E_1+\Delta_1}$	$A_{E_1+\Delta_1}$	$\bar{E}_0$	t
(eV)	(meV)	(1)	(°)	(eV)	(meV)	(1)	(eV)	(nm)
1.280[a]	60	5.5	74	1.739	91	3.1	NA	NA
1.276	62	5.8	72	1.736	91	3.1	0.416	127
1.281	58	5.3	73	1.737	91	3.1	0.417	98.8
1.284	61	4.9	78	1.741	91	3.1	0.419	69.0
1.278[b]	59	5.1	68	1.732	91	3.0	0.416	97.9

[a] Simultaneaous fit of several epilayers

[b] Grown on CdTe (001)

given by $\vec{k}\cdot\vec{p}$ theory[23] as (Cardona 1969)

$$A_{E_1} = 44\frac{E_1+\frac{1}{3}\Delta_1}{a_0 E_1^2} = 5.9, \quad (55)$$

$$A_{E_1+\Delta_1} = 44\frac{E_1+\frac{2}{3}\Delta_1}{a_0\left(E_1+\Delta_1\right)^2} = 3.6, \quad (56)$$

where a_0 is the lattice constant of α-Sn in Å and the energies are given in eV. Our measured amplitudes of 5.3±0.3 and 3.1±0.1 for E_1 and $E_1+\Delta_1$ are in excellent agreement with the values calculated from this simple theory. They are also in excellent agreement with the results published previously[23] as 5.6 and 3.4. The agreement with theory suggests that excitonic enhancement of these transitions is less important in α-Sn than in other materials like GaAs, GaSb, or Si (Lautenschlager 1987, Zollner 1991), where the calculated amplitudes are much lower than the measured ones.

According to Yu and Cardona,[21] only interband transitions from the VB to the CB can be considered van Hove singularities and give rise to CPs with n-dimensional line shapes. Since we believe that intravalence band transitions contribute to $\bar{E}_0$, this is not a van Hove singularity and cannot be described like other CPs. Therefore, we are unable to list CP parameters for $\bar{E}_0$.

7.2.9 Strain and compression due to substrate-epilayer lattice mismatch

Following Yu and Cardona,[21] we will discuss in some detail the shifts and splittings of the various bands at Γ and L due to the biaxial stress induced by the lattice mismatch between the α-Sn epilayer and the InSb or CdTe substrate,[114, 115] within continuum elasticity theory.[14]

For pseudomorphic growth of α-Sn on InSb or CdTe (001) with a lattice mismatch, the in-plane lattice constant $a_{\parallel}$ is equal to that of the substrate a_S (pseudomorphic condition), see Table 7.4. This creates a biaxial stress along the surface of the wafer described by a symmetric stress tensor

$$\mathbf{X} = \begin{pmatrix} X & 0 & 0 \\ 0 & X & 0 \\ 0 & 0 & 0 \end{pmatrix}. \tag{57}$$

(There is no stress along the growth direction, defined as the z-axis.) This stress tensor is related to a strain tensor ϵ through the elastic constants C_{ij} or the compliance constants S_{ij} (Cardona & Christensen 1987).

An arbitrary strain tensor can be decomposed into hydrostatic, [001] pure (traceless) shear, and [111] shear corresponding to the Γ_1, Γ_{12}, and Γ'_{25} representations of the diamond point group.[21] The third component is zero for a biaxial stress resulting from pseudomorphic growth of a cubic material on a (001)

substrate. In this case, the strain tensor becomes

$$\begin{pmatrix} \epsilon_{\parallel} & 0 & 0 \\ 0 & \epsilon_{\parallel} & 0 \\ 0 & 0 & \epsilon_{\perp} \end{pmatrix} = \epsilon_H \begin{pmatrix} 1 & 0 & 0 \\ 0 & 1 & 0 \\ 0 & 0 & 1 \end{pmatrix} + \epsilon_S \begin{pmatrix} -1 & 0 & 0 \\ 0 & -1 & 0 \\ 0 & 0 & 2 \end{pmatrix} \tag{58}$$

with perpendicular (out-of-plane) and parallel (in-plane) strain components $\epsilon_{\perp}$ and $\epsilon_{\parallel}$. The biaxial stress causes a non-zero volume change given by $3\epsilon_H$. The hydrostatic and [001] shear strain components are given by[21] (Cardona & Christensen 1987)

$$\epsilon_H = \tfrac{1}{3}\left(\epsilon_{\perp} + 2\epsilon_{\parallel}\right) \quad \text{and} \quad \epsilon_S = \tfrac{1}{3}\left(\epsilon_{\perp} - \epsilon_{\parallel}\right). \tag{59}$$

The in-plane strain is

$$\epsilon_{\parallel} = \frac{\Delta a}{a_{\text{tin}}} = \frac{a_S - a_{\text{tin}}}{a_{\text{tin}}}, \tag{60}$$

where negative strain indicates a reduction of the lattice parameter (compressive strain), while a positive strain indicates an increase of the lattice parameter (tensile strain). Strain is usually a small dimensionless number stated as a percentage. Growth of α-Sn on either InSb or CdTe results in compressive (negative) in-plane strain, which is almost twice as large for growth on InSb compared to CdTe, see Table 7.4.

The cubic (bulk) unit cell deforms tetragonally and the perpendicular (out-of-plane) lattice constant of the α-tin epitaxial layer measured with symmetric (004) high-resolution x-ray diffraction becomes

$$a_{\perp} = (1 + \epsilon_{\perp})\, a_{\text{tin}}, \tag{61}$$

where the out-of-plane strain (Cardona & Christensen 1987)

$$\epsilon_\perp = -2\frac{C_{12}}{C_{11}}\epsilon_\parallel = -\frac{2\nu}{1-\nu}\epsilon_\parallel \tag{62}$$

is calculated using the elastic constants C_{ij} or the Poisson ratio ν=$C_{12}/(C_{11}+C_{12})$=0.30 (calculated from the elastic constants discussed below).

The status of the elastic constants of α-Sn deserves some discussion. For a cubic material, there are three elastic constants C_{11}, C_{12}, and C_{44}, which are usually determined by ultrasound techniques (McSkimin 1953, 1963). Difficulties with preparing and working with single crystals of α-Sn have so far discouraged such measurements.[131] Therefore, Price, Rowe, and Nicklow[131] calculated the elastic constants for α-Sn from the parameters of a shell model fitted to inelastic neutron scattering data of the phonon dispersion. They found C_{11}=69 GPa, C_{12}=29.3 GPa, and the ratio C_{12}/C_{11}=0.43. There are several problems with this model: The 11-parameter space does not have a well defined least-square minimum, there are strong correlations between parameters, and some parameters lead to unphysical results. For example, the high-frequency dielectric constant ϵ_∞ calculated from this model is 12, while the commonly accepted value for ϵ_∞ of α-tin is 24. Also, this shell model[131] is no longer state-of-the-art and has been replaced for group-IV elements by the more commonly accepted bond charge model of Weber (1977), where the 11 parameters from Ref. 131 are replaced by only four. Weber calculates elastic constants C_{11}=79 GPa and C_{12}=35 GPa, which yields

Table 7.4: In-plane ($a_\parallel$) and out-of-plane lattice constant ($a_\perp$) for pseudomorphic α-Sn on InSb (001), on CdTe (001), and for bulk α-tin, calculated from the elastic constants using Eq. (61). In-plane, out-of-plane, hydrostratic, and shear strain. Hydrostatic shifts of $\bar{E}_0$ and $E_{L_6^+}$; shear splittings of the $E_{\Gamma_8^+}$ VB (in meV).

	on InSb	on CdTe	bulk α-Sn
$a_\parallel$ (Å)	6.479	6.483	6.489
$a_\perp$ (Å)	6.497	6.494	6.489
$\epsilon_\parallel$	−0.15%	−0.09%	0
$\epsilon_\perp$	0.13%	0.08%	0
ϵ_H	−0.06%	−0.04%	0
ϵ_S	0.10%	0.06%	0
$\Delta\bar{E}_0 = -3a\epsilon_H$	−12	−7	0
$\Delta E_{L_6^+}$	4	2	0
$\Delta E_{\Gamma_8^+} = 6\,\lvert b\epsilon_S\rvert = 2\,\lvert\delta_0\rvert$	13	8	0

the ratio C_{12}/C_{11}=0.44. Only the ratio of the elastic constants is required for the calculation of the tetragonal unit cell distortion and the out-of-plane strain, therefore the choice of which set of elastic constants to use does not matter.

Using these elastic constants, we calculate $a_\perp$=6.497 Å for α-Sn on InSb from Eq. (61), see Table 7.4, which agrees very well with our x-ray diffraction results (6.498 Å). We emphasize that the out-of-plane strain for pseudomorphic growth of α-tin on InSb or CdTe is tensile, resulting in an increased out-of-plane lattice constant of α-tin relative to the bulk.

In summary, pseudomorphic α-tin layers on (001) InSb or CdTe substrates experience a small biaxial compressive in-plane stress, which causes a hydrostatic compression and a tensile [001] pure shear strain, which leads to shifts and splittings of electronic band energies.

7.2.10 Shifts and splittings of bands due to substrate-epilayer lattice mismatch

The shifts and splittings of the various bands at Γ and L due to the strain components in Table 7.4 can be calculated using deformation potentials.[21]

A compressive hydrostatic strain in Ge or GaAs causes an increase of the direct gap E_0 given by

$$\Delta E_0 = 3a\epsilon_H, \tag{63}$$

where a is the hydrostatic deformation potential for the E_0 gap. In other words, the Γ_7^- CB in Ge moves up under hydrostatic compression relative to the VB maximum, because both a and ϵ_H are negative. If we assume that the same statement holds true for α-tin, then its Γ_7^- VB will move up also (closer to Γ_8^+), causing a *decrease* of $\bar{E}_0$ by $3a\epsilon_H$.

The hydrostatic deformation potential for the Γ_7^- band (or Γ_2' in single-group notation) relative to the VB maximum equals -8.6 eV for Ge and is similar for the same gap in all diamond or zincblende semiconductors (Paul's rule, 1961, 1998). Brudevoll *et al.*[121] calculated a=-7 eV for α-tin, indeed quite similar to Ge.

The $\bar{E}_0$ gap will therefore shrink by $\Delta\bar{E}_0$=$-3a\epsilon_H$=-12 meV (or -7 meV) in pseudomorphic α-tin grown on InSb (or CdTe). This shift is within the experimental error of our ellipsometry measurements (about 0.01 eV).

The hydrostatic compression will also move up the L_6^+ CB relative to the Γ_8^+ VB maximum (but at a slower rate than the Γ_7^- VB). This L_6^+ shift is given by a deformation potential of -2 eV, also calculated in Ref. 121. This results in an *increase* of the indirect gap between Γ_8^+ and L_6^+ of 4 meV (or 2 meV) in epitaxial α-Sn on InSb (or CdTe) relative to the same indirect gap in bulk α-Sn.

Within the Pikus-Bir (1959) notation[21] the splitting of the Γ_8^+ bands is given by the b and d deformation potentials. Only the former is related to a (001) biaxial stress. The Γ_8^+ splitting under (001) biaxial stress is (Van de Walle 1989)

$$\Delta E_{\Gamma_8^+} = 6b\epsilon_S = 2\delta_0. \tag{64}$$

The value of b=-2.3 eV (very similar to Ge) was measured using conductivity and low-field Hall measurements under uniaxial compression.[2] This results in a magnitude of the Γ_8^+ splitting of 13 meV (or 8 meV) for pseudomorphic α-Sn grown on InSb (or CdTe). The splitting of 13 meV for α-Sn on InSb is much smaller than the result of 30 meV calculated using a GW quasiparticle calculation[118] (Zhang 2018), but consistent with the estimate $\pm$5 meV (for α-tin on CdTe) given in Ref. 115. The parameter $\delta_0 = 3b\epsilon_S$ describes one half of the splitting of the Γ_8^+ band. Note that δ_0 changes sign depending on the sign of ϵ_S. Since b is negative, a tensile

[001] pure shear strain with positive ϵ_S (such as for α-tin on InSb) will lead to a negative δ_0 following our convention (adopted from Cardona 1967). Some papers (especially by Liu) take δ_0 as a positive value for tensile shear strain, which leads to a sign change in many equations.

To first order in spin-orbit splitting Δ_0, the positions of the three valence bands $v1$ ($\left|\frac{3}{2},\pm\frac{1}{2}\right\rangle$), $v2$ ($\left|\frac{3}{2},\pm\frac{3}{2}\right\rangle$), and $v3$ ($\left|\frac{1}{2},\pm\frac{1}{2}\right\rangle$) change by (Chandrasekhar & Pollak 1977, Van de Walle 1989, Schmid 1990)

$$\Gamma_6^+(\text{hh}) \quad \Delta E_{v2} = \quad -3b\epsilon_S \quad = +6 \text{ meV}, \tag{65}$$

$$\Gamma_7^+(\text{lh}) \quad \Delta E_{v1} = \quad 3b\epsilon_S + 18b^2\epsilon_S^2/\Delta_0 \quad = -6 \text{ meV}, \tag{66}$$

$$\Gamma_7^+(\text{so}) \quad \Delta E_{v3} = \quad -18b^2\epsilon_S^2/\Delta_0 \quad \approx 0. \tag{67}$$

Numerical values for the splittings given in Eqs. (65-66) are for α-tin on InSb. More precise equations are given by Van de Walle (1989). While the heavy hole $j_z = \pm\frac{3}{2}$ band moves linearly with strain, the $j_z = \pm\frac{1}{2}$ light "hole" band has the same symmetry (same total angular momentum j_z along the z-axis) as the split-off band and the resulting coupling leads to a parabolic shift of the light "hole" band with strain, see Fig. 7.12. Under a compressive in-plane (tensile out-of-plane) strain, shown on the right hand side of Fig. 7.12, the heavy hole VB moves towards higher energies, while the light "hole" CB moves down, which leads to a Dirac crossing[111] of the Γ_8^+ bands described below. Under a tensile in-plane strain (left half of Fig. 7.12), the heavy hole VB moves down and the light "hole"

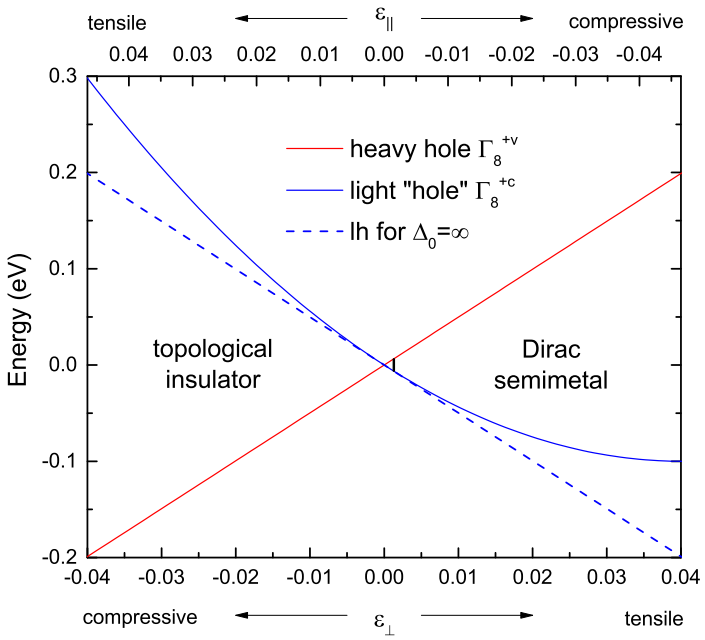

Figure 7.12: Strained heavy and light "hole" energies (solid) as a function of out-of-plane (bottom axis) and in-plane strain (top axis), calculated from Eqs. (65-66). The dashed line shows the light "hole" energy in the linear approximation, i.e., ignoring the mixing of the light and split-off bands, which gives rise to a quadratic correction. The vertical line at $\epsilon_\perp$=0.13% indicates the magnitude of the splitting for α-tin on InSb.

CB moves up, thus opening a gap of $2|\delta_0|$ (for large Δ_0). (Ref. 114; Cardona 1967; Liu 1973; Leung & Liu 1975; Averous 1979.)

Equations (65-66) predict that the magnitude of the splitting reaches a maximum of 0.40 eV for a tensile out-of-plane strain of $\epsilon_\perp$=8.0% and then decreases for even higher strain, because the quadratic term in Eq. (66) gets larger than the linear term. (Such high strains can only be achieved in very thin α-tin layers, see Wegscheider 1990.) The linear approximation can be used for small strains up to about 1%. Figure 7.13 shows the splitting of the Γ_8^+ bands as a function

of out-of-plane and in-plane strain, calculated from Eqs. (65-66) with a deformation potential b=−2.3 eV and a spin-orbit splitting Δ_0=0.8 eV. Our splitting as a function of strain is off by a factor of about three from Fig. 1 in the supplementary materials of Ref. 111 (the sign is convention). Figure 2c in Zhang (2018) is also different, because it is the result of a density functional theory (DFT) calculation with an HSE functional, not based on experimental deformation potentials. The quadratic shear strain term for α-Sn on InSb or CdTe is less than 0.1 meV and can be neglected.

Figure 7.14 shows the Γ_8^+ and Γ_7^- bands in the vicinity of Γ for strained α-tin on InSb, calculated using the non-spherical Pikus-Bir Hamiltonian[2] as described below, along directions of high symmetry. We conclude that the strain splittings and shifts are less than half of k_BT at room temperature and therefore strain in pseudomorphic α-Sn on InSb or CdTe is not a significant factor in the discussion of the room-temperature dielectric function presented in the main text.

The [001] pure shear strain does not split the degeneracy of the eight L_6^+ states, because $\hat{k}\cdot\epsilon\cdot\hat{k}$=0 for all eight L-points, where $\hat{k}$ is the unit vector along one of the eight [111] directions and ϵ is the strain tensor for pseudomorphic growth on a (001) surface.[21]

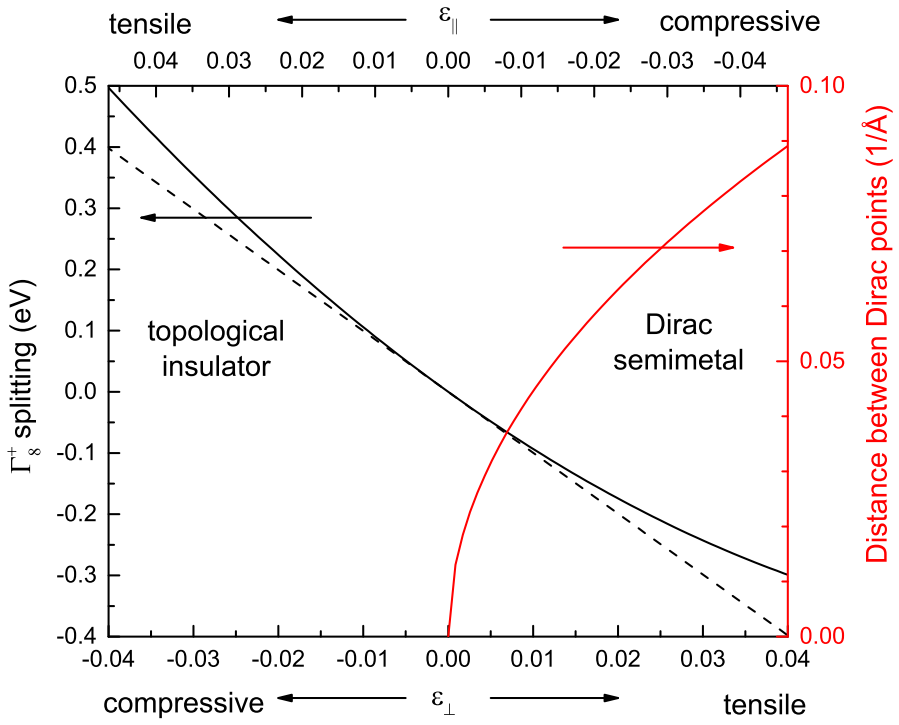

Figure 7.13: Splitting of the Γ_8^+ bands in α-tin grown pseudomorphically on a (001) substrate (black), calculated from Eqs. (65-66), as a function of out-of-plane (bottom axis) and in-plane strain (top axis). The dashed line ignores the quadratic correction for the light "hole" band due to its interaction with the split-off band. The sign of this splitting follows convention (Cardona 1967). The red line shows the distance between the two Dirac points from Eq. (88). Compare Fig. S1 of Ref. 111 and Fig. 2(c) of Zhang (2018).

7.2.11 Symmetry of diamond structure under [001] strain

Under a [001] unaxial shear strain, the O_h point group symmetry of the diamond crystal structure[21] (space group 227, also known as O_h^7 or $Fd\bar{3}m$, see Bilbao) is reduced to D_{4h}, which contains the symmetry elements E, $2C_4^z$, C_2^z, $2C_2'$, $2C_2''$, I, $2S_4$, σ_h, $2\sigma_v$, and $2\sigma_d$, where the prime denotes the horizontal [100] and [010] axes in the cubic coordinate system, while the double-prime denotes the diagonal

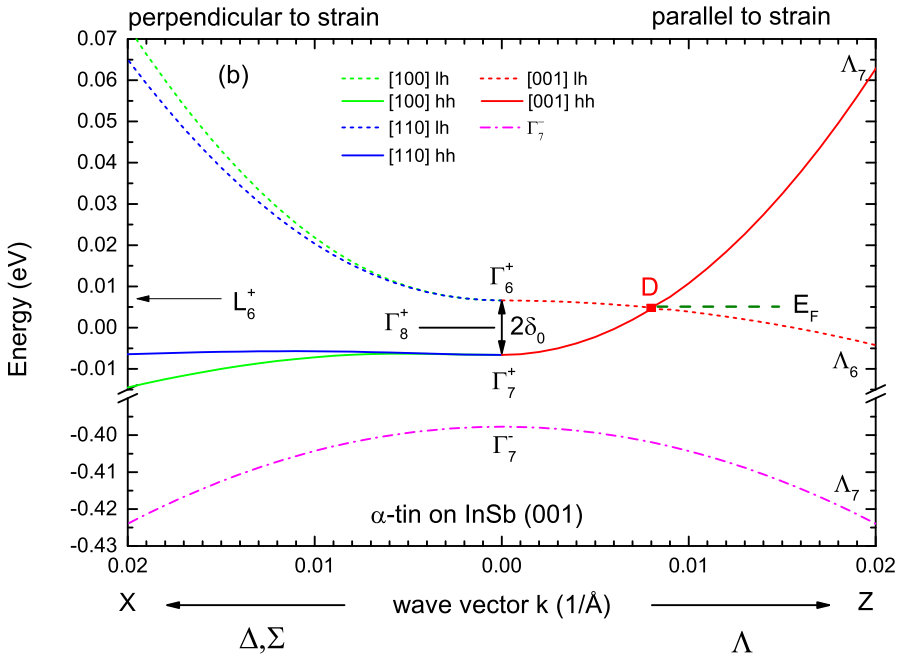

Figure 7.14: Electronic bands near Γ for strained α-tin grown pseudomorphically on InSb (001), calculated using a Pikus-Bir Hamiltonian.[2] Γ_7^- VB (dash-dotted). Bands derived from the Γ_7^+ light "hole" CB (Γ_6^+ heavy hole VB) are shown by dashed (solid) lines. Energies for wave vectors parallel (perpendicular) to the [001] strain are shown in red (blue, green). Since this Hamiltonian ignores the Γ_7^--Γ_7^+ interaction, the Γ_7^- band is parabolic in this approximation. The Dirac point (D) and the Fermi level E_F are indicated. Miller indices in fcc notation.

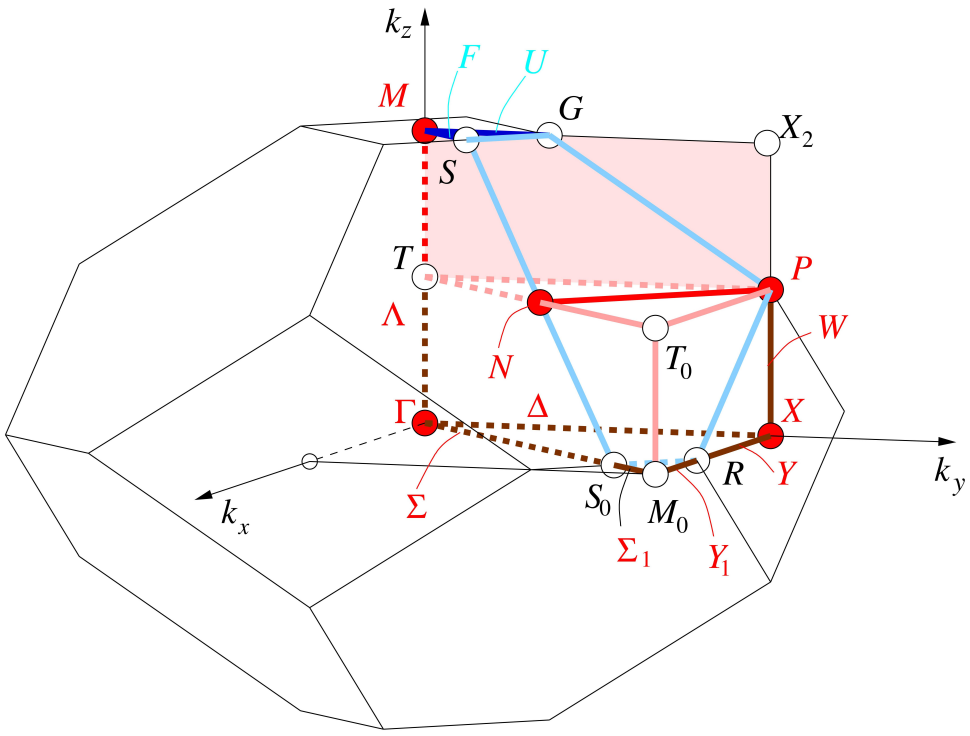

Figure 7.15: The Brillouin zone for space group 141 (D_{4h}^{19} or $I4_1/amd$) of the body-centered tetragonal structure (strained diamond structure) for c>a. High-symmetry points and lines are indicated. Source: Bilbao crystallographic server. Note that the M-point is called Z in Setyawan 2010.

[1±10] axes (Snoke 2008, Karlowatz 2009). The $\Gamma_7^{\pm}$ representations remain irreducible, but the $\Gamma_8^{\pm}$ representations split into $\Gamma_6^{\pm} \oplus \Gamma_7^{\pm}$ (Snoke 2008) in the reduced symmetry.

The corresponding space group of the diamond structure under [001] strain is D_{4h}^{19} (SG number 141 or $I4_1/amd$), compare Zhang (2018). The strained diamond fcc lattice is commonly described with a body-centered tetragonal (bct) Bravais lattice. (A face-centered tetragonal lattice is not one of the standard 14 Bravais lattices, but equivalent to a bct lattice.) This requires a rotation of the fcc cube by 45° about the cubic z-axis. The half-diagonals in the bottom face of the cube become the new bct $\vec{a}$ and $\vec{b}$ lattice vectors of the tetragonal lattice. See Fig. 1 in Ref. 111. The lattice parameters of the bct lattice in terms of the (unstrained) cubic lattice constant a_0 are $c = a_0\,(1 + \epsilon_\perp)$ and $a = b = a_0/\sqrt{2}$. For small strains, $c > a$, which is variation 2 of the bct lattice (Setyawan 2010). The conventional bct unit cell has an approximate volume of $a_0^3/2$ and contains four tin atoms. The primitive unit cell for the bct lattice is defined by (Setyawan 2010)

$$\vec{a}_1' = (-0.5a, 0.5a, 0.5c)\,, \tag{68}$$

$$\vec{a}_2' = (0.5a, -0.5a, 0.5c)\,, \tag{69}$$

$$\vec{a}_3' = (0.5a, 0.5a, -0.5c)\,. \tag{70}$$

The primes indicate that we operate in the rotated coordinate system. The primitive bct unit cell has a volume of $a^2c/2 \approx a_0^3/4$ and contains two atoms, just like

the primitive cell for the unstrained diamond structure.

The Brillouin zone (BZ) for the bct lattice is shown by Setyawan (2010, Fig. 6) and in Fig. 7.15. Note that Ref. 111 shows the BZ for the simple tetragonal lattice, which is not relevant here. The basis vectors for the reciprocal space lattice (in the rotated coordinate system, calculated from the primitive unit cell lattice vectors) are

$$\vec{b}'_1 = (0, 2\pi/a, 2\pi/c)\,, \tag{71}$$

$$\vec{b}'_2 = (2\pi/a, 0, 2\pi/c)\,, \tag{72}$$

$$\vec{b}'_3 = (2\pi/a, 2\pi/a, 0)\,. \tag{73}$$

In Table 7.5, we list the high-symmetry points and lines of the BZ of the unstrained diamond structure, both in units of the primitive reciprocal lattice vectors $\vec{b}_1$, $\vec{b}_2$, $\vec{b}_3$ and in the usual Cartesian coordinates with unit vectors $\hat{i}$, $\hat{j}$, $\hat{k}$. Similarly, Table 7.6 lists the high-symmetry points and lines in units of the bct primitive reciprocal lattice vectors $\vec{b}'_1$, $\vec{b}'_2$, $\vec{b}'_3$, in the rotated Cartesian coordinate system (primed, where $\hat{i}'$, $\hat{j}'$, and $\hat{k}'$ are aligned with the tetragonal axes), and finally in the original Cartesian coordinates of the unstrained cubic system.

By comparing the last three columns of these tables, we recognize that the points X and Z in the bct BZ are equivalent to the X-point in the diamond BZ. The $\vec{k}$-vector Z in the bct BZ is along the [001] strain axis, while X is perpendicular to the strain axis and either parallel to the original cubic axis or

Table 7.5: High-symmetry points and lines in the Brillouin zone for the face-centered cubic (diamond) structure, given in terms of the primitive reciprocal lattice vectors $\vec{b}_1$, $\vec{b}_2$, $\vec{b}_3$; and also in terms of the conventional reciprocal space lattice vectors $2\pi\hat{i}/a_0$, $2\pi\hat{j}/a_0$, $2\pi\hat{k}/a_0$. Compare Setyawan 2010 or Bilbao. u is an internal coordinate.

	$\times\vec{b}_1$	$\times\vec{b}_2$	$\times\vec{b}_3$	$\times 2\pi\hat{i}/a_0$	$\times 2\pi\hat{j}/a_0$	$\times 2\pi\hat{k}/a_0$
Γ	0	0	0	0	0	0
X	0	0.5	0.5	1	0	0
L	0.5	0.5	0.5	0.5	0.5	0.5
K	3/8	3/8	3/4	0.75	0.75	0
W	0.5	0.25	0.75	0.5	1	0
U	5/8	1/4	5/8	0.25	1	0.25
M^a	0.5	0.5	1	1	1	0
Δ	0	u	u	$2u$	0	0
Λ	u	u	u	u	u	u
Σ	u	u	$2u$	$2u$	$2u$	0

[a]This point is outside of the first Brillouin zone.

Table 7.6: High-symmetry points and lines in the BZ for the body-centered tetragonal structure, given in terms of the primitive reciprocal lattice vectors $\vec{b}'_1$, $\vec{b}'_2$, $\vec{b}'_3$; and also in terms of unit vectors in the rotated (tetragonal) and the original (cubic) coordinate system. Compare Setyawan 2010 or Bilbao. u and ξ are internal coordinates.

	$\times\vec{b}'_1$	$\times\vec{b}'_2$	$\times\vec{b}'_3$	$\times\hat{i}'$	$\times\hat{j}'$	$\times\hat{k}'$	$\times\hat{i}$	$\times\hat{j}$	$\times\hat{k}$
Γ	0	0	0	0	0	0	0	0	0
X	0	0	0.5	π/a	π/a	0	$2\pi/a_0$	0	0
Z=M	0.5	0.5	-0.5	0	0	$2\pi/c$	0	0	$2\pi/c$
N	0	0.5	0	π/a	0	π/c	π/a_0	π/a_0	π/c
P	0.25	0.25	0.25	π/a	π/a	π/c	$2\pi/a_0$	0	π/c
S_0	$-3/8$	$3/8$	$3/8$	$3\pi/2a$	0	0	$3\pi/2a_0$	$3\pi/2a_0$	0
Δ	0	0	u	u	u	0	ξ	0	0
Λ	u	u	$-u$	0	0	$2u$	0	0	$2u$
Σ	$-u$	u	u	$2u$	0	0	ξ	ξ	0

along the diagonal of the bottom plate of the tetragon. (We prefer Setyawan's label Z over the label M used by Bilbao.) The N (S_0) point in the bct BZ is equivalent to the L (K) point of the diamond BZ. The N and S_0 points have no special symmetry in the bct space group. Table 7.7 compares points and lines of high symmetry in both structures, showing conventions listed by Setyawan (2010) and by the Bilbao crystallographic server.

The bct directions perpendicular to the strain along the cubic [100] and [110]

Table 7.7: Equivalency of high-symmetry points and lines in the diamond and body-centered tetragonal (bct) Brillouin zones (adapted from Bilbao and Setyawan 2010).

diamond	Γ	X	L	K	W	U	M
bct	Γ	$X/Z = M$	N	S_0	$G = Y_1/P/R = Y$	S	M_0
diamond	Δ	Λ	Σ				
bct	Δ/Λ	gen	Σ				

directions are known as $\Delta = \Gamma X$ and $\Sigma = \Gamma S_0$, respectively, while the [001] direction parallel to the strain is called $\Lambda = \Gamma Z$. In the (unstrained) diamond structure, the group of the wave vector Δ contains the symmetry elements E, C_2^z, $2C_4^z$, $2\sigma_h$, and $2\sigma_d$.[21] If we now apply a uniaxial [001] strain, then the group of Λ (along the strain) still contains the same elements (because the strain reduces the symmetry in the same way as moving away from k=0, conserving j_z) and the representations of electronic states in the double-group notation are therefore Λ_6 and Λ_7, just like Δ_6 and Δ_7 in the unstrained diamond structure. The compatibilities for the Γ and Δ bands in the unstrained diamond structure are (Elliot 1954) $\Gamma_8^+ \rightarrow \Delta_6 \oplus \Delta_7$ and $\Gamma_7^\pm \rightarrow \Delta_7$. In the bct structure, we write the same compatibility as $\Gamma_8^+ \rightarrow \Gamma_6^+ \oplus \Gamma_7^+ \rightarrow \Lambda_6 \oplus \Lambda_7$ and $\Gamma_7^\pm \rightarrow \Lambda_7$.

If the wave vector is along Δ, i.e., perpendicular to the [001] strain, then we lose the four-fold rotations about the z-axis ($2C_4^z$) and the diagonal mirror planes, leaving only the identity E, the rotation C_2^x, and the mirror reflections σ_x and σ_z,

forming the symmetry group C_{2v}, which has only one (trivial) extra representation (Elliot 1954).

7.2.12 Anisotropy of strained Γ_8^+ bands

Pikus-Bir Formalism

Following Pikus & Bir (1960), the energies of the $\Gamma_8^+ = \Gamma_6^+ \oplus \Gamma_7^+$ bands for a small [001] shear strain are given by[2]

$$\begin{aligned} E_{\pm} \quad & = 3a_V\epsilon_H + Ak^2 \pm \\ \pm \quad & \left\{B^2k^4 + C^2\left(k_x^2k_y^2 + k_x^2k_z^2 + k_y^2k_z^2\right) + \right. \\ +\tfrac{1}{2}b^2 \quad & \left[(\epsilon_{xx} - \epsilon_{yy})^2 + (\epsilon_{yy} - \epsilon_{zz})^2 + (\epsilon_{xx} - \epsilon_{zz})^2\right] \\ +3Bb \quad & \left.\left(k_x^2\epsilon_{xx} + k_y^2\epsilon_{yy} + k_z^2\epsilon_{zz} - k^2\epsilon_H\right)\right\}^{\frac{1}{2}} \end{aligned} \tag{74}$$

where $\vec{k}$ is the wave vector and ϵ the 3×3 strain tensor. Terms belonging to a [111] shear strain have been set to zero. The deformation potential a_V is the absolute deformation potential for the Γ_8^+ VB. Its value is not known precisely, but probably close to zero (Cardona & Christensen 1987, Van de Walle 1989, Li 2006) and therefore the term $3a_V\epsilon_H$ will be neglected. This term is not important anyway, because it only affects the absolute shift of the average VB relative to the vacuum level (not the change of a band gap), which is difficult to measure optically. For this work, we treat the average of $v1$ and $v2$ as our energy reference level. The [001] shear deformation potential b=−2.3 eV has been mentioned previously.[2]

A=19.2, B=26.3, and C^2=−1100 are the inverse effective mass parameters,[21] in units of $\frac{\hbar^2}{2m_0}$=3.812 Å^{2}eV or $\left(\frac{\hbar^2}{2m_0}\right)^2$, respectively, determined from Shubnikov-de Haas measurements (Booth & Ewald 1968). The negative sign of C^2 is related to the negative $\bar{E}_0$ band gap of α-tin. Also, A and B are negative for Ge and other diamond and zincblende semiconductors,[21] but positive for α-Sn, because the heavy and light "hole" bands have opposite curvature. For α-Sn, the positive sign before the square root in expression (74) applies to the "light hole" CB, while the negative sign applies to the heavy hole VB.[2] (These signs are reversed in Ge, because it does not have an inverted band structure.) We will use this sign to label curves in our figures to be shown below. Note that other values of the inverse effective mass parameters have also been calculated by Cardona (1967), Lawaetz (1971), and Liu & Leung (1974). Also note the misprints in Eq. (27) of Averous 1979.

In the case of pseudomorphic growth on a (001) surface, where the z-axis denotes the growth direction, $\epsilon_{xx} = \epsilon_{yy} = \epsilon_{\|}$ and $\epsilon_{zz} = \epsilon_{\perp}$. We introduced $\delta_0 = 3b\epsilon_S$ earlier. The band energies therefore become[2]

$$\begin{aligned} E_{\pm} &= Ak^2 \pm \left[B^2k^4 + C^2\left(k_x^2k_y^2 + k_x^2k_z^2 + k_y^2k_z^2\right) + \right. \\ &+ \left. B\delta_0\left(2k_z^2 - k_x^2 - k_y^2\right) + \delta_0^2\right]^{\frac{1}{2}}. \end{aligned} \tag{75}$$

(When comparing with Liu 1973, note that Liu ignores the warping of the Γ_8^+ bands (C=0) and uses the magnitude of δ_0 to describe the strain splitting, thus

causing a sign change compared to the equation above.) The inverse effective mass parameters (expressed in units of $\hbar^2/2m_0$) are related to the dimensionless Luttinger parameters γ_i (Luttinger 1956) by[21, 111]

$$\gamma_1 = -A = -19.2, \tag{76}$$

$$\gamma_2 = -B/2 = -13.2, \tag{77}$$

$$\gamma_3 = \sqrt{(B^2/4) + (C^2/12)} = 9.01. \tag{78}$$

This convention works to compare both sets of parameters in Yu and Cardona,[21] see Tables 2.24 and 4.3, but Leung and Liu 1973 and 1975 seem to apply a different unit convention. Just like for C^2, different sign conventions exist for γ_3, see Ref. 111. A slightly different set of parameters was calculated by Lawaetz (1971). Cardona (1967) uses a positive inverse effective mass parameter C^2 and Lawaetz (1971) and Brudevoll *et al.*[121] a negative Luttinger parameter γ_3 compared to Roman & Ewald.[2] This changes the sign of the warping and therefore the ordering of the bands in the [100] and [110] directions.

Roman & Ewald[2] as well as Leung & Liu (1975) separate the wave vector into components parallel and perpendicular to the (001) shear stress, by defining $k_\parallel = k_z$, $k_\perp = \sqrt{k_x^2 + k_y^2}$ and $k_x = k_\perp \cos\alpha$, $k_y = k_\perp \sin\alpha$, where the azimuth α is the angle between the in-plane component of the wave vector and the x-axis. Note that the parallel direction of the wave vector in this convention is the [001] pure shear strain axis (z-axis), not the plane of the substrate. That is different

from our choice of subscripts for the strain tensor, see Eq. (58). This allows us to rewrite Eq. (75) as

$$\begin{aligned} E_{\pm} &= Ak^2 \pm \left[B^2k^4 + C^2\left(\tfrac{1}{4}k_{\perp}^4 \sin^2 2\alpha + k_{\perp}^2 k_{\parallel}^2\right) + \right. \\ &+ \left. B\delta_0\left(2k_{\parallel}^2 - k_{\perp}^2\right) + \delta_0^2\right]^{\frac{1}{2}}. \end{aligned} \tag{79}$$

This expression was given by Leung & Liu (1975), considering the trigonometric identity $2\sin^2 2\alpha = 1 - \cos 4\alpha$, which shows the explicit four-fold symmetry for the wavevector perpendicular to the [001] shear direction. It is also possible to rewrite Eq. (79) by expressing k in spherical coordinates (Rodríguez-Bolívar 2005).

For a wave vector perpendicular to the [001] shear strain, $k_{\parallel}$=0 and $k_{\perp} = k$. The energies of the Γ_8^+ bands in the xy-plane become (Cardona 1967)

$$E_{\pm} = Ak^2 \pm \sqrt{\delta_0^2 - B\delta_0 k^2 + \left(B^2 + \tfrac{1}{4}C^2 \sin^2 2\alpha\right)k^4}. \tag{80}$$

Cardona (1967) expands the square root to second order in k^2/δ_0, but we can't quite find the same result along [100]. Cardona's equation along [100] clearly contains a misprint, since the energy is proportional to Bk^2 (not B^2k^2). We also find a different prefactor for the B^2k^4 term. For a given α, Cardona (1967) plots the value of k, where E_- has a maximum under compressive [001] shear strain. The location of this maximum in k-space can be obtained by setting the derivative of E_- in Eq. (80) with respect to wave vector to zero (for a given α). This leads to an biquadratic equation in k, which can be solved analytically (see below).

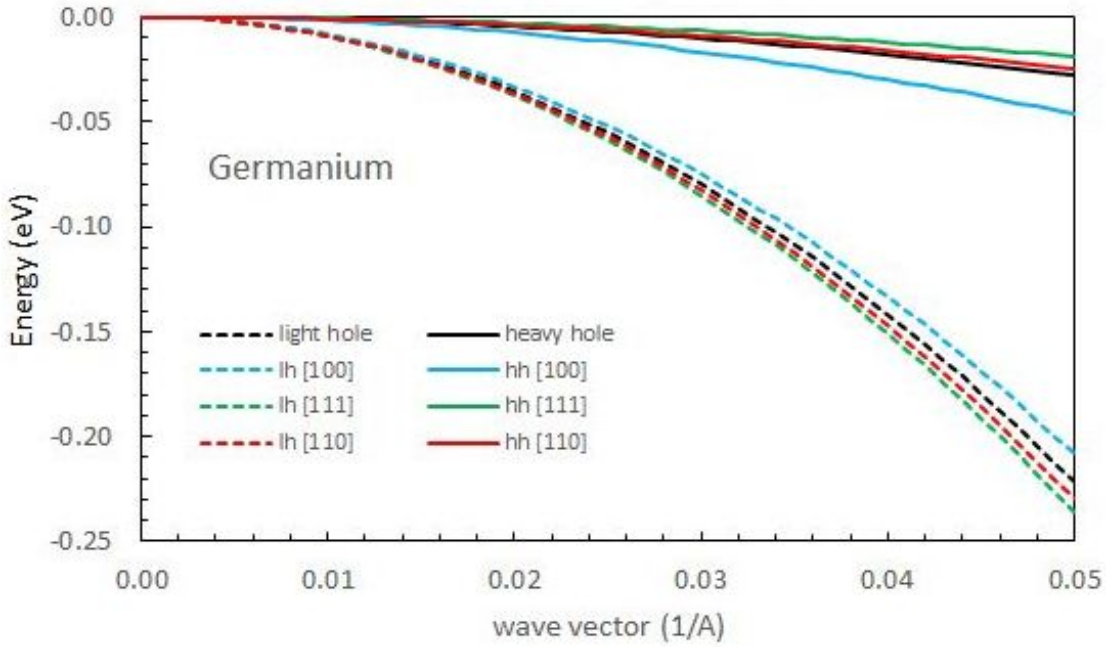

Figure 7.16: Warped (unstrained) j=3/2 valence bands of germanium calculated from the inverse effective mass parameters A=−13.38, B=−8.5, C^2=173 (in units of $\hbar^2/2m_0$) taken from Yu and Cardona[21] along high-symmetry directions (colored) in comparison to the spherical bands (black) calculated from the effective masses m_{lh}=0.043 and m_{hh}=0.34. The light and heavy hole bands are shown by dashed and solid lines, respectively. Compare Fig. 1 of Kane (1956).

Examples for unstrained Ge and α-Sn

Without strain, Eq. (75) leads to the following expressions for the warped Γ_8^+ bands along the specified directions[21]

$$[100] \qquad E_\pm = \left(A \pm |B|\right) k^2, \tag{81}$$

$$[111] \qquad E_\pm = \left(A \pm |B| \sqrt{1 + C^2/3B^2}\right) k^2, \tag{82}$$

$$[110] \qquad E_\pm = \left(A \pm |B| \sqrt{1 + C^2/4B^2}\right) k^2. \tag{83}$$

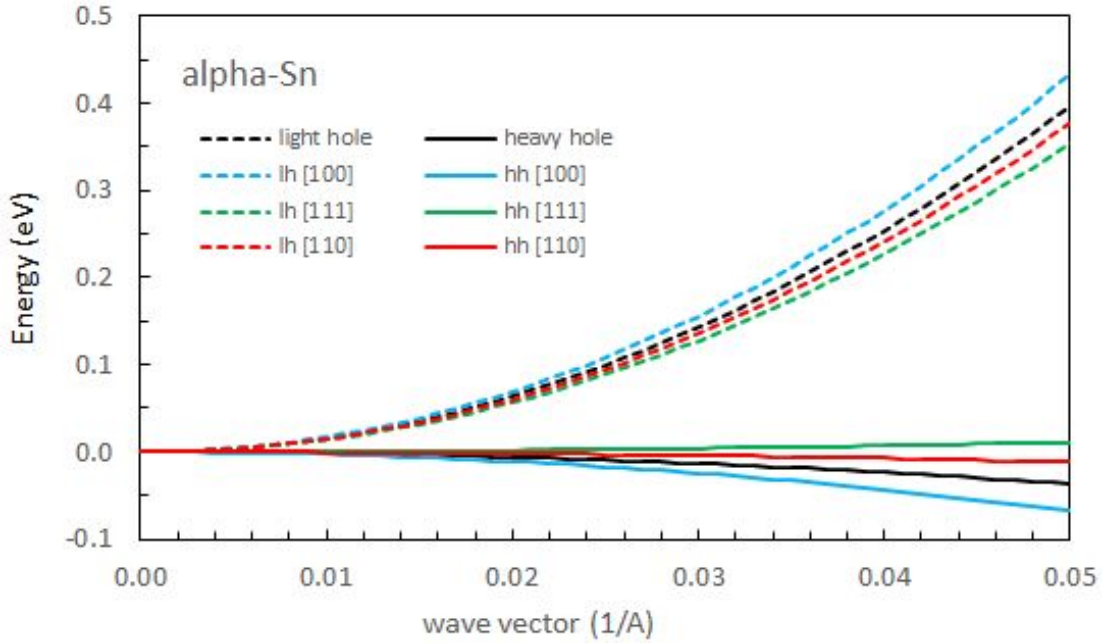

Figure 7.17: Warped (unstrained) j=3/2 bands of α-Sn calculated from the inverse effective mass parameters A=19.2, B=26.3, C^2=−1100 (in units of $\hbar^2/2m_0$) taken from Booth and Ewald (1968) along high-symmetry directions (colored) in comparison to the spherical bands (black) calculated from the effective masses in Table 7.1. The Γ_8^+ conduction and valence bands are shown by dashed and solid lines, respectively. The light "hole" is now a conduction band with an upward curvature. The same is true also for the heavy hole band along the [111] direction, at least for our choice of inverse effective mass parameters.

Yu and Cardona[21] (2.67-2.68) list similar expressions to calculate the heavy and light hole masses along high-symmetry directions. We note that the absolute magnitude of B must be inserted into these expressions to yield the correct effective masses.

The dispersion of the unstrained warped Γ_8^+ VBs of Ge and α-tin versus wave vector near the BZ center are shown in Figs. 7.16 and 7.17 along the [100], [111], and [110] directions in comparison with the spherical bands calculated from the light and heavy hole effective masses. For Ge, we selected[21] A=−13.38, B=−8.5, and C^2=173, in units of $\hbar^2/2m_0$.

In Ge (Fig. 7.16), the curvature (effective mass) for the wave vector along the [100] direction (blue solid line) is larger (smaller) than in the isotropic approximation (black solid line) for the heavy hole band, but smaller (larger) for wave vectors along [111] and [110] due to the C^2 warping term under the square root. The situation is reversed for the light hole band (dashed), where the curvature for wave vectors along [100] is smaller than in the isotropic approximation. The parabolic approximation is only accurate up to about k=0.05 Å^{-1}, see Fig. 1 in Kane (1956) and Fig. 1 in Rodríguez-Bolívar (2005).

For α-tin (Fig. 7.17), the statements above are true only for the heavy hole band. The light' "hole" Γ_8^+ CB has a larger curvature (smaller effective mass) than in the isotropic approximation for wave vectors along the [001] direction and a smaller curvature in the other directions. The different warping of Ge and α-Sn

arises from the opposite curvatures of the two Γ_8^+ bands. For the heavy hole band in unstrained α-tin, the warping is so strong that the curvature and mass change sign along the [111] direction. Along [111], the heavy hole band bends upward for small wave vectors and has positive energies, at least for our choice of inverse effective mass parameters.

While there is ample evidence for the warping in Ge given by the inverse effective mass (or Luttinger) parameters, the magnitude and sign of the warping parameter C^2 in α-tin relies only on one 50 year-old experiment (angle-dependent Shubnikov-de Haas magneto-resistance oscillations) by Booth & Ewald (1968). A different sign (and magnitude) of C^2 and γ_3 is obtained, if they are calculated from the well-established band gaps using $\vec{k}\cdot\vec{p}$ and LMTO-ASA theory[121] (Cardona 1967, Lawaetz 1971). Additional experiments or a detailed analysis of modern *ab initio* band structure calculations to obtain the Luttinger parameters would be useful. For α-tin, the parabolic approximation might be valid for larger wave vectors than for Ge, because the light "hole" band has the opposite curvature and therefore is further away from the split-off hole band than in Ge.

Strained valence bands in Ge

If we now consider a pseudomorphic epitaxial layer under biaxial stress on a (001) substrate with a strain tensor given in Eq. (58), then the band energies from (75)

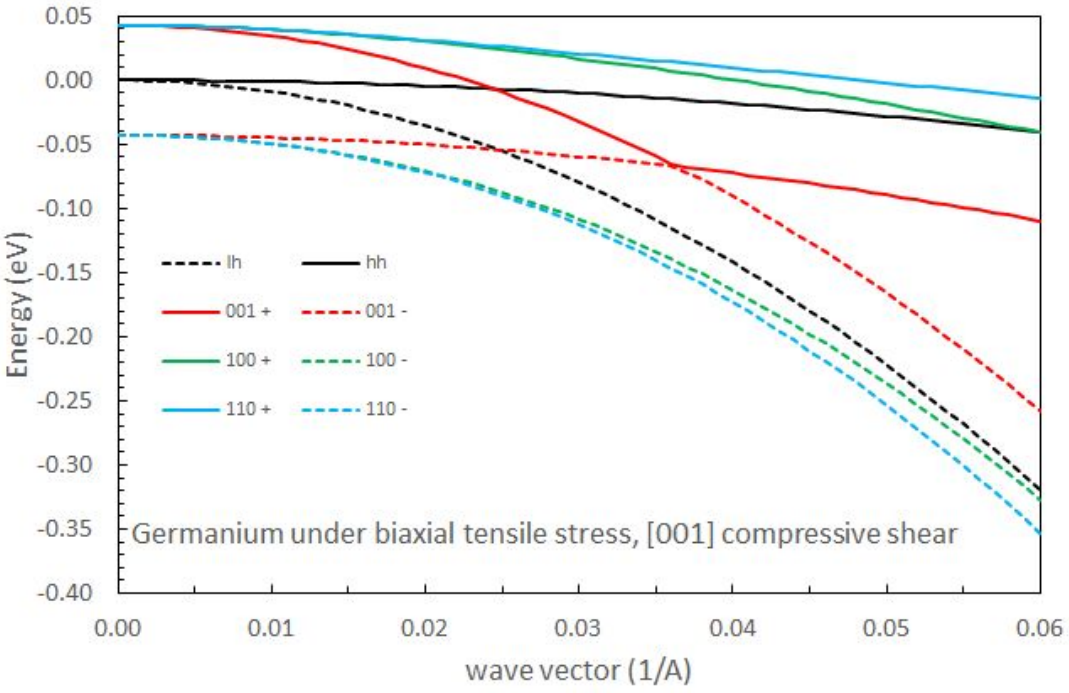

Figure 7.18: Warped j=3/2 (Γ_8^+) bands of Ge under a biaxial tensile stress ($\epsilon_\parallel$=1%), resulting in a compressive [001] shear, along different directions (colored). The black lines show the spherical unstrained heavy and light hole bands. Solid (dashed) lines show the E_+ (E_-) bands derived from the heavy (light) hole bands. The red (green, blue) lines show the dispersion for a wave vector parallel (perpendicular) to the [001] shear strain. Axes in fcc notation. Compare Fig. 1a in Pikus & Bir (1960). The heavy and light hole bands cross for a wave vector along the [001] strain axis (red), but not in other directions.

along the specified high-symmetry directions are

$$E_\pm = \quad Ak^2 \pm$$

$$[100] \qquad \pm\sqrt{\delta_0^2 - B\delta_0 k^2 + B^2 k^4}, \tag{84}$$

$$[001] \qquad \pm\left|\delta_0 + Bk^2\right|, \tag{85}$$

$$[111] \qquad \pm\sqrt{\delta_0^2 + \left(B^2 + C^2/3\right)k^4}, \tag{86}$$

$$[110] \qquad \pm\sqrt{\delta_0^2 - B\delta_0 k^2 + \left(B^2 + C^2/4\right)k^4}. \tag{87}$$

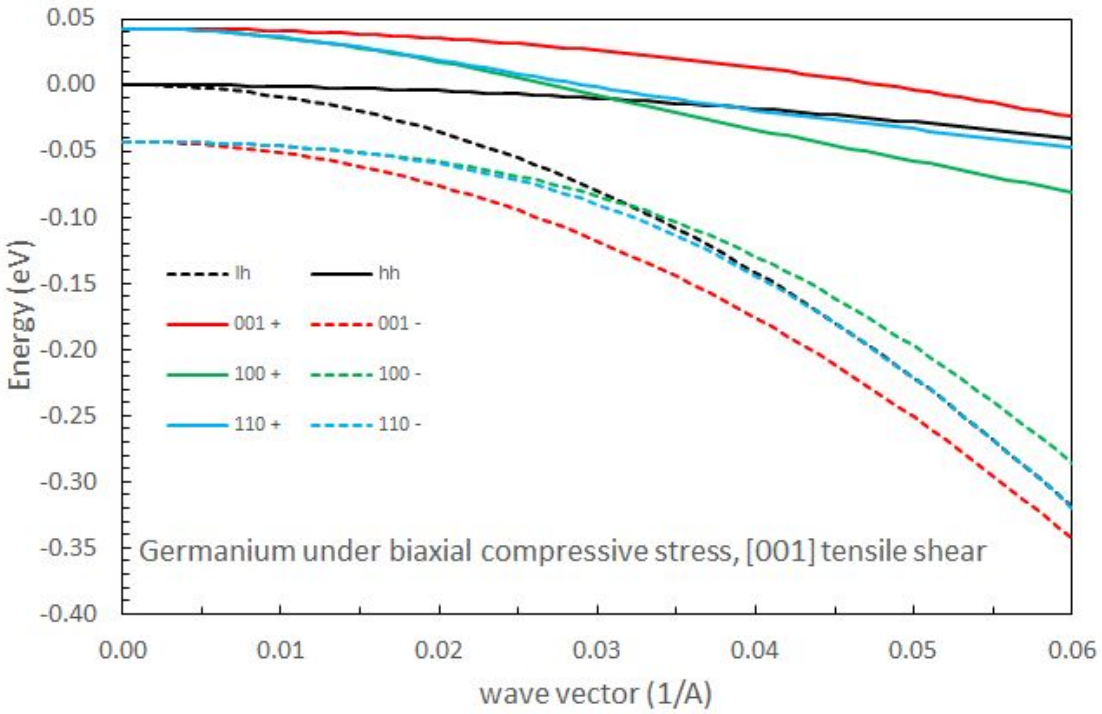

Figure 7.19: Warped j=3/2 (Γ_8^+) bands of Ge under a biaxial compressive stress ($\epsilon_\parallel$=−1%), resulting in a tensile [001] shear, along different directions (colored). The black lines show the spherical unstrained heavy and light hole bands. Solid (dashed) lines show the E_+ (E_-) bands derived from the heavy (light) hole bands. The red (green, blue) lines show the dispersion for a wave vector parallel (perpendicular) to the [001] shear strain. Axes in fcc notation. The heavy and light hole bands do not cross in this case.

The equation along [001] can be found in Cardona (1967) and Ref. 111. Also compare Eq. (29) in Averous (1979).

We apply Eqs. (84-87) to calculate the warped VBs of Ge under a tensile and compressive biaxial stress with $\epsilon_{\|}=\pm 1\%$ and $b=-2.3$ eV (Schmid 1990), see Figs. 7.18 and 7.19. A recent photoreflectance measurement of Ge epitaxial layers on Si resulting in $b=-1.88$ eV is also very credible (Liu 2004). As shown by Pikus & Bir (1960), a compressive [001] shear strain, see Fig. 7.18, leads to a crossing of the heavy and light hole bands for a wave vector parallel to the [001] strain axis, but not in the other directions. This is not a Dirac point, however, because these bands cross within the VB, below the VB maximum. The situation is different for a compressive biaxial stress (resulting in a tensile [001] shear strain), see Fig. 7.19: A gap of width $2\delta_0$ opens at the Γ-point, but there is no crossing of the heavy and light hole bands.

Strained valence bands in α-Sn

Compressive in-plane strain

The situation is reversed in α-tin compared to Ge, see Figs. 7.20 and 7.21, shown for a $\pm 1\%$ in-plane strain, much larger than for pseudomorphic growth on InSb or CdTe, see Table 7.4. There is a crossing of the Γ_8^+ VB and CB under *compressive* biaxial stress (tensile [001] strain) for a wave vector parallel to the [001] shear strain, but not if the wave vector and shear strain direction are perpendicular,

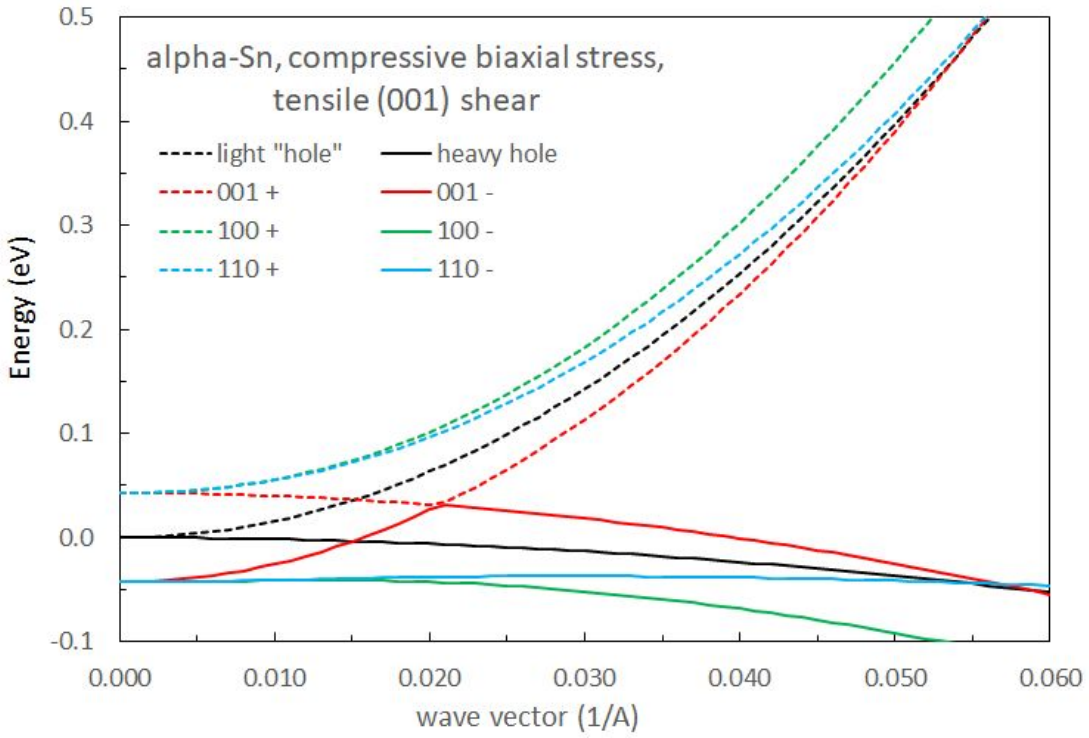

Figure 7.20: Warped j=3/2 (Γ_8^+) bands of α-tin under a biaxial compressive stress ($\epsilon_\parallel$=-1%), resulting in a tensile [001] shear along different directions (colored). The black lines show the spherical unstrained heavy and light "hole" bands. Solid (dashed) lines show the E_+ (E_-) bands derived from the heavy (light) hole bands. The red (green, blue) lines show the dispersion for a wave vector parallel (perpendicular) to the [001] shear strain. Axes in fcc notation. The heavy and light "hole" bands cross for a wave vector along the [001] strain axis (Dirac point), but not in the other directions.

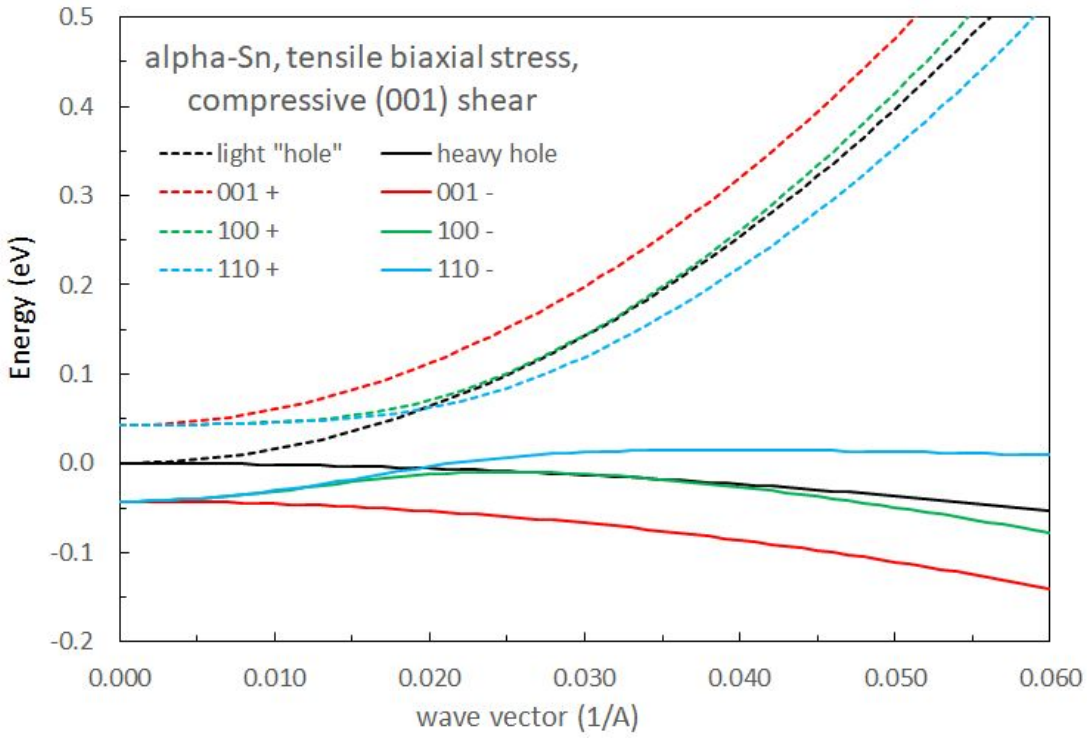

Figure 7.21: Warped j=3/2 (Γ_8^+) bands of α-tin under a biaxial tensile stress ($\epsilon_\parallel$=1%), resulting in a compressive [001] shear along different directions (colored). The black lines show the spherical unstrained heavy and light "hole" bands. Solid (dashed) lines show the E_+ (E_-) bands derived from the heavy (light) hole bands. The red (green, blue) lines show the dispersion for a wave vector parallel (perpendicular) to the [001] shear strain. Axes in fcc notation. Because of the anti-crossing of the heavy and light "hole" bands for in-plane wave vectors perpendicular to the [001] strain, the VB maximum does not occur at Γ.

see Fig. 7.20, because the term under the square root in Eqs. (84)-(87) is always positive and never becomes zero, since δ_0<0. This crossing occurs at[111] (Leung and Liu 1975, Averous 1979)

$$k_D = \pm\sqrt{\frac{-\delta_0}{B}} \tag{88}$$

at an energy

$$E_D = Ak_D^2 = -\frac{\delta_0 A}{B} \tag{89}$$

(relative to the average Γ_8^+ energy). For α-Sn on InSb, we find k_D=0.0077 Å^{-1} and E_D=4.4 meV. Since Eq. (88) neglects the interaction between the heavy and split-off hole bands, the results should only be accurate for small strains on the order of 2% or less. Parallel to the shear strain, the Γ_8^+ VB becomes a CB and *vice versa*. Because of this crossing, the VB maximum does not occur at Γ. Instead, the crossing gives rise to a Dirac point in the band structure of α-Sn under a compressive in-plane (tensile pure shear) strain and makes α-tin a Dirac semimetal, where the energy changes linearly with wave vector[111] (also Rogalev 2017, Zhang 2018). For $\vec{k}$-vectors along the [001] strain axis ($k_\perp = 0$), an expansion of Eq. (79) with $k_\parallel = k_D + \kappa$ around the Dirac point yields

$$E_\pm = E_D + 2\kappa k_D\left(A \pm B\right) + O\left(\kappa^2\right) \tag{90}$$

to first order in κ. For wave vectors in a plane perpendicular to the [001] strain axis with small $k_\perp = \kappa$ through the Dirac point ($k_\parallel = k_D$), the expansion yields

to first order in κ

$$E_{\pm} = E_D \pm \kappa k_D \sqrt{C^2 + 3B^2} + O\left(\kappa^2\right). \tag{91}$$

Since the term under the square root is positive, we find indeed that the carrier energy depends linearly on κ (for small κ) near the Dirac point in all three directions and therefore two three-dimensional Dirac points exist in α-Sn layers under compressive in-plane strain.

For quasi-relativistic Dirac Fermions with wave vectors along the [001] strain axis, the velocity is

$$v_{\parallel} = \frac{2k_D}{\hbar}\left(A \pm B\right), \tag{92}$$

which equals $4.1{\times}10^5$ and $6.3{\times}10^4$ m/s, barely more than 0.1% of the speed of light in vacuum. Similarly, for wave vectors perpendicular to the [001] strain axis, the velocity is

$$v_{\perp} = \pm\frac{k_D}{\hbar}\sqrt{C^2 + 3B^2}, \tag{93}$$

which equals $\pm 1.4{\times}10^5$ m/s for α-Sn on InSb. These Dirac Fermion velocities could be improved by increasing the strain (through growth on a substrate with a smaller lattice constant than InSb), which will move the Dirac point further away from Γ. The mechanical strength of α-Sn limits the magnitude of the strain that can be achieved.

(In our calculation, we do not find the dip in the heavy hole band near k=0 for k perpendicular to the shear stress shown in Fig. 2 of Liu 1973. This might

be due to a higher-order interaction, see Rogalev 2017 Fig. S4 or Zhang 2018 Fig. 2h.) A contour plot of Γ_8^{+v} VB energies through the Dirac point for wave vectors perpendicular to the strain axis is given in Fig. 7.22.

Tensile in-plane strain

No crossing can occur for tensile biaxial stress (compressive [001] shear strain), see Eq. (85), because $\delta_0>0$ in this scenario. $\delta_0 + Bk^2$ is always positive and never reaches zero. For a wave vector parallel to the shear strain, $E_+=\delta_0 + (A + B)\, k^2$ (CB-like curvature) and $E_-=-\delta_0-(B - A)\, k^2$ (VB-like curvature, because $B>A$). Therefore, there is no crossing, see Fig. 7.21.

We also consider the bands for wave vectors oriented perpendicular to the compressive [001] shear strain using Eq. (80). For small k, $E_\pm \approx \pm\delta_0 + (A \mp B/2)\, k^2$. Since $A>B/2$, both bands initially curve like a CB for wave vectors perpendicular to the [001] shear. This leads to a VB maximum of the Γ_8^{+v} band at a non-zero k. Warping sets in for larger k and therefore the location of this VB maximum in k-space is determined by the warping term $k^4C^2\left(\sin^2 2\alpha\right)/4$. For positive C^2, the VB maxima would occur in the four [100] directions. However, we are using a negative value of C^2 (Booth & Ewald 1968) and therefore the VB maxima occur along the four [110] directions.

The band gap of α-tin under a compressive [001] shear strain is indirect and smaller than the splitting $2\delta_0$. We can find the location of the maximum energy

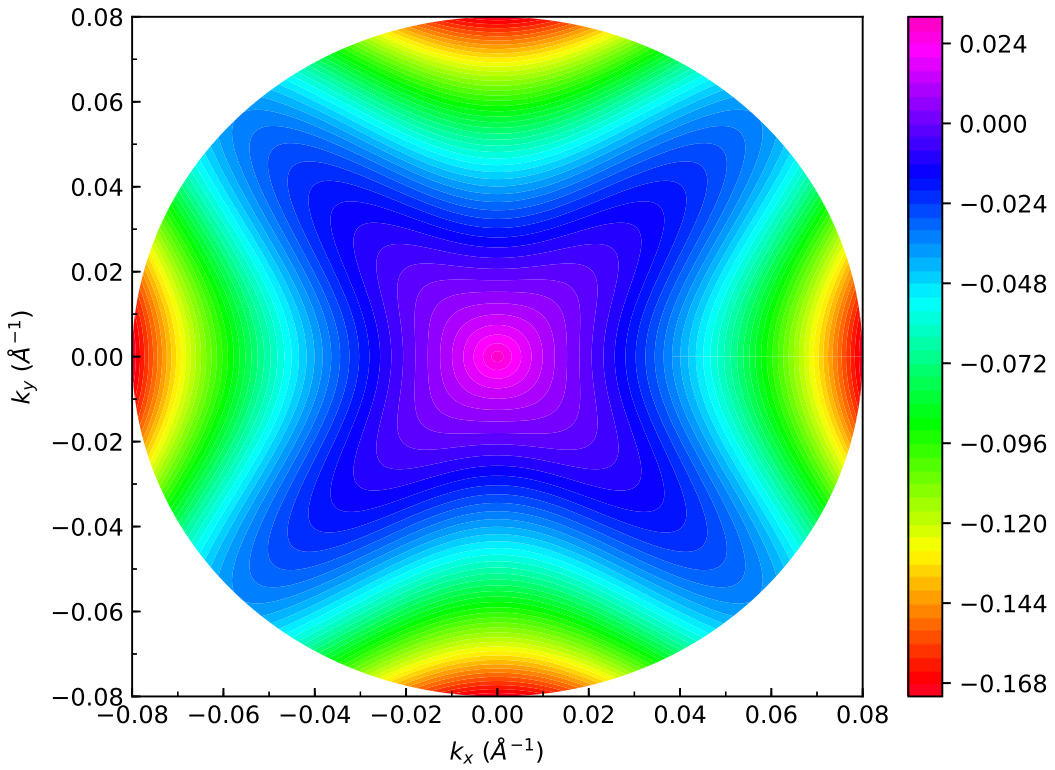

Figure 7.22: Contour map of the Γ_8^{+v} VB of α-tin (energy in eV) under compressive in-plane (tensile [001] shear) strain $\epsilon_{\|}$=−1% for wave vectors perpendicular to the strain axis through the Dirac point with k_z given by Eq. (88).

for each azimuth α by determining the maximum of E_- for a given α in Eq. (80). Setting the derivative dE_-/dk to zero leads to a biquadratic equation for the maximum at k

$$D^2k^4 - B\delta_0 k^2 + \delta_0^2 \frac{A^2 - B^2/4}{A^2 - D^2} = 0, \tag{94}$$

which can be solved analytically. We defined $D^2 = B^2 + C^2\left(\sin^2 2\alpha\right)/4$. The location of the maximum calculated from Eq. (94) is shown by the black line in Fig. 7.23.

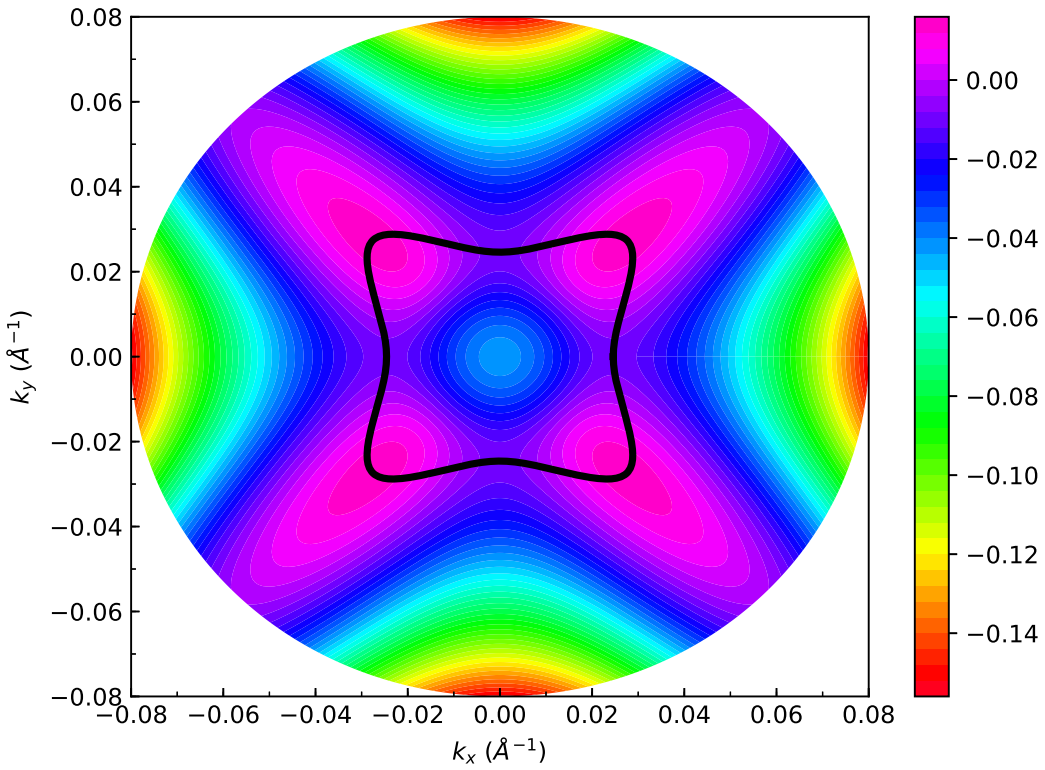

Figure 7.23: Contour plot of the Γ_8^{+v} VB of α-tin (energy in eV) under tensile in-plane (compressive [001] shear) strain $\epsilon_{\|}$=1% for wave vectors perpendicular to the strain axis (with k_z=0). The maximum energy for each direction is shown by the thick black line. The VB maximum is four-fold degenerate and located along the [111] directions, since C^2 is negative.

Therefore, the k_z-component (parallel to the [001] shear strain) of the VB band maximum is zero, as shown by the red lines in Fig. 7.21. The in-plane component ($k_\perp$ perpendicular to the [001] shear) of the VB maximum is non-zero (blue, green). The band gap is now indirect, since the CB minimum still occurs at Γ. A qualitatively similar result was obtained by Cardona (1967) under a unaxial [001] compression, but there are notable differences: In the CB, our differences between the [110] and [100] directions are much larger than obtained by Cardona. Also, the

[100] and [110] directions in the VBs are reversed compared to Cardona (because the C^2 inverse effective mass parameter was positive in Cardona's work). These differences are due to different inverse effective mass parameters, since Cardona's work predates the accurate determination of these parameters by Booth & Ewald (1968) using Shubnikov-de Haas measurements. Our results for the Γ_8^+ energies show very good agreement with Roman & Ewald,[2] whose inverse effective mass parameters are the same as ours. The opening of a band gap combined with the inverted band structure, where the parity of the VBs changes from even (Γ_7^+) to odd (Γ_7^-) and back to even (Γ_8^+), makes α-tin under a compressive [001] shear strain a topological insulator[118, 111] (see especially Fig. S2 in Rogalev 2017).

We performed a detailed study of the shape of the VB maximum of α-tin under compressive [001] shear strain (tensile in-plane strain $\epsilon_{\parallel}$=1%) using the inverse effective mass parameters given by Booth & Ewald (1968), see Fig. 7.23. The energy at Γ is about 68 meV below the VB maximum. For non-zero $k_{\perp}$, the energy first increases and then decreases. The energy of this maximum (shown by the black line) depends on the azimuthal angle α. The VB maximum is four-fold degenerate and occurs at four points $(\pm k_m, \pm k_m, 0)$, where k_m=0.038 Å^{-1}.

The Γ_8^{+v} heavy holes with wave vectors perpendicular to the [001] strain axis experience a warped Goldstone potential, where the valence band maximum (minimum hole energy) depends not only on the radius, but also on the azimuth. In a conventional Goldstone potential, the particle energy has azimuthal or spherical

symmetry, but the energy minimum occurs at a finite (non-zero) radius.

Very nice band structure graphs parallel and perpendicular to the [001] pure shear axis, for compressive and tensile shear strains, are given as supplementary materials by Rogalev *et al.* (2017). Their tight-binding calculation includes more bands than our simple Pikus-Bir model and therefore shows features not seen in our calculations. See also Ref. 111 and Zhang (2018). As always, it is a challenge in the literature to assign consistent group-theory notations to the bands and calculate the correct magnitude of the strain splittings using the various pre-factors of deformation potentials, such as in Eq. (64). The purpose of our simple calculations is to investigate the magnitude of the strain effects and show the dominant source of the band crossings and anticrossings.

Strained α-tin on InSb (001)

Since the in-plane strain for α-tin on InSb is only -0.15% (see Table 7.4), we also show the bands for this scenario in Fig. 7.14. There is a splitting of the Γ_8^+ bands in the amount of $2|\delta_0|$=13 meV, as mentioned earlier. For wave vectors perpendicular to the [001] shear strain direction, for example along [100] or [110], the Γ_8^{+c} and Γ_8^{+v} bands still bend upward and downward, as expected for a CB and VB. However, these two bands bend in the opposite direction for wave vectors parallel to the shear strain and cross at k_z=$\pm$ 0.0077 Å^{-1} at an energy of 5 meV (relative to the average Γ_8^+ energy), see Eq. (88). Under such a tensile [001] shear strain, α-tin

is a Dirac semimetal with two symmetric Dirac points given by Eq. (88). The distance between the two Dirac points is shown in Fig. 7.13. Their location is tunable with the magnitude of the strain. Liu (1973) states that the crossing of the heavy and light hole bands "should be removed by interactions other than $\vec{k}\cdot\vec{p}$ interactions," but Huang and Liu[111] explain (also Zhang 2018) that the band crossing (Dirac point) arises from the symmetry of the strained crystal, because the heavy and light "hole" bands along $\Lambda = \Gamma Z$ belong to different irreducible representations Λ_6 and Λ_7 of the group of the k-vector. No crossing occurs along the other directions.

The Fermi level is located exactly at the energy of the Dirac points[111] (Liu & Leung 1975). The Fermi surface (at 0 K in the absence of dopants) consists of two isolated points given by Eq. (88) resulting in a three-dimensional Dirac semimetal.[111]

Finally, we note that the Pikus-Bir Hamiltonian ignores the Γ_7^--Γ_7^+ interactions and therefore the Γ_7^- band is parabolic in this approximation. If this interaction is included in a more precise calculation, then the Γ_7^- VB assumes a slight M-shape[118] (also called camelback shape by Rogalev 2017).

8 Dielectric function and band structure of $Sn_{1-x}Ge_x$ (x<0.06) alloys on InSb

This article was published in Applied Physics Letters, volume **114**, 062102 (2019).

Rigo A. Carrasco, Stefan Zollner,

Department of Physics, New Mexico State University, P.O. Box 30001, Las Cruces, New Mexico 88003, USA

Stephanie A. Chastang, Jinsong Duan, Gordon J. Grzybowski,

KBRwyle, 2601 Mission Point Blvd., Suite 300, Dayton, Ohio 45431, USA

Bruce B. Claflin, and Arnold M. Kiefer

Air Force Research Laboratory, Sensors Directorate, Wright-Patterson Air Force Base, Ohio 45433, USA

8.1 Abstract

Tin-rich $Sn_{1-x}Ge_x$ alloys with Ge contents up to 6% were grown pseudomorphically on InSb (001) substrates by molecular beam epitaxy at room temperature. The alloys show a germanium-like lattice and electronic structure and respond to the biaxial stress within continuum elasticity theory, which influences bands and interband optical transitions. The dielectric function of these alloys was determined from 0.16 to 4.7 eV using Fourier-transform infrared and spectroscopic ellipsometry. The E_1 and $E_1 + \Delta_1$ critical points decrease with increasing Ge

content with a bowing parameter similar to one established for Ge-rich $Sn_{1-x}Ge_x$ alloys. On the other hand, the inverted direct band gap $\bar{E}_0$ is nearly independent of Ge content, which requires a bowing parameter of about 0.8 eV, much lower than what has been established with photoluminescence experiments of Ge-rich relaxed $Sn_{1-x}Ge_x$ alloys.

Dilute $Sn_{1-x}Ge_x$ alloys ($x \ll 1$) are randomly disordered germanium-like semiconductors with an inverted band structure[1] and a negative energy gap $\bar{E}_0 = -0.41$ eV, because the s-antibonding orbital with Γ_7^- symmetry has a lower energy than the p-bonding Γ_8^+ orbital, see Fig. 8.1(a). Because of the degeneracy of the Γ_8^+ band, the band gap of unstrained $Sn_{1-x}Ge_x$ alloys (with small x) is exactly zero, protected by the cubic symmetry of the crystal. If grown pseudomorphically strained on a suitable substrate (like InSb), the alloys undergo a topological phase transition from a Dirac semimetal ($x<1.2\%$) to a topogical insulator ($x>1.2\%$) as the in-plane strain changes from compressive to tensile[142, 111, 143] (near $x=1.2\%$ for growth on InSb), see Fig. 8.1. At some value of x (probably between 25% and 75%), the direct gap $\bar{E}_0$ becomes zero and changes sign,[144, 145, 146, 147] but such alloys have not yet been studied experimentally, since Sn and Ge are barely miscible. Thin films of stable $Sn_{1-x}Ge_x$ alloys can be grown epitaxially through non-equilibrium growth methods (e.g. molecular beam epitaxy and chemical vapor deposition) allowing their properties to be explored.

Many quantities of $Sn_{1-x}Ge_x$ alloys, such as lattice constants and band gaps,

vary smoothly with composition and follow Vegard's Law (linear interpolation) with quadratic corrections[14]

$$E(x) = E_{\mathrm{Ge}}x + E_{\mathrm{Sn}}(1-x) - bx(1-x), \tag{95}$$

where the subscripts indicate the element and b is the bowing parameter. A positive bowing parameter indicates that the quantity E for the alloy is smaller than given by a linear interpolation. Examples of such quantities and their bowing parameters determined from Ge-rich $Sn_{1-x}Ge_x$ alloys (x>0.85) are shown in Table 8.2.1. Some quantities, especially the inverse effective mass (Luttinger) parameters, diverge as $\bar{E}_0$ crosses zero and require a different interpolation scheme as explained in the supplemental materials.

The purpose of this manuscript is to describe the dielectric function (determined from spectroscopic ellipsometry) and band structure of $Sn_{1-x}Ge_x$ alloys (x<0.06). Our work follows similar studies for Ge-rich alloys[22, 99] and α-tin,[23] but the dielectric function and critical-point (CP) parameters for Sn-rich $Sn_{1-x}Ge_x$ alloys have not yet been reported. It is of particular interest if bowing parameters determined on the Ge-rich side can also be applied to Sn-rich alloys.

Our $Sn_{1-x}Ge_x$ alloys were grown on InSb (001) substrates by molecular beam epitaxy at room temperature as described previously.[114, 115, 144, 24] The composition was varied by changing the Ge effusion cell temperature while keeping the tin flux constant. The growth rate was 8−10 nm/min. Post-growth examina-

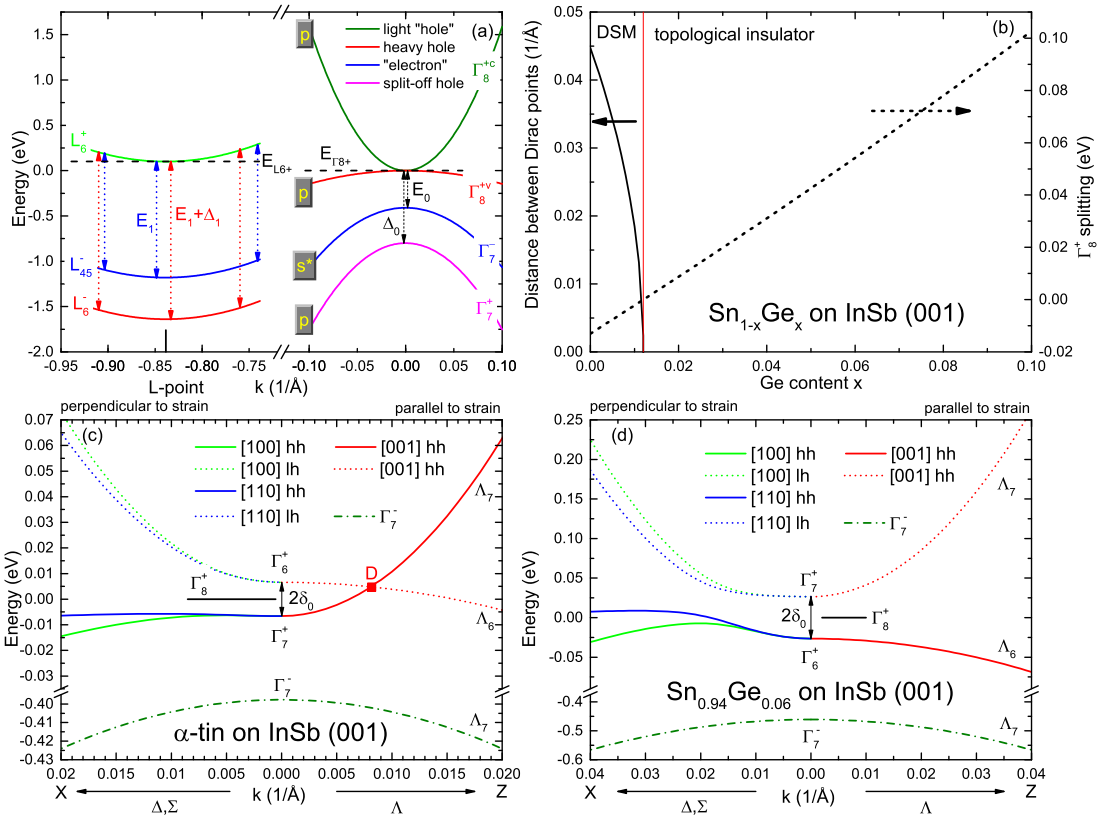

Figure 8.1: (a) Schematic band structure of unstrained α-tin with interband transitions and band symmetries. (b) Splitting $2\delta_0$ of Γ_8^+ energy levels versus Ge content; separation of the two Dirac points in the Dirac semimetal (DSM) phase. (c) Conduction and valence band energies for wave vectors parallel and perpendicular to the [001] shear strain. Compressive in-plane stress makes α-tin (x=0) a DSM. The Dirac point (D) is indicated. (d) Tensile in-plane stress makes $Sn_{1-x}Ge_x$ (x=6%) on InSb a topological insulator with a small gap.

Table 8.1: Ge content x and thickness t determined from x-ray diffraction (XRD) and spectroscopic ellipsometry (SE). Energies E, broadenings Γ, and phase angle ϕ of the $\bar{E}_0$, E_1 and $E_1 + \Delta_1$ gaps from SE.

x %	t(XRD) (nm)	t(SE) (nm)	$\bar{E}_0$ (eV)	E_1 (eV)	$E_1 + \Delta_1$ (eV)	Γ_{E_1} (meV)	$\Gamma_{E_1+\Delta_1}$ (meV)	ϕ_{E_1} (°)
0	67.2	68.6	0.418	1.281	1.739	60	91	74
1.5	97.8	100.4	0.425	1.269	1.719	64	97	70
2.0	100.5	103.4	0.427	1.250	1.707	77	110	73
2.4[a]		73.9	0.428	1.275	1.738	59	87	98
2.5	119.0	119.7	0.428	1.255	1.709	70	101	64
3.6[a]	81.4	81.2	0.429	1.245	1.681	54	102	41
4.0	103.4	103.1	0.432	1.263	1.711	67	99	65
4.1[a]	81.5	81.4	0.428	1.247	1.692	63	101	58
5.0[b]		188	0.423					
5.6	50.1	50.3	0.433	1.232	1.669	85	129	55
5.9[a]	75.0	75.1	0.429	1.239	1.665	?	102	40

[a]Difficult to fit because of the the overlap with an interference fringe.
[b]Partially relaxed

tion by high-resolution x-ray diffraction (XRD) establishes the diamond crystal structure and high crystalline quality. The Ge content and layer thickness were determined from the (004) Bragg reflections assuming that the lattice constant of $Sn_{1-x}Ge_x$ varies linearly with composition[148] (bowing parameter b=0) and that the alloys are fully strained, which was verified with asymmetric XRD reciprocal space maps for selected samples. Pure α-tin on InSb is under compressive in-plane strain, while $Sn_{1-x}Ge_x$ alloys on InSb with a Ge content above 1.2% display tensile in-plane strain, see Fig. 8.2. All layers reported here were fully strained with strong *Pendellösung* fringes, but thicker alloys at high strain showed some relaxation. Table 8.1 describes the layers investigated in this study, especially their composition and thickness.

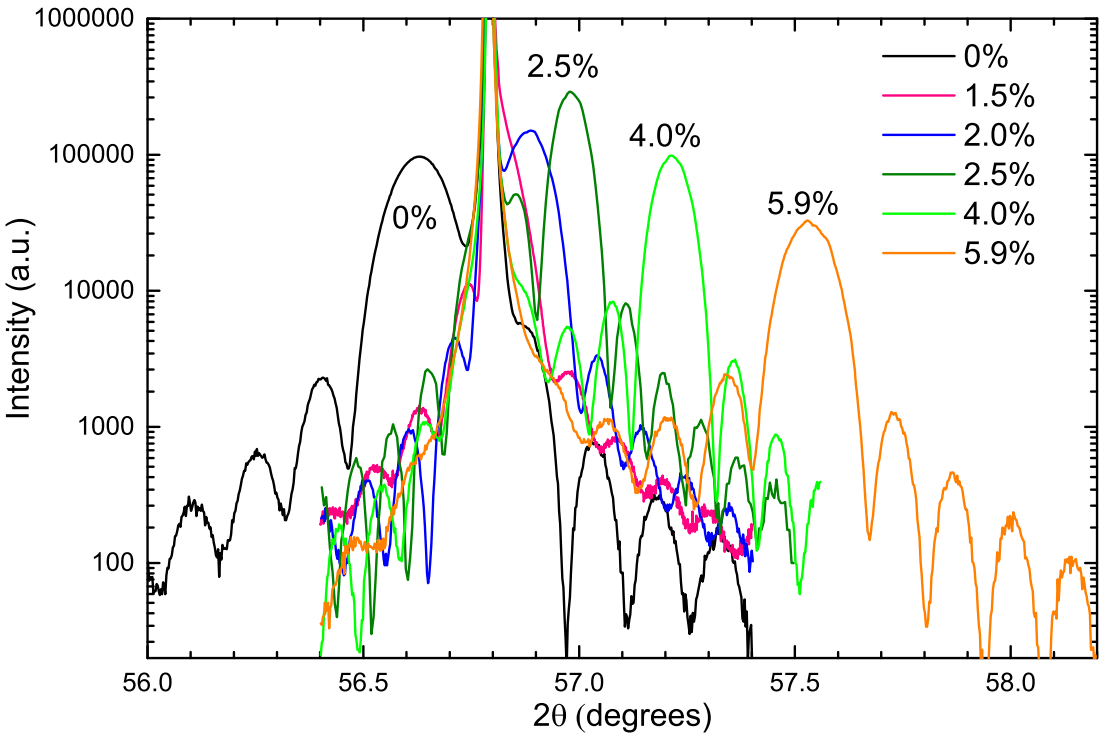

Figure 8.2: (004) Bragg reflections of $Sn_{1-x}Ge_x$ alloy layers (x=0−5.9%) grown on InSb (001) were used to determine composition and thickness. Alloys below (above) 1.2% Ge are under compressive (tensile) in-plane stress.

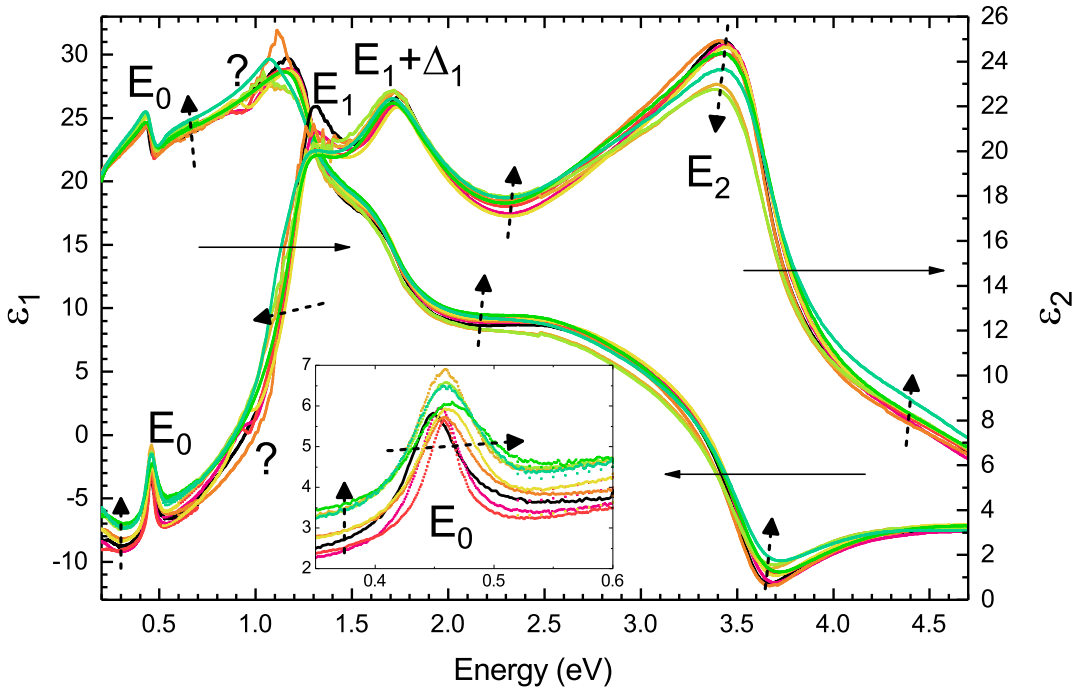

Figure 8.3: Dielectric function of α-Sn (black) and $Sn_{1-x}Ge_x$ alloys (x<0.06) on InSb (001) from a point-by-point fit to spectroscopic ellipsometry data. Colors from red to blue indicate increasing Ge content. The magnified inset of ϵ_2 versus photon energy shows a slight blueshift of $\bar{E}_0$ with increasing Ge content. The question mark points out a numeric instability of the point-by-point fit near an interference fringe. Dashed arrows show trends with increasing Ge content. Tabulated data for this figure are included as supplemental material.

Ellipsometric angles at room temperature were acquired from 0.16 eV (the band gap of the InSb substrate) to 4.7 eV at three angles of indicence ($65°-75°$) on two different instruments and analyzed as described elsewhere.[14, 24] All pseudo-dielectric function spectra showed $\bar{E}_0$, E_1, $E_1+\Delta_1$, and E_2 CPs[21] and one interference fringe between $\bar{E}_0$ and E_1 at an energy that depended on thickness.[24] The data were fitted using a three-layer model (oxide, epilayer, substrate) and the optical constants of the epilayer were determined using a two-step process. We first described the optical constants of the epilayer with a Kramers-Kronig-consistent semiconductor parametric oscillator model to determine the thicknesses. We then fixed the thicknesses to values found in the first step, discarded the parametric oscillator model to avoid bias, and fitted the optical constants of the epilayer independently at each wavelength. Both steps in this fitting process yielded approximately the same optical constants. The overall fit throughout the entire spectral range was usually better with the parametric oscillator model, while the point-by-point fit gave more accurate results near the CPs and for the calculation of derivative spectra. The point-by-point fit sometimes diverged or produced noise or steps in the data, especially near interference fringes. Such artifacts can be reduced by performing a multi-sample fit for epilayers with different thicknesses (but the same composition) using the same optical constants for all $Sn_{1-x}Ge_x$ epilayers (for constant x). Since the optical constants for the native oxide on $Sn_{1-x}Ge_x$ alloys are not known, we used the optical constants for the native oxide

on InSb instead, similar to our earlier analysis of ellipsometry measurements on α-Sn layers.[24]

Figure 8.3 shows the dielectric function of α-Sn and $Sn_{1-x}Ge_x$ alloys from 0.2 to 4.7 eV grown pseudomorphically on InSb (001), as determined from a point-by-point fit. Trends shown by dashed arrows include reduced amplitudes, increased broadenings, a redshift of the E_1 and E_2 CPs, and an increased background at the lowest energies with increasing Ge content. The $\bar{E}_0$ peak shows a slight blueshift with increasing x, as shown by the inset.

Two optical interband transitions are easily accessible to spectroscopic ellipsometry to study the band structure of $Sn_{1-x}Ge_x$ alloys, see Figs. 8.1(a) and 8.3. The $\bar{E}_0$ gap separates the Γ_7^- VB from the Γ_8^+ valence/conduction band. Also, the E_1 and $E_1 + \Delta_1$ transitions occur from the $L_{4,5}^-$ and L_6^- VBs to the L_6^+ CB at the L-point and along the [111] directions.

We first discuss the E_1 and $E_1 + \Delta_1$ CPs, since this is more straightforward based on previous research on other materials like Ge.[21] Ellipsometry measurements on Ge, α-Sn, and Ge-rich $Sn_{1-x}Ge_x$ alloys established the E_1 and $E_1 + \Delta_1$ energies for the elements and the bowing parameters in the Ge-rich regime, see Table 8.2.1. Predictions from prior data, including strain corrections, are shown in Fig. 8.4 in comparison with our experimental data, which were determined by calculating the second derivatives of the data shown in Fig. 8.3 and fitting them

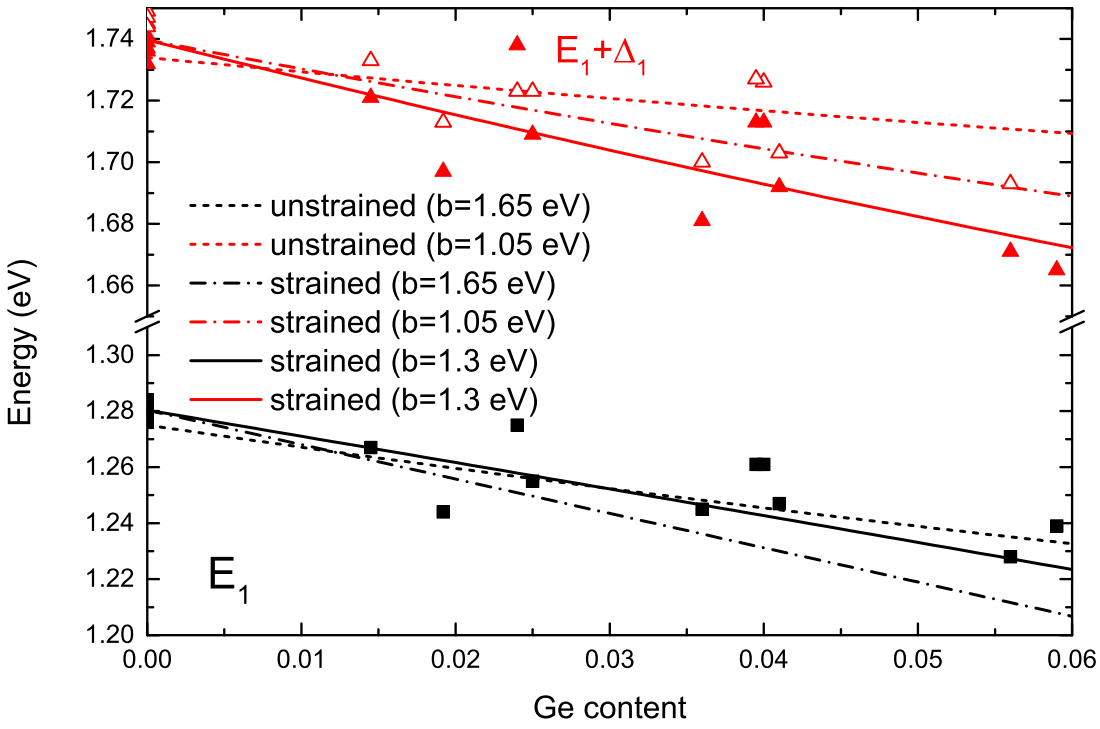

Figure 8.4: E_1 and $E_1 + \Delta_1$ energies from ellipsometry (symbols) along with predictions calculated from established bowing parameters for relaxed (dotted) and strained (dash-dotted) alloys. Our data fit best with a single bowing parameter for both CPs (solid). Closed (open) symbols show results where both phase angles were required to be the same (allowed to differ).

with two-dimensional CP line shapes of the form[21, 14, 24]

$$\epsilon\left(\hbar\omega\right) = C - A\ln\left(\hbar\omega - E_g - i\Gamma\right)e^{i\phi}, \tag{96}$$

where E_g, A, Γ, and ϕ are the energy, amplitude, broadening, and excitonic phase angle of the CP.

Since the E_1 energies for bulk diamond and zinc blende semiconductors are usually determined with an accuracy of about 1 meV, our experimental data in Fig. 8.4 show an unexpected amount of scatter, considering that the clearly

pronounced XRD peaks in Fig. 8.2 suggest a high accuracy of the Ge content. Perhaps the presence of an interference fringe just below the E_1 CP affects the accuracy of our second-derivative analysis. Despite these errors, the agreement of our data with calculated E_1 and $E_1 + \Delta_1$ energies from established bowing parameters[22] is good. Even better agreement can be achieved, if a single bowing parameter of b=1.3 eV is used to describe the dependence of these CPs on Ge content, rather than different bowing parameters for E_1 and $E_1 + \Delta_1$.

We now proceed to discuss the dependence of the $\bar{E}_0$ gap in $Sn_{1-x}Ge_x$ alloys on Ge content. An $\bar{E}_0$ peak was recently discovered in the dielectric function of α-Sn.[24] Comparing predictions from established bowing parameters with experiments is not straightforward, because the mechanism giving rise to the $\bar{E}_0$ peak in ellipsometry data is not fully understood yet. Therefore, no analytical lineshape has been derived yet that could be compared with dielectric function spectra.[24] Our best current theory[24] attributes $\bar{E}_0$ to intravalence band transitions from Γ_7^- to the highest hole band (Γ_7^+ or Γ_6^+, whatever is lower) and places the maximum of ϵ_2 approximately 30 meV (about kT) above $\bar{E}_0$. We therefore subtract this value from our peak energies of ϵ_2 to determine the $\bar{E}_0$ energies of $Sn_{1-x}Ge_x$, see Table 8.1.

We thus find $\bar{E}_0$=0.418 eV for strained α-Sn on InSb (001), which corresponds to the energy difference between Γ_7^+ and Γ_7^- (Fig. 8.1). To obtain the $\bar{E}_0$ energy for unstrained α-Sn, we must add $|\delta_0|$ (6 meV, half the Γ_8^+ splitting under [001]

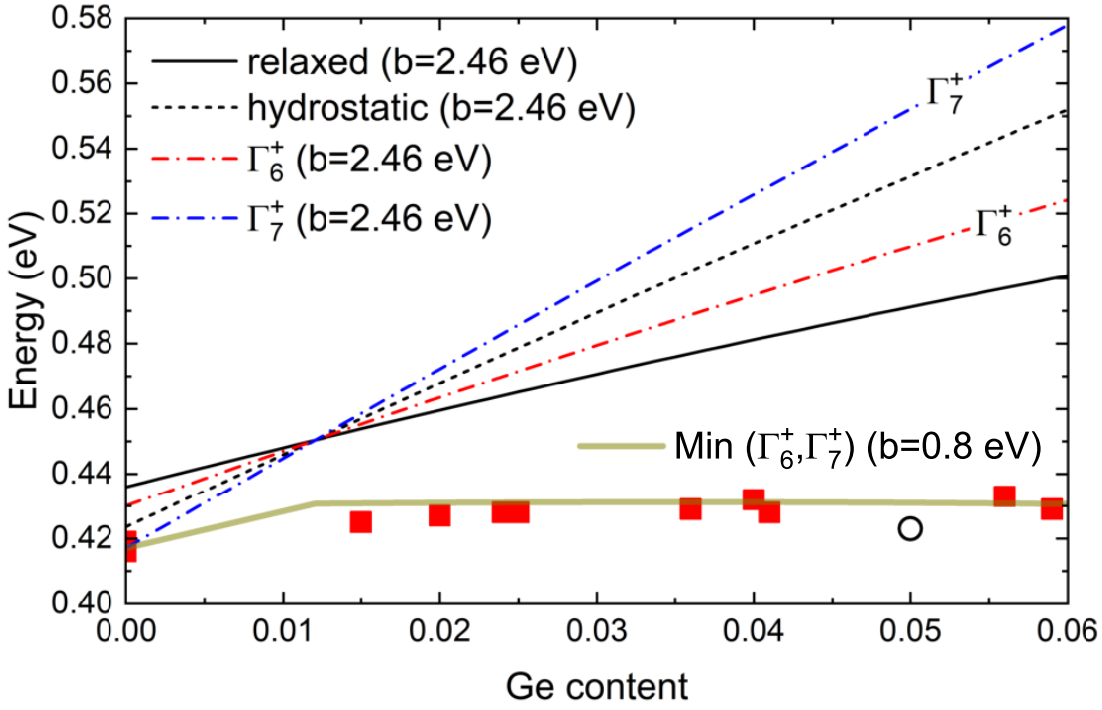

Figure 8.5: $\bar{E}_0$ gaps of pseudomorphic $Sn_{1-x}Ge_x$ alloys on InSb (001) from infrared ellipsometry (■) in comparison with predictions using a bowing parameter of 3.04 eV for relaxed $Sn_{1-x}Ge_x$ (solid), modified by hydrostatic volume change (dotted), and split by [001] shear strain (dash-dotted). A good fit to the experimental data requires a bowing parameter of 0.8 eV (thick line). One layer is partially relaxed (○).

shear strain) and the hydrostatic shift (12 meV) to obtain the energy difference between Γ_8^+ and Γ_7^- in unstrained α-Sn, which yields 0.436 eV. (A detailed discussion of the influence of biaxial stress on the band structure can be found in the supplemental materials.) We consider this value the $\bar{E}_0$ energy for unstrained α-Sn and enter it in Table 8.2.1. See also Fig. 8.5. Our $\bar{E}_0$ of 0.436 eV for unstrained α-Sn is in reasonable agreement with the established value of 0.413 eV, which was determined using magnetoreflectance.[113] A better agreement should not be expected due to the significant non-parabolicity of the Γ_8^+ bands (Fig. 8.1) and the M-shape of the Γ_7^- VB.[118] Our room-temperature ellipsometry measurement probes an energy range of about 30 meV around the Γ_7^- and Γ_8^+ extrema, while magnetoreflectance[113] at 1.5 K measures at much higher energies (up to 150 meV) and extrapolates downward to determine $\bar{E}_0$. The $\bar{E}_0$ gap is independent of temperature between 1.5 and 85 K, determined from magneto-reflectance measurements.[113] and not expected to change up to room temperature.[24]

Using photoluminescence measurements on unstrained Ge-rich $Ge_{1-x}Sn_x$ alloys,[50] a large bowing parameter of b=2.46 eV was found for the E_0 gap, see Table 8.2.1. A recent density-functional calculation[147] finds an even larger value of b=3.02 eV. This suggests a decrease of the Γ_7^- VB energy for relaxed tin-rich $Sn_{1-x}Ge_x$ alloys with increasing Ge content relative to the Γ_8^+ VB maximum, which would lead to an increase in the observed $\bar{E}_0$ energy, as shown in Fig. 8.5. The hydrostatic portion of the in-plane biaxial stress in pseudomorphic $Sn_{1-x}Ge_x$ on InSb

(001) will modify the $\bar{E}_0$ gap and will cause an decrease by 12 meV for pure α-Sn on InSb (001) and an increase for $Sn_{1-x}Ge_x$ alloys with x>1.2% (by 51 meV for x=0.06). Finally, the [001] shear strain splits the doubly degenerate Γ_8^+ band into non-degenerate Γ_6^+ and Γ_7^+ states. If we attribute $\bar{E}_0$ to intravalence band transitions from Γ_7^- to the lowest hole band, then the experimentally observed $\bar{E}_0$ peak should follow the lower of the Γ_7^+ and Γ_6^+ energies. (See also Fig. 8.1 and supplementary material.)

We observe, however, that these predictions do not agree at all with our experimental data. As the Ge content is increased up to 6%, our $\bar{E}_0$ energy increases by no more than 10 meV. This behavior can be described with a bowing parameter of about 0.8 eV, as shown by the thick line in Fig. 8.5.

In summary, we have determined the dielectric function of pseudomorphic tin-rich $Sn_{1-x}Ge_x$ alloys on InSb (001) for Ge contents up to 6% using infrared and spectroscopic ellipsometry. These measurements suggest a germanium-like band structure for such alloys, similar to the elemental endpoints. The E_1 and $E_1 + \Delta_1$ critical points (which originate from interband optical transitions along [111] and at the L-point) show a decrease with increasing Ge content at a rate not entirely incompatible with the bowing parameters determined for Ge-rich alloys. The inverted direct band gap $\bar{E}_0$ is nearly independent of Ge content up to 6%, which suggests a bowing parameter on the order of 0.8 eV, much lower than the value of 2.46 eV determined using photoluminescence of Ge-rich alloys.

See supplementary material for tabulated optical constants of $Sn_{1-x}Ge_x$ alloys, an interpolation scheme of inverse effective mass parameters, a discussion of the influence of biaxial stress on the valence band structure and critical points of $Sn_{1-x}Ge_x$ alloys, critical-point parameters, and characterization results for our epitaxial layers using atomic force microscopy and high-resolution x-ray diffraction.

This work was supported by the Air Force Office of Scientific Research (FA9550-16RYCOR296). RAC and SZ acknowledge support from the AFOSR Summer Faculty Fellowship Program. We are grateful to José Menéndez for stimulating discussions. One of us (SZ) is grateful to the Institute of Physics, Czech Academy of Sciences, for hospitality and support in Prague, Czech Republic, where this article was revised after review.

8.2 Supplementary Material

8.2.1 Valence band warping in $Sn_{1-x}Ge_x$ alloys

Warping of the Γ_8^+ p-bonding orbitals is of critical importance in $Sn_{1-x}Ge_x$ alloys, especially under a biaxial in-plane stress. In a very simple $\vec{k}\cdot\vec{p}$ model, this warping

is described by three inverse effective mass parameters[21] (Dresselhaus 1955)

$$A = 1 - \frac{2}{3}\left(\frac{P^2}{m_0 E_0} + \frac{2Q^2}{m_0 E_0'}\right), \quad (97)$$

$$B = \frac{2}{3}\left(\frac{-P^2}{m_0 E_0} + \frac{Q^2}{m_0 E_0'}\right), \quad (98)$$

$$C^2 = \frac{16P^2Q^2}{3m_0^2 E_0 E_0'}, \quad (99)$$

expressed in units of $\hbar^2/2m_0$, where m_0 is the free electron mass, P and Q are the momentum matrix elements connecting the Γ_{25}' band with the Γ_2' and Γ_{15} bands, respectively, and E_0 and E_0' the corresponding direct band gaps at the Γ-point.

In Ge, A=−13.38 is negative, because the term in parentheses in Eq. (97) is much larger than one. B=−8.5 is also negative, because E_0<E_0' in Eq. (98); and finally C^2=173 is positive, because all parameters in Eq. (99) are positive. In α-tin, A=19.2 is positive, because E_0 is negative and its magnitude is less than E_0'. B=26.3 is positive, because E_0 is negative and all other factors are positive. For the same reason C^2 is negative. (For Ge, the values of the inverse effective mass parameters are not controversial and were taken from Yu and Cardona,[21] Table 2.24. We adopted values for α-tin measured using angle-dependent Shubnikov-de Haas experiments by Booth and Ewald 1968, which are different from calculated inverse effective mass parameters, for example Cardona 1963, Cardona 1967, Lawaetz 1971, or Leung and Liu 1973. Different conventions for signs and units of these parameters are common.)

If we introduce E_P=$2P^2/m_0$ and E_Q=$2Q^2/m_0$ and stress that the inverse

effective mass parameters depend on composition, we can rewrite Eqs. (97-99) as

$$A(x) = 1 - \frac{E_P(x)}{3E_0(x)} - \frac{2E_Q(x)}{3E_0'(x)}, \tag{100}$$

$$B(x) = = -\frac{E_P(x)}{3E_0(x)} + \frac{E_Q(x)}{3E_0'(x)}, \tag{101}$$

$$C^2(x) = \frac{4E_P(x)E_Q(x)}{3E_0(x)E_0'(x)}. \tag{102}$$

In $Sn_{1-x}Ge_x$ alloys, all three parameters A, B, and C^2 will diverge as E_0 crosses from negative to positive values with increasing x. The associated effective masses[21]

$$\vec{k} \parallel [100] \qquad \frac{1}{m_{\rm hh}} = -A + B \tag{103}$$

$$\frac{1}{m_{\rm lh}} = -A - B \tag{104}$$

$$\vec{k} \parallel [111] \qquad \frac{1}{m_{\rm hh}} = -A + B\sqrt{1 + \frac{C^2}{3B^2}} \tag{105}$$

$$\frac{1}{m_{\rm lh}} = -A - B\sqrt{1 + \frac{C^2}{3B^2}} \tag{106}$$

will become very small at this cross-over and the Γ_8^+ bands will take a very large curvature for small wave vectors $\vec{k}$. The divergence is caused by the increased interactions (repulsion) of the Γ_7^- and Γ_8^+ bands with small energy denominators in $\vec{k}\cdot\vec{p}$ theory.

Because of this divergence, it is completely inappropriate to attempt a linear interpolation of the inverse effective mass parameters with tin content. Instead, we note that the matrix elements E_P and E_Q are similar for Ge and tin and therefore should tolerate a linear interpolation (Lawaetz 1971). We also know

the dependence of the direct band gaps E_0 and E_0' on composition (including quadratic bowing for some gaps,[23, 14] Viña 1984) and we might want to calculate composition-dependent inverse effective mass parameters using Eqs. (100-102). The problem is, of course, that we are attempting to predict three parameters A, B, and C^2 with only two variables E_P and E_Q, since the energies E_0 and E_0' are known from spectroscopic measurements. We address this dilemma by introducing an artificial third parameter E_{PQ}, which should be similar to the product of E_P and E_Q:

$$A(x) = 1 - \frac{E_P(x)}{3E_0(x)} - \frac{2E_Q(x)}{3E_0'(x)}, \tag{107}$$

$$B(x) = = -\frac{E_P(x)}{3E_0(x)} + \frac{E_Q(x)}{3E_0'(x)}, \tag{108}$$

$$C^2(x) = \frac{4E_{PQ}(x)}{3E_0(x)E_0'(x)}. \tag{109}$$

We now have three equations and three unknowns, which are easy to solve:

$$E_P = E_0(1 - A - 2B), \tag{110}$$

$$E_Q = E_0'(1 - A + B), \tag{111}$$

$$E_{PQ} = \tfrac{3}{4}E_0E_0'C^2. \tag{112}$$

In conclusion, to determine the inverse effective mass parameters A, B, and C^2 as a function of Ge content x, we start with their values for the elements listed in Table 8.2.1. We then calculate E_P, E_Q, and E_{PQ} for the elements using Eqs. (110-112) and interpolate them linearly with composition (Lawaetz 1971).

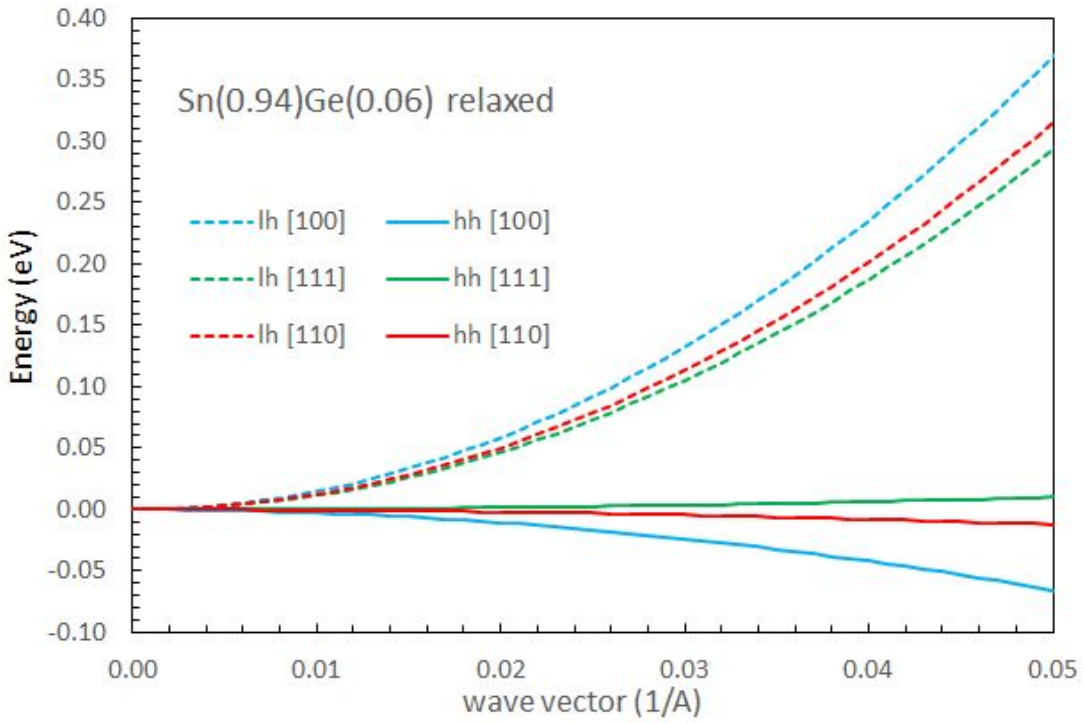

Figure 8.6: Warped (unstrained) Γ_8^+ bands of $Sn_{0.94}Ge_{0.06}$ calculated from the inverse effective mass parameters in Table 8.2.1 along high-symmetry directions. The light and heavy "hole" bands are shown by dashed and solid lines, respectively.

Finally, we use Eqs. (107-109) to find the inverse effective mass parameters for the alloys. From A, B, and C^2, we can also calculate the Luttinger (1956) parameters and the average isotropic effective masses from[21] (Persson 2001)

$$m_{hh,lh}^{-1} = A \pm |B| \sqrt{1 + C^2/5B^2}. \tag{113}$$

(We believe that this corrected equation was the intent of Yu and Cardona.[21] The factor 3/15 can be obtained by writing the Dresselhaus-Kip-Kittel expression in polar coordinates and integrating over the unit sphere with certain approximations.) This expression works very well for Si and Ge, but only for the light "hole" mass of α-tin. The average heavy hole mass of α-tin and tin-rich $Sn_{1-x}Ge_x$ alloys comes out much too large. This interpolation is shown in Table 8.2.1. Results for E_P and E_Q of Ge and Sn are quite reasonable (Lawaetz 1971) and E_{PQ} is within a factor of two of the product $E_P E_Q$. Figure 8.6 shows the warped Γ_8^+ bands of unstrained $Sn_{1-x}Ge_x$ (x=0.06) for small wave vectors in high-symmetry directions. The results are similar to α-Sn,[24] including the positive (electron-like) curvature of the heavy hole for wave vectors along the [111] directions.

8.2.2 Stress and strain in $Ge_{1-x}Sn_x$ alloys

For pseudomorphic growth of α-Sn or $Sn_{1-x}Ge_x$ alloys on InSb (001), the in-plane lattice constant $a_\parallel$ is equal to that of the substrate a_S (pseudomorphic condition). This creates a biaxial stress along the surface of the wafer described by a stress

Table 8.2: Important material parameters for Sn, Ge, and $Sn_{1-x}Ge_x$ alloys (at room temperature) and their interpolation. An example is given for an alloy with x=0.06. Units in parenthesis. b(GeSn) is the bowing parameter. We do not interpolate the elastic constants C_{11} and C_{12}, only their ratio. Interpolation of inverse effective mass parameters A, B, and C^2 is described in the supplemental materials. Most parameters from Ref. 14 (except where noted).

	Ge	Sn	b(GeSn)	alloy (6%)
a (Å)	5.658	6.489	0	6.439
C_{11} (GPa)	128.5	69.0	NA	NA
C_{12} (GPa)	48.3	29.3	NA	NA
C_{12}/C_{11}	0.376	0.425	0	0.422
E_1 (eV)	2.120	1.275[a]	1.65	1.233
E_1 (eV)[b]	2.120	1.275	1.35	1.250
$E_1+\Delta_1$ (eV)	2.310	1.734[a]	1.05	1.709
$E_1+\Delta_1$ (eV)[b]	2.310	1.734	1.35	1.692
Δ_1 (eV)	0.190	0.459[a]	-0.60	0.477
Δ_1 (eV)[b]	0.190	0.459	0	0.443
E_0 (eV)	0.796	-0.436[a]	2.46	-0.501
E_0 (eV)[b]	0.796	-0.436	0.8	-0.407
$E_0+\Delta_0$ (eV)	1.096	0.364	3.04	0.236
Δ_0 (eV)	0.30	0.8	0.58	0.737
E_0' (eV)	3.1[c]	2.4[d]	0	2.44
A ($\hbar^2/2m_0$)	-13.38	19.2	NA	15.9[e]
B ($\hbar^2/2m_0$)	-8.5	26.3	NA	22.8[e]
C^2 ($\hbar^4/4m_0^2$)	173	-1100	NA	-898[e]
E_P (eV)	25.0	29.2	0	29.0
E_Q (eV)	18.2	19.4	0	19.4
E_{PQ} (eV^2)	320	818	0	788
$a(E_0)$ (eV)	-9.5[f]	-7.0[g]	0	-7.2
$b(\Gamma_8^+)$ (eV)	-1.9[h]	-2.3[i]	0	-2.3

[a] Ref. 24.
[b] This work.
[c] Viña 1984.
[d] Ref. 23.
[e] Calculated using Eqs. (107-109).
[f] C.G. Van de Walle, Phys. Rev. B **39**, 1879 (1989).
[g] T. Brudevoll, D.S. Citrin, M. Cardona, and N.E. Christensen, Phys. Rev. B **48**, 8629 (1993).
[h] J. Liu, D. D. Cannon, K. Wada, Y. Ishikawa, D.T. Dielson, S. Jongthammanurak, J. Michel, and L. Kimerling, Phys. Rev. B **70**, 155309 (2004).
[i] Ref. 115.

tensor

$$\mathbf{X} = \begin{pmatrix} X & 0 & 0 \\ 0 & X & 0 \\ 0 & 0 & 0 \end{pmatrix}. \tag{114}$$

(There is no stress along the growth direction, defined as the z-axis.) This biaxial stress is related to a strain tensor (Cardona & Christensen 1987)

$$\begin{pmatrix} \epsilon_{\parallel} & 0 & 0 \\ 0 & \epsilon_{\parallel} & 0 \\ 0 & 0 & \epsilon_{\perp} \end{pmatrix} = \epsilon_H \begin{pmatrix} 1 & 0 & 0 \\ 0 & 1 & 0 \\ 0 & 0 & 1 \end{pmatrix} + \epsilon_S \begin{pmatrix} -1 & 0 & 0 \\ 0 & -1 & 0 \\ 0 & 0 & 2 \end{pmatrix} \tag{115}$$

with perpendicular (out-of-plane) and parallel (in-plane) components $\epsilon_{\perp}$ and $\epsilon_{\parallel}$. ϵ_H and ϵ_S are the hydrostatic and [001] pure shear strain components[21] (Cardona & Christensen 1987)

$$\epsilon_H = \tfrac{1}{3}\left(\epsilon_{\perp} + 2\epsilon_{\parallel}\right) \quad \text{and} \quad \epsilon_S = \tfrac{1}{3}\left(\epsilon_{\perp} - \epsilon_{\parallel}\right). \tag{116}$$

The in-plane strain is defined as

$$\epsilon_{\parallel} = \frac{\Delta a}{a\,(x)} = \frac{a_S - a\,(x)}{a\,(x)}, \tag{117}$$

where $a\,(x)$ is the (cubic) lattice constant of the unstrained $Sn_{1-x}Ge_x$ alloy. Negative strain indicates a reduction of the lattice parameter (compressive strain), while a positive strain indicates an increase of the lattice parameter (tensile strain). Strain is usually a small dimensionless number stated as a percentage. Growth of α-Sn on InSb (x=0) results in compressive (negative) in-plane strain. The magnitude of this in-plane strain decreases with increasing x in $Sn_{1-x}Ge_x$ alloys and vanishes for $x \approx 1.2\%$. For larger x, the in-plane strain becomes tensile, see Fig. 8.7.

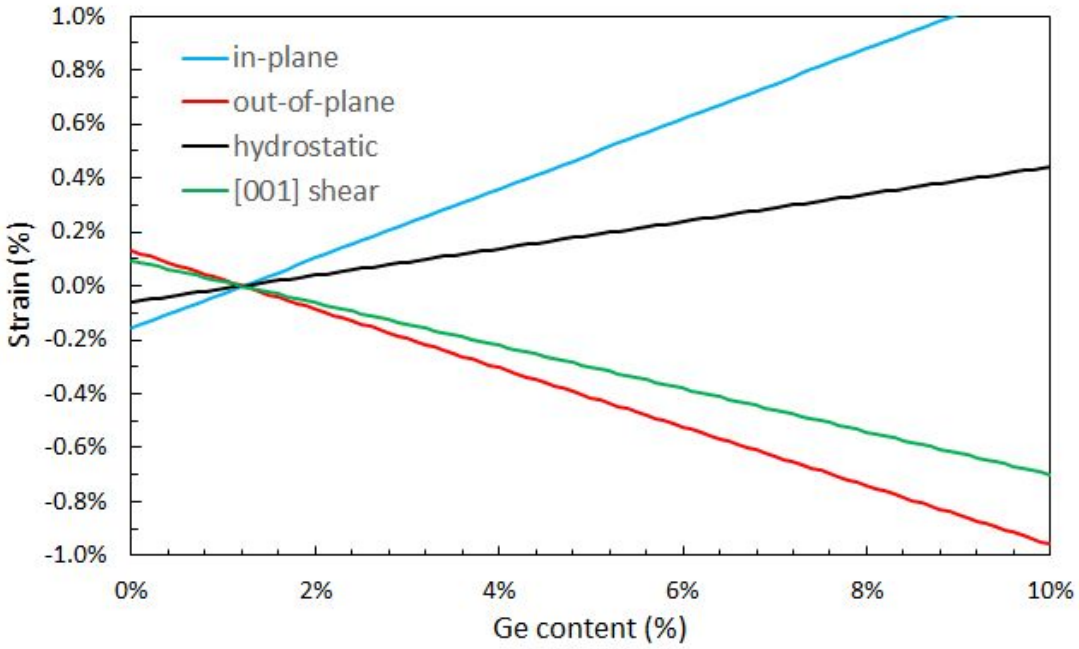

Figure 8.7: In-plane, out-of-plane, hydrostratic, and [001] pure shear strain as a function of Ge content x for $Sn_{1-x}Ge_x$ alloys grown pseudomorphically on InSb (001).

The cubic (bulk) unit cell deforms tetragonally and the perpendicular (out-of-plane) lattice constant of the epitaxial layer measured with symmetric (004) high-resolution x-ray diffraction becomes

$$a_\perp = (1 + \epsilon_\perp)\, a\,(x)\,, \tag{118}$$

where the out-of-plane strain (Cardona & Christensen 1987)

$$\epsilon_\perp = -2\frac{C_{12}}{C_{11}}\epsilon_\parallel = -\frac{2\nu}{1-\nu}\epsilon_\parallel \tag{119}$$

is calculated using the elastic constants C_{ij} (see Table 8.2.1) or the Poisson ratio ν=$C_{12}/(C_{11}+C_{12})$=0.30.

Figure 8.7 shows the in-plane, out-of-plane, hydrostatic, and [001] shear strain components for $Sn_{1-x}Ge_x$ alloys on InSb (001). We see clearly how the in-plane strain changes sign as a function of x. While the in-plane strain is compressive for pure α-Sn (x=0), it becomes tensile for x>1.2%. The in-plane and out-of-plane strain have opposite signs. The hydrostatic strain has the same sign as the in-plane strain, but is much smaller. The [001] shear strain has the same sign as the out-of-plane strain.

8.2.3 Response of valence bands to strain

The strain described above for $Sn_{1-x}Ge_x$ alloys on InSb (001) splits the Γ_8^+ bands and either creates a Dirac-crossing of the heavy and light "hole" bands (for x<1.2%) or opens a gap $2\delta_0$ (for x>1.2%), as shown in Fig. 8.1. The dispersion

of the strained bands can be described within Pikus-Bir (1959) theory (Hoffmann 1989) by

$$\begin{aligned} E_{\pm} &= Ak^2 \pm \left[B^2k^4 + C^2\left(k_x^2k_y^2 + k_x^2k_z^2 + k_y^2k_z^2\right) + \right. \\ &+ \left. B\delta_0\left(2k_z^2 - k_x^2 - k_y^2\right) + \delta_0^2\right]^{\frac{1}{2}}, \end{aligned} \tag{120}$$

where $\delta_0 = 3b\epsilon_S$ is half the strain splitting of the Γ_8^+ bands, b the deformation potential listed in Table 8.2.1, and ϵ_S the pure (traceless) shear component of the strain.

As an example, we show the Γ_8^+ bands for small wave vectors in Fig. 8.1. In the compressive in-plane case shown in Fig. 8.1(c) for x<1.2%, the heavy and light "hole" bands have the expected curvature (downward and upward, respectively) for wave vectors perpendicular to the [001] shear strain, but they curve in the opposite direction for wave vectors parallel to the [001] shear strain and cross at the so-called Dirac point. At 0 K, electronic states below the Dirac point are filled, while those above it are empty. In the tensile in-plane case shown in Fig. 8.1(d) for x>1.2%, the heavy and light "hole" bands are nearly parabolic and show the expected curvature (upward or downward) for wave vectors oriented parallel to the [001] shear strain axis. In the other directions, however, there is a significant non-parabolicity. The heavy hole band first curves upward and only turns to negative energies for larger wave vectors. This was first treated by Cardona (1967) and is described in more detail in Ref. 24. $Sn_{1-x}Ge_x$ alloys on InSb (x>1.2%) are

indirect semiconductors with a small band gap, because the VB maximum does not occur exactly at the Γ-point. Current MBE growth techniques can achieve Ge contents up to about 6% in pseudomorphic $Sn_{1-x}Ge_x$ alloys on InSb (001), which leads to a Γ_8^+ splitting of about 50 meV. See Ref. 24 (supplemental materials) for additional detail.

8.2.4 Response of $\bar{E}_0$ gap to strain

The $\bar{E}_0$ gap separates the Γ_7^- valence band from the Γ_8^+ state. The [001] shear portion of the strain splits this gap due to the splitting of the Γ_8^+ states given by Eq. (120). In addition, the hydrostatic portion of the strain changes the Γ_7^- energy by $3a\epsilon_H$, where a is the hydrostatic deformation potential for the $\bar{E}_0$ gap given in Table 8.2.1. a has a negative value of about -7 eV. For the compressive in-plane strain of α-Sn on InSb (001), ϵ_H is negative and therefore Γ_7^- moves up by about 12 meV, which decreases the $\bar{E}_0$ gap compared to unstrained α-Sn by the same amount. On the other hand, in $Sn_{1-x}Ge_x$ alloys with x>1.2%, the tensile in-plane strain causes a hydrostatic expansion (ϵ_H<0), which increases $\bar{E}_0$ (by 51 meV for x=6%) relative to a relaxed alloy with the same composition, see Fig. 8.5.

8.2.5 Response of E_1 and $E_1 + \Delta_1$ critical point energies to strain

The dependence of the E_1 and $E_1+\Delta_1$ critical points (see Fig. 8.1) on composition for unstrained (relaxed) $Sn_{1-x}Ge_x$ alloys was calculated using Eq. (95) with the

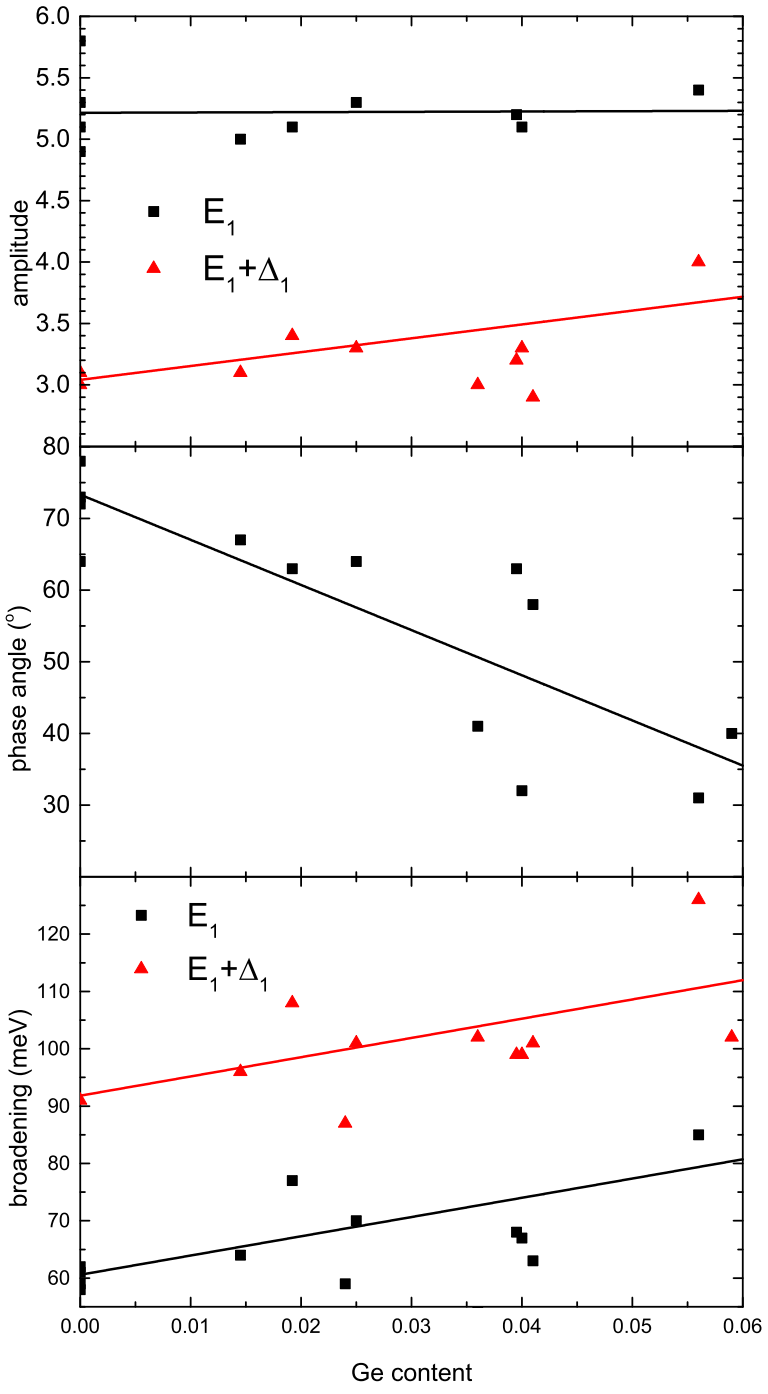

Figure 8.8: Amplitudes, broadenings, and phase angles for the E_1 and $E_1 + \Delta_1$ critical points versus Ge content determined from spectroscopic ellipsometry (symbols). The straight lines show the best linear fit.

parameters given in Table 8.2.1. The spin-orbit splitting Δ_1 of the VB at the L point is taken as the difference between the E_1 and $E_1 + \Delta_1$ energies with parameters in Table 8.2.1. Note the bowing for Δ_1, which is common for semiconductor alloys[22] (Logothetidis 1991). Under a biaxial in-plane stress, the energies are[14]

$$E_1^s = E_1^0 + \tfrac{1}{2}\Delta_1 + \Delta E_H - \sqrt{\tfrac{1}{4}\left(\Delta_1\right)^2 + \left(\Delta E_S\right)^2}, \tag{121}$$

$$\begin{aligned}\left(E_1 + \Delta_1\right)^s &= \left(E_1 + \Delta_1\right)^0 - \tfrac{1}{2}\Delta_1 + \Delta E_H + \\ &\quad + \sqrt{\tfrac{1}{4}\left(\Delta_1\right)^2 + \left(\Delta E_S\right)^2},\end{aligned} \tag{122}$$

where the superscripts s and 0 denote the band gaps of the strained and relaxed alloys, respectively. ΔE_H and ΔE_S are the energy shifts due to hydrostatic and [001] shear strain, respectively, calculated using

$$\Delta E_H = \sqrt{3} D_1^1 \epsilon_H \quad \text{and} \quad \Delta E_S = \sqrt{6} D_3^3 \epsilon_S, \tag{123}$$

where D_1^1=−5.4 eV and D_3^3=−3.8 eV are the hydrostatic and shear deformation potentials for $Ge_{1-y}Sn_y$ alloys taken from D'Costa (2014), which is significantly lower than for bulk Ge. The sign of D_3^3 affects the intensities of the two critical points and therefore we follow the sign convention of Pantelides & Zollner (2002).

We previously[24] determined the strained values E_1^s=1.280 eV and $\left(E_1 + \Delta_1\right)^s$=1.739 eV with ϵ_H=−0.06% and ϵ_S=0.10% from ellipsometry of pseudomorphic α-Sn on InSb (001). This yields the unstrained values E_1^0=1.275 eV and $\left(E_1 + \Delta_1\right)^0$=1.734 eV, as shown in Table 8.2.1. For such a small shear strain (for x=0) and the large

spin-orbit splitting Δ_1, the shear splitting under the square root of Eqs. (121-122) can be ignored and only the hydrostatic shift ΔE_H contributes. The shear contribution ΔE_S becomes measurable for larger x near 5%.

8.2.6 Amplitudes, broadenings, and phase angles for E_1 and $E_1 + \Delta_1$ critical points

The parameters used to described the E_1 and $E_1 + \Delta_1$ critical points, see Eq. (96), are the amplitude A, energy E, broadening Γ, and phase angle ϕ. It is customary to use the same phase angle for E_1 and $E_1 + \Delta_1$. The energies, broadenings, and phase angles are listed in Table 8.1. The energies are plotted in Fig. 8.4 and discussed in the main text. Figure 8.8 shows the amplitudes, broadenings, and phase angles as a function of Ge content. Compare Ref. 14 for a similar discussion of pseudomorphic Ge-rich $Ge_{1-x}Sn_x$ alloys on Ge.

Our broadenings are comparable to, or perhaps a bit smaller than those reported in Ref. 23, indicating the high quality of our epilayers. They increase with Ge content at a rate of 0.34 eV, as shown by the straight lines, due to alloy scattering. The phase angle decreases from 70° for pure α-Sn to 32° for $Ge_{0.94}Sn_{0.06}$ at a rate of 6.3° per atomic percent Ge. Increased alloy scattering in disordered alloys reduces the excitonic enhancement of the E_1 critical point and therefore ϕ decreases with increasing Ge content [14] (Logothetidis 1991) to values below 90°.

The amplitudes of E_1 and $E_1 + \Delta_1$ show interesting trends. While the E_1

amplitude is nearly constant at 5.2±0.2, the $E_1 + \Delta_1$ amplitude increases linearly at a rate of 0.11 per atomic percent Ge. According to $\vec{k}\cdot\vec{p}$ theory, the [001] pure shear strain changes the amplitudes of these critical points as a function of shear strain ϵ_S by (Pantelides and Zollner 2002)

$$\Delta A\left(\epsilon_S\right)/A_0 = \pm\sqrt{6}D_3^3\epsilon_S/\Delta_1, \tag{124}$$

where the + sign is for the $E_1+\Delta_1$ amplitude and the − sign for the E_1 amplitude. A_0 is the amplitude of the CPs in relaxed alloys. For x>1.2%, both the shear strain and the deformation potential D_3^3=−3.8 eV are negative and therefore the amplitude of E_1 should decrease and that of $E_1 + \Delta_1$ should increase with increasing Ge content (and thus increasing magnitude of the compressive [001] shear strain). The relative rate of change calculated from Eq. (124) is 0.02 per atomic percent Ge, which corresponds to a decrease of the E_1 amplitude at a rate of 0.1 and an increase of the $E_1 + \Delta_1$ amplitude at a rate of 0.06 (per atomic percent Ge). As shown in Fig. 8.8, we do not observe the expected decrease of the E_1 amplitude, but the observed increase of the $E_1 + \Delta_1$ amplitude is twice as large as predicted.

The absolute values of the amplitudes for relaxed alloys are given by[23, 24]

$$A_{E_1} = 44\frac{E_1 + \frac{1}{3}\Delta_1}{aE_1^2}, \tag{125}$$

$$A_{E_1+\Delta_1} = 44\frac{E_1 + \frac{2}{3}\Delta_1}{a\left(E_1+\Delta_1\right)^2}, \tag{126}$$

where a is the lattice constant of the alloy in Å and energies are in eV. For pure

α-tin we calculated amplitudes of 5.9 and 3.6 for E_1 and $E_1+\Delta_1$, respectively, see Ref. 24, in excellent agreement with our experiments, see Fig. 8.8. The agreement of our experiment with this theory for uncorrelated electron-hole pairs indicates that the excitonic contribution to the E_1 and $E_1+\Delta_1$ critical points is weak in α-Sn and smaller than in other materials like Si, GaAs, or GaSb.[24]

8.2.7 Epilayer characterization

Atomic force micrographs with 5×5 μm^2 scan range were taken for selected $Sn_{1-x}Ge_x$ epilayers on InSb (001). The rms roughness was usually on the order of 0.5 nm. No misfit dislocation networks due to stress relaxation were seen. Some layers showed β-tin defects. A typical AFM image for a layer with x=0.059 and 75 nm thickness is shown in Fig. 8.9. Since the roughness is very small (0.5 nm rms), it can be neglected in the analysis of ellipsometry data, where only the native oxide was considered.

8.2.8 Layer analysis using x-ray diffraction

To assess the strain within the films, we measured each $Sn_{1-x}Ge_x$ epilayer using a PANalytical Empyrean x-ray diffractometer configured with a monochromatic Cu Kα_1 line source (1.540598 Å) and triple-axis analyzer crystal. For the purpose of demonstration, a highly strained film with 5.5% Ge is analyzed below because it represents an extreme case. Lower compositions display nearly ideal

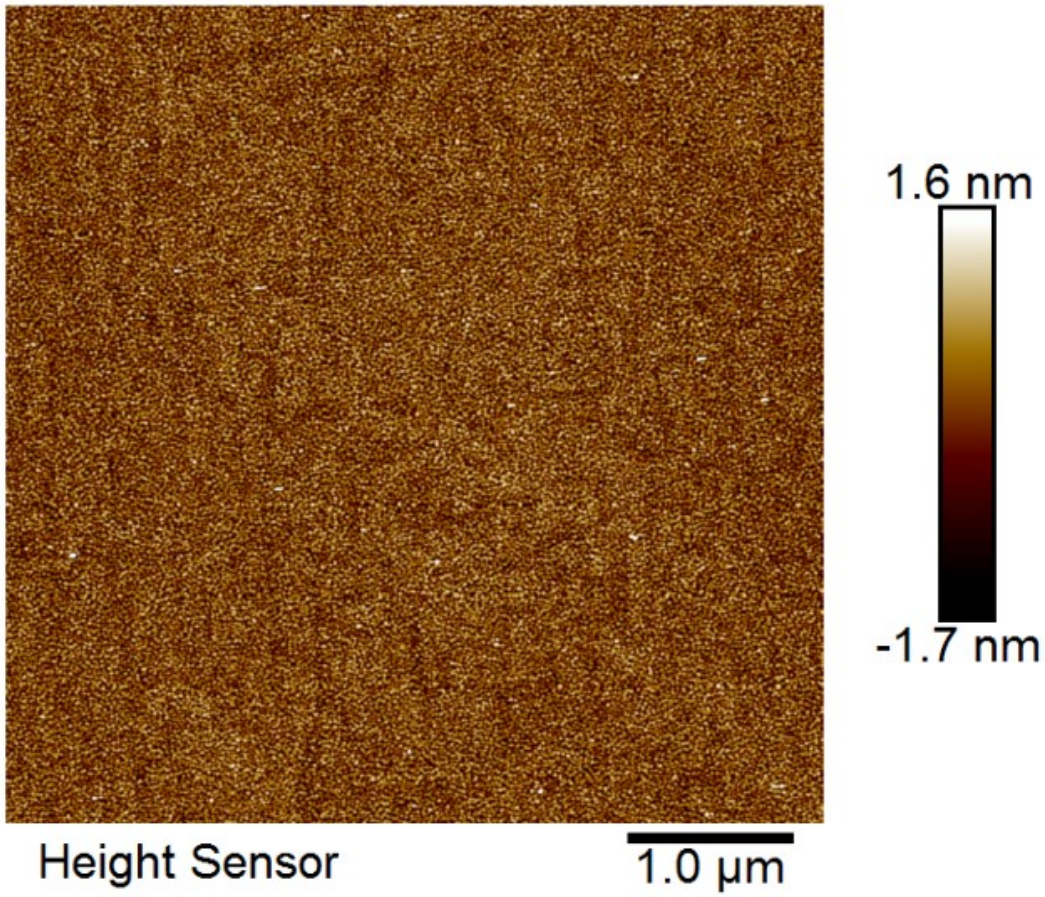

Figure 8.9: Atomic force micrograph (5×5 μm^2 scan range) of a $Sn_{1-x}Ge_x$ alloy on InSb (001) with x=0.059 and 75 nm thickness. The rms roughness is 0.5 nm.

characteristics.

A symmetric 2θ-ω scan was performed near the InSb (004) peak for each epilayer. The data were then modeled using full dynamical diffraction theory (PANalytical Epitaxy and Smoothfit software) to provide film composition and film thickness (for example, see Fig. 8.10). The software uses Vegard's Law (95) without bowing (b=0) to determine film composition, with parameters given in Table 8.2.1. See also Kiefer (2017). Though the model shown in Fig. 8.10 follows the measured peak positions well, the intensity profile fits relatively poorly compared to the other samples in the set with lower Ge compositions. The intensity mismatch may indicate potential relaxation or inhomogeneous composition as discussed below.

Additionally, rocking curves (ω-scans with fixed 2θ) centered on the (004) substrate and film peaks were measured to qualitatively determine film relaxation. (Films with epilayer peaks overlapping the substrate peak could not be measured separately.) Film-peak broadening greater than the substrate-peak breadth often indicates a dislocation density beyond that inherited from the substrate. A typical FWHM for an InSb (004) substrate peak is less than 0.004° (∼14"), near the limit of instrument resolution (12"). Each film has a peak FWHM the same or nearly the same as the substrate peak, implying a high degree of crystallinity; however, diffuse broadening appears around peaks of $Sn_{1-x}Ge_x$ epilayers with Ge compositions x>5% (Fig. 8.11), from which we infer the onset of film relaxation

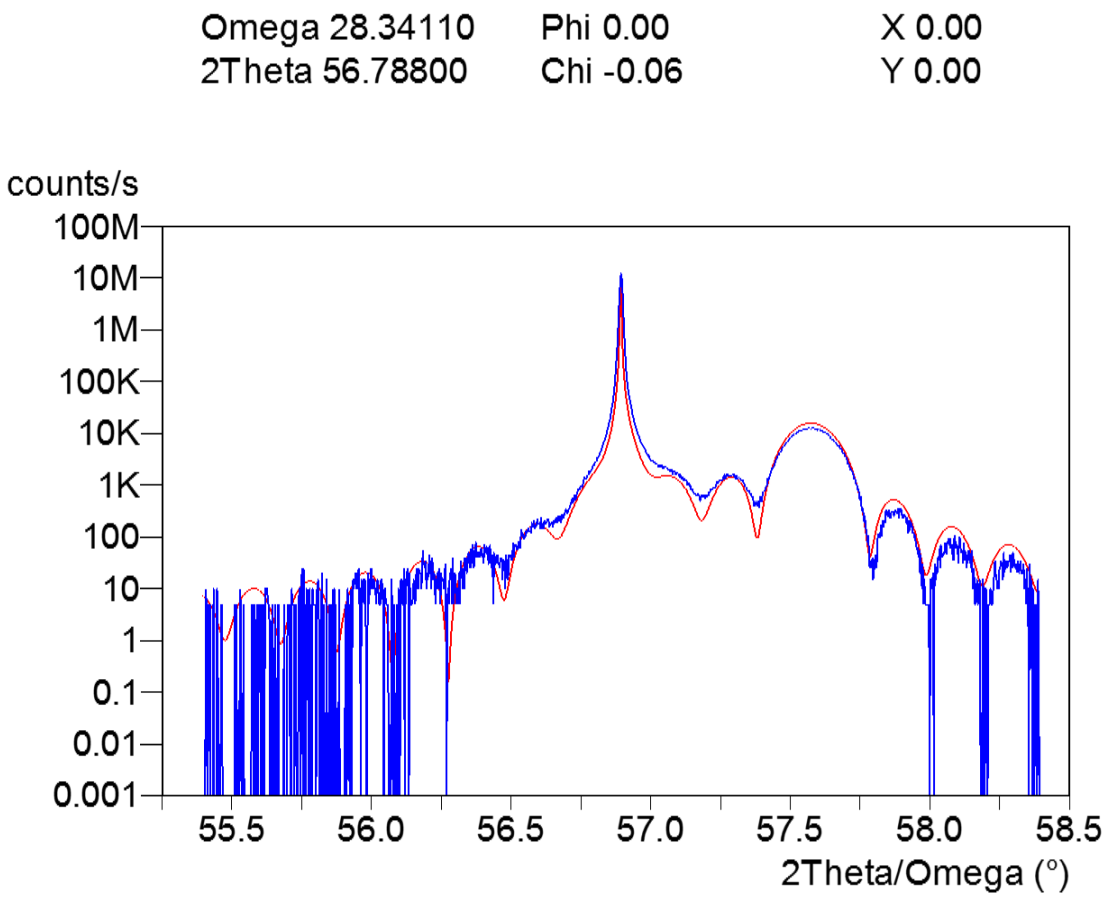

Figure 8.10: (Color online) A 2θ-ω scan of a $Sn_{0.945}Ge_{0.055}$ film (50 nm thickness) on an InSb (001) substrate (blue) at the (004) Bragg reflection with an overlay of a single-layer model simulation (red). The *Pendellösung* "fringe"peaks correspond to the film thickness.

by dislocation formation and glide.

Under the assumption of fully-coherent pseudomorphic growth, the film's strain state can be adequately assessed using only the symmetric (004) 2θ-ω scan and knowledge of the film's and substrate's "bulk" lattice constants and elastic properties. Any strain relaxation, however, shifts the film peak with respect to the substrate peak, causing misinterpretation of the alloy composition. To avoid this ambiguity, we measure the in-plane and out-of-plane lattice constants using asymmetric Bragg reflections, *i.e.* the atomic planes are tilted away from the substrate normal. A conventional approach is to record the diffracted intensity around these asymmetric points in a reciprocal space map (RSM).

An RSM is a section of the diffraction plane corresponding physically to the plane containing the source beam and detector acceptance angle in real space. The diffractometer is aligned so the diffraction plane passes through the reflections of interest. Several linear scans, either 2θ vs. ω or 2θ-ω vs. ω, comprise an intensity map $I(\omega,2\theta)$ that is represented as a reciprocal space map $I(q_{\|},\mathrm{q}_{\perp})$ using the following transformation (Fewster, 2003):

$$q_{\|} = [\cos(\omega) - \cos(2\theta - \omega)]\,/\lambda, \tag{127}$$

$$q_{\perp} = [\sin(\omega) + \sin(2\theta - \omega)]\,/\lambda. \tag{128}$$

The measured angular relations $I(\omega,2\theta)$ are thus transformed into a Euclidean vector space $I(q_{\|},\mathrm{q}_{\perp})$, allowing for convenient data analysis. The reciprocal lattice

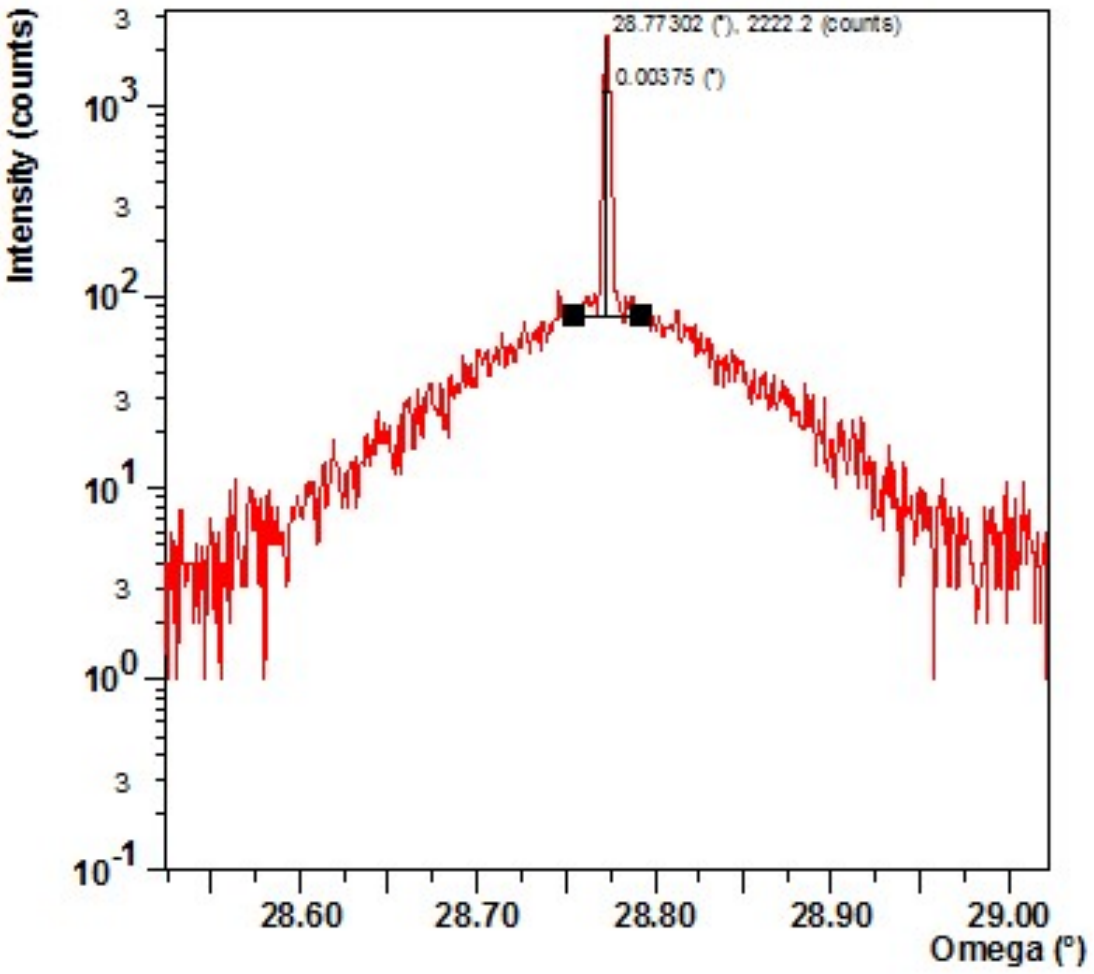

Figure 8.11: (Color online) Rocking curve (ω-scan) of the epilayer peak from a $Sn_{0.945}Ge_{0.055}$ film (50 nm) on a InSb (001) substrate plotted on a logarithmic scale. Though the FWHM of the film peak is very narrow, broad diffuse-scattering is evident near the peak's base.

of a crystal structure with orthorhombic symmetry or higher is particularly easy to analyze. The normal vectors of the atomic planes in real space correspond to the reciprocal space vectors such that the angular measurements between planes are preserved under transformation. For a crystal oriented with the (001) surface normal to the diffraction plane and the [110] in-plane direction within the diffraction plane, $\vec{q}_{\perp} = \vec{q}_{001}$ and $\vec{q}_{\parallel} = \vec{q}_{110}$. Using Bragg's law, the length of a reciprocal space vector is related to the distance d between planes: $|\vec{q}| = 1/d = 2\sin\theta/\lambda$. Linear distances in real space can then be read directly from the RSM. The reciprocal lattice vectors may be cast in absolute units ($1/\text{Å}$) or in dimensionless units of $\lambda/2d$. We choose the latter in the following analysis.

The (004) RSMs were compiled using 2θ-ω scans with step sizes of 0.01° for 2θ and incrementing ω by 0.01° after each scan; the (335) RSMs by using 2θ scans with step sizes of 0.02° and increments of ω by 0.02° after each scan. For purposes of display, a single (335) RSM with higher resolution (0.01° step sizes) and longer counting time per step was taken and is shown in Fig. 8.12. Peak positions were determined using the software's built-in peak-finding algorithm. The measured peak positions of reciprocal lattice points (RLPs) of the substrate and α-$Sn_{0.945}Ge_{0.055}$ film (50 nm) in the orthogonal [110] (ϕ=0°) and [1$\bar{1}$0] (ϕ=90°) zones are shown in Table 8.3. Measurement in two orthogonal zones allows substrate miscut and film lattice-tilt to be assessed. As the InSb (001) substrates are nominally cut on-axis, the analysis below confirms that the lattice tilt with re-

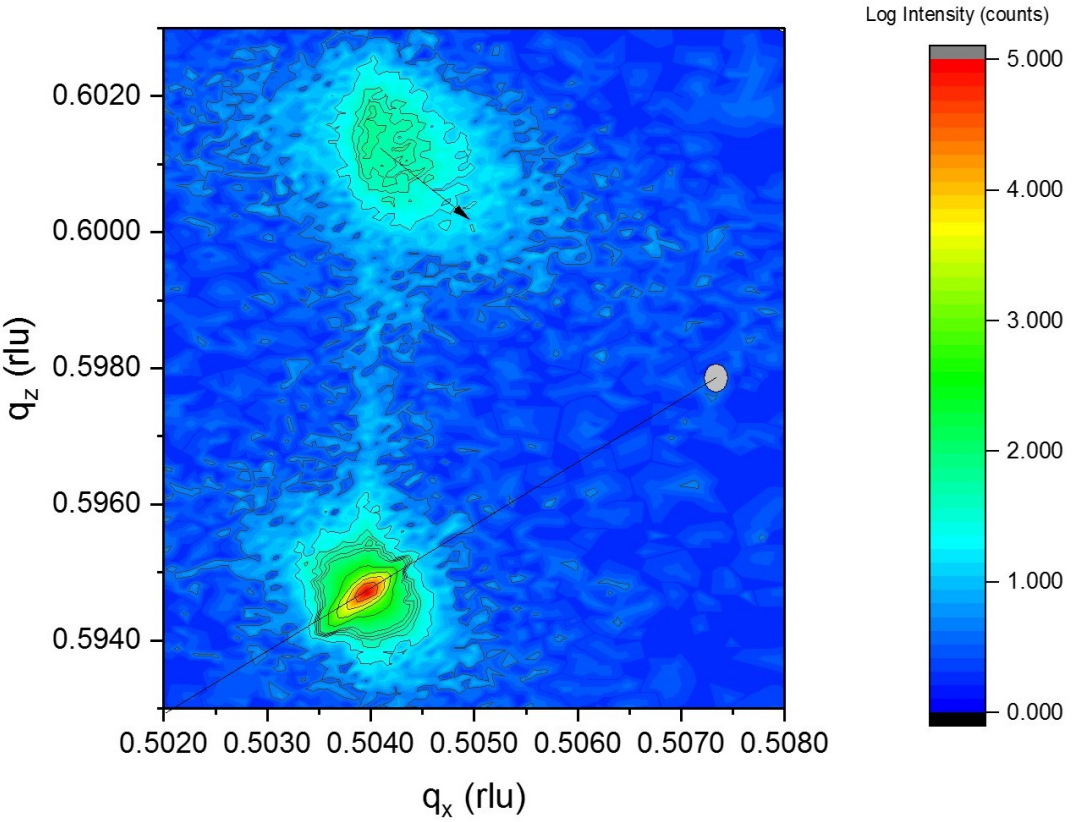

Figure 8.12: (Color online) A (335) reciprocal space map of a $Sn_{0.945}Ge_{0.055}$ film (50nm) on a InSb (001) substrate. The q_x and q_z axes are parallel to the [110] and [001] directions, respectively, plotted in dimensionless reciprocal lattice units of $\lambda/2d$ and $\log_{10}$ intensity. The dot represents the theoretical location of a fully-relaxed film and the arrow the direction of relaxation.

Table 8.3: Measured peak positions of reciproal lattice points (hkl) taken by x-ray diffraction of a $Sn_{0.945}Ge_{0.055}$ film (50 nm) on a InSb (001) substrate. ϕ = azimuthal angle; ω = incident angle; 2θ = detector angle; q_x = abscissa; q_z = ordinate; $|q_{hkl}|$ = modulus of reciprocal lattice vector; d_{hkl} = interplanar distance; and, a_{hkl} = lattice constant derived from d_{hkl}. rlu = reciprocal lattice units.

	ϕ(°)	h	k	l	Geometry[a]	ω(°)	2θ(°)	q_x(rlu)	q_z(rlu)	$\|q_{hkl}\|$(rlu)	d_{hkl}(Å)	a_{hkl}(Å)
InSb	0.00	0	0	4	sym	28.4735	56.790	-0.00065	0.47555	0.47555	1.6198	6.4793
	0.00	3	3	5	GI	10.9655	102.411	0.50348	0.59495	0.77940	0.9883	6.4809
	0.27	$\overline{3}$	$\overline{3}$	5	GE	91.6100	102.420	-0.50507	0.59367	0.77945	0.9883	6.4805
	90.00	0	0	4	sym	28.5687	56.790	-0.00144	0.47555	0.47555	1.6198	6.4793
	90.13	3	$\overline{3}$	5	GI	91.7100	102.440	-0.50608	0.59296	0.77956	0.9881	6.4796
	90.13	$\overline{3}$	3	5	GE	11.0800	102.431	0.50247	0.59595	0.77951	0.9882	6.4800
	-0.43	3	3	5	GI	10.9355	102.431	0.50397	0.59468	0.77951	0.9882	6.4800
α-SnGe	0.00	0	0	4	sym	28.8085	57.460	-0.00066	0.48068	0.48068	1.6025	6.4100
	0.00	3	3	5	GI	11.7766	103.391	0.50368	0.60175	0.78473	0.9816	6.4369
	0.27	$\overline{3}$	$\overline{3}$	5	GE	91.7700	103.340	-0.50528	0.60004	0.78445	0.9820	6.4391
	90.00	0	0	4	sym	28.8987	57.450	-0.00146	0.48060	0.48061	1.6028	6.4111
	90.13	3	$\overline{3}$	5	GI	91.8700	103.420	-0.50619	0.59985	0.78488	0.9814	6.4356
	90.13	$\overline{3}$	3	5	GE	11.8300	103.351	0.50265	0.60233	0.78451	0.9819	6.4386
	-0.43	3	3	5	GI	11.4055	103.351	0.50396	0.60123	0.78451	0.9819	6.4386

[a] Incident beam and diffracted beam configuration: sym = symmetrical; GI = grazing incidence; and, GE = grazing exit

spect to the goniometer axis is <0.2° and is negligible; therefore, we can disregard possible asymmetric strain effects.

As Fig. 8.12 demonstrates, the in-plane lattice constants of the substrate and film are nominally the same. The film's peak width (Δq_x) is 2 to 3 times greater than the substrate peak, and the presence of diffuse scattering in the vicinity of the film peak indicates the onset of plastic relaxation and/or compositional variation. From this cursory analysis, we conclude the film is coherent to the substrate and elastically strained.

More rigorously, we derive the lattice constants from the RLPs. The analysis can be done by various methods. We choose the straightforward method of deriving the lattice constants of the unit cell from the measured RLPs. Each RLP,

$\vec{G}_{(hkl)}$, represents a linear combination of basis vectors $\{\vec{q}_x, \vec{q}_y, \vec{q}_z\}$ in the laboratory reference frame. Measuring at least two non-coplanar RLPs along two different azimuths (ϕ) provides enough information to determine a complete set of basis vectors; additional points allow a least-squares determination of the basis vectors, as in our case.

Let $\vec{G}_m = h_m\vec{q}_x + k_m\vec{q}_y + l_m\vec{q}_z$ and $\vec{q}_n = q_{n1}\hat{e}_1 + q_{n2}\hat{e}_2 + q_{n3}\hat{e}_3$, where $n \in \{x, y, z\}$ and the orthonormal vectors $\{\hat{e_1}, \hat{e_2}, \hat{e_3}\}$ correspond to the laboratory reference frame. In matrix notation,

$$\begin{pmatrix} G_{11} & G_{12} & G_{13} \\ G_{21} & G_{22} & G_{23} \\ G_{31} & G_{32} & G_{33} \\ & \vdots & \\ G_{m1} & G_{m2} & G_{m3} \end{pmatrix} = \begin{pmatrix} h_1 & k_1 & l_1 \\ h_2 & k_2 & l_2 \\ h_3 & k_3 & l_3 \\ & \vdots & \\ h_m & k_m & l_m \end{pmatrix} \begin{pmatrix} q_{x1} & q_{x2} & q_{x3} \\ q_{y1} & q_{y2} & q_{y3} \\ q_{z1} & q_{z2} & q_{z3} \end{pmatrix}, \tag{129}$$

where $m \geq 3$. If the equation is over-determined, it can be solved in the usual least-squares manner, *e.g.*,

$$[Q] = \{[H]^T[H]\}^{-1}[H]^T[G]. \tag{130}$$

The resulting q_{pn} are the coordinates of the basis vectors within the laboratory reference frame. Since the {335} RLPs lie within the {110} zones, we only directly derive the base diagonals of the unit cell. The [100] and [010] basis vectors are a linear combination of these: $|\vec{q}_{100}| = |\vec{q}_{010}| = |\vec{q}_{110} + \vec{q}_{1\bar{1}0}|/2$. The analytical results are provided in Table 8.4.

Recall that the RLPs are three-dimensional and the diffraction plane defined by the diffractometer's source and detector may intersect the RLPs obliquely.

Table 8.4: Basis vectors derived from reciprocal lattice points (hkl) represented in the laboratory reference frame. $q_{\parallel}$ corresponds to the appropriate in-plane direction; $q_{\perp}$ corresponds to the out-of-plane direction; d_{hkl} is the interplanar distance in the $[hkl]$ direction.

	hkl	$q_{\parallel}$ (rlu)	$q_{\perp}$ (rlu)	d_{hkl} (Å)
InSb	110	0.16809	0.00021	4.5826
	001	-0.00016	0.11887	6.4803
	$1\bar{1}0$	0.16811	0.00051	4.5822
	001	-0.00037	0.11888	6.4794
	100,010	0.11886	0.00036	6.4804
α-SnGe	110	0.16813	0.00028	4.5817
	001	-0.00016	0.12019	6.4090
	$1\bar{1}0$	0.16811	0.00041	4.5822
	001	-0.00036	0.12021	6.4077
	100,010	0.11888	0.00035	6.4798

Any misalignment of the two low-precision axes, azimuth ϕ and tilt χ, results in missing the true center of the RLP. Additionally, the x-ray line source has significant axial divergence which extends the RLPs further outward from the diffraction plane. Since we do not calibrate the ϕ and χ axes, we block the data into two sets corresponding to $\phi \approx 0^{\circ}$ and $\phi \approx 90^{\circ}$ and analyze them separately. Henceforth we assume the two basis vectors $\vec{q}_{110}$ and $\vec{q}_{1\bar{1}0}$ are orthogonal.

From this analysis we find that the measured InSb lattice constant is 6.480 Å, which compares well with the expected value of 6.4793 Å (Straumanis 1965). The α-SnGe film's in-plane lattice constant of 6.480 Å matches the substrate's lattice constant, confirming coherency to the substrate lattice and unrelaxed, elastic strain. The lattice tilt ψ of the substrate and film with respect to the laboratory reference frame are the same and negligible. Tilt can be determined directly from the $\vec{q}_{001}$ vectors, with ψ=0.08° and 0.18° for azimuths ϕ=0° and ϕ=90°, respectively. The $\{\vec{q}_{001}\}$ and $\{\vec{q}_{110}\}$ are orthogonal with a deviation of $< 0.004°$ for the substrate and $< 0.03°$ for the film, consistent with the assumed tetragonal geometry.

The relaxed cubic lattice constant $a\,(x)$ of the tetragonally distorted $Sn_{1-x}Ge_x$ alloy is then calculated from the measured out-of-plane and in-plane lattice constants $a_\perp$ and $a_\parallel$, respectively, using elasticity theory (Freund & Suresh 2004). The in-plane strain $\epsilon_\parallel$ and out-of-plane strain $\epsilon_\perp$ are related by Eq. (119). Substituting the definitions of strain (117,118) into Eq. (119) and solving for $a\,(x)$ yields

$$a\,(x) = \frac{a_\perp + (2C_{12}/C_{11})a_\parallel}{1 + 2C_{12}/C_{11}}. \tag{131}$$

We assume that ratios of the elastic constants of the α-$Sn_{1-x}Ge_x$ film follows Vegard's Law, see Table 8.2.1. The ratios of $2C_{12}/C_{11}$ are 0.85 and 0.75 for α-Sn and Ge, respectively, giving a ratio of 0.84 for the assumed composition, x=0.055. Using this value along with $a_\perp$ and $a_\parallel$ derived from XRD measurements gives a

lattice constant of 6.442 Å for the α-$Sn_{0.945}Ge_{0.055}$ pseudomorphic film, consistent with the lattice constant of 6.443Å determined directly from Vegard's rule applied to lattice constants for x=0.055.

In summary, the analysis of the XRD data shows that the α-$Sn_{0.945}Ge_{0.055}$ film grown on the InSb (001) substrate is highly crystalline and coherent to the substrate lattice. This epilayer (x=0.055) shows signs of the onset of plastic relaxation but is otherwise elastically strained.

9 Conclusion

In conclusion, we explored different design spaces that have potential in satisfying the need for high performance, mid-wave infrared photodetectors. The design space of the In(Ga)As/InAsSb superlattices was explored and the fundamental benefits of adding Ga to the conventional InAs/InAsSb mid-wave superlattice were determined and discussed, suggesting a path to pursue for high performance mid-wave sensing. A recombination rate analysis was performed to further quantify the effect of adding Ga to the superlattice in regards to the minority carrier lifetime. Then, a radiation tolerance experiment was performed on a *pBpn* superlattice device to gauge its long-term performance in a radiation-harsh environment. A bulk solution to a potential III-V mid-wave infrared sensing device is proposed through alloying Bi with GaInAsSb. The improvement in the minority carrier lifetime with the incorporation of Bi is attributed to the surfactant behavior of introducing Bi during growth.

Then, the optical constants of group IV GeSn alloys were determined as a function of Sn contents up to 27% Sn. Absorption beyond 6 μm was observed, showing evidence that the index of refraction and absorption coefficient can be tuned by alloying Ge with Sn. Then, the optical constants of the endpoint constituent, α-Sn(Ge) was investigated and strong absorption was observed at $\sim$0.41 eV as a function of temperature, strain state and dilute Ge content.

10 Future work

10.1 III-V superlattice front

Before a viable mid-wave infrared III-V superlattice is realized, various detector designs and structures should be explored for mid-wave sensing. More specifically, designing a detector that minimizes the tunneling dark-current would allow for further improvement to the signal-to-noise ratio with decreasing operating temperature. This would include tuning the doping profiles of *pBpn* detector structures to achieve an acceptable minority carrier lifetime while decreasing the tunneling dark-current.

10.2 Quinary Bi front

A single bulk quinary was grown and reported to have a high minority carrier lifetime in comparison to a quaternary GaInAsSb grown at 400 °C. Growth conditions such as the V/III flux ratios and Ga content need to be explored to maximize the amount of Bi incorporation, while also improving the minority carrier lifetime. Optical properties of GaInAsSbBi need to be explored to further probe the effects of Bi mole fraction in the quinary, one example is exploring the spin-orbit splitting. This will require spectroscopic ellipsometry measurements ranging from the mid-infrared to the vacuum ultraviolet to probe the interband transitions and fundamental band structure of the quinary material. Then, with

an acceptable minority carrier lifetime, device *nBn* structures will be grown to examine the mobility of the quinary and its radiation hardness.

10.3 Group IV front

Before process evaluation devices are processed and fabricated on group IV semiconductor alloys, the minority carrier lifetime needs to be measured on the high Sn content GeSn alloys before resources are used to fabricate a device. A relation between growth conditions and minority carrier lifetime needs to be established to determine fundamental trends between device design and detector performance. Furthermore, device structures such as device *nBn*s need to be explored to maximize detector performance while mitigating surface shunt currents. For the endpoint constituent, α-Sn, the strong absorption and lineshape of the $\bar{E}_0$ peak requires more investigation. This is due to the fact that there is degeneracy at the Γ-point of the Brillouin zone for α-Sn leading to the breakdown of assumptions such as parabolic bands and Boltzamnn statistics of electrons. The peak behavior needs to be investigated as a function of doping in α-Sn, and **k**.**p** calculations need to be performed to consider band structure nonparabolicity. Augmenting the doping study with **k**.**p** theory calculations and Fermi-Dirac statistics would allow us to accurately model the $\bar{E}_0$ peak. The results of this study would be applicable to other materials with nontrival bandstructures.

A.1 Introduction

In many data analysis scenarios, quantifying and extracting physical parameters from from experimental measurements would require fitting a model with adjustable parameters. These parameters are iteratively modified through a linear or nonlinear least squares computer algorithm in order to arrive at a global minimum of a goodness-of-fit metric vs parameter space. A review on nonlinear least squares and error analysis in model parameters will be explored and applied. General background and a more in-depth examination on least-squares fitting can be found in chapters 6 - 8 of Bevington's *Data Reduction and Error Analysis for the Physical Sciences*.

A.2 Goodness-of-fit metric

A method of quantifying the goodness-of-fit of a nonlinear model with adjustable parameters $f(\mathbf{a}, x_i)$ to measured data $y(x_i)$ is through examining the chi-square metric in Equation (A1),[53]

$$\chi^2 = \sum_{i=1}^{N} \left[\frac{y_i - f(\mathbf{a}, x_i)}{\sigma_i} \right]^2, \tag{A1}$$

where $\mathbf{a}$ is the vector of adjustable parameters, x_i is the independent variable, and σ_i is the error or uncertainty on the measured data point. The uncertainty of a data point is related to the weighting w, where $w_i = 1/\sigma_i^2$. So a data point

with a large uncertainty will have a small influence to the chi-square metric (small weighting), while a data point with small uncertainty will have a large influence on the chi-square (large weighting).

A.3 Parameter space analysis

Suppose that there exists a set of parameter coefficients $\mathbf{a}_{min}$ such that the chi-square metric is a global minimum in a space of possible sets of model parameters $\mathbf{a}$. For the case of nonlinear least squares, one would iteratively arrive at a global minimum.[53] A problem that could arise in nonlinear fitting is that there may exist local minima in parameter space which may cause a range of initial guesses that drive the solution to a local minimum. As a result, an incorrect set of parameters may be erroneously reported as the best-fit parameters. One method around this scenario would be to fit the model function with multiple sets of initial guesses, which was applied in chapter 3 of this dissertation. There, fitting was performed on 100 initial guesses and the result with the lowest root-mean-square error was reported.

Figure A1 further investigates the deviation of the chi-square if two model parameters are kept at fixed values while allowing the other model parameters to vary. Figure A1(a) is a contour showing the deviation of the chi-square from the reported global minimum as the doping density and defect level deviate away from $\mathbf{a}_{min}$ while allowing the defect-concentration product and the Bloch overlap

integral to vary to minimize χ^2.[53] The horizontal and vertical lines denote confidence intervals that deviate one and two σ away from the Chi-Square minimum.

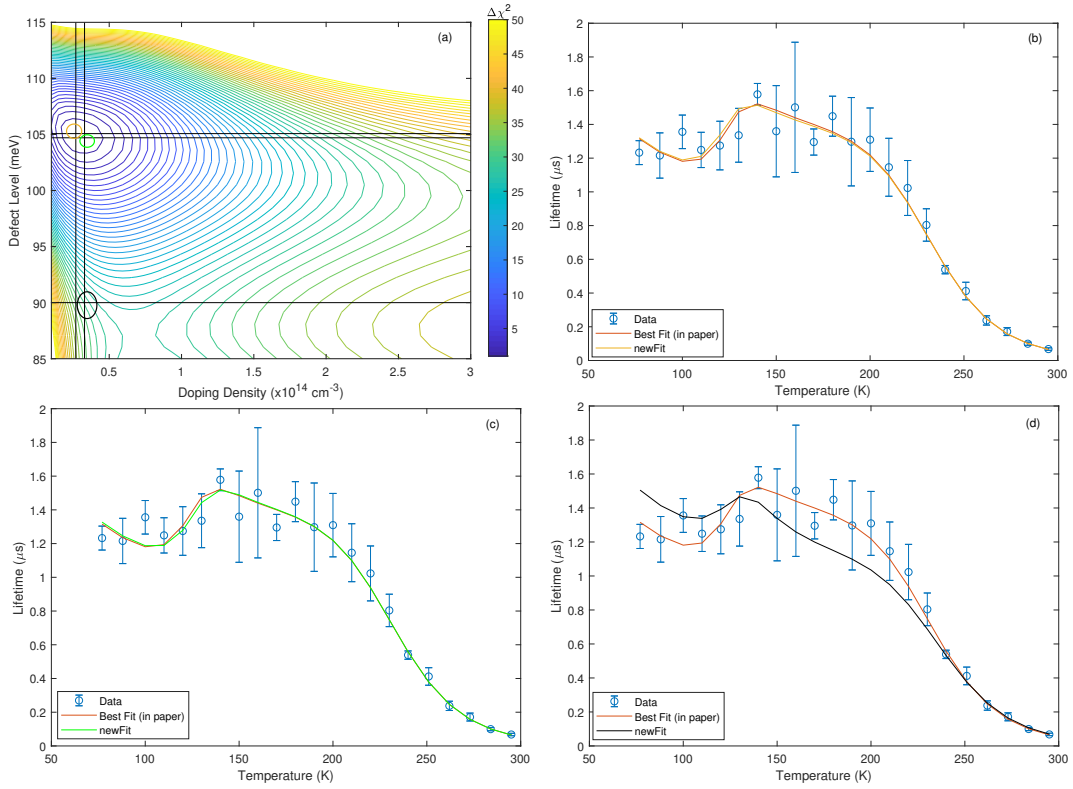

Figure A1: Chi-square analysis of the recombination rate model parameters on Sample B. Subplot (a) is a contour plot of the difference of chi-squares with the best-fit parameters reported in chapter 3. The doping densities and defect levels were kept at fixed values denoted by the horizontal and vertical axes, while the defect concentration-cross-section product and the Bloch overlap parameter were allowed to vary. Subplot (b) is the resulting model fit from fixing the doping density and defect level 1σ away from the global minimum and corresponds to the yellow ellipse at $\sim$105 meV. The data points, and orange lines in subplots (b) (c) and (d) are the temperature-dependent minority carrier lifetimes and best fit model as reported in chapter 3. The Green line in Subplot (c) corresponds to fixing the doping density and defect level 2σ away from the best-fit values. The black line in Subplot (d) corresponds to fixing the doping density 2σ away from the best fit and fixing the defect level at 90 meV below the conduction band.

REFERENCES

[1] S. Groves and W. Paul, Phys. Rev. Lett **11**, 194 (1963).

[2] B. J. Roman and A. W. Ewald, Phys. Rev. B **5**, 3914 (1972).

[3] D. Z. Ting, A. Soibel, A. Khoshakhlagh, S. B. Rafol, S. A. Keo, L. Höglun, A. M. Fisher, E. M. Luong, and S. D. Gunapala, Appl. Phys. Lett. **113**, 021101 (2018).

[4] D. Popa and F. Udrea, Sensors **19**, 2076 (2019).

[5] A. B. Seddon, Phys. Status Solidi B. **250**, 1020 (2013).

[6] R. F. C. Farrow, *Molecular Beam Epitaxy: Applications to Key Materials* (Noyes Publications, Park Ridge, 1995).

[7] H. Li, S. Liu, O. O. Cellek, D. Ding, X.-M. Shen, E. H. Steenbergen, J. Fan, Z. Lin, Z.-Y. He, Q. Zhang, P. T. Webster, S. R. Johnson, L. Ouyang, D. J. Smith, and Y.-H. Zhang, J. Cryst. Growth **378**, 145 (2013).

[8] W. Braun, *Applied RHEED: Reflection High-Energy Electron Diffraction During Crystal Growth* (Springer, Berlin, 1999).

[9] P. T. Webster, A. J. Shalindar, N. A. Riordan, C. Gogineni, H. Liang, A. R. Sharma, and S. R. Johnson, J. Appl. Phys. **119**, 225701 (2016).

[10] P. Petluru, P. C. Grant, A. J. Muhowski, I. M. Obermeier, M. S. Milosavljevic, S. R. Johnson, D. Wasserman, E. H. Steenbergen, and P. T. Webster, Appl. Phys. Lett **117**, 061103 (2020).

[11] V. B.-Yekta, T. Tiedje, and M. M.-Shirazi, Semicond. Sci. Technol. **30**, 094007 (2015).

[12] P. T. Webster, N. A. Riordan, C. Gogineni, S. Liu, J. Lu, X.-H. Zhao, D. J. Smith, Y.-H. Zhang, and S. R. Johnson, J. Vac. Sci. Technol. B **32**, 02C120 (2014).

[13] S. T. Schaefer, R. R. Kosireddy, P. T. Webster, and S. R. Johnson, J. Appl. Phys. **126**, 083101 (2019).

[14] N. S. Fernando, R. A. Carrasco, R. Hickey, J. Hart, R. Hazbun, S. Schoeche, J. N. Hilfiker, J. Kolodzey, and S. Zollner, J. Vac. Sci. Technol. B **36**, 021202 (2018).

[15] M. Fox, *Optical Properties of Solids* (Oxford University Press, New York, 2010).

[16] J. D. Jackson, *Classical Electrodynamics* (John Wiley & Sons, Massachusetts, 1999).

[17] H. G. Tompkins and E. A. Irene, *Handbook of Ellispometry* (Springer, Heidelberg, 2005).

[18] C. Emminger, F. Abadizaman, N. S. Samarasingha, T. E. Tiwald, and S. Zollner, J. Vac. Sci. Technol. **38**, 012202 (2020).

[19] J. A. W. Co., *Mark II Features* (Accessed 04-18-2021).

[20] *Guide to using WVASE, Spectroscopic ellipsometry data acquisition and analysis software*, J. A. Woolam Co., Lincoln, NE 68508 (2008).

[21] P. Yu. and M. Cardona, *Fundamentals of Semiconductors* (Springer, Heidelberg, 2010).

[22] V. R. D'Costa, C. S. Cook, A. G. Birdwell, C. L. Littler, M. Canonico, S. Zollner, J. Kouvetakis, and J. Menéndez, Phys. Rev. B. **73**, 125207 (2006).

[23] L. Viña, H. Höchst, and M. Cardona, Phys. Rev. B. **31**, 958 (1985).

[24] R. A. Carrasco, C. M. Zamarripa, S. Zollner, J. Menéndez, S. A. Chastang, J. Duan, G. J. Grzybowski, B. B. Claflin, and A. M. Kiefer, Appl. Phys. Lett. **113**, 232104 (2018).

[25] F. V. de Wiele, in *NATO Advanced Study Institute on Solid State Imaging*, edited by P. G. Jespers, F. van de Wiele, and M. H. White (Belgium, 1975) p. 47.

[26] J. B. Wang, S. R. Johnson, D. Ding, S.-Q. Yu, and Y.-H. Zhang, J. Appl. Phys. **100**, 043502 (2006).

[27] S. R. Johnson, D. Ding, J.-B. Wang, S.-Q. Yu, and Y.-H. Zhang, J. Vac. Sci. Technol. B. **25**, 1077 (2007).

[28] D. K. Schroder, IEEE Trans. Electron Devices **29**, 1336 (1982).

[29] W. Shockley and W. T. Read, Phys. Rev. **87**, 835 (1952).

[30] B. V. Olson, E. A. Shaner, J. K. Kim, J. F. Klem, S. D. Hawkins, and M. E. Flatté, Appl. Phys. Lett. **103**, 052106 (2013).

[31] W. V. Roosbroeck and W. Shockley, Phys. Rev. **94**, 1558 (1954).

[32] S. Zollner, P. P. Paradis, F. Abadizaman, and N. S. Samarasingha, J. Vac. Sci. Technol. B **37**, 012904 (2019).

[33] S. E. Schacham and E. Finkam, J. Appl. Phys. **57**, 2001 (1985).

[34] M. A. Kinch, M. J. Brau, and A. Simmons, J. Appl. Phys. **44**, 1649 (1973).

[35] V. C. Lopes, A. J. Syllaios, and M. C. Chen, Semicond. Sci. Technol. **8**, 824 (1993).

[36] I. Vurgaftman, J. R. Meyer, and L. R. Ram-Mohan, J. Appl. Phys. **89**, 5815 (2001).

[37] J. S. Blakemore, *Semiconductor Statistics* (Pergamon Press, London, 1962).

[38] A. R. Beattie and P. T. Landsberg, Proc. R. Soc. London **249**, 16 (1959).

[39] Y.-H. Zhang, Appl. Phys. Lett. **66**, 118 (1995).

[40] P. T. Webster, N. A. Riordan, S. Liu, E. H. Steenbergen, R. A. Synowick, Y.-H. Zhang, and S. R. Johnson, J. Appl. Phys. **118**, 245706 (2015).

[41] E. H. Steenbergen, B. C. Connelly, G. D. Metcalfe, H. Shen, M. Wraback, D. Lubyshev, Y. Qiu, J. M. Fastenau, A. W. K. Liu, S. Elhamri, O. O. Cellek, and Y.-H. Zhang, Appl. Phys. Lett. **99**, 251110 (2011).

[42] L. Höglund, D. Z. Ting, A. Soibel, A. Fisher, A. Khoshakhlagh, C. J. Hill, S. Keo, and S. D. Gunapala, Appl. Phys. Lett. **105**, 193510 (2014).

[43] Y. Aytac, B. V. Olson, J. K. Kim, E. A. Shaner, S. D. Hawkins, J. F. Klem, M. E. Flatté, and T. F. Boggess, Phys. Rev. Appl. **5**, 054016 (2016).

[44] E. A. Kadlec, B. V. Olson, M. D. Goldflam, J. K. Klem, S. D. Hawkins, W. T. Coon, M. A. Cavaliere, A. Tauke-Pedretti, T. R. Fortune, C. T. Harris, and E. A. Shaner, Appl. Phys. Lett. **109**, 261105 (2016).

[45] P. T. Webster, N. A. Riordan, S. Liu, E. H. Steenbergen, R. A. Synowicki, Y.-H. Zhang, and S. R. Johnson, Appl. Phys. Lett. **106**, 061907 (2015).

[46] L. K. Casias, C. P. Morath, E. H. Steenbergen, G. A. U.-Membreno, P. T. Webster, J. V. Logan, J. K. Kim, G. Balakrishnan, L. Faraone, and S. Krishna, App. Phys. Lett. **116**, 182109 (2020).

[47] B. V. Olson, J. F. Klem, E. A. Kadlec, J. K. Kim, M. D. Goldflam, S. D. Hawkins, A. T.-Pedretti, W. T. Coon, T. R. Fortune, and E. A. Shaner, Phys. Rev. Appl. **7**, 024016 (2017).

[48] G. Ariyawansa, C. J. Reyner, J. M. Duran, J. D. Reding, J. E. Scheihing, and E. H. Steenbergen, Appl. Phys. Lett. **109**, 021112 (2016).

[49] N. Yoon, C. J. Reyner, G. Ariyawansa, J. M. Duran, J. E. Scheihin, J. Mabon, and D. Wasserman, J. Appl. Phys. **122**, 074503 (2017).

[50] L. Jiang, J. D. Gallagher, C. L. Senaratne, T. Aoki, J. Mathews, J. Kouvetakis, and J. Menéndez, Semicond. Sci. Technol. **29**, 115028 (2014).

[51] S. T. Schaefer, S. Gao, P. T. Webster, R. R. Kosireddy, and S. R. Johnson, J. Appl. Phys. **127**, 165705 (2020).

[52] G. D. Jenkins, C. P. Morath, and V. M. Cowan, Proc. SPIE **9226**, 92260S (2014).

[53] P. Bevington and D. K. Robinson, *Data Reduction and Error Analysis for the Physical Sciences* (McGraw Hill, Boston, 2003).

[54] D. Donetsky, S. P. Svensson, L. E. Vorobjev, and G. Belenky, Appl. Phys. Lett. **95**, 212104 (2009).

[55] C. Claeys and E. Simoen, *Radiation Effects in Advanced Semiconductor Materials and Devices* (Springer, Heidelberg, 2002).

[56] A. Rogalski, P. Martyniuk, and M. Kopytko, Prog. Quant. Electron. **68**, 100228 (2019).

[57] L. Höglund, D. Z. Ting, A. Khoshakhlagh, A. Soibel, A. Fisher, C. J. Hill, S. Keo, S. Rafol, and S. D. Gunapala, Appl.Phys. Lett. **108**, 263504 (2016).

[58] G. D. Jenkins, C. P. Morath, and V. M. Cowan, Proc. SPIE **9616**, 96160G (2015).

[59] V. M. Cowan, C. P. Morath, J. E. Hubbs, S. Myers, E. Plis, and S. Krishna, Appl. Phys. Lett. **101**, 251108 (2012).

[60] C. P. Morath, E. A. Garduno, G. D. Jenkins, E. A. Steenbergen, and V. M. Cowan, Inf. Phys. Technol. **97**, 448 (2019).

[61] C. P. Morath, E. A. Garduno, V. M. Cowan, and G. Jenkins, IEEE Trans. Nucl. Sci. **64**, 74 (2017).

[62] E. A. Garduno, V. M. Cowan, G. D. Jenkins, C. P. Morath, and E. H. Steenbergen, IEEE Trans. Nucl. Sci. **64**, 1042 (2017).

[63] S. Maimon and G. W. Wicks, Appl. Phys. Lett. **89**, 151109 (2006).

[64] V. M. Cowan, C. P. Morath, S. M. Swift, S. Myers, N. Gautum, and S. Krishna, Proc. SPIE **7945**, 79451S (2011).

[65] G. D. Jenkins, C. P. Morath, and V. M. Cowan, J. Electron. Mater. **46**, 5405 (2017).

[66] F. Capasso, K. Mohammed, and A. Cho, IEEE J. Quant. Electr. **22**, 1853 (1986).

[67] R. A. Carrasco, C. P. Morath, P. C. Grant, G. Ariyawansa, C. A. Stephenson, C. N. Kadlec, S. D. Hawkins, J. F. Klem, E. A. Shaner, E. H. Steenbergen, *et al.*, J. Appl. Phys. **129**, 184501 (2021).

[68] C. P. Morath, V. M. Cowan, L. A. Treider, G. D. Jenkins, and J. E. Hubbs, IEEE Trans. Nucl. Sci. **62**, 512 (2015).

[69] V. M. Cowan, C. P. Morath, S. M. Swift, P. D. LeVan, S. Myers, E. Plis, and S. Krishna, Proc. SPIE **7780**, 778006 (2010).

[70] D. Z. Ting, A. Soibel, A. Khoshakhlagh, S. A. Keo, A. M. Fisher, S. B. Rafol, L. Höglund, C. J. Hill, B. J. Pepper, and S. D. Gunapala, Appl. Phys. Lett. **118**, 133503 (2021).

[71] C. M. Castaneda, in *Proceedings of the IEEE Radiation Effects Data Workshop* (IEEE, 2001) p. 77.

[72] J. E. Hubbs, P. W. Marshall, C. J. Marshall, M. E. Gramer, D. Maestas, J. P. Garcia, G. A. Dole, and A. A. Anderson, IEEE Trans. Nucl. Sci. **54**, 2435 (2007).

[73] R. A. Carrasco, C. P. Morath, and P. T. Webster, (unpublished).

[74] R. A. Carrasco, J. George, D. Maestas, Z. M. Alsaad, D. Garnham, C. P. Morath, J. M. Duran, G. Ariyawansa, and P. T. Webster, J. Appl. Phys. **130**, 114501 (2021).

[75] Z. M. Fang, K. Y. Ma, R. M. Cohen, and G. B. Stringfellow, J. Appl. Phys. **68**, 1187 (1990).

[76] P. T. Webster, A. J. Shalindar, S. T. Schaefer, and S. R. Johnson, Appl. Phys. Lett. **111**, 082104 (2017).

[77] S. P. Svensson, D. Donetsky, D. Wang, H. Hier, F. J. Crowne, and G. Belenky, J. Cryst. Growth **334**, 103 (2011).

[78] A. Tixier, M. Adamcyk, and T. Tiedje, Appl. Phys. Lett. **82**, 2245 (2003).

[79] A. Janotti, S.-H. Wei, and S. B. Zhang, Phys. Rev. B. **65**, 115203 (2002).

[80] A. R. Reisinger, R. N. Roberts, S. R. Chinn, and T. H. M. II, Rev. Sci. Instrum. **60**, 82 (1989).

[81] B. C. Connelly, G. D. MEtcalfe, H. Shen, M. Wraback, C. J. Canedy, I. Vurgaftman, J. S. Melinger, C. A. Affouda, E. M. Jackson, J. A. Nolde, J. R. Meyer, and E. H. Aifer, J. Electron Mat. **42**, 3203 (2013).

[82] S. Wirths, D. Buca, and S. Mantl, Prog. Cryst. Growth Charact. Mater. **62**, 1 (2016).

[83] S. Gupta, B. Magyari-Köpe, Y. Nishi, and K. C. Saraswat, J. Appl. Phys. **113**, 073707 (2013).

[84] S. Kim, N. Bhargava, J. Gupta, M. Coppinger, and J. Kolodzey, Opt. Express **22**, 11029 (2014).

[85] W. Wang, S. Vajandar, S. L. Lim, Y. Dong, V. R. D'Costa, T. Osipowicz, E. S. Tok, and Y. C. Yeo, J. Appl. Phys. **119**, 155704 (2016).

[86] J. P. Gupta, N. Bhargava, S. Kim, T. Adam, and J. Kolodzey, Appl. Phys. Lett. **102**, 251117 (2013).

[87] W. Du, Y. Zhou, S. A. Ghetmiri, A. Mosleh, B. R. Conley, A. Nazzal, R. A. Soref, G. Sun, J. Tolle, J. Margetis, H. A. Naseem, and S.-Q. Yu, Appl. Phys. Lett. **104**, 241110 (2014).

[88] R. Roucka, J. Mathews, R. T. Beeler, J. Tolle, J. Kouvetakis, and J. Menéndez, Appl. Phys. Lett. **98**, 061109 (2011).

[89] M. Oehme, K. Kostecki, T. Arguirov, G. Mussler, K. Ye, M. Gollhofer, M. Schmid, M. Kaschel, R. A. Korner, M. Kittler, D. Buca, E. Kasper, and J. Schulze, IEEE Photonics Technol. Lett. **26**, 187 (2014).

[90] J. Hart, T. Adam, Y. Kim, Y. C. Huang, A. Reznicek, R. Hazbun, J. Gupta, and J. Kolodzey, J. Appl. Phys. **119**, 093105 (2016).

[91] S. Wirths, R. Geiger, N. V. D. Driesch, G. Mussler, T. Stoica, S. Mantl, Z. Ikonic, M. Luysber, S. Chiussi, J. M. Hartmann, H. Sigg, J. Faist, D. Buca, and D. Grützmacher, Nat. Photonics **9**, 88 (2015).

[92] R. Soref, Nat. Photonics **4**, 495 (2010).

[93] H. Tran, W. Du, S. A. Ghetmiri, A. Mosleh, G. Sun, R. A. Soref, J. Margetis, J. Tolle, B. Li, H. A. Naseem, and S.-Q. Yu, J. Appl. Phys. **119**, 103106 (2016).

[94] J. P. Fleurial and A. Borshchevsky, J. Electrochem. Soc. **137**, 2928 (1990).

[95] N. Bhargava, M. Coppinger, J. P. Gupta, L. Wielunski, and J. Kolodzey, Appl. Phys. Lett. **103**, 041908 (2013).

[96] N. Taoka, G. Capellini, V. Schlykow, M. Montanari, P. Zaumseil, O. Nakatsuka, S. Zaima, and T. Schroeder, Mater. Sci. Semicond. Process. **70**, 139 (2017).

[97] W. Doua, M. Benamara, A. Mosleh, J. Margetis, P. Grant, Y. Zhou, S. Al-Kabi, J. T. W. Du, B. Li, M. Mortazavi, and S. Q. Yu, Sci. Rep. **8**, 1 (2018).

[98] V. R. D'Costa, W. Wang, and Y. C. Yeo, J. Appl. Phys. **120**, 063104 (2016).

[99] V. R. D'Costa, W. Wang, Q. Zhou, E. S. Tok, and Y. C. Yeo, Appl. Phys. Lett. **104**, 022111 (2014).

[100] V. R. D'Costa, W. Wang, Q. Zhou, T. K. Chan, T. Osipowicz, E. S. Tok, and Y. C. Yeo, J. Appl. Phys. **116**, 053520 (2014).

[101] M. Medikonda, G. R. Muthinti, R. Vasic´, T. N. Adam, A. Reznicek, M. Wormington, G. Malladi, Y. Kim, Y.-C. Huang, and A. C. Diebold, J. Vac. Sci. Technol. B **32**, 061805 (2014).

[102] V. P. Martovitsky, Y. A. Aleshchenko, V. S. Krivobok, A. V. Muratov, A. V. Klekovkin, and A. B. Mehiya, Bull. Russ. Acad. Sci.: Phys. **82**, 418 (2018).

[103] R. Hickey, N. Fernando, S. Zollner, J. Hart, R. Hazbun, and J. Kolodzey, J. Vac. Sci. Technol. B **35**, 021205 (2017).

[104] C. J. K. Richardson, L. He, and S. Kanakaraju, J. Vac. Sci. Technol. B **29**, 03C126 (2011).

[105] W. X. Ni, K. Lyutovich, J. Alami, C. Tengstedt, M. Bauer, and E. Kasper, J. Cryst. Growth , 756 (2001).

[106] T. N. Nunley, T. I. Willett-Gies, J. A. Cooke, F. S. Manciu, P. Marsik, C. Bernhard, and S. Zollner, J. Vac. Sci. Technol. A **34**, 051507 (2016).

[107] D. W. Snoke, *Solid State Physics: Essential Concepts* (Addison-Wesley, San Francisco, 2009).

[108] T. N. Nunley, N. S. Fernando, N. Samarasingha, J. M. Moya, C. M. Nelson, A. A. Medina, and S. Zollner, J. Vac. Sci. Technol. B **34**, 061205 (2016).

[109] H. H. Li, J. Phys. Chem. Ref. Data **9**, 561 (1980).

[110] C. Kittel, *Introduction to solid-state physics* (Wiley, Hoboken, NJ, 2005).

[111] H. Huang and F. Liu, Phys. Rev. B **95**, 201101 (2017).

[112] A. W. Ewald and O. N. Tufte, J. Appl. Phys. **29**, 1007 (1958).

[113] S. H. Groves, C. R. Pidgeon, A. W. Ewald, and R. J. Wagner, J. Phys. Chem. Solids **31**, 2031 (1970).

[114] R. F. C. Farrow, D. S. Robertson, G. M. Williams, A. G. Cullis, G. R. Jones, I. M. Young, and P. N. J. Dennis, J. Cryst. Growth **54**, 507 (1981).

[115] C. A. Hoffman, J. R. Meyer, R. J. Wagner, F. J. Bartoli, M. A. Engelhardt, and H. Höchst, Phys. Rev. B **40**, 11693 (1989).

[116] C. L. Senaratne, P. M. Wallace, J. D. Gallagher, P. E. Sims, J. Kouvetakis, and J. Menéndez, J. Appl. Phys. **120**, 025701 (2016).

[117] S. Wirths, R. Geiger, N. von den Driesch, G. Mussler, T. Stoica, Z. I. S. Mantl, M. Luysberg, S. Chiussi, J. M. Hartmann, *et al.*, Nat. Photonics **9**, 88 (2015).

[118] A. Barfuss, L. Dudy, M. R. Scholz, H. Roth, P. Höpfner, C. Blumenstein, G. Landolt, J. H. Dil, N. C. Plumb, M. Radovic, *et al.*, Phys. Rev. Lett. **111**, 157205 (2013).

[119] F. H. Pollak, M. Cardona, C. W. Higginbotham, F. Herman, and J. P. V. Dyke, Phys. Rev. B **2**, 352 (1970).

[120] J. R. Chelikowsky and M. L. Cohen, Phys. Rev. B **14**, 556 (1976).

[121] T. Brudevoll, D. S. Citrin, M. Cardona, and N. E. Christensen, Phys. Rev. B **48**, 8629 (1993).

[122] M. Rohlfing, P. Krüger, and J. Pollmann, Phys. Rev. B **57**, 6485 (1998).

[123] S. Küfner, J. Furthmüller, L. Matthes, M. Fitzner, and F. Bechstedt, Phys. Rev. B **87**, 235307 (2013).

[124] H. U. Middelmann, L. Sorba, V. Hinkel, and K. Horn, Phys. Rev. B **35**, 718 (1987).

[125] R. E. Lindquist and A. W. Ewald, Phys. Rev. **135**, A 191 (1964).

[126] M. Cardona and D. L. Greenaway, Phys. Rev. **125**, 1291 (1962).

[127] M. Cardona, P. McElroy, F. H. Pollak, and K. L. Shaklee, Solid State Commun. **4**, 319 (1966).

[128] C. W. Higginbotham, F. H. Pollak, and M. Cardona, Solid State Commun. **5**, 513 (1967).

[129] S. Takatani and Y. W. Chung, Phys. Rev. B **31**, 2290 (1985).

[130] P. Fantini, M. G. Betti, C. Mariani, E. Magnano, M. Pivetta, and M. Sancrotti, Surf. Sci. **454-456**, 807 (2000).

[131] D. L. Price, J. M. Rowe, and R. M. Nicklow, Phys. Rev. B **3**, 1268 (1971).

[132] S. Zollner, Appl. Phys. Lett. **63**, 2523 (1993).

[133] D. Sherrington and W. Kohn, Rev. Mod. Phys. **40**, 767 (1968).

[134] D. Y. Smith, in *Handbook of Optical Constants*, edited by E. D. Palik (Academic Press, San Diego, 1998).

[135] H. B. Briggs and R. C. Fletcher, Phys. Rev. **91**, 1342 (1953).

[136] A. H. Kahn, Phys. Rev. **97**, 1647 (1955).

[137] E. O. Kane, J. Phys. Chem. Solids **1**, 249 (1956).

[138] J. R. Arthur, A. C. Baynham, W. Fawcett, and E. G. S. Paige, Phys. Rev. **156**, 740 (1966).

[139] We assume here, like in Ref. [119], that the second highest VB and the lowest CB at L have L_6^- and L_6^+ symmetry, respectively, in α-tin, just like in Ge, but this is actually an open question that should be answered by inspecting the symmetry of the wave functions obtained from band structure calculations .

[140] R. J. Wagner and A. W. Ewald, J. Phys. Chem. Solids **32**, 697 (1971).

[141] C. F. Lavine and A. W. Ewald, J. Phys. Chem. Solids **32**, 1121 (1971).

[142] C.-Z. Xu, Y.-H. Chan, Y. Chen, P. Chen, X. Wang, C. Dejoie, M.-H. Wong, J. A. Hlevyack, H. Ryu, H.-Y. Kee, *et al.*, Phys. Rev. Lett. **118**, 146402 (2017).

[143] D. Zhang, H. Wang, J. Ruan, G. Yao, and H. Zhang, Phys. Rev. B **97**, 195139 (2018).

[144] E. A. Fitzgerald, P. E. Freeland, M. T. Asom, W. P. Lowe, J. R. A.M̃acharrie, B. E. Weir, A. R. Kortan, F. A. Thiel, Y.-H. Xie, . M. S. A, *et al.*, J. Electron. Mater. **20**, 489 (1991).

[145] D. Imbrenda, R. Hickey, R. A. Carrasco, N. S. Fernando, J. VanDerslice, S. Zollner, and J. Kolodzey, Appl. Phys. Lett. , 122104 (2018).

[146] H.-S. Lan, S. T. Chang, and C. W. Liu, Phys. Rev. B **95**, 201201 (2017).

[147] M. P. Polak, P. Scharoch, and R. Kudrawiec, J. Phys. D **50**, 195103 (2017).

[148] C. Xu, C. Senaratne, R. J. Culbertson, J. Kouvetakis, and J. Menéndez, J. Appl. Phys. **122**, 125702 (2017).